

JAERI - M
93-149

MATERIAL AND DESIGN CONSIDERATIONS FOR
THE CARBON ARMORED ITER DIVERTOR

July 1993

Ivica ŠMID*, Masato AKIBA, Masanori ARAKI,
Satoshi SUZUKI and Kazuyoshi SATOH

日本原子力研究所
Japan Atomic Energy Research Institute

JAERI-M レポートは、日本原子力研究所が不定期に公刊している研究報告書です。
入手の問合せは、日本原子力研究所技術情報部情報資料課（〒319-11 茨城県那珂郡東海村）あて、お申しこしください。なお、このほかに財団法人原子力弘済会資料センター（〒319-11 茨城県那珂郡東海村日本原子力研究所内）で複写による実費頒布をおこなっております。

JAERI-M reports are issued irregularly.

Inquiries about availability of the reports should be addressed to Information Division Department of Technical Information, Japan Atomic Energy Research Institute, Tokaimura, Naka-gun, Ibaraki-ken 319-11, Japan.

© Japan Atomic Energy Research Institute, 1993

編集兼発行 日本原子力研究所
印 刷 いばらき印刷株

Material and Design Considerations for
the Carbon Armored ITER Divertor

Ivica ŠMID*, Masato AKIBA, Masanori ARAKI, Satoshi SUZUKI
and Kazuyoshi SATOH

Department of Fusion Engineering Research
Naka Fusion Research Establishment
Japan Atomic Energy Research Institute
Naka-machi, Naka-gun, Ibaraki-ken

(Received July 1, 1993)

The properties of materials for the carbon armored ITER divertor were evaluated from literature and manufacturers' documentation. Most of these data, however, have been not known or not published yet.

We have evaluated an optimum data set of the candidate materials of the ITER divertor, which were needed for finite element analyses (FEM). The materials evaluated are as follows; MFC-1, CX2002U, SEP-N112, P-130, IG-430U for the carbon based materials, and Oxygen Free Copper (OFCu), Dispersion Strengthened Copper (DSCu), TZM, W5Re and W-Cu as a heat sink material. It should be noted that W-Cu is first proposed for a heat sink application of the ITER divertor plate.

The finite element analyses were performed for the residual stress induced by brazing, thermal response and thermal stresses under a uniform heat flux of 15 MW/m^2 to the plasma facing surface. The stress free temperature of 750°C is assumed for the residual stress by brazing. Ten different geometries of the divertor were considered in the analyses including possible material combinations.

The FEM results show that the material combinations of MFC-1 and W-30Cu or DSCu in the flat-plate geometry satisfy the presently accepted ITER requirements. The combinations of CX2002U and TZM or W5Re is con-

* Austrian Research Centre

sidered a good choice in terms of residual and thermal stresses, whereas the surface temperature exceeds the ITER requirements.

Keywords: ITER, Divertor, Carbon Based Materials, Heat Sink Materials, W-Cu Materials, FEM Analysis, Material Database, Material Design, Residual Stress, Thermal Stress

炭素系材料をアーマに用いた I T E R ダイバータの材料と設計について

日本原子力研究所那珂研究所核融合工学部

Ivica ŠMID*・秋場真人・荒木政則

鈴木 哲・佐藤和義

(1993年7月1日受理)

従来、炭素アーマ材料をもつ I T E R ダイバータ板の材料物性値は文献及びメーカーの資料から評価してきた。しかし、物性値の中にはまだデータが得られていないか、又は公表されていないものが多くある。

そこで、 I T E R ダイバータ板の候補材料の物性値について、有限要素解析を行う上で最適なデータセットを評価した。評価した材料は、炭素系材料として、 M F C - 1 , C X 200 2 U , S E P - N 112 , P - 130 , I G - 430 U , ヒートシンク材料として無酸素銅 (O F C u) , 分散強化銅 (D S C u) , T Z M , W 5 R e , W - C u である。なかでも、 W - C u は今回初めて I T E R ダイバータ板への適用が提案されたものである。

有限要素解析は、ろう付け時の残留応力並びにプラズマに面する表面に $15 \text{MW}/\text{m}^2$ の一様定常熱負荷が加わった時の熱応答および熱応力について、汎用有限要素コード A B A Q U S を用いて行った。ろう付け時の応力開放温度には750度Cを採用した。また、解析に用いたダイバタ板の形状には異なる10種類の形状を採用するとともに、可能な材料の組み合わせについても検討を行った。

その結果、平板型の M F C - 1 と W - 30 C u , M F C - 1 と D S C u の組み合わせが I T E ダイバータ板の設計条件を満たすことが明かとなった。一方、 C X 200 2 U は T Z M または W 5 R e と組み合わせることにより、応力を緩和できることが明かとなったが、表面温度が I T E R 設計条件を越えることが明かとなった。

Contents

1. Summary	1
2. Introduction	2
3. Material Properties	3
3.1 Carbon-Fiber-Reinforced-Carbon (C/C) Materials, and Graphite ..	3
3.2 Copper Alloys	6
3.3 Molybdenum, and Alloys	6
3.4 Tungsten, and Re Alloys	7
3.5 Cu-Infiltrated W-Cu Composite Materials (Pseudo-Alloys)	7
3.6 Nb-1Zr	9
4. Joining of Dissimilar Materials	9
5. Design Prestudy: Brazing Angles	10
5.1 Combinations with CX2002U	10
5.2 Combinations with MFC-1	11
6. Finite Element Modeling of Different Divertor Designs	12
6.1 Thermal FEM Analyses	12
6.2 Elastic and Inelastic Stress Analyses	13
7. Divertor Designs and FEM Evaluation	14
7.1 Closed Designs	14
7.1.1 Monoblock Type	14
7.1.2 Piped Monoblock Type	15
7.2 Open Designs	16
7.2.1 Flat-Plate Type	16
7.2.2 Saddle Type	16
7.2.3 Bent Brazing Interface Types	17
7.2.4 Angle at the Open End of the Brazing Interface in Combinations of: MFC-1 + DS-Cu	17
7.2.5 Angle at the Open End of the Brazing Interface in Combinations of: MFC-1 + W-30Cu	18
8. Comparison of 2-dim. and 3-dimensional FEM-Analyses	18
9. Double Heat Flux and Other Thermal Considerations	19
10. Conclusions	20
Acknowledgments	20
References	21

目 次

1. 概要	1
2. はじめに	2
3. 材料物性値	3
3.1 炭素繊維強化炭素材料, 炭素	3
3.2 銅合金	6
3.3 モリブデン, モリブデン合金	6
3.4 タングステン, レニウム合金	7
3.5 銅合浸タングステン銅複合材料	7
3.6 ニオブ1ジルコニウム	9
4. 異種材料の接合	9
5. 予備設計: 接合角	10
5.1 CX2002Uとの組合せ	10
5.2 MFC-1との組合せ	11
6. 異種ダイバータデザインの有限要素解析	12
6.1 有限要素法による熱解析	12
6.2 弹性, 非弾性応力解析	13
7. ダイバータデザイン, 有限要素法による評価	14
7.1 開放端をもたないデザイン	14
7.1.1 モノブロック型	14
7.1.2 パイプモノブロック型	15
7.2 開放端をもつデザイン	16
7.2.1 平板型	16
7.2.2 サドル型	16
7.2.3 ベント接合型	17
7.2.4 MFC-1+DS-Cu	17
7.2.5 MFC-1+W-30Cu	18
8. 有限要素解析における二次元モデルと三次元モデルの比較	18
9. 热流束が2倍の場合及び他の热条件考察	19
10. まとめ	20
謝 辞	20
参考文献	21

1. Summary

The properties of candidate materials for the carbon armored ITER divertor were evaluated from literature and manufacturers' documentation. Many of these data were not known or not published yet. For the armor the following materials were considered: MFC-1 (uni-directional (1D) carbon-fiber-composite (C/C) material, maker Mitsubishi Kasei Corp., Japan), CX2002U (2D C/C, Toyo Tanso Co., Japan), SEP-N112 (3D C/C, Société Européenne de Propulsion, France), P-130 (1D C/C, Amoco Performance Products Inc., USA) and IG430U (isotropic graphite, Toyo Tanso Co., Japan). For the heat sink the following alloys were considered: oxygen free copper (OF-Cu), dispersion strengthened copper (DS-Cu), TZM, W5Re and the pseudo-alloy W-30Cu. For every material an optimum data set, as needed for finite element modeling, was evaluated.

The thermal response to a uniform heat flux of 15 MW/m^2 (steady state) applied to the plasma facing surface, and the residual as well as thermal stresses were calculated using the finite element code ABAQUS. Braze solidification at 750°C was assumed. The output of each thermal analysis was used as the final condition for the subsequent stress analysis. Ten different divertor plate geometries were generated, and applied to several possible material combinations. In total 65 2-dimensional cases, and one 3-dimensional case, were analyzed. The geometry of the ten different divertor plate models was chosen such, that a direct comparison of the thermal response and the stress levels is possible not only among the geometries, but also between different materials combinations.

The pseudo-alloy W-30Cu is proposed for a heat sink application in ITER divertor plates for the first time. The thermal performance as well as the residual brazing and the thermal stresses are predicted for combinations with a MFC-1 or CX2002U armor for different geometries.

The impact of the angle in the brazing constituents at the open end of the interface on the residual stress was evaluated by 2-dimensional FEM. For the 2D composite material CX2002U, DS-Cu with and without an intermediate OF-Cu layer, TZM and W5Re substrates, respectively, were considered, whereas MFC-1 was combined with either DS-Cu or W-30Cu.

With regard to the presently accepted ITER requirements, the material combinations MFC-1 plus W-30Cu, and MFC-1 plus DS-Cu, in the flat-plate as well as bent-braze-interface design, qualify best for a divertor plate application. For the monoblock design the combinations CX2002U plus TZM or W5Re are considered a good choice in terms of residual and thermal stresses, whereas even with a copper based heat sink the allowable peak surface temperatures are exceeded.

2. Introduction

From today's point of view the Tokamak magnetic confinement is the only promising concept for a successful and efficient energy production by controlled thermonuclear fusion. Of major challenge in materials R&D as well as design are the divertor plates - the only deliberate interface between the burning plasma and solid matter [1-3].

Heat fluxes of 15-30 MW/m² in normal operation are expected due to the incident ions, electrons and γ , causing severe materials erosion. Fatigue due to cyclic operation and sweeping of the X-point, thermal shocks due to uncontrollable plasma disruptions and run-away electron events, plus damage and materials degradation due to neutron-irradiation, will contribute to the harsh environment.

The requirements for divertor and first wall materials, in particular for brazed components, are listed in table 2. A solution to every single point is available today. No design concept, however, can meet all demands at the same time. Some desired properties - top priority issues for the first wall, are only of secondary importance for near-term divertor plates: post activation/disposal, repeated exchange, price, etc. The main (experimental) activities of today's R&D on divertor plates aim at improving the heat removal and fatigue capabilities, reliability and overall operation, see e.g. [4-11].

The presently accepted parameters for the normal operation of ITER divertor plates are as follows:

- 15 MW/m² steady state heat removal,
- with peak surface temperatures $\leq 1000^\circ\text{C} \sim 1100^\circ\text{C}$,
- use of high strength alloys for the heat sink,
- only minor deformation under one-sided heating,
- resistance to more than 10.000 plasma discharges at full power,
- low erosion off the plasma exposed surface, and
- neutron irradiation resistance,

to enable continuous operation without divertor replacement for ~ 1 year.

Further, in the present study the following criteria were taken as a basis, if a material/design qualifies for an application in divertor targets:

- no permanent (i.e. no inelastic) deformation due to the residual brazing stresses,
or due to the thermal loading at 15 MW/m²,
- the predicted residual and/or thermal stresses must not exceed the ultimate strength of the respective material.

In order to keep the $Z_{\text{effective}}$ low in the plasma, facing surfaces may either be composed of low-Z materials, or contain only low-erosion high-Z elements combined with lower plasma edge temperatures.

For near-term fusion machines carbon-fiber-reinforced-carbon materials (C/C) are considered as prime candidates for the plasma facing armor. Advanced carbon fibers have been developed recently with a thermal conductivity beyond 1000 W/mK (see e.g. [26-29]). This happens to be ~ 10 (!) times the value of isotropic graphite, which served as the reference plasma facing material only a few years ago. New brazing techniques are to be developed for the probable materials combinations [12-14].

3. Material Properties

The aim of the present study was to compare materials and material combinations, based upon thermal as well as deformation/stress finite element (FEM) analyses. A rather conservative approach was taken: only (commercially) available and characterized materials were applied in the evaluations.

A very useful and comprehensive data base of divertor candidate materials for finite element modeling was collected and reported by E. Zolti [15]. More thermal and mechanical properties for all considered materials were evaluated from literature [16-65], from manufacturer's documentation/private communication [66-75], or newly measured, such as for MFC-1 (1992) [76]. For almost all of the considered materials more than one data set was available. The properties chosen for the analyses were either measured or reported later, in better agreement with other authors, or measured for a material/component, which was already tested for its fusion relevant performance. The relevant properties of all considered materials are listed in tables 3.a-d and plotted in figures 3.a-b.

Since the main purpose of running tokamak experiments at present is to study the basic plasma performance rather than to prove the technological reliability of divertor plates over a full life-time period, any plasma resistant & highly conductive material combination/design makes a reasonable candidate for the divertor. For the so-called physics and technology phase of ITER, not only excellent overall heat removal will be needed. Also resistance to fatigue and neutron irradiation plus a wide margin in passive safety in off-normal events and integrity after long-term operation are required. Thus only high strength materials are to be considered for the heat sink.

3.1 Carbon-Fiber-Reinforced-Carbon (C/C) Materials, and Graphite

For their high thermal conductivity, good thermal shock resistance and favorable erosion properties plus a very high sublimation temperature and low activation after 14 MeV neutron irradiation, C/C armored divertor plates are very promising for ITER.

For the preset study only carbon materials were considered as the plasma facing armor of divertor plates, namely the following one-, two- and three-directional (1D, 2D and 3D) C/Cs:

MFC-1 (1992), 1D, maker: Mitsubishi Kasei Corp., Japan,
 CX2002U, 2D, maker: Toyo Tanso Co., Japan,
 SEP-N112, 3D, maker: Société Européenne de Propulsion, France,
 P-130, 1D, thermal analyses only, Amoco Performance Products, Inc., USA

In addition a reactor grade graphite was included in the analyses:

IG430U, isotropic graphite, maker: Toyo Tanso Co., Japan.

It should be noted here that for the carbon materials considered in the analyses a temperature dependence of the thermal expansion was not always available.

The thermal conductivity of graphites and C/Cs was reported to decrease after short neutron irradiation [23, 24]. The percentage of reduction is comparable for similar materials, and typically bigger for C/Cs with an initially high value. The remaining conductivity after neutron irradiation, however, still appears to be better for C/Cs with an initially higher value.

The tritium retention is a severe drawback for C-based materials in a fusion-like environment. By reducing the open porosity this situation is improved. The thermal shock resistance and/or fracture toughness, however, might be impaired by a higher density [72, 73].

Uni-Directional (1D): MFC-1 (1992)

MFC-1 (Mitsubishi Kasei Corp., Japan) is a uni-directional C/C with a high orientation of its pitch-type fibers and a distinct anisotropy of its thermal and mechanical properties in different directions:

the thermal conductivity parallel (\parallel) to the fibers is a factor of ~25 higher than perpendicular (\perp) to the fibers. For the Young's modulus (YM) and the tensile strength this anisotropy factor is ~100. Naturally different properties \parallel and \perp to the fiber direction had to be used in the FEM calculations. Since the Poisson ratio (PR) must be smaller than the square root of the ratio of the corresponding two YM_i - PR₂₁ < (YM₁/YM₂)^{1/2} - the stiffness matrix had to be used to describe the elastic properties instead of giving the YM_i, shear moduli and the PRs; see [83] and CX2002U (see later).

The high thermal expansion of MFC-1 perpendicular to the fibers ($\alpha \sim 12 \times 10^{-6}/K$) does not compare to the negative or "no" expansion parallel to the fibers ($\alpha \sim -0.9 \times 10^{-6}/K$) at all. That phenomenon is already known for pyrolytic graphite [19]. The thermal expansion of $\sim 12 \times 10^{-6}/K$ of MFC-1 (\perp), however, can easily be met by W-Cu (pseudo-)alloys, see there.

Today's uni-directional C/Cs typically feature a lower porosity than two-directional C/Cs or isotropic graphite. In theory (nearly) full density should be achievable for 1D C/Cs, if both, the orientation/packing of the fibers and the graphitization can be optimized. Full density of 100% without porosity is most desirable and could have a big impact on the tritium retention, and thus on the applicability of such materials for DT-plasma operation.

In the finite element modeling the fiber direction was oriented perpendicular to the plasma facing surface.

The material properties were collected from literature [16, 25], and manufacturer's documentation [66]. The thermal conductivity was newly measured [76], see tables and figures 3.a-d.

Two-Directional (2D): CX2002U

CX2002U (Toyo Tanso Co., Japan) is a felt-type C/C with a typical fiber length of ~10 mm. Non-uniform compacting and chemical vapor infiltration to deposit pyrolytic carbon inside the fiber fabric are used to increase the density and the thermal conductivity of the precursor material. This not only increases the cost of production, it also contributes to the anisotropy of CX2002U and thus complicates analytical modeling. For the thermal as well as stress calculations, temperature *and* direction dependent properties (*different in all three directions*: thermal conductivity and expansion, Young's (YM) and shear (SM) moduli, where the shear moduli were calculated by: $SM_i = YM_i / 2(1+Poiss.\text{ratio}_i)$) had to be used for a correct prediction of the thermal response and the stresses in CX2002U/metal bonds - see [83].

For its low thermal expansion and high thermal conductivity CX2002U appears to be a suitable armor in the closed designs (monoblock, piped monoblock), in particular with a TZM or W5Re heat sink. Joining to soft copper is also possible due to the early yielding of OF-Cu.

The material properties were collected from literature [16], and manufacturer's documentation [68], see tables and figures 3.a-d.

In the modeling the direction of best thermal conductivity was oriented perpendicular, the direction of second best conductivity parallel to the plasma facing surface, whereas the direction of lowest conductivity was oriented parallel to the tube axis.

Three-Directional (3D): SEPCARB N112

SEP-N112 (SEP) (Société Européenne de Propulsion, France) is composed of multiple layers (2D weave), needled to each other. Therefore it is an "almost" 3D C/C. It features rather homogeneous thermal and mechanical properties in all directions, particularly a high compressive strength. Same as for CX2002U, chemical vapor infiltration is used to deposit the carbon matrix inside the fiber structure [70].

For the modeling, the main fiber plain, with higher thermal conductivity and strength, was oriented perpendicular to the tube axis.

The material properties were taken from the manufacturer's documentation and/or private communication [70, 71], see tables and figures 3.a-c.

Uni-Directional (1D): P-130

The development of carbon fibers with an "ultra-high" thermal conductivity was reported recently [26-29]. The reported mechanical properties of these are also rather impressive [29].

Since the data base for a composite bulk material with these fibers were not available, only thermal analyses in combination with a W-30Cu heat sink were performed. The thermal conductivity for a "bulk" P-130 parallel to the fiber direction was supplied by [74]. Perpendicular to the fiber direction the same thermal conductivity as for MFC-1 (1992) was assumed, from [76], see table and figure 3.a.

Isotropic Graphite: IG430U

Since isotropic graphite served as the reference plasma facing material until a few years ago, for the monoblock and the flat-plate type the combination with a TZM heat sink was included in the FEM analyses. The peak surface temperatures reached, however, are too high for any reasonable armor thickness here.

The material properties were collected from literature [16] and manufacturer's documentation [68], see tables and figures 3.a-c.

3.2 Copper Alloys

For its good conductivity, ductility and well characterized properties, copper was an obvious candidate for the heat sink of high heat flux components. In particular the easy brazability to non-metals, such as C/Cs, due to a low yield stress, makes the use of "soft"- or oxygen-free copper (OF-Cu) interesting for divertor plate development and for application in present tokamaks. A copper alloy with a higher strength, such as dispersion strengthened copper (DS-Cu) would be of high interest for ITER divertor plates, if the problems of joining to C/Cs can be fully overcome [14].

A rather comprehensive discussion of the fusion relevant properties of Cu-alloys was reported recently [30]. The material properties for the present analyses were collected from literature [15, 16, 30-34], and manufacturer's documentation [67], see tables and figures 3.a-d.

3.3 Molybdenum, and Alloys

Rather small amounts of titanium- and zirconium-(oxide) can improve the mechanical properties of pure molybdenum significantly. TZM, which still contains 99.3 wt% Mo, is the most important molybdenum alloy - containing Ti and Zr - for high temperature application. It is machinable at RT, has a high ductility, and a higher recrystallization temperature and strength than pure Mo [35-53, 69]. TZM is widely used for brazed composites, see e.g. [77], and was already successfully applied and tested in carbon-armored divertor plate mock-ups of different geometries, see e.g. [10, 11, 13, 77-80]. The material properties for the present analyses were collected from literature [34-53], and manufacturer's documentation [69], see tables and figures 3.a-c.

Mo41Re, with a high ductility even after recrystallization as well as improved weldability and higher recrystallization temperature than TZM, can be used as the coolant tube material in combination with a TZM heat sink [79, 80]. For its rather low thermal conductivity (see table and figure 3.a/II) it was not considered in the present analyses.

The thermophysical and mechanical properties of Mo5Re are similar to TZM, and thus a similar temperature/stress distribution is to be expected in FEM analyses. Therefore no extra calculations with Mo5Re were performed.

3.4 Tungsten, and Re Alloys

Most attractive for W and W-Re alloys are their high melting temperature, the rather low thermal expansion, and an interesting thermal conductivity (at lower rhenium contents). A high melting temperature is of interest for a wide margin in passive safety, and even for a possible in-situ annealing of C/Cs after longer neutron irradiation. A low thermal expansion (together with a high thermal conductivity) is favorable in combinations with 2D or 3D C/Cs for better match and also for lower stresses under one-sided heating.

A rhenium addition improves the strength of W alloys significantly, but degrades the thermal conductivity. Thermal conductivities of some tungsten alloys with differing rhenium contents are shown in table and figure 3.a/III.

The high temperature performance, the ductility and recrystallization resistance, ductile brittle transition temperature, fracture toughness as well as low temperature machinability are improved by a rhenium addition. W-5(wt%)Re was chosen for the analyses here, because its thermal conductivity is still ~90 W/mK, and the mechanical properties might be acceptable. This material is commercially available and mainly used for W-WRe thermo couples. The manufacture of high strength tubes and brazing to C/Cs is yet to be developed [75].

The material properties for technical tungsten and some W-Re alloys, as used in the present analyses were collected from literature [33-55], manufacturer's documentation [69] or private communication [71, 75]; the properties are listed in tables 3.a-d, and plotted in figures 3.a-b.

The ultimate strength of 1100 MPa was not reached in any of the analyses, although W5Re has the highest elastic modulus of all considered heat sink materials.

3.5 Cu-Infiltrated W-Cu Composite Materials (Pseudo-Alloys)

When tungsten powder is compacted and (partly) sintered to achieve only 50-90% of the possible density, a material with an extensive open porosity is produced. The tungsten particles are sintered to each other with intergranular bridging. Infiltration with liquid Cu leads to a dense composite material with properties in between pure copper and tungsten. A successful production of dense specimens in the range 10-50vol% Cu - due to the good wettability of tungsten with liquid copper - was reported [58]. However, almost no mutual solid solubility is reported for the W-Cu system - therefore "pseudo-alloy" [55-65], and thus the thermal conductivity in particular of the copper filler matrix is not impaired due to alloying. W-Cu alloys are commercially available and rather inexpensive.

Most important, the thermal expansion can be adjusted to any value between 6×10^{-6} and $12 \times 10^{-6}/K$.

Applying a different production method - mixing of W and Cu powder and subsequent sintering - materials with lower tungsten concentrations and thus thermal expansions up to the value of pure copper can be achieved. This production method, however, is not desired here. Due to the low sintering temperature (... low melting point of copper) no firm connection between the tungsten particles is established. If such W-Cu composites are subjected to temperatures in excess of the melting point of Cu, overall melting will occur.

For copper infiltrated composites with a coherent tungsten matrix this is not the case. Exceeding the melting temperature locally of course results in a melting of the copper filler, but the tungsten body will keep its shape. More important, the ultimate tensile strength of infiltration composites was reported twice as high as of directly sintered powder mixtures [58].

The fact, that the properties of copper-infiltrated W-Cu composites will not be degraded when subjected to temperatures up to even 1050°C is a clear advantage compared to DS-Cu.

The solubility of Mo in Cu was reported to be 0.6at% [58]. Since the thermal conductivity of Cu drops dramatically with little additions of other elements (e.g. Ni, Zn; see [31]), W-Cu alloys are to be preferred here. Pure Mo has a higher thermal expansion than W, requiring less Cu to match the expansion of MFC-1. Thus the thermal conductivity of Mo-Cu would be lower than for a W-Cu with the corresponding expansion value.

W-Cu is machinable at RT. Mo-Cu, however, can be machined much easier - even coined - due to the better ductility of Mo [65].

W-Cu (infiltration) composite materials are widely used as electrodes for electrical discharge machining (EDM, spark erosion), and as contact materials in high voltage switches.

Today's W-Cu composite materials are not optimized yet for a divertor heat sink application. Manufacture, thermal conductivity, ductility, brazability and machinability - possibly acceptable at the present stage - still could be improved by optimizing the sintering and infiltration process, changing the grain size, etc. [58, 59]. It might even be possible to use a tungsten powder of lengthy shape to achieve direction dependent properties (e.g. better thermal conductivity perpendicular to the brazing interface, combined with a lower electrical conductivity in the other directions to reduce eddy current forces). For a controlled tailoring of the mechanical properties tungsten fibers can be used instead of a powder to fabricate the porous tungsten body for infiltration with copper [55-57].

W-Cu parts can be produced up to big sizes (only limited by the production facilities). Some important properties for fusion application, such as formation of volatile oxides, corrosion, erosion, thermal shock resistance, neutron irradiation, activation, afterheat generation and recycling, still have to be evaluated. High heat flux loading experiments of W-Cu brazed to MFC-1 or CX2002U have already been started at JEBIS (JAERI Electron Beam Irradiation Stand) - K. Satoh, to be published [81].

The material properties for the present analyses were collected from literature [55-65], and manufacturer's documentation [69]; the data are listed in tables 3.a-d, and plotted in figures 3.a-b.

3.6 Nb-1Zr

The alloy Nb-1Zr is being studied in the field of nuclear fission, since it is rather promising for space nuclear power applications. That material was proposed for the heat-sink of a C/C-armored ITER divertor [82]. For its poor thermal conductivity, low strength before n-irradiation, a long lasting and rather high radioactive decay [42-44, 52-54], it was not considered in the present evaluations. Some thermal analyses, however, were performed to compare the heat removal performance of Nb-based materials to Cu-, Mo- and W-based alloys.

The material properties collected from literature [42-44, 52-54] are shown in tables and figures 3.a-b.

4. Joining of Dissimilar Materials

The principal ways of joining materials are [84]:

- a) mechanical, such as bolting, clamping (poor heat transfer),
- b) adhesive, or "gluing" (not heat resistant),
- c) reaction joining: hot isostatic pressing,
welding,
diffusion bonding,
active metal brazing.

From today's point of view, combinations of materials with a distinct difference in their chemical, physical as well as mechanical properties - such as C/Cs plus metal - need to be joined by brazing, to endure a typical fusion environment.

For the present study a braze with a melting/solidification temperature of 750°C was assumed. This comes close to the properties of "TiCuSil", a commonly used braze to join carbon materials to metals.

The effect of the thermo-physical or mechanical properties of the braze usually was not considered in the analyses. For the two closed designs (monoblock - table and figures 7.1.1, piped monoblock - table and figures 7.1.2) and the saddle type design (table and figures 7.2.2) the effect of a OF-Cu layer (0.5 mm thickness) between the tubular heat sink and the armor was considered. Since TiCuSil has a rather low yield strength, the above approach might not simulate only a coating with soft copper, but also the behavior of a braze layer.

3.6 Nb-1Zr

The alloy Nb-1Zr is being studied in the field of nuclear fission, since it is rather promising for space nuclear power applications. That material was proposed for the heat-sink of a C/C-armored ITER divertor [82]. For its poor thermal conductivity, low strength before n-irradiation, a long lasting and rather high radioactive decay [42-44, 52-54], it was not considered in the present evaluations. Some thermal analyses, however, were performed to compare the heat removal performance of Nb-based materials to Cu-, Mo- and W-based alloys.

The material properties collected from literature [42-44, 52-54] are shown in tables and figures 3.a-b.

4. Joining of Dissimilar Materials

The principal ways of joining materials are [84]:

- a) mechanical, such as bolting, clamping (poor heat transfer),
- b) adhesive, or "gluing" (not heat resistant),
- c) reaction joining: hot isostatic pressing,
welding,
diffusion bonding,
active metal brazing.

From today's point of view, combinations of materials with a distinct difference in their chemical, physical as well as mechanical properties - such as C/Cs plus metal - need to be joined by brazing, to endure a typical fusion environment.

For the present study a braze with a melting/solidification temperature of 750°C was assumed. This comes close to the properties of "TiCuSil", a commonly used braze to join carbon materials to metals.

The effect of the thermo-physical or mechanical properties of the braze usually was not considered in the analyses. For the two closed designs (monoblock - table and figures 7.1.1, piped monoblock - table and figures 7.1.2) and the saddle type design (table and figures 7.2.2) the effect of a OF-Cu layer (0.5 mm thickness) between the tubular heat sink and the armor was considered. Since TiCuSil has a rather low yield strength, the above approach might not simulate only a coating with soft copper, but also the behavior of a braze layer.

5. Design Prestudy: Brazing Angles

The singularity at the open end of the braze line is a well known problem when joining dissimilar materials, see e.g. [85-93]. A comprehensive literature study of the many analytical and experimental evaluations is under way - R.D. Watson, to be published [74].

5.1 Combinations with CX2002U

To optimize the micro-geometry at the open end of a braze interface, in particular to reduce singularity effects, the residual stresses vs. the angle between the interface and the open surface were evaluated in both, a CX2002U (CX) armor and a metal substrate.

Two series of calculations were performed:

- (I) CX2002U combined directly with a DS-Cu substrate,
or with an OF-Cu interlayer of 0.3, 0.6 and 1.8 mm thickness, respectively;
- (II) CX2002U combined with the refractory alloys TZM or W5Re.

All possible combinations of the angles 45°, 90°, 135° and 180° in the CX2002U and/or the metal were considered, totaling 16 calculations per materials combination, see figures 5.1.

The combination CX2002U with DS-Cu was chosen for the high mismatch in thermal expansion, and the rather high yield strength of DS-Cu. The combination CX plus DS-Cu with an OF-Cu interlayer is interesting for two reasons: to study the effect of:

- a soft compliant layer, and
- a thicker braze layer, since OF-Cu comes close to the properties of a soft braze.

At the left end surface of the model a symmetry plane was introduced by restraining all nodes of that edge in the x-x (i.e. horizontal) direction, see figures 5.a-c. The distance to the "brazing angle", i.e. to the open end at the right side of the braze line in every case was 20 mm.

8-noded quadrilateral generalized plain strain elements with biquadratic integration were used. A temperature of 750°C was assumed for braze solidification (i.e. the stress free condition). The residual stresses at RT were calculated. The direction dependence of the properties of CX2002U can be translated as follows:
direction x in figures 5.a-c corresponds with direction 1 in tables and figures 3.a-d,
direction y with direction 2, and z with 3.

The distribution of the von Mises stresses for two selected geometries is plotted in figures 5.a-c. The peak von Mises stresses near the brazing interface are plotted in figures 5.1 (note that every diagram is plotted twice: normalized to the angles in CX, e.g. 5.1.1/I, and normalized to the angles in the metal, e.g. 5.1.1/II).

In the case of CX2002U + DS-Cu combinations the stresses in Cu were limited by the yield strength of DS-Cu, ~460 MPa (at RT). Only for 45° in CX2002U the peak von Mises stresses were found to be significantly below yielding for any angle in DS-Cu. The relatively low stresses in the combinations 45° in CX with 90°, 135° or 180° in DS-Cu, however, still exceed the strength of CX2002U.

The use of an OF-Cu interlayer reduces in particular the stresses in the CX2002U, whereas in the DS-Cu there is a systematic, but compared to the strength rather insignificant change in the stress pattern - see figures 5.1. Small angles in CX and in the OF- plus DS-Cu substrate are found to generate lower residual stresses in CX.

The refractory alloys TZM and W5Re was combined with CX for their thermal expansion, which happens to range between the low (\parallel) and high (\perp) values of CX. The same tendency for the peak residual stress is found as for CX + DS-Cu combinations, only the stresses here appear to be typically 4~5 times lower. In particular combinations of 45° in CX with 90°, 135° or 180° in TZM or W5Re show low residual stresses, with the values in CX below its (tensile and) compressive strength and thus acceptable.

As a consequence to the above stress behavior, the piped monoblock divertor design was developed to reduce in particular the stresses on top of the coolant tube, but to keep the newly introduced singularity stresses as small as possible, see chapter 7.1.2.

5.2 Combinations with MFC-1

Since for MFC-1 only geometries with the fiber direction in MFC-1 parallel to an open and plane lateral surface (i.e. the combined angle in armor and heat sink = 180°) are of interest, the influence of the angles in the constituents at the open end of the brazing interface was studied directly in the divertor plate models, see 7.2.4 and 7.2.5.

6. Finite Element Modeling of Different Divertor Designs

The finite element modeling (FEM) was carried out on a FACOM VP-2600 supercomputer (4 gigaflops, maker: Fujitsu of Japan). The finite-element code ABAQUS (Version 4-9-1, 1992) [83] was used to predict the thermal response at a uniform heat flux to the top surface of 15 MW/m^2 (*steady state*) and the residual as well as thermal stresses. Braze solidification at 750°C (i.e. the stress free temperature) was assumed in all cases, with subsequent cooling to room temperature (RT, 20°C), where the residual stresses were taken. The output of the thermal calculation was used as the final condition for the subsequent stress analysis. The two-dimensional models were constructed with 8-noded isoparametric quadrilateral elements. In all elements the inside angles were $60^\circ \leq \angle \leq 120^\circ$. The lateral length was always smaller than 1.2 mm, near the braze line or in regions of higher stress preferably 0.3-0.8 mm. The number of nodes and elements, and the principal geometry for all divertor models is given in table 7.a.

8-noded generalized plain strain elements (i.e. "quasi-three-dimensional") with bi-quadratic integration were used to account for the stresses in the z-z direction (\parallel to the axis of the coolant tube). Since the used code does not provide for a coupled thermal/stress analysis with that kind of elements, the modeling had to be performed in two independent runs. For an incident heat flux of 15 MW/m^2 the temperature for every nodal point - the output of the thermal analysis - was used as input for the subsequent stress analysis.

When available, temperature-dependent properties were used for the armor and the heat sink. Anisotropic material properties were used in the case of MFC-1, CX2002U, SEP-N112 and P-130, to account for the preferred orientation of the fibers. Full-size two-dimensional models were applied in the calculations, whereas only one half is presented in figures 7. and 9. In the case of 3-dimensional analyses only a half-sized model was applied in the calculations, figures 8.b-c.

Issues concerning the material selection, design and/or the critical heat flux - with regard to FEM - of future divertor plates are being studied eagerly. The references in [96-106] are an arbitrary selection of recent papers.

6.1 Thermal FEM Analyses

The operational parameters for the ITER physics phase, combined with the following assumptions, were chosen as input for the thermal analyses:

- a uniform surface heat flux of 15 MW/m^2 , in steady state mode,
- coolant water conditions: 60°C , 3.5 MPa and 10 m/s flow velocity,
- a subroutine within ABAQUS [83] was used to calculate the increase in heat transfer film coefficient from simple forced-flow convection to subcooled nucleate boiling, in a self-consistent manner;
 - the non-boiling regime was modeled using the Dittus-Boelter equation [94], including $f(T_{\text{film}})$,
 - the boiling regime, including subcooled nucleate boiling, was modeled using Thom's correlation [95], figure 6.1

- d) to increase the level of the critical heat flux, a flow enhancement for vortex promotion - such as a twisted tape - is considered essential within the coolant channels of ITER divertor plates; a twisted tape insert, however, was *not* used in the present analyses, because no commonly accepted correlation was available, in particular for one-sided heating,
- e) to ease a direct comparison of the different material combinations and divertor designs analyzed, no heat radiation off the top or lateral surfaces was considered.

6.2 Elastic and Inelastic Stress Analyses

A linear temperature *decrease* was used for all node points to describe the transition from the temperature of assumed braze solidification at 750°C to room temperature (20°C). A uniform temperature over the entire model was assumed in each of the 25 increments. The prevailing stresses at RT were defined as the "residual stresses after brazing".

The steady state temperature profile at 15 MW/m² to the top surface was used to define the final temperature for the thermal stress analyses. Now a linear temperature *increase* was used for all node points to describe the transition from RT to steady-state conditions at 15 MW/m², over 25 increments. For a more realistic description of the loading conditions the actual transient is to be considered. But since the assumed linear temperature increase will deviate from the effective sequence of the temperature profiles by the rate of change rather than due to the prevailing temperatures itself, the effect on the predicted peak stresses can be neglected. When using inelastic material properties in a lifetime evaluation based on creep and fatigue, that assumption was not permitted. Since the maximum stresses will occur either at RT (*high residual stresses*, in particular with a big mismatch in thermal expansion), or when reaching the highest thermal gradients (*high thermal stresses* at 15 MW/m², in cases of low thermal conductivity together with a high elastic modulus), the above simplification is justified here.

A water pressure of 3.5 MPa was applied to the tube inner wall when calculating the "thermal stresses".

For OF-Cu, DS-Cu and TZM elastic and inelastic properties were available from literature. Thus plastic yielding was considered in the stress analyses.

The presently available data base for W-Re and W-Cu alloys is rather scarce, typically with a lack of the needed mechanical properties at elevated temperatures. No inelastic yielding was considered in the stress analyses. Also for all C/Cs and graphite only elastic behavior was assumed.

For the graphical output in figures 7. - 9. the stresses, temperatures and heat fluxes were extrapolated over the range of the integration points to the element edges, whereas for the tabular listings in tables 7. - 9. the values at the integration points were used (except for the temperature: monitored at some selected nodal points). This explains the sometimes higher values in the plots.

7. Divertor Designs and FEM Evaluation

The classification of divertor designs used here was with regard to the fact, if individual tiles are de-/re-brazable in situ.

The principal geometry applied in all calculations was: 25 mm total width, 32 mm overall height, 15 mm tube inner diameter, 1.5 mm min. heat sink thickness, 10 mm min. armor thickness (i.e. 11.5 mm for the minimum distance between the plasma facing surface and the coolant). The number of nodes, elements and the principal geometry for each considered design is given in table 7.a. A qualitative comparison of the "open" designs (flat, saddle, bent: individual armor tiles are exchangeable in situ) with the closed designs (monoblock, piped: a replacement of individual tiles is not possible) is given in table 7.b. Figure 7 shows the cross section through eight of the ten considered designs.

7.1 Closed Designs

7.1.1 Monoblock Type

In particular for 2D and 3D C/C armor the monoblock divertor plate type bears advantages in brazing and passive safety of performance. The development of machining and manufacture of divertor-shaped geometries is under way. Monoblock divertor mock-ups with different material combinations were already successfully manufactured and tested, see e.g. [1-9, 13]. The main advantage of the monoblock geometry is the uniform stress distribution around the coolant tube by eliminating singularities within the brazing interface (in the 2-dim. projection parallel to the axis of the coolant tube).

A listing of the maximum residual as well as thermal stresses in the armor and the coolant tube for different materials combinations, and the thermal performance is given in table 7.1.1. In figures 7.2.1.a-1 the corresponding plots, as generated by ABAQUS [83], are shown.

For 2D and 3D armor, such as CX2002U and SEP-N112, the lowest residual and/or thermal stresses are predicted with a TZM or W5Re heat sink. The thermal stresses in the heat sink are well below the corresponding ultimate or yield strength of these alloys. For the copper alloys with their higher thermal expansion the residual stresses are predicted even higher than the thermal stresses.

In the monoblock design the peak surface temperatures for any material combination exceed the ITER design limit. With a 1D armor, such as MFC-1, these temperatures are considerably higher than in combinations with the open designs (flat, bent); compare tables and figures 7.1 and 7.2; the peak stresses, however, appear to be unacceptably high in both, the armor and the heat sink.

The monoblock seems most attractive for combinations of 2D and 3D armor, such as CX2002U and SEP-N112, with a low-expansion heat sink, such as the refractory alloys TZM and W5Re. The stresses predicted in the armor typically do not exceed the strength, whereas the achieved surface temperatures are too high for the ITER operational requirements.

7.1.2 Piped Monoblock Type

Although the main advantage of the monoblock design is the lack of a stress singularity within the brazing interface, in the piped monoblock additional openings ("pipes") are introduced for a stress reduction on top of the coolant tube, see table and figures 7.1.2. Singularity points for stress are generated.

The shape of the piped openings in the CX2002U armor was studied in preceding analyses of the brazing angle for combinations with different metal substrates, see chapter 5. No braze joining is foreseen between the piped openings at the bottom side of the tube.

The comparison with the monoblock type (compare table and figures 7.1.1) shows, that the thermal performance of the piped monoblock design is only negligibly impaired by the piped openings. The stresses on top of the coolant tube can be somewhat reduced. Around the open end of the brazing interface higher stresses are predicted due to the distinct singularity.

Under one-sided heating and high incident heat fluxes in the monoblock lower peak stresses will occur than in the piped design. The openings along the coolant tube parallel to its axis, however, help to reduce the stresses in y-y direction within the plasma facing side - i.e. the important region for heat removal.

7.2 Open Designs

The heat sink for all open designs was made of one piece only. An additional tube for the coolant within the heat sink body, as used for divertor mock-ups formerly [1-7, 10-14], was not considered. Due to the shorter way of heat removal, a better thermal performance is achieved. In addition, a direct comparison to the closed geometries (monoblock, piped - see 7.1.) is possible.

7.2.1 Flat-Plate Type

Since brazing of graphite to refractory metal substrates was first developed for plane interfaces [77], the flat-plate type design was developed first for fusion high heat flux components. In fact for that simple design only standard machining is needed, plus it meets the heat removal requirements in combination with uni-directional C/C armor rather well. Due to the low elastic modulus of MFC-1, see table 3.d, the predicted residual and thermal stresses in combination with DS-Cu or W-30Cu will stay below the strength of all constituent materials.

Of the open designs, the flat-plate type is the easiest in terms of machining, surface pre-conditioning and metallizing. Also for the brazing no additional precautions are needed with respect to a possible mismatch in thermal expansion perpendicular to the brazing interface, certainly an advantage compared with the saddle type or with bent brazing interfaces.

A listing of the maximum residual as well as thermal stresses in the armor and the heat sink for different materials combinations, and the thermal performance is given in table 7.2.1. In figures 7.2.1.a-j the corresponding plots, as generated by ABAQUS [83], are shown.

The analyses with the material combinations MFC-1 plus DS-Cu, and MFC-1 plus W-30Cu for all open designs (flat, bent, saddle) are compared in tables and figures 7.2.4-5, see chapters 7.2.4 and 7.2.5.

Further the temperatures and stresses as predicted by 2-dim. and 3-dimensional FEM analyses are presented in table and figures 8., and the thermal performance at 30 MW/m² to the top surface is shown in table and figures 9., see chapter 9.

7.2.2 Saddle Type

The saddle type design combines advantages of the monoblock design as well as the open types. Not only the thermal performance with a 2D armor is as good as of the monoblock, it also is a good choice for 1D armor. Since the armor tiles are saddle-shaped, a displacement of the tiles in the brazing process is easier to control than for the flat-plate type. The heat sink consists of the bottom part of the armor and the coolant tube. This eases manufacture, and further allows to combine two different materials, such as OF-Cu and DS-Cu, or OF-Cu and TZM.

A listing of the maximum residual as well as thermal stresses in the armor and the heat sink for different material combinations, and the thermal performance is given in table 7.2.2. In figures 7.2.2.a-k the corresponding plots are shown.

Due to the distinct singularity of the 90° edge within the brazing interface, rather high stresses are predicted. In combinations with OF-Cu, however, this design has a very good thermal performance and was already successfully applied in divertor plate mock-ups [4, 7, 104]. It should be noted here, that the predicted stresses around the singularity point are such, that even a limited "micro"-failure in the joint still might not lead to immediate and overall disintegration.

7.2.3 Bent Brazing Interface Types

The bent interface types try to combine the properties of the saddle type without a distinct singularity within the brazing interface.

Two principal groups of designs were analyzed (figure 7.):

- (I) the "double-bent" kind (bent-10-bent, bent-15-bent and bent-30-bent), where the angle in the constituents at the open end of the braze line is always 90°.
- (II) the "oblique-angled" kind (bent-10-straight, bent-15-straight, bent-30-straight), where the inclination of the brazing interface is kept constant after reaching its maximum deviation from the horizontal; the angle at the open end is 80°, 75° and 60° in the armor, and 100°, 105° and 120° in the heat sink, respectively.

For both kinds, the flat-plate design is the extreme, with a bending angle of 0° (it represents bent-0-bent *and* bent-0-straight). The saddle type in a way is the extreme for 90° (bent-90-..), although not exactly double-bent or oblique-angled.

The degree of bending within the interface for every design is given with its name, e.g. bent-"30"-bent. The number gives the maximum inclination to the horizontal braze line of the flat-plate type.

7.2.4 Angle at the Open End of the Brazing Interface in Combinations of: MFC-1 + DS-Cu

For all open designs the material combination MFC-1 + DS-Cu was analyzed. The results are summarized in table and figures 7.2.4.

The thermal performance is very similar for all geometries. The predicted stresses particularly in the armor are *higher* in the bent--straight than in the bent--bent types. The most probable reason is a favorable stress distribution in the bent-bent types after deformation. If the problems with brazing DS-Cu to C/Cs can be overcome [14], all bent--bent types, as well as the flat-plate type, seem attractive candidate designs for that material combination.

The high stresses in the saddle type are due to the singularity point within the brazing interface.

7.2.5 Angle at the Open End of the Brazing Interface in Combinations of: MFC-1 + W-30Cu

Same as for DS-Cu in 7.2.4, the material combination MFC-1 + DS-Cu was analyzed for all open designs. The results are summarized in table and figures 7.2.5.

Here the thermal performance is very similar for all geometries too. The predicted stresses now are typically lower than in MFC-1 + DS-Cu combinations, and *lower* in the bent--straight than in the bent--bent types. This can be explained by a smaller deformation than in 7.2.4 due to the better match in thermal expansion.

The high stresses in the saddle type again are due to the singularity point in the brazing interface.

In terms of overall performance - peak surface temperature and maximum stresses - the bent-15-straight design with a MFC-1 armor and a W-30Cu heat sink, scored best with regard to the ITER operational requirements.

8. Comparison of 2-dim. and 3-dimensional FEM-Analyses

8-noded generalized plain strain elements with biquadratic integration were applied for all geometries and material combinations. For one combination, MFC-1 armor with a W-30Cu heat sink in the flat-plate geometry, additional calculations were performed to benchmark the technique of analysis:

- (1) 4-noded generalized plain strain elements with bilinear integration,
2-dimensional, and
- (2) 8-noded brick elements, 3-dimensional, with 12.5 mm thickness of the model in the z direction, realized in 16 parallel layers of elements,
both, (1) and (2) were compared to:
- (3) *8-noded generalized plain strain elements with biquadratic integration,
2-dimensional (chapters 6.and 7.).*

The geometry of the models and the size of the elements were kept constant, i.e. the 2-dim. projection of all three meshes was identical in terms of element size and the coordinates of the corner nodes of each element. The position of the integration points, however, was different in all three cases.

The principal geometry of all models is given in table 7.a. The results are compared in table 8.1 (see also table 7.2.1), and figures 8.1 and 7.2.1.d.

The thermal performance (temperature and heat flux profile) is predicted almost identically in all three cases. The - very small - difference in the peaking factor for the heat flux inside the coolant tube is caused by the different position of the integration points (closer to the element edge in case (3) - see ABAQUS [83]). No difference is predicted for the temperature, which is monitored at the nodal points.

7.2.5 Angle at the Open End of the Brazing Interface in Combinations of: MFC-1 + W-30Cu

Same as for DS-Cu in 7.2.4, the material combination MFC-1 + DS-Cu was analyzed for all open designs. The results are summarized in table and figures 7.2.5.

Here the thermal performance is very similar for all geometries too. The predicted stresses now are typically lower than in MFC-1 + DS-Cu combinations, and *lower* in the bent--straight than in the bent--bent types. This can be explained by a smaller deformation than in 7.2.4 due to the better match in thermal expansion.

The high stresses in the saddle type again are due to the singularity point in the brazing interface.

In terms of overall performance - peak surface temperature and maximum stresses - the bent-15-straight design with a MFC-1 armor and a W-30Cu heat sink, scored best with regard to the ITER operational requirements.

8. Comparison of 2-dim. and 3-dimensional FEM-Analyses

8-noded generalized plain strain elements with biquadratic integration were applied for all geometries and material combinations. For one combination, MFC-1 armor with a W-30Cu heat sink in the flat-plate geometry, additional calculations were performed to benchmark the technique of analysis:

- (1) 4-noded generalized plain strain elements with bilinear integration,
2-dimensional, and
- (2) 8-noded brick elements, 3-dimensional, with 12.5 mm thickness of the model in the z direction, realized in 16 parallel layers of elements,
both, (1) and (2) were compared to:
- (3) *8-noded generalized plain strain elements with biquadratic integration,
2-dimensional (chapters 6.and 7.)*

The geometry of the models and the size of the elements were kept constant, i.e. the 2-dim. projection of all three meshes was identical in terms of element size and the coordinates of the corner nodes of each element. The position of the integration points, however, was different in all three cases.

The principal geometry of all models is given in table 7.a. The results are compared in table 8.1 (see also table 7.2.1), and figures 8.1 and 7.2.1.d.

The thermal performance (temperature and heat flux profile) is predicted almost identically in all three cases. The - very small - difference in the peaking factor for the heat flux inside the coolant tube is caused by the different position of the integration points (closer to the element edge in case (3) - see ABAQUS [83]). No difference is predicted for the temperature, which is monitored at the nodal points.

The predicted peak stresses in the MFC-1 armor are very similar in all three cases. It should be noted, however, that a 2-dimensional model cannot predict a change in the stress level in the z-z direction, although the MFC-armor is very sensitive to tensile (and compressive) stresses perpendicular to the fiber direction.

Compared to the 3-dimensional calculation, the peak compressive thermal stresses in the heat sink are predicted rather accurate by 2-dim. FEM, and the peak tensile thermal stresses are only slightly under-estimated.

9. Double Heat Flux and Other Thermal Considerations

For the materials combination MFC-1 and "bulk" P-130 armor with a W-30Cu heat sink in the flat-plate and bent-15-straight design the thermal performance was calculated for both, a heat flux of 15 and 30 MW/m². The thermal stresses at 30 MW/m² were calculated for a MFC-1 armor only, since the mechanical properties for a bulk composite material with P-130 fibers were not available. The results are presented in table 9.1, and in the figures 7.2.1.d, 7.2.5.d and 9.a-c.

Again it should be noted here, that no twisted tape insert for vortex promotion was considered in the thermal analyses.

The thermal stresses in the MFC-1 armor appear to be acceptable for the bent-15-straight design at 30 MW/m², whereas in the heat sink the predicted stresses exceed the strength of W-30Cu, see table 9.1 and figures 9.c.

The thermal performance at 15 MW/m² for the material combination Nb-1Zr heat sink with a MFC-1 armor, was simulated for the flat-plate and bent-15-straight designs. Since in both cases the peak surface temperature exceeds 2000°C, the residual and thermal stresses were not calculated.

The predicted peak stresses in the MFC-1 armor are very similar in all three cases. It should be noted, however, that a 2-dimensional model cannot predict a change in the stress level in the z-z direction, although the MFC-armor is very sensitive to tensile (and compressive) stresses perpendicular to the fiber direction.

Compared to the 3-dimensional calculation, the peak compressive thermal stresses in the heat sink are predicted rather accurate by 2-dim. FEM, and the peak tensile thermal stresses are only slightly under-estimated.

9. Double Heat Flux and Other Thermal Considerations

For the materials combination MFC-1 and "bulk" P-130 armor with a W-30Cu heat sink in the flat-plate and bent-15-straight design the thermal performance was calculated for both, a heat flux of 15 and 30 MW/m². The thermal stresses at 30 MW/m² were calculated for a MFC-1 armor only, since the mechanical properties for a bulk composite material with P-130 fibers were not available. The results are presented in table 9.1, and in the figures 7.2.1.d, 7.2.5.d and 9.a-c.

Again it should be noted here, that no twisted tape insert for vortex promotion was considered in the thermal analyses.

The thermal stresses in the MFC-1 armor appear to be acceptable for the bent-15-straight design at 30 MW/m², whereas in the heat sink the predicted stresses exceed the strength of W-30Cu, see table 9.1 and figures 9.c.

The thermal performance at 15 MW/m² for the material combination Nb-1Zr heat sink with a MFC-1 armor, was simulated for the flat-plate and bent-15-straight designs. Since in both cases the peak surface temperature exceeds 2000°C, the residual and thermal stresses were not calculated.

10. Conclusions

The monoblock divertor design seems most attractive for combinations of a 2D- and 3D-C/C armor, such as CX2002U and SEP-N112, with a low-expansion heat sink, such as the refractory alloys TZM and W5Re. The stresses predicted in the armor typically do not exceed the strength, whereas the achieved surface temperatures are too high for the present operational requirements of ITER.

Under one-sided heating and high incident heat fluxes in the monoblock lower peak stresses will occur than in the piped monoblock design due to the additional stress singularity. The openings along the coolant tube parallel to its axis, however, help to reduce the stresses in the plasma facing region - i.e. the important side for heat removal.

The saddle type design combines advantages of the monoblock design as well as the open types. Due to the distinct singularity of the 90° edge within the brazing interface, rather high stresses are predicted. In combinations with OF-Cu, however, this design has a very good thermal performance and was already successfully applied in divertor plate mock-ups. The predicted stresses around the singularity point, however, are such that even a limited "micro"-failure in the joint still might not lead to immediate and overall disintegration.

The pseudo-alloy W-30Cu is proposed for a heat sink application in ITER divertor plates for the first time. The thermal performance as well as the residual brazing and the thermal stresses are predicted for combinations with a MFC-1 or CX2002U armor for different geometries.

The flat-plate design meets the heat removal requirements of ITER in combination with uni-directional C/C armor rather well. Due to the low elastic modulus of MFC-1 the predicted residual and thermal stresses in combination with DS-Cu or W-30Cu are well below the strength of all constituent materials.

MFC-1 plus W-30Cu with the flat-plate design was applied in a 3-dimensional FEM analysis to benchmark the 2-dimensional analytical method. Compared to the 3-dimensional calculation, the peak compressive thermal stresses in the heat sink are predicted accurately by 2-dimensional FEM, and the peak tensile thermal stresses are only slightly under-estimated. The predicted peak stresses in the MFC-1 armor are rather similar for 2-dimensional and 3-dimensional FEM analyses.

In terms of overall performance - peak surface temperature and maximum predicted stresses - the bent-15-straight design with a MFC-1 armor and a W-30Cu heat sink, scored best with regard to the present operational requirements of ITER.

Acknowledgments

The authors wish to thank Mr. W. Hashimoto of Nikon Systems, Japan, for his continuous support and advice in computer related work.

10. Conclusions

The monoblock divertor design seems most attractive for combinations of a 2D- and 3D-C/C armor, such as CX2002U and SEP-N112, with a low-expansion heat sink, such as the refractory alloys TZM and W5Re. The stresses predicted in the armor typically do not exceed the strength, whereas the achieved surface temperatures are too high for the present operational requirements of ITER.

Under one-sided heating and high incident heat fluxes in the monoblock lower peak stresses will occur than in the piped monoblock design due to the additional stress singularity. The openings along the coolant tube parallel to its axis, however, help to reduce the stresses in the plasma facing region - i.e. the important side for heat removal.

The saddle type design combines advantages of the monoblock design as well as the open types. Due to the distinct singularity of the 90° edge within the brazing interface, rather high stresses are predicted. In combinations with OF-Cu, however, this design has a very good thermal performance and was already successfully applied in divertor plate mock-ups. The predicted stresses around the singularity point, however, are such that even a limited "micro"-failure in the joint still might not lead to immediate and overall disintegration.

The pseudo-alloy W-30Cu is proposed for a heat sink application in ITER divertor plates for the first time. The thermal performance as well as the residual brazing and the thermal stresses are predicted for combinations with a MFC-1 or CX2002U armor for different geometries.

The flat-plate design meets the heat removal requirements of ITER in combination with uni-directional C/C armor rather well. Due to the low elastic modulus of MFC-1 the predicted residual and thermal stresses in combination with DS-Cu or W-30Cu are well below the strength of all constituent materials.

MFC-1 plus W-30Cu with the flat-plate design was applied in a 3-dimensional FEM analysis to benchmark the 2-dimensional analytical method. Compared to the 3-dimensional calculation, the peak compressive thermal stresses in the heat sink are predicted accurately by 2-dimensional FEM, and the peak tensile thermal stresses are only slightly under-estimated. The predicted peak stresses in the MFC-1 armor are rather similar for 2-dimensional and 3-dimensional FEM analyses.

In terms of overall performance - peak surface temperature and maximum predicted stresses - the bent-15-straight design with a MFC-1 armor and a W-30Cu heat sink, scored best with regard to the present operational requirements of ITER.

Acknowledgments

The authors wish to thank Mr. W. Hashimoto of Nikon Systems, Japan, for his continuous support and advice in computer related work.

References

- [1] T. Kuroda, G. Vieider, M. Akiba et al.
ITER Plasma Facing Components
 ITER Documentation Series, No. 30, IAEA/ITER/DS/30, October 1991,
 Vienna, Austria
- [2] G. Vieider, A. Cardella, M. Akiba, R. Matera and R. Watson
ITER Plasma Facing Components, Design and Development
 Fusion Engrg. Design 16 (1991) 23-34
- [3] R.D. Watson, G. Vieider, G. Shatalov et al.
ITER Divertor Engineering Design
Summary of June-October Joint Working Session
 ITER-TN-PC-8-9-1, October 1989, Garching, FRG
- [4] M. Akiba, H. Takatsu, T. Kuroda, H. Hashizume, M. Araki, M. Dairaku, H. Ise,
 S. Suzuki, S. Tanaka, K. Yokoyama and M. Seki
Development of Plasma Facing Components at JAERI
 Fusion Engrg. Design 18 (1991) 99-104
- [5] R.T. McGrath, J.A. Koski, R.D. Watson, R.A. Causey, C.D. Croessmann, J.F.
 Dempsey, M. Hosking, K.A. Neimer, A.J. Russo, J.C. Salmonson, J. Stephens,
 M.F. Smith, J.G. Watkins and J.B. Whitley
Design Considerations for ITER Plasma Facing Components
 Sandia Report, SAND89-0901, July 1989
- [6] M. Seki, M. Guseva, G. Vieider and J.B. Whitley
ITER Related R&D on Low-Z Plasma-Facing Materials for Divertor and
First Wall
 J. Nucl. Mater. 179-181 (1991) 1189-1192
- [7] M. Akiba, H. Bolt, R. Watson, G. Kneringer and J. Linke
The Development of Divertor and First Wall Armour Parts at JAERI,
Sandia N.L. and KFA Jülich
 Fusion Engrg. Design 16 (1991) 111-125
- [8] A. Cardella, E. Di Pietro, M. Brossa, U. Guerreschi, M. Reale, N. Reheis and
 G. Vieider
Design Manufacturing and Testing of the Monoblock Divertor
 17th Symp. On Fusion Technology (SOFT), Sept. 1992, Rome, Italy
- [9] R.D. Watson, F.M. Hosking, M.F. Smith and C.D. Croessmann
Development and Testing of the ITER Divertor Monoblock Braze Design
 Fusion Technology 19 (1991) 1794-1798
- [10] I. Smid, A. Cardella, C.D. Croessmann, R.D. Watson, N. Reheis and G. Kneringer
Response to High Heat Fluxes and Metallurgical Examination of a Braze
Carbon-Fiber-Composite / Refractory-Metal Divertor Mock-Up
 Fusion Engrg. Design 18 (1991) 125-133

- [11] I. Smid, C.D. Croessmann, R.D. Watson, J. Linke, A. Cardella, H. Bolt, N. Reheis and E. Kny
Performance of Brazed Graphite, Carbon-Fiber Composite, and TZM Materials for Actively Cooled Structures: Qualification Tests
Fusion Technology 19 (1991) 2035-2040
- [12] F. Brossa, E. Franconi and P. Schiller
Development of Graphite/Metals Bondings for Fusion Reactor Applications
J. Nucl. Mater. 191-194 (1992) 469-472
- [13] N. Reheis, M. Witwer, G. Kneringer, G. Vieider, A. Cardella and E. Di Petro
Industrial Aspects in the Fabrication of Prototypes for Different Divertor Concepts
17th Symp. On Fusion Technology (SOFT), Sept. 1992, Rome, Italy
- [14] G. Chaumat, G. Lovato and P. Lemoine
Brazing CFC on DS-Copper for Divertor Flat Tiles
17th Symp. On Fusion Technology (SOFT), Sept. 1992, Rome, Italy
- [15] E. Zolti
Material Data for Predesign Analysis of In-Vessel Components
NET Internal Note N/I/3300/5/A, April 9, 1990; rev. Sept. 4, 1990
- [16] C.H. Wu, R. Behrisch, H. Bolt, T.D. Burchell, M. Budd, J. Davis, A.A. Haasz, J. v.d.Laan, I. Mazul, J. Roth, D. Smith, H. Takatsu, N. Vasiljev, E. Vietzke and G. Vieider
Notes of the Specialist Meeting on Material Data Base "Plasma Facing Materials"
Feb. 1990, Garching, FRG
- [17] A.T.D. Butland and R.J. Maddison
The Specific Heat of Graphite: An Evaluation of Measurements
J. Nucl. Materials 49 (1973/74) 45-56
- [18] W. Delle, J. Linke, H. Nickel and E. Wallura
Comparison of High Purity Fine Grain Graphites from Different Suppliers with Regard to Physical, Mechanical and Thermal Properties
JüL-Spez-401, May 1987, ISSN 0343-7639
- [19] E.P. Roth, R.D. Watson, M. Moss and W.D. Drotning
Thermophysical Properties of Advanced Carbon Materials for Tokamak Limiters
Sandia Report, SAND88-2057, UC-423, April 1989
- [20] J.W. Sapp, T.D. Burchell, C.R. Kennedy, F.R. Williams, J.R. Haines, J.W. Davis, D.A. Bowers, M.A. Witten, T.D. Smyka and M.D. McSmith
Status Report on Divertor and First Wall Material Selection for the Compact Ignition Tokamak
McDonnell Douglas, Report No. CIT-89-011, April 1989

- [21] M. Yamamoto, T. Ando, H. Takatsu, M. Shimizu, T. Arai, K. Kodama, H. Horiike, K. Teruyama, A. Kiuchi and Y. Goto
Evaluation Tests on First Wall and Divertor Plate Materials for JT-60 Upgrade
JAERI-M 90-119, July 1990
- [22] C. Garcia-Rosales, E. Gauthier, J. Roth, R. Schwörer and W. Eckstein
Temperature-Dependent Sputtering of Doped Graphites and Boron Carbide
J. Nucl. Materials 189 (1992) 1-8
- [23] B.A. Thiele, L. Binkele, K. Koizlik and H. Nickel
Effect of Neutron Irradiation on Thermal Conductivity of Carbon/Carbon Fiber Materials at 400 and 600 °C in the Fluence Range 10^{22} to 10^{24} m^{-2}
16th Int. Symp. ASTM STP, N.H. Packan, R.E. Stoller and A.S. Kumar, Eds. (American Society for Testing and Materials), Philadelphia 1992, USA
- [24] T. Maruyama and M. Harayama
Neutron Irradiation Effect on the Thermal Conductivity and Dimensional Change of Graphite Materials
J. Nucl. Materials 195 (1992) 44-50
- [25] K. Ioki, K. Namiki, S. Tsujimura, M. Toyoda, M. Seki and H. Takatsu
Development of High Conductive C/C Composite Tiles for Plasma Facing Armor
Fusion Engrg. Design 15 (1991) 31-38
- [26] J.W. Sapp and D.A. Bowers
Development of High Thermal Conductivity Carbon-Carbon Composites
Ex-Abs. 20th Biennial Conf. on Carbon (1991)
- [27] D.A. Bowers and J.W. Sapp
Carbon-Based Materials Thermal Development Testing and Selection Process for First Wall and Divertor Applications
J. Nucl. Materials 191-194 (1992) 305-308
- [28] M. Merola and R. Matera
Optimization of the Monobloc Divertor Plate by the Use of Ultrahigh Thermal Conductivity Carbon Fibers
Comm. of the European Communities, JRC-Ispra, EUR 13594 EN, 1991
- [29] R. Matera and M. Merola
High Thermal Performance CFC Divertor
10th Topical Meeting on the Technology of Fusion Energy, June 1992, Boston, USA
- [30] G.J. Butterworth and C.B.A. Forty
A Survey of the Properties of Copper Alloys for Use as Fusion Reactor Materials
J. Nucl. Materials 189 (1992) 237-276
- [31] G.J. Butterworth
Transmutation and Activation Effects in High-Conductivity Copper Alloys Exposed to a First Wall Fusion Neutron Flux
J. Nucl. Materials 135 (1985) 160-172

- [32] J.J. Stephens and D.T. Schmale
The Effect of High Temperature Braze Thermal Cycles on Mechanical Properties of a Dispersion Strengthened Copper Alloy
 Sandia Report, SAND87-1296, UC-20, August 1988
- [33] K. Kitamura, K. Nagata, M. Shibui, T. Fuse, N. Tachikawa, M. Akiba, M. Araki and M. Seki
Experimental and Analytical Studies on Residual Stress in the Tungsten-Copper Duplex Structure for a Divertor Application
 Fusion Engrg. Design 18 (1991) 173-178
- [34] Japan Society of Mechanical Engineers, JSME Data Book,
 4th Edition, Tokyo 1986
- [35] R.I. Jaffee, C.T. Sims and J.J. Harwood
The Effect of Rhenium on the Fabricability and Ductility of Molybdenum and Tungsten
 Proc. 3. Plansee-Seminar pp. 380-411, June 1958, Reutte, Austria
- [36] J.G. Booth, R.I. Jaffee and E.I. Salkovitz
The Mechanisms of the Rhenium-Alloying Effect in Group VI-A Metals
 Proc. 5. Plansee-Seminar pp. 547-564, June 1964, Reutte, Austria
- [37] B.F. Kieffer, G.S. Root and S.A. Worcester
Some Properties of Tungsten-Rhenium Alloys
 Proc. 5. Plansee-Seminar pp. 571-576, June 1964, Reutte, Austria
- [38] R.R. Vandervoort and W.L. Barmore
Elevated Temperature Deformation and Electron Microscope Studies of Polycrystalline Tungsten and Tungsten-Rhenium Alloys
 Proc. 6. Plansee-Seminar pp. 108-137, June 1968, Reutte, Austria
- [39] P. Krautwasser, H. Derz and E. Kny
Influence of Fast Neutron Fluence on the DBTT of Tungsten, W10Re and W3.4Ni1.6Fe
 Proc. 12. Plansee-Seminar, Vol. 1, pp. 673-681, May 1989, Reutte, Austria
- [40] H.H. Smith and D.J. Michel
The Effect of Irradiation on the Fatigue and Flow Behavior of TZM Alloy
 J. Nucl. Materials 66 (1977) 125-142
- [41] W.C. Hagel, J.A. Shields, Jr., and S.M. Tuominen
Processing and Production of Molybdenum and Tungsten Alloys
 Symp. Proc.: "Refractory Alloy Technology for Space Nuclear Power Applications", pp. 98-113; held at Oak Ridge, Tennessee, Aug. 1983, USA
- [42] R.E. Gold and D.L. Harrod
Refractory Metal Alloys for Fusion Reactor Applications
 J. Nucl. Materials 85&86 (1979) 805-815
- [43] F.W. Wiffen; *Effects of Irradiation on Properties of Refractory Alloys with Emphasis on Space Power Reactor Applications*
 Symp. Proc.: "Refractory Alloy Technology for Space Nuclear Power Applications", pp. 252-277, held at Oak Ridge, Tennessee, Aug. 1983, USA

- [44] D.J. Mazey and C.A. English
Role of Refractory Metal Alloys in Fusion Reactor Applications
J. Less-Common Metals 100 (1984) 385-427
- [45] R. Eck
Molybdän-Rhenium Legierungen als Schweißbare Hochtemperatur-Konstruktionswerkstoffe
Proc. 11. Plansee-Seminar, Vol. 2, pp. 39-57, May 1985, Reutte, Austria
- [46] R.L. Ammon, M.L. Bleiberg, R.W. Buckman, Jr., L. Westfall, D. Petrasek and D. McDanel
Refractory Metal-Matrix Composites for Space Nuclear Power Applications
CONF-860102--SUMMS. P. RA-4.1-RA-4.3. / 1986; presented: 3. Symposium on Space Nuclear Power Systems, Albuquerque, NM, Jan. 13-16, 1986, USA
- [47] F. Morito
Effect of Heat Treatment on Mechanical Behavior of Electron Beam Welded Sintered Molybdenum
J. Nucl Materials 165 (1989) 142-148
and
Weldability of Sintered Mo-Re Alloys
Proc. 12. Plansee-Seminar, Vol. 1, pp. 417-431, May 1989, Reutte, Austria
- [48] S.A. Fabritsiev, V.A. Gosudarenkova, V.A. Potapova, V.V. Rybin, L.S. Kosachev, V.P. Chakin, A.S. Pokrovsky and V.R. Barabash
Effects of Neutron Irradiation on Physical and Mechanical Properties of Mo-Re alloys
J. Nucl. Materials 191-194 (1992) 426-429
- [49] Y. Hiraoka, M. Okada and H. Irie
Alloying to Improve the Properties of Welded Molybdenum
J. Nucl. Materials 155-157 (1988) 381-385
- [50] P. Falbriard, P. Rochette and Guy Nicolas
Refractory Materials Likely to be Used in the NET Divertor Armour
Refractory Metals & Hard Materials 10 (1991) 37-43
- [51] Y. Hirooka, M. Bourham, J.N. Brooks, R.A. Causey, G. Chevalier, R.W. Conn, W.H. Eddy, J. Gilligan M. Khandagle and Y. Ra
Evaluation of Tungsten as a Plasma-Facing Material for Steady State Magnetic Fusion Devices
UCLA PPG#1430, May 1992, Los Angeles, CA, USA
- [52] S. Schider
Hochschmelzende Metalle
Verlag moderne Industrie, ISBN 3-478-93044-8, München 1990, FRG
- [53] R.H. Titran, T.L. Grobstein and D.L. Ellis
Advanced Materials for Space Nuclear Power Systems
DOE/NASA/16310-16, NASA TM-105171, AIAA-91-3530;
presented: Conf. on Advanced Space Exploration Initiative Technologies, Cleveland, Ohio, Sept. 4-6, 1991

- [54] A.M. Hammad, S.M. El-Mashri and M.A. Nasr
Mechanical Properties of the Zr - 1% Nb Alloy at Elevated Temperatures
J. Nucl. Materials 186 (1992) 166-176
- [55] Y. Umakoshi, K. Nakai and T. Yamane
Effect of Interfacial Reaction Zone on Tensile Strength of Tungsten Fiber-Reinforced Copper Alloy Composites
Metallurgical Transactions 5 (1974) 1250-1251
- [56] H. Lilholt
Hardening in Two-Phase Materials - I.
Strength Contributions in Fibre-Reinforced Copper-Tungsten
Acta Metallurgica 25 (1977) 571-585
- [57] D.L. McDanel
Tungsten Fiber Reinforced Copper Matrix Composites
NASA Technical Paper 2924, 1989
- [58] E. Kny
Properties and Uses of the Pseudobinary Alloys of Cu with Refractory Metals
Proc. 12. Plansee-Seminar, Vol. 1, pp. 763-772, May 1989, Reutte, Austria
- [59] W. Neumann and E. Kny
Thermal Properties of Materials Used for Heat-Sink Applications
High Temps. - High Press. 21 (1989) 525-532
- [60] A.V. Choba, V.I. Ziskin, V.V. Pasichnyi, G.A. Frolov, Yu.L. Pilipovskii and L.N. Pereselentseva
Determination of Temperature Fields in an Electric-Arc-Heated Disk of a Tungsten-Copper Pseudoalloy
Poroshkovaya Metallurgiya 2/266 (1985) 65-70
- [61] A.V. Egorov, A.G. Kostornov, V.A. Koshelev, G.N. Mel'nikov, A.V. Pustogarov, V.P. Semenets and L.I. Chernyeshov
Properties of Porous Tungsten-Copper and Molybdenum Copper Pseudoalloys
Poroshkovaya Metallurgiya 2/290 (1987) 47-50
- [62] A.P. Gavrilenko, M.S. Koval'chenko, A.A. Kravchenko and Yu.M. Solonin
Effect of the Grain Size of Tungsten on the Erosion Resistance of Tungsten-Copper Pseudoalloys
Poroshkovaya Metallurgiya 10/310 (1988) 86-88
- [63] I.I. Petrova and V.Ya. Chekhovskoi
Study of the Thermophysical Properties of a Tungsten-Copper Pseudo-alloy at High Temperatures
Teplofizika Vysokikh Temperatur 27/4 (1989) 688-696
- [64] P. Frey, N. Klink, R. Michal and K.E. Saeger
Metallurgical Aspects of Contact Materials for Vacuum Switching Devices
IEEE Trans. on Plasma Science 17/5 (1989) 734-740

- [65] R. Klemencic, E. Kny and W. Schmidt
Multilayer Circuit Boards with Molybdenum-Copper Metal Cores
Circuit World 15/4 (1989)
- [66] documentation: Mitsubishi Kasei Corp., Japan
- [67] documentation: Toshiba Corp., Japan
- [68] documentation: Toyo Tanso Co., Japan
- [69] documentation: Metallwerk Plansee GmbH., Austria
- [70] documentation: Société Européenne de Propulsion (SEP), France
- [71] documentation and private communication:
 Ansaldo Ricerche, Italy, and/or A. Cardella, The NET Team
- [72] private communication: Y. Goto, Hitachi Research Laboratory , Japan
- [73] private communication: T. Sogabe, Toyo Tanso Co., Japan
- [74] private communication: R.D. Watson, Sandia National Laboratories, USA
- [75] private communication: R. Eck and N. Reheis, respectively
 Metallwerk Plansee GmbH., Austria
- [76] private communication: T. Baba, National Research Laboratory of Metrology,
 June 1992, Tsukuba, Japan
- [77] G. Knerner and N. Reheis; *Brazing of Bulk Graphite to Metal-Substrates*
 Proc. 11. Plansee-Seminar, Vol. 3, pp. 323-344, May 1985, Reutte, Austria
- [78] H. Shinno, M. Kitajima and M. Okada
Thermal Stress Analysis of High Heat Flux Materials
J. Nucl. Materials 155-157 (1988) 290-294
- [79] I. Smid, R.D.Watson and C.D. Croessmann
Numerical Analysis as a Tool to Corroborate Loading Experiments and
Benchmark Properties of First-Wall Materials for Fusion Devices
High Temp.-High Press. 23 (1991) 111-117
- [80] S. Deschka, M. Akiba, G. Breitbach, A. Cardella, J. Linke, H. Nickel and
 N. Reheis
Thermal Response and Fatigue Behaviour of Brazed CFC/TZM/Mo41Re-
Divertor Mock-Ups Under Electron Beam Loading
17th Symp. On Fusion Technology (SOFT), Sept. 1992, Rome, Italy
- [81] K. Satoh, I. Smid, M. Akiba, M. Araki, S. Suzuki, K. Nakamura, K. Yokoyama
 and M. Dairaku
Heating Experiments of Bonded Structures with a Unidirectional CFC
Material and a W-Cu Composite
 to be presented at: 6. Int. Conf. on Fusion Reactor Materials (ICFRM-6),
 Sept./Oct. 1993, Stresa, Lago Maggiore, Italy

- [82] W.B. Gauster et al.
US Position Paper: ITER Technology R&D for Plasma Facing Components
presented at the Meeting of Home Team Leaders & The Director, June 11-13, 1992, in San Diego, USA
- [83] Hibbit, Karlsson & Sorensen, Inc., Providence, RI, 1992
ABAQUS Version 4.9, Users' Manual
- [84] K. Suganuma, Y. Miyamoto and M. Koizumi
Joining of Ceramics and Metals; Ann. Rev. Mat. Sci. 18 (1988) 47-73
- [85] M. Shibui, K. Kitamura, K. Nagata, T. Fuse, N. Tachikawa and M. Tezuka
Edge Stresses in Bonded Armor System for Divertor Plate
Proc. 14th IEEE/NPSS Symp. On Fusion Engineering (14th SOFE), Vol. 1 (1991) 368-371; held: Sept./Oct. 1991, San Diego, USA
- [86] J.P. Blanchard and N.M. Ghoniem
Analysis of Singular Stress Fields in Duplex Fusion Components
J. Nucl. Materials 172 (1990) 54-70
- [87] E.D. Reedy, Jr.; *Intensity of the Stress Singularity at the Interface Corner Between a Bonded Elastic and Rigid Layer*
Engrg. Fracture Mechanics 36/4 (1990) 575-583
- [88] J.E. Schiermeier and B.A. Szabó
Numerical Analysis of Stress Singularities in Composite Materials
Engrg. Fracture Mechanics 32/6 (1989) 979-996
- [89] K.Y. Lin and H.H. Hartmann
Numerical Analysis of Stress Singularities at a Bonded Anisotropic Wedge
Engrg. Fracture Mechanics 32/2 (1989) 211-224
- [90] W.C. Carpenter and G.C. Patton
Comparison of the Maximum Stress and the Stress Intensity Approaches in the Analysis of Bonded Joints
Proc. "Advances in Adhesively Bonded Joints" pp. 23-31, The Winter Annual Meeting of The American Society of Mechanical Engineers, Nov. 27 - Dec. 2, 1988, Chicago, Illinois, USA
- [91] K. Suganuma, T. Okamoto and K. Kamachi
Influence of Shape and Size on Residual Stress in Ceramic/Metal Joining
J. Material Sci. 22(1987) 2702-2706
- [92] I.S. Raju and J.H. Crews, Jr.
Interlaminar Stress Singularities at a Straight Free Edge in Composite Laminates
Computers & Structures 14/1-2 (1981) 21-28
- [93] M.L. Williams
Stress Singularities Resulting From Various Boundary Conditions in Angular Corners of Plates in Extension
J. Appl. Mech. 19 (1952) 526-528

- [94] F.W. Dittus and L.M.K. Boelter
Univ. Calif. Publs. Engrg. 2 (1930) 443
- [95] J.R.S. Thom, W.M. Walker, T.A. Fallon and G.F.S. Reising
Boiling in Sub-Cooled Water During Flow Up Heated Tubes or Annuli
Proc. Instn. Mech. Engrs. 180/3 (1965-66) 226-246
- [96] M. Araki, M. Ogawa, M. Akiba and S. Suzuki
Experimental and Analytical Evaluations on Critical Heat Flux Under One Sided Heating Condition for Fusion Applications
presented: ANS Annual Meeting 1992, to be published in Fusion Technology
- [97] J.A. Koski, R.D. Watson, P.L. Goranson, A.M. Hassanein and J.C. Salmonson
Thermal-Hydraulic Design Issues and Analysis for the ITER Divertor
Fusion Technology 19 (1991) 1729-1735
- [98] M. Akiba and R.D. Watson
Thermo-Hydrodynamic Coupling with Coolants
to be published in: Nuclear Fusion (IAEA) 1993
- [99] A. Cardella, G.P. Celata, G. Dell'Orco, G.P. Gaspari, G. Cattadori and A. Mariani
Thermal-Hydraulic Experiments for the NET Divertor
17th Symp. On Fusion Technology (SOFT), Sept. 1992, Rome, Italy
- [100] J. Schlosser, A. Cardella, P. Chappuis, J.F. Coston, P. Deschamps and M. Lipa
Development of High Thermal Flux Components for Continuous Operation in Tokamaks
Proc. 14th IEEE/NPSS Symp. On Fusion Engineering (14th SOFE),
Vol. 1 (1991) 350-356; held: Sept./Oct. 1991, San Diego, USA
- [101] E. Di Pietro, M. Brossa, U. Guerreschi, D. Suresh, A. Cardella and N. Reheis
Technological Development of the Monobloc Divertor Concept
Proc. 14th IEEE/NPSS Symp. On Fusion Engineering (14th SOFE),
Vol. 1 (1991) 342-345; held: Sept./Oct. 1991, San Diego, USA
- [102] R. Matera, W. Janssens and P. de Meester
Critical Issues and Innovative Solutions for the Divertor Plate Design in Future Experimental Tokamak-Type Fusion Reactors
Fusion Technology 21 (1992) 1823-1827; presented at: 10th Topical Meeting on the Technology of Fusion Energy, June 1992, Boston, Mass., USA
- [103] G. Breitbach, U. Wolf and M. Rödig
Thermische Belastung eines Divertors
Internal Report of KFA Jülich, IRW-TN-45/91, July 1991
- [104] S. Suzuki, M. Akiba, M. Araki, M. Seki, H. Ise, Y. Ozawa, N. Tachikawa,
M. Toyoda and S. Yamazaki
Development of Divertor Modules for Fusion Experimental Reactors
Proc. 2nd Japan Int. SAMPE (Soc. for the Advancement of Material and Process Engineering) Symp. and Exhibition, Dec. 1991, Chiba, Japan

- [105] F. Gordaninejad
Enhancement of Thermal Conductivities in Polymeric Fiber Reinforced Composite Materials
 Trans. ASME 114 (1992) 416-421
- [106] I. Smid, M. Akiba, M. Araki, E. Kny, K. Nakamura, K. Satoh and S. Suzuki
W-Cu Pseudo-Alloys for the Heat Sink of the ITER Divertor
 to be presented at: 6. Int. Conf. on Fusion Reactor Materials (ICFRM-6),
 Sept./Oct. 1993, Stresa, Lago Maggiore, Italy

Table 2 Requirements for Divertor and First Wall Materials
 in Particular for Braze Components

-
- a) high heat conductivity and capacity
 - b) high melting or sublimation temperature
 - c) resistance to thermal shocks and thermal fatigue
 - d) interface integrity even after long-term/cyclic operation
 - e) matched thermal expansion at the interface
 - f) low thermal expansion in the heat sink to reduce deformation due to one-sided heating
 - g) low-Z number for the plasma facing material
 - h) thermomechanical reliability against high heat fluxes
 - i) resistance to disruption and run-away events
 - j) chemical, physical and thermodynamical compatibility with the burning plasma
 - k) easy removal of adsorbed and absorbed impurities
 - l) low rate of physical and chemical erosion (due to: arcing, evaporation, sputtering, sublimation)
 - m) compatibility with ultrahigh vacuum
 - n) favorable irradiation behavior due to 14 MeV neutrons: activation, loss of ductility and thermal conductivity, swelling, disintegration
 - o) exchangeability by remote handling
 - p) wide safety margin under accidental conditions (loss of coolant, flow, vacuum...)
-

Table 3.a/I Thermal Conductivity of Carbon Materials (W/mK)

	temp./°C	MFC-1 (1)"!!"	MFC-1 (2+3)	"bulk" P-130	CX2002U (1)	CX2002U (2)	CX2002U (3)	SEP N112 (1+2)	SEP N112 (3)	IG430U	temp./°C
1	20.000			850.00				280.00		210.00	20.000
2	27.000				381.00	320.10	215.00			155.00	27.000
3	57.000	640.00	25.000								57.000
4	100.00	570.00	23.550								100.00
5	127.00				299.00	251.30	180.00			142.00	127.00
6	200.00	495.00	21.000	700.00							200.00
7	227.00				254.00	213.50	150.00			128.00	227.00
8	300.00	442.08	19.000								300.00
9	350.00										350.00
10	400.00	397.31	17.000	525.00				140.00	123.00		400.00
11	427.00				193.00	161.70	116.60			100.00	427.00
12	500.00	359.72	15.500					131.00	105.00		500.00
13	600.00	328.31	14.200	440.00							600.00
14	627.00				153.00	127.10	94.500			80.000	627.00
15	700.00	302.12	13.100								700.00
16	800.00	280.27	12.300								800.00
17	900.00	261.91	11.600								900.00
18	1000.0	246.25	11.100	325.00	120.00	100.00	74.000	95.000	76.000	63.000	1000.0
19	1100.0	232.57	10.700								1100.0
20	1200.0	220.17	10.300								1200.0
21	1300.0	208.45	10.050								1300.0
22	1400.0	196.83	9.8000								1400.0
23	1500.0	184.79	9.6000			104.00	85.000	65.000	76.000	62.000	1500.0
24	1600.0	176.00	9.4000								1600.0
25	2000.0								58.000	52.000	44.700
											2000.0

Table 3.a/II Thermal Conductivity of Cu, Mo-Alloys, W-Cu (W/mk)

	temp./°C	pure Mo	TZM	Mo5Re	Mo41Re	Nb-1Zr	OF-Cu	DS-Cu	W-30Cu	temp./°C
1	0.0000							350.00		0.0000
2	20.000		125.00			47.500				20.000
3	27.000						398.00			27.000
4	100.00	137.00		118.00	50.900			340.00	293.00	100.00
5	200.00	136.00		115.00	54.300	50.200		325.00	285.00	200.00
6	300.00	134.00		114.00	57.400			315.00	276.00	300.00
7	327.00						383.00			327.00
8	400.00	131.00		113.00	61.500			300.00	267.00	400.00
9	500.00		115.00	112.00	63.200	54.500		290.00	258.00	500.00
10	527.00						371.00			527.00
11	600.00	124.00			64.300					600.00
12	700.00					57.500				700.00
13	727.00						357.00			727.00
14	927.00						342.00			927.00
15	1000.0				100.00					1000.0
16	1500.0				87.000					1500.0
17	2000.0				75.000					2000.0

Table 3.a/III Thermal Conductivity of W and Alloys (W/mK)

	temperature/°C	W	W3Re	W5Re	W10Re	W26Re	W-30Cu	temperature/°C
1	20.000	145.00						20.000
2	100.00	118.00				39.500	293.00	100.00
3	200.00	115.00				47.600	285.00	200.00
4	227.00		88.500					227.00
5	300.00		116.00			51.900	276.00	300.00
6	400.00		113.00			55.300	267.00	400.00
7	500.00	128.00	110.00			59.200	258.00	500.00
8	527.00			90.000				527.00
9	550.00				68.900			550.00
10	600.00			108.00		60.900		600.00
11	650.00					70.100		650.00
12	750.00					71.800		750.00
13	850.00					73.200		850.00
14	950.00					74.400		950.00
15	1000.0	113.00				66.720		1000.0
16	1050.0					75.300		1050.0
17	1500.0	106.00					64.050	1500.0
18	2000.0	102.00					62.820	2000.0

Table 3.b Expansion Coefficients (1/K)

temp./°C	MFC(1,"1")	MFC(2+3)	CX(1+2)	CX(3)	SEP(1+2)	SEP(3)	IG430U	pure Mo	TZM	W	WSRe	W-30Cu	Nb-1Zr	pure Cu	DS-Cu
1															
2	-9.0000e-07	1.2000e-05	1.6000e-06	5.8000e-06			4.7000e-06					1.1500e-05			
3															
4	20.000														
5	27.000														
6	100.00														
7	200.00														
8	300.00														
9	327.00														
10	350.00														
11	400.00														
12	500.00														
13	527.00														
14	600.00														
15	700.00														
16	800.00														
17	927.00														
18	1000.0														

Table 3.c Density, Elastic Moduli, Yield and Ultimate Strength, and Poisson Ratio

	MFC-1	CX2002	SEP N112	IG430U	OF-Cu	DS-Cu	TZM	W5Re	W-30Cu
density at RT, g/cm ³	1.96	1.67	1.95	1.81	8.9	8.9	10.2	19.4	14.0
elastic modulus, GPa	100. (II) 0.8 (I)	10.7 (1) 8.1 (2)	28.0 (II) 24.0 (I)	9.5 3.4 (3)	82.4 (20°C) 78.5 (100°C) 73.5 (200°C) 65.7 (500°C) 58.8 (800°C)	134. (20°C) 121. (200°C) 106. (400°C) 91. (600°C) 75. (800°C)	300. (20°C) 260. (500°C) 220.(1000°C) 140.(1500°C)	400. (27°C) 382. (527°C)	218.
yield strength, MPa. (%) - °C at 20° and 400°C					44.1(2)-20. 103.(4)-20. 34.3(2)-400. 66.7(4)-400.	462.(2)-20. 516.(10)-20. 228(.2)-400. 270.(4)-400.	710.(2)-20. 1150(17)-20. 550.(2)-400. 970.(15)-400.		
ultimate strength at RT, MPa, tensile/compressive	400./216. (II) 3./16. (I)	35./49. (1) 31./50. (2)	65./160. (II) 35./180. (I)	42./94. 11./54. (3)	245. 516.	516. 1150.	1100.	520.	
Poisson ratio	0.15	0.19	0.11	0.18	0.33	0.3	0.32	0.3	0.3

Table 3.d Material Properties *)

	CX2002U	MFC-1 (1992)	W-30Cu	DS-Cu
Ultimate tensile/compr. /bend. strength (MPa), at RT or higher	<u>11 / 49 / 15 (min.)</u> <u>50 / 54 / 50 (max)</u>	<u>400 / 216 / 480 (//)</u> <u>3 / 16 / 5 (L)</u>	<u>520</u>	<u>410 - 520</u>
Tensile elongation at RT	—	—	2-3 %	16 %
Young's modulus (GPa)	10.7 ¹⁾ , 8.12 ²⁾ , 3.4 ³⁾	100 (//), 0.8 (L)	218	134
Poisson ratio	0.19	0.15	0.3	0.3
Melt/sublim. temp. (°C)	3500	3500	1080 (Cu)	1080
Density (g/cm ³)	1.67	1.96	14.0	8.9
Thermal conductivity, (W/mK)	20°C 300°C	380.0 ¹⁾ 240.0 ¹⁾	640.0 (//, 57°C) 442.0 (//)	~ 290.0 276.0
Specific heat at RT (J/gK)	0.71	0.71	0.24	0.39
Thermal expansion coeff. (10 ⁻⁶ /K)	1.5 ¹⁾ , 1.72 ²⁾ , 5.8 ³⁾	~ 0.9 (//), 12.0 (L)	11.5	17.0

*) data measured, from literature and manufacturer's documentation, respectively - see chapter 3.
 MFC-1 (1992): uni-directional pitch-type carbon-fiber-reinforced-carbon material, Mitsubishi Kasei, Japan
 CX2002U: two-directional felt-type carbon-fiber-reinforced-carbon material, Toyo Tanso, Japan
 DS-Cu: dispersion strengthened copper, 0.5% Al₂O₃, "GildCop"
 W-30(wt%)Cu: copper-infiltrated W-Cu (pseudo-)alloy
 I.Smid, M.Akiba, M.Araki, S.Suzuki - NBI Heating Lab./ JAERI

W/mK

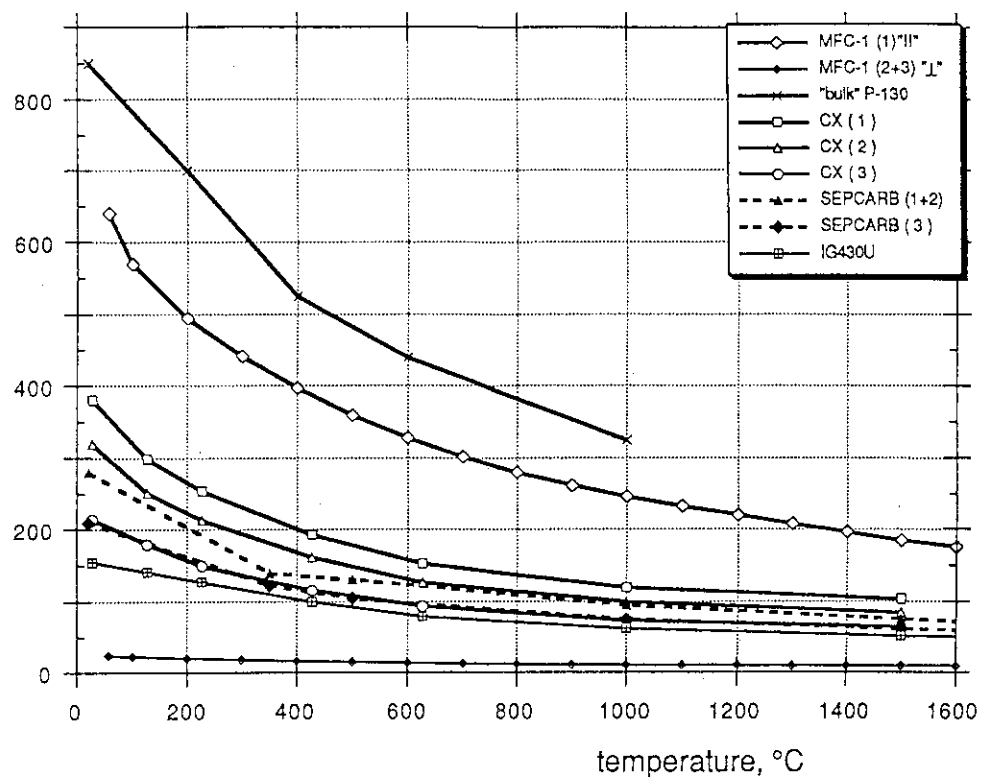


Fig. 3.a/I Thermal Conductivity of Carbon Materials

W/mK

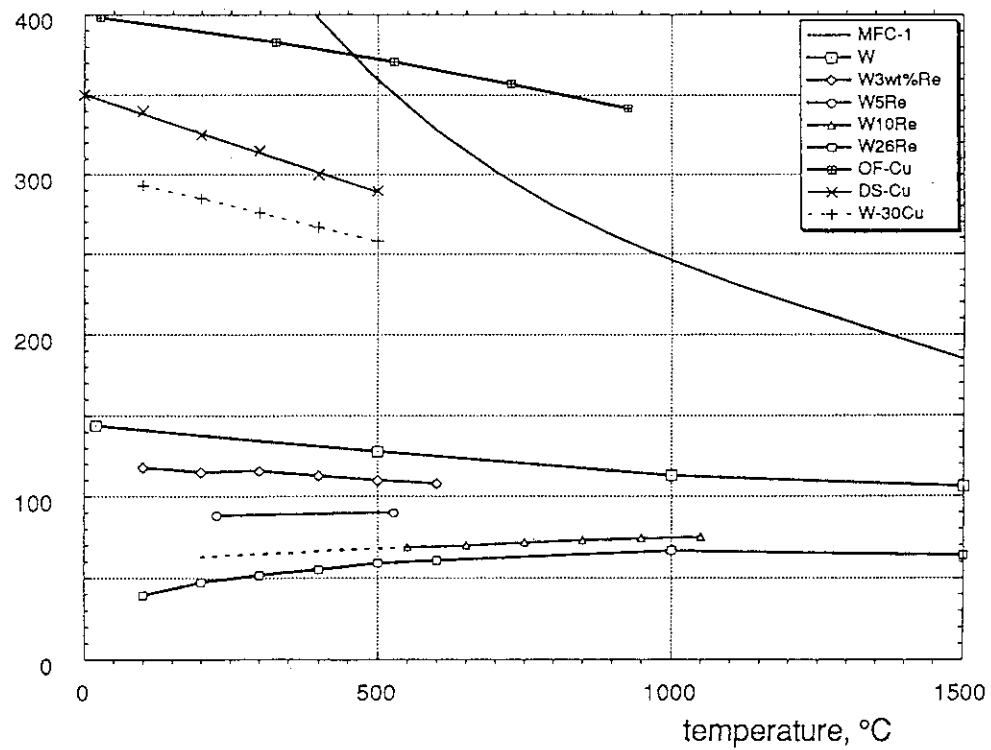


Fig. 3.a/II Thermal Conductivity of Cu, Mo-Alloys, W-Cu

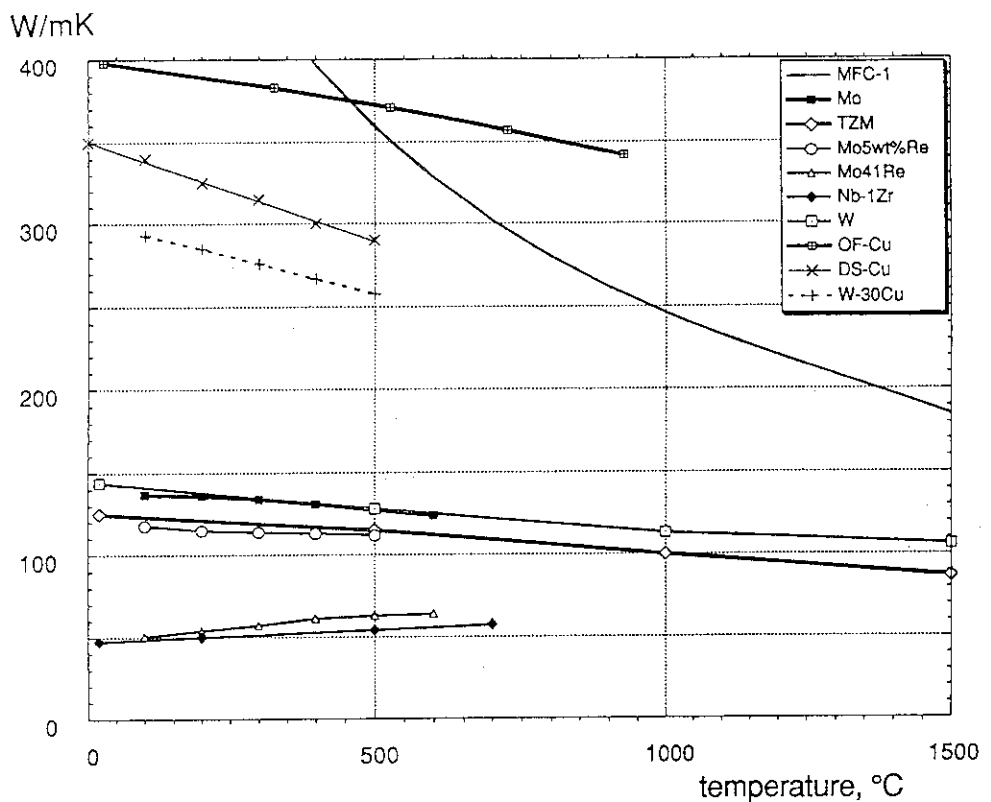


Fig. 3.a/III Thermal Conductivity of W and Alloys

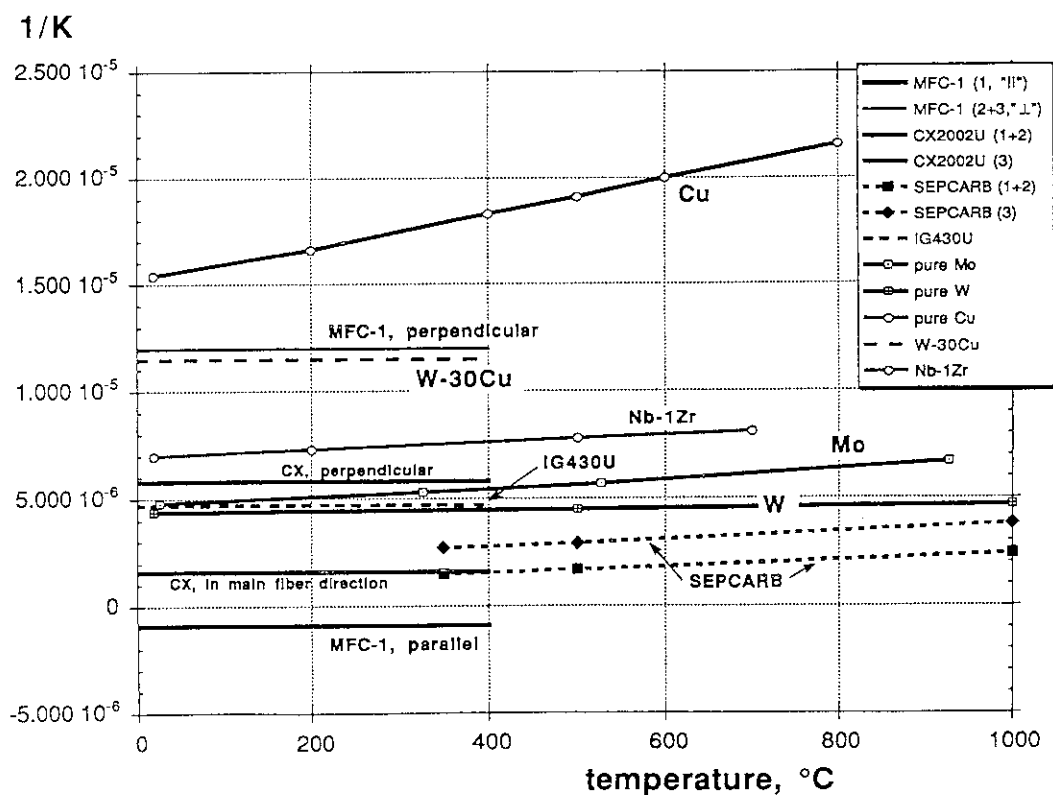


Fig. 3.b Expansion Coefficients

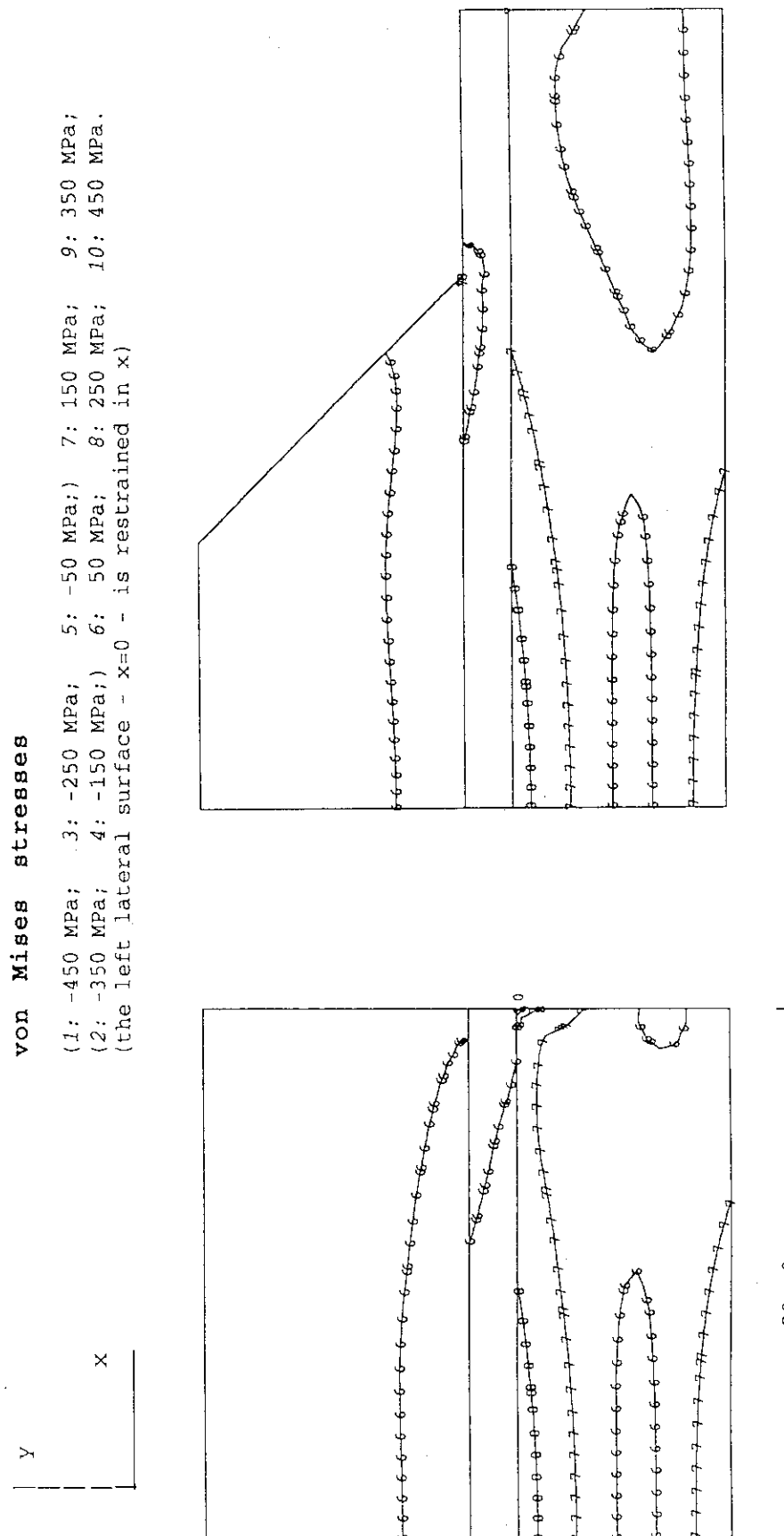
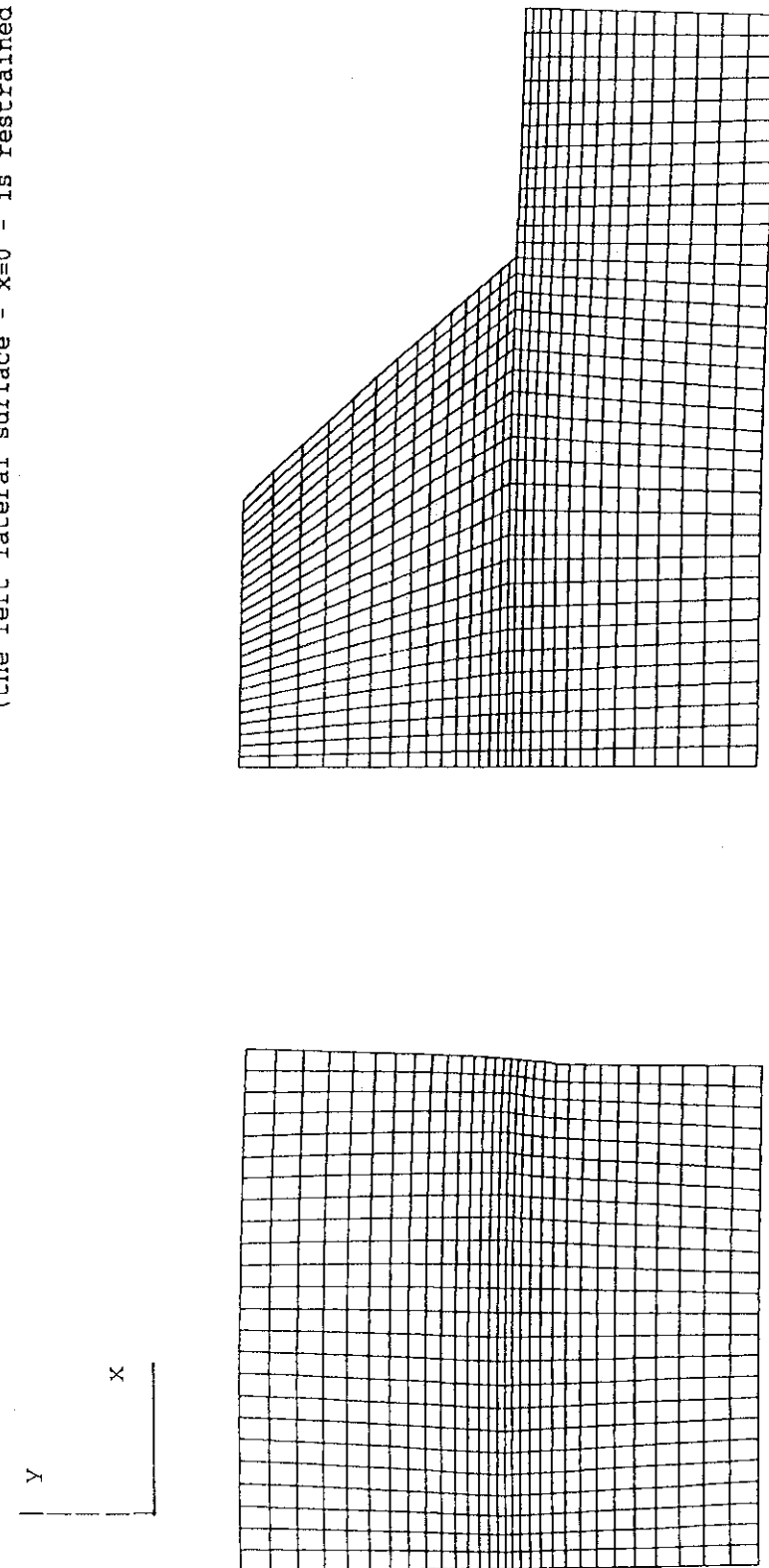


Fig. 5.a Residual Stresses at the Open End of the Braze Line after an Assumed Brazing Cycle, with Braze Solidification at 750°C for 90° in CX2002U (10 mm) + 90° in OF-Cu (1.8 mm)/DS-Cu (8.2 mm), left and 45° in CX2002U (10 mm) + 180° in OF-Cu (1.8 mm)/DS-Cu (8.2 mm), right

(the left lateral surface - $x=0$ - is restrained in x)



| 20. 0 mm |

Fig. 5.b Mesh Displacement after an Assumed Braze Solidification at 750°C
for 90° in CX2002U + 90° in OF-Cu (1.8 mm)/DS-Cu (8.2 mm), left magnification factor: 3.6x
and 45° in CX2002U + 180° in OF-Cu (1.8 mm)/DS-Cu (8.2 mm), right magnification factor: 4.2x

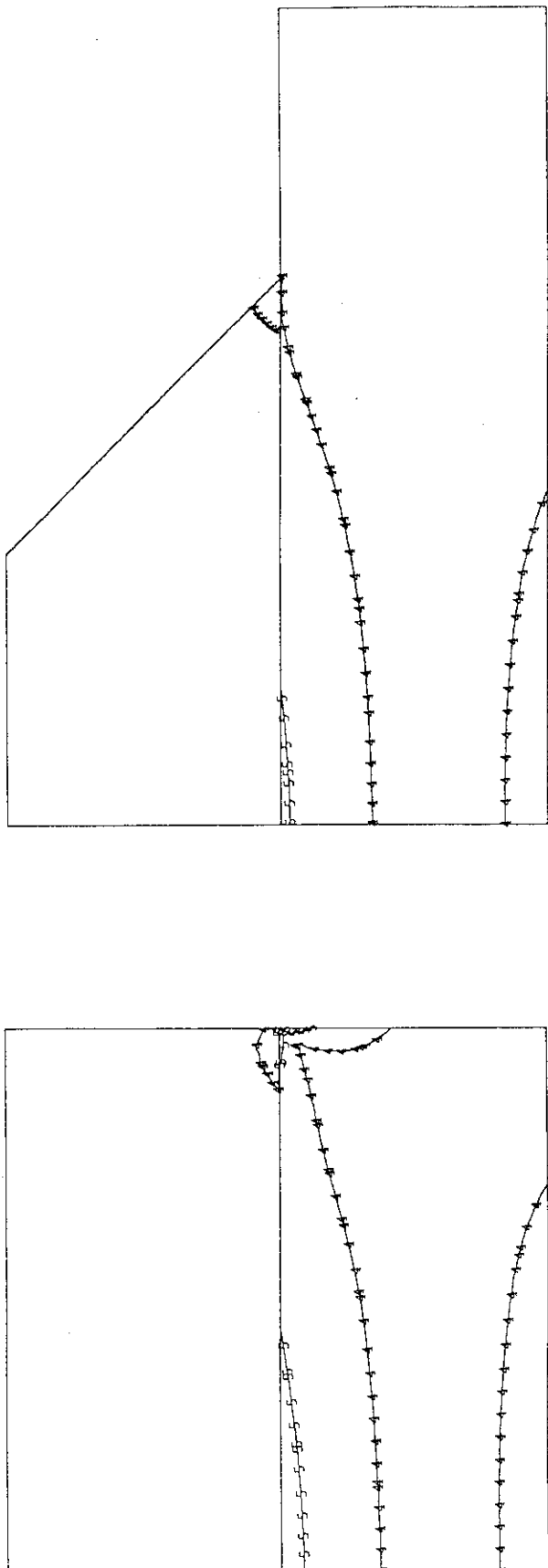
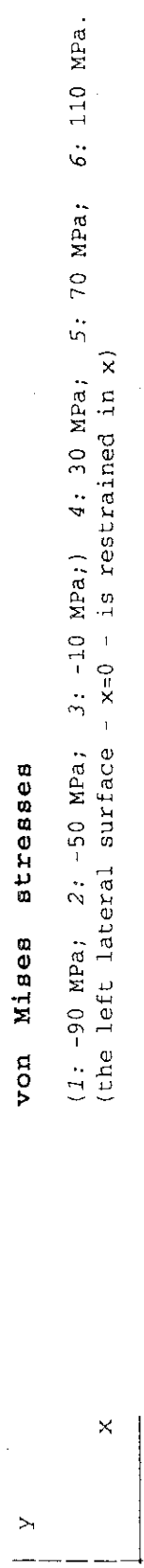


Fig. 5.c Residual Stresses at the Open End of the Braze Line after an Assumed Brazing Cycle, with Braze Solidification at 750°C for 90° in CX2002U (10 mm) + 90° in TZM (10 mm), left and 45° in CX2002U (10 mm) + 180° in TZM (10 mm), right

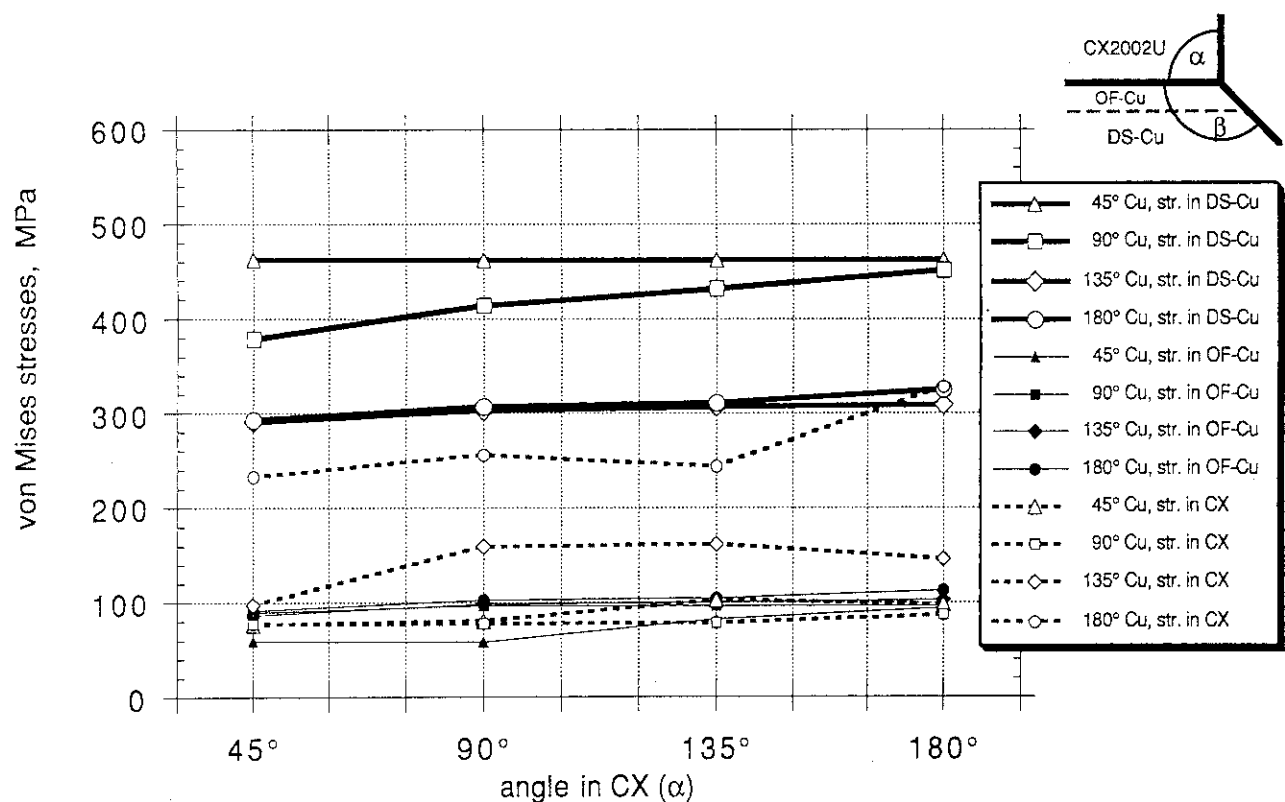


Fig. 5.1.1/I CX2002U Armor + OF (1.8 mm) & DS-Cu Substrate Peak Residual Stresses near the Brazing Interface

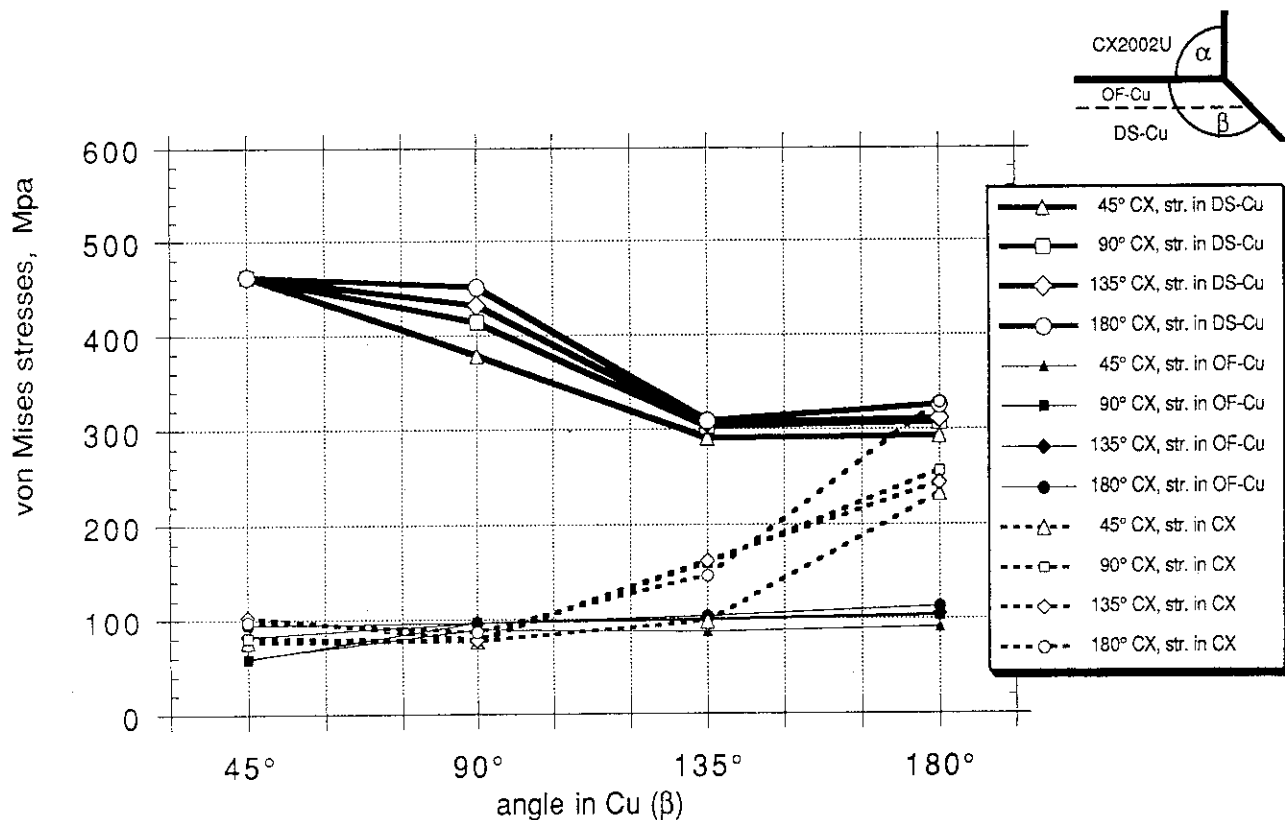


Fig. 5.1.1/II CX2002U Armor + OF (1.8 mm) & DS-Cu Substrate Peak Residual Stresses near the Brazing Interface

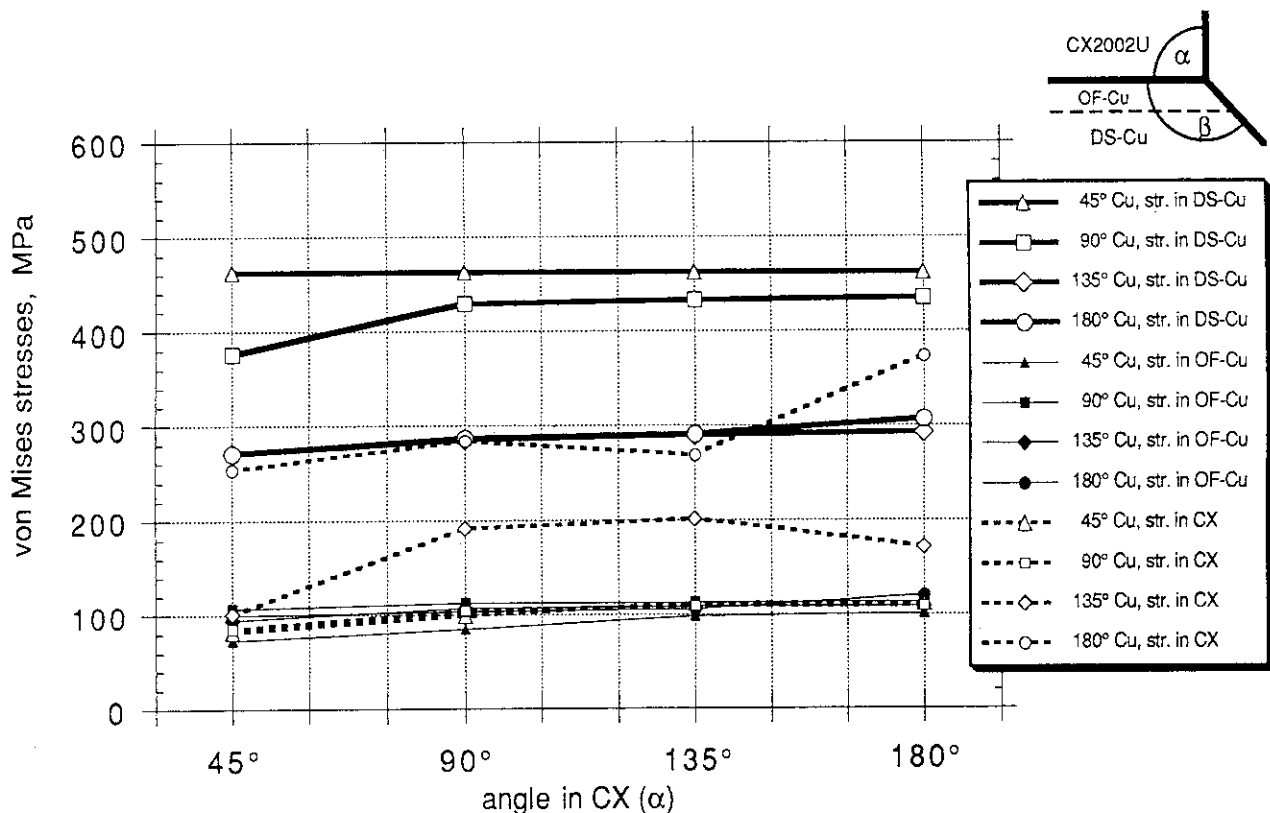


Fig. 5.1.2/I CX2002U Armor + OF (0.6 mm) & DS-Cu Substrate Peak Residual Stresses near the Brazing Interface

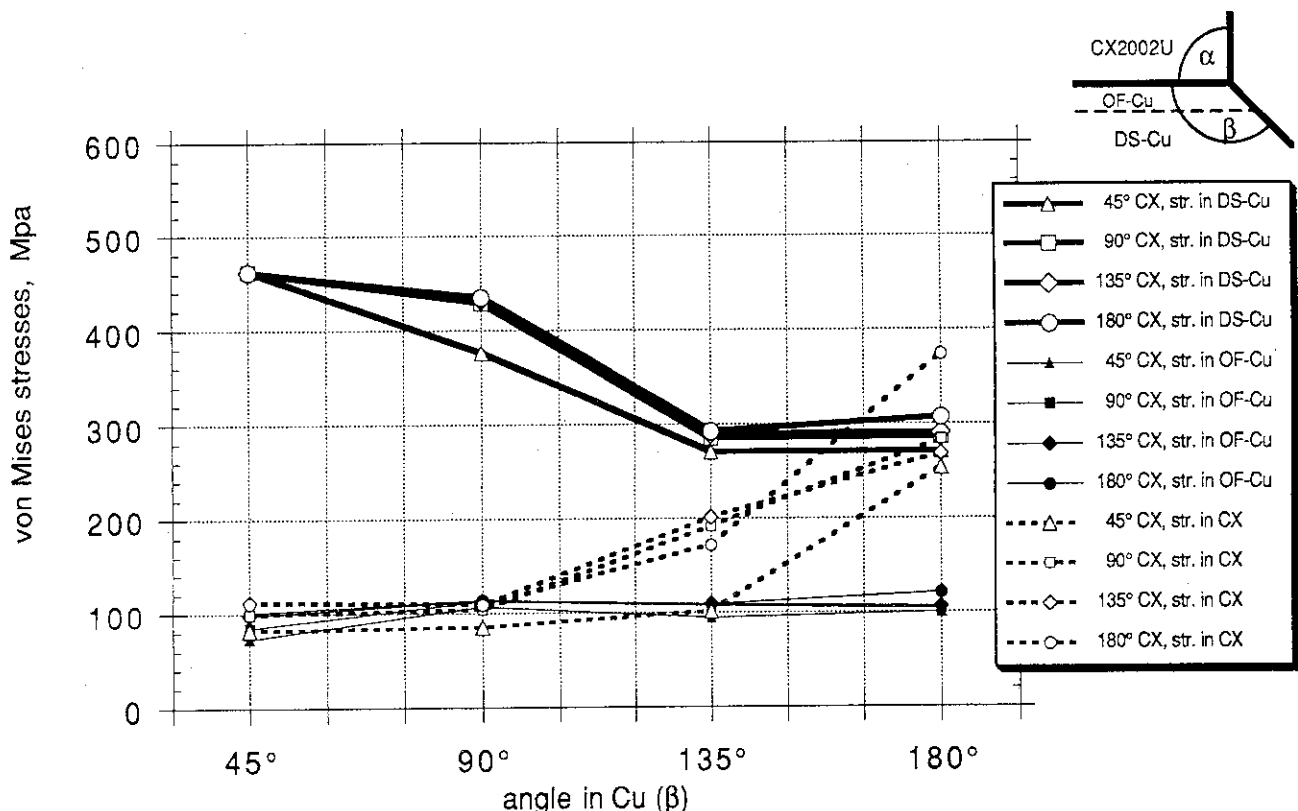


Fig. 5.1.2/II CX2002U Armor + OF (0.6 mm) & DS-Cu Substrate Peak Residual Stresses near the Brazing Interface

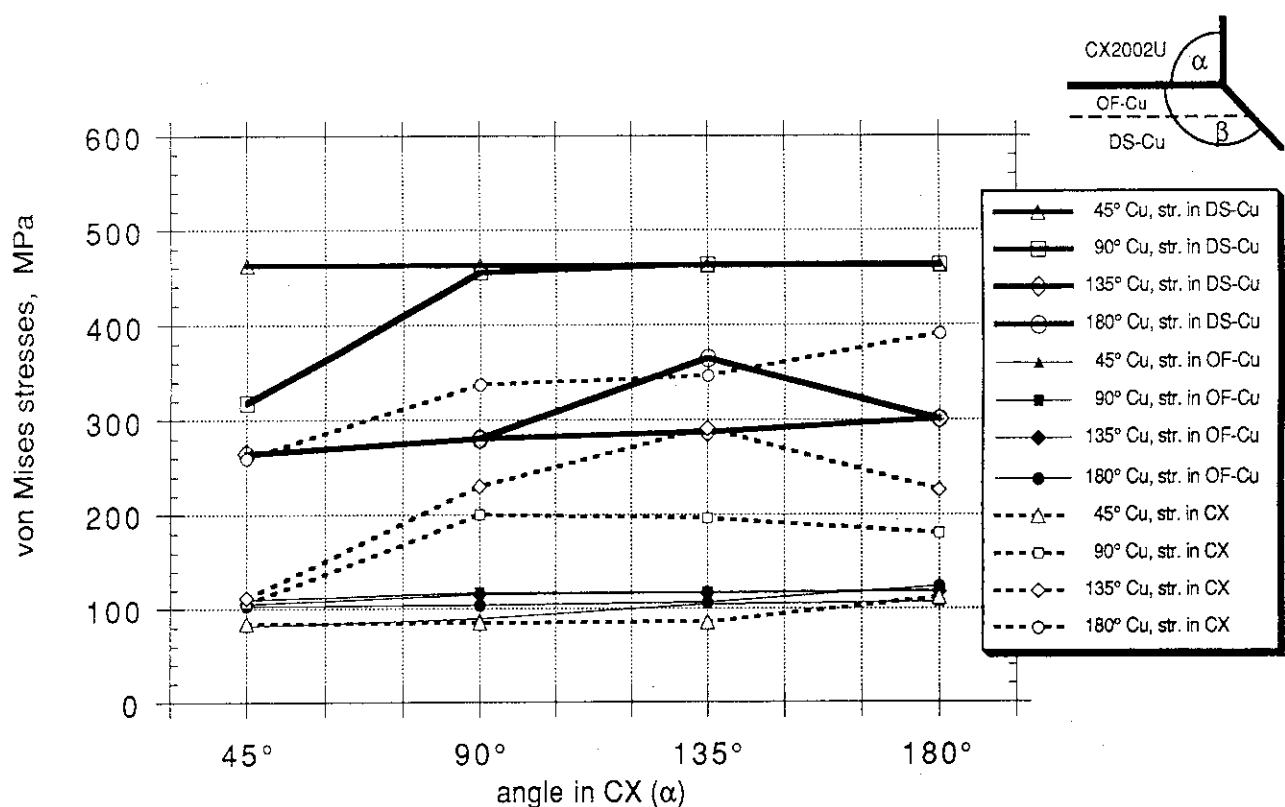


Fig. 5.1.3/I CX2002U Armor + OF (0.3 mm) & DS-Cu Substrate Peak Residual Stresses near the Brazing Interface

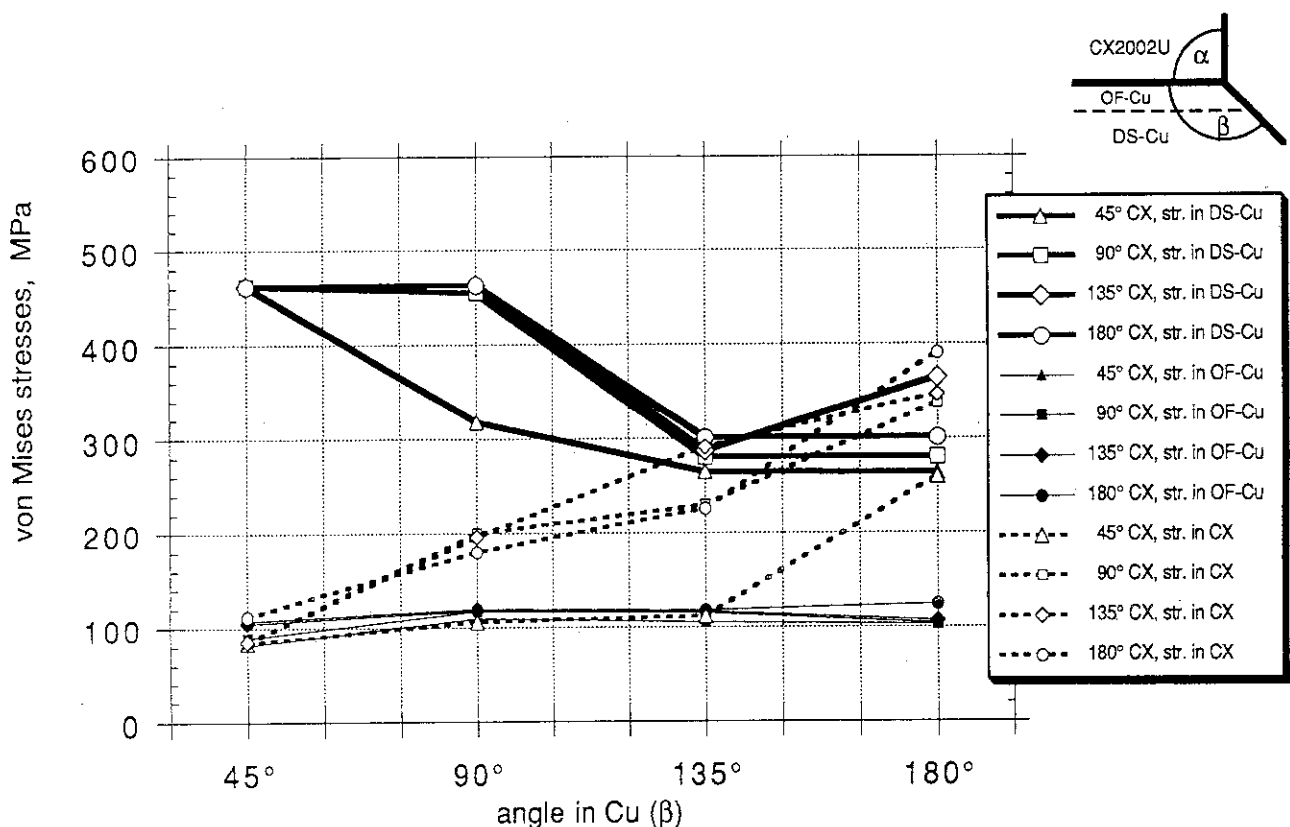


Fig. 5.1.3/II CX2002U Armor + OF (0.3 mm) & DS-Cu Substrate Peak Residual Stresses near the Brazing Interface

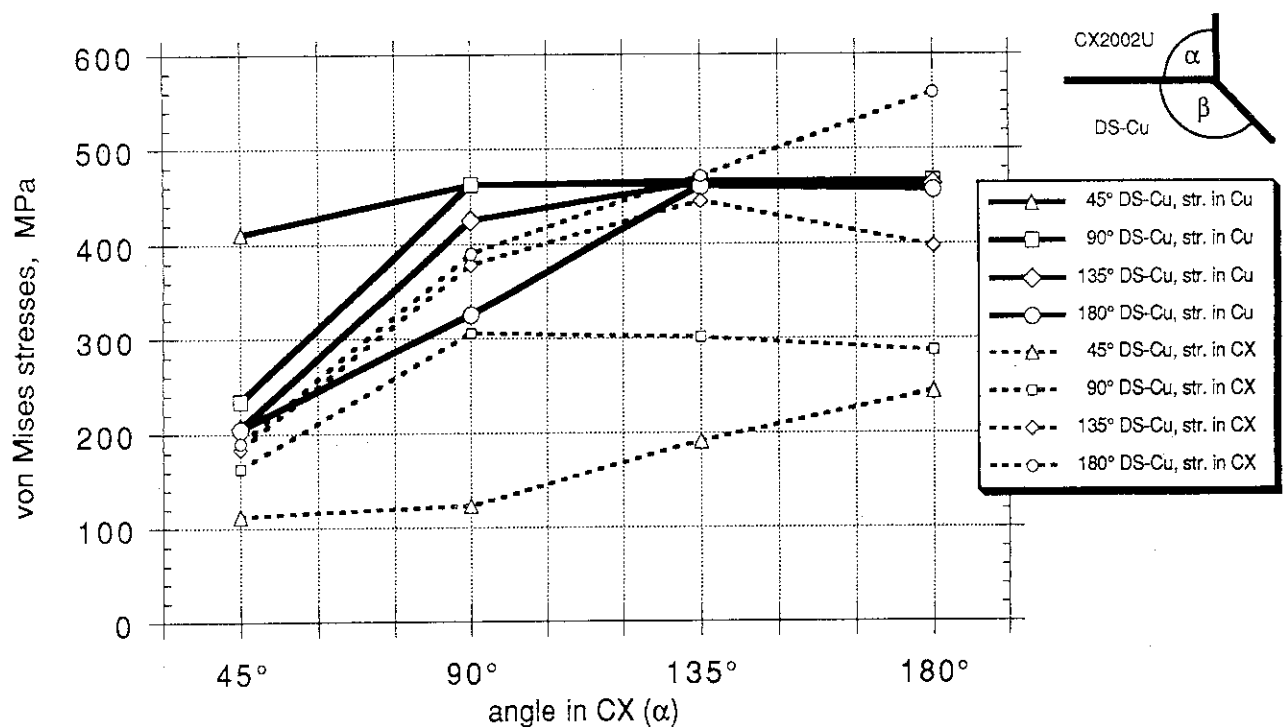


Fig. 5.1.4/I CX2002U Armor + DS-Cu Substrate Peak Residual Stresses near the Brazing Interface

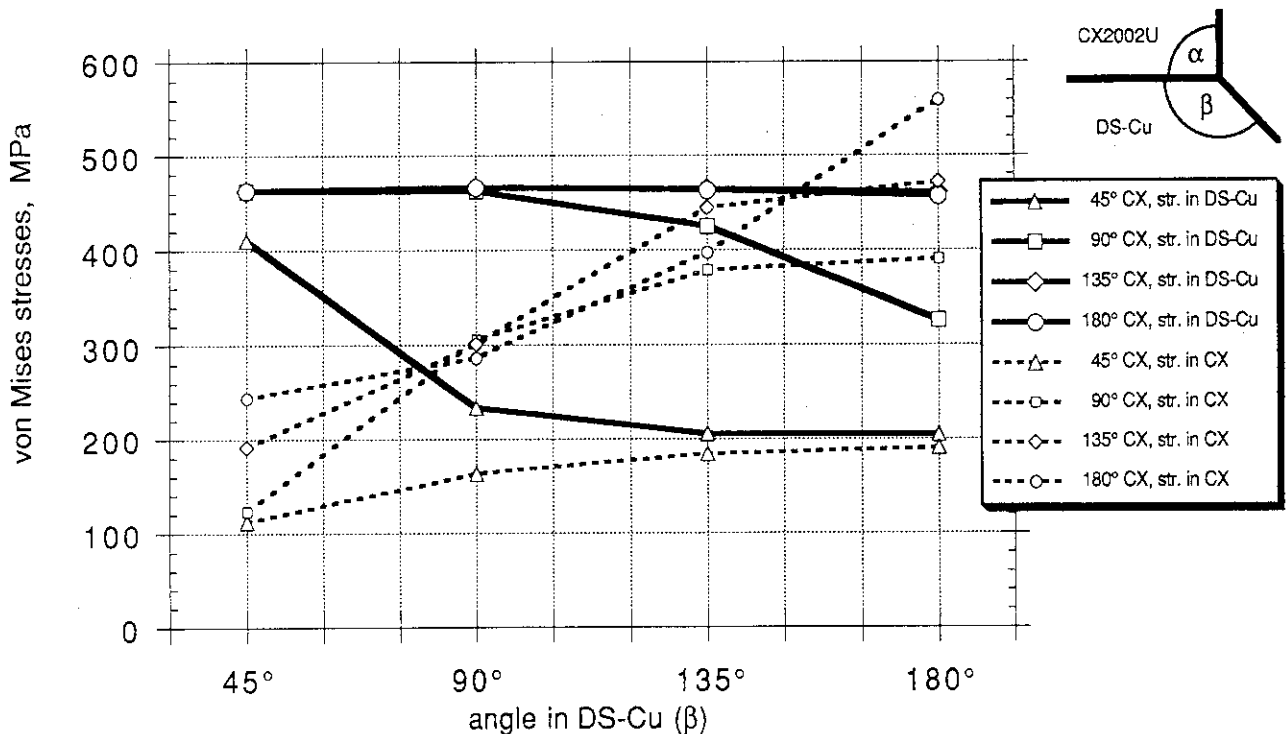


Fig. 5.1.4/II CX2002U Armor + DS-Cu Substrate Peak Residual Stresses near the Brazing Interface

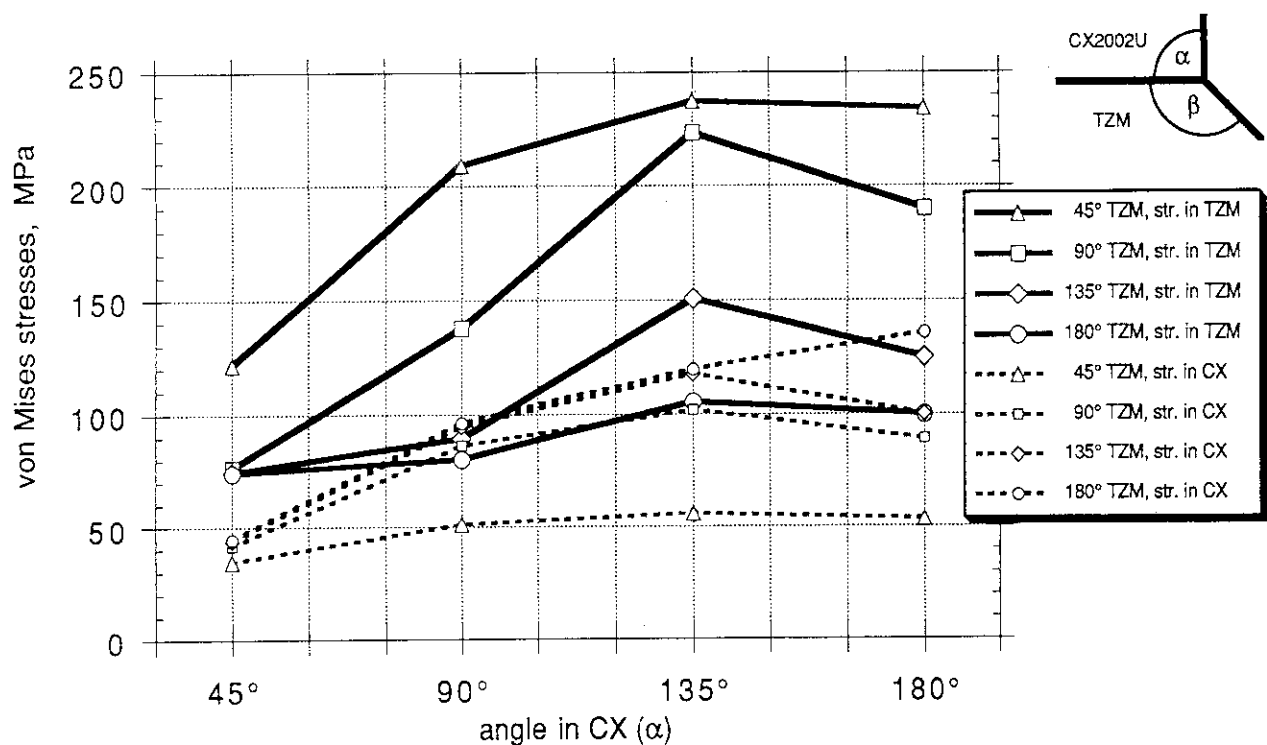


Fig. 5.1.5/I CX2002U Armor + TZM Substrate Peak Residual Stresses near the Brazing Interface

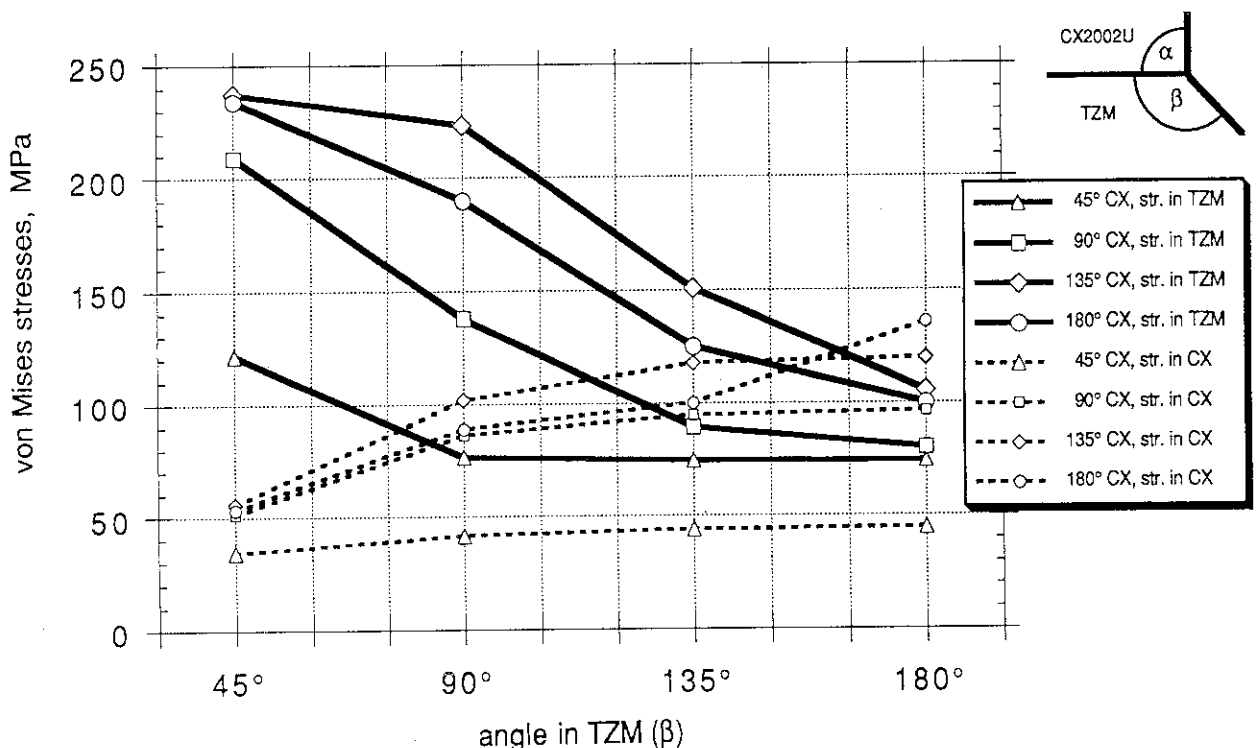


Fig. 5.1.5/II CX2002U Armor + TZM Substrate Peak Residual Stresses near the Brazing Interface

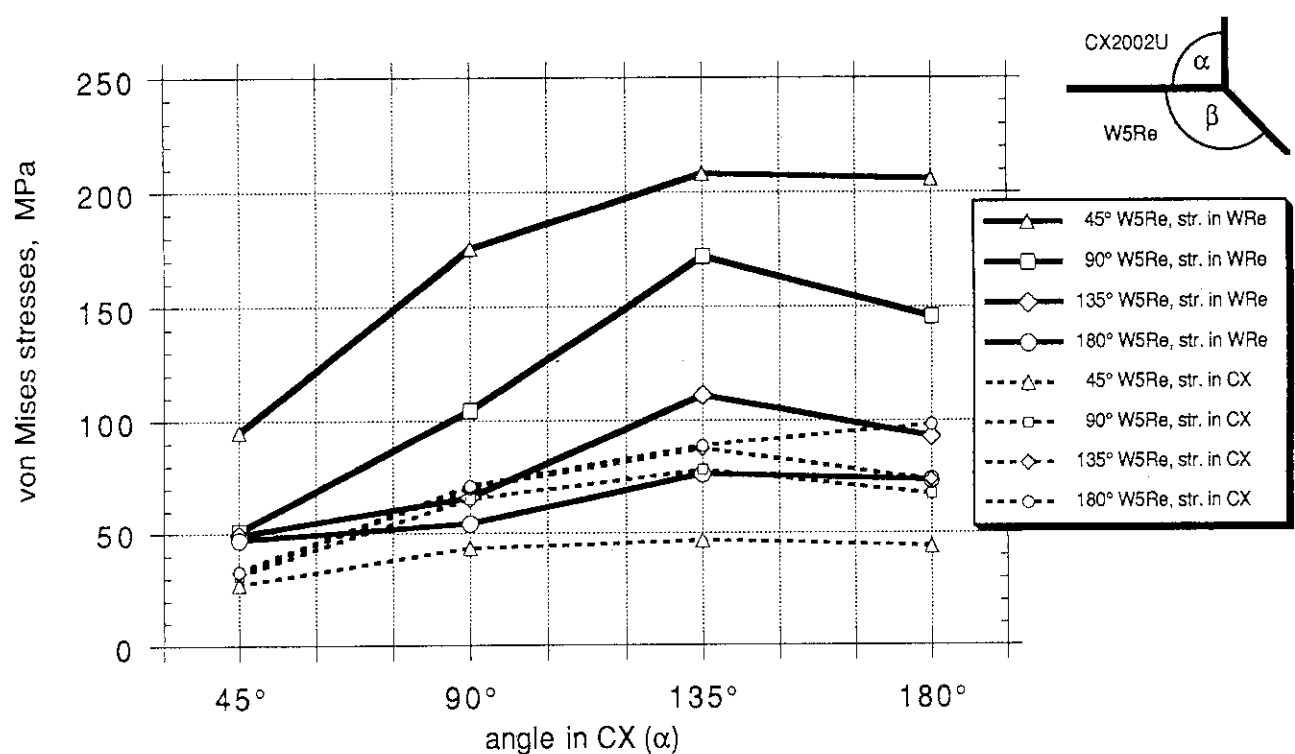


Fig. 5.1.6/I CX2002U Armor + W5Re Substrate Peak Residual Stresses near the Brazing Interface

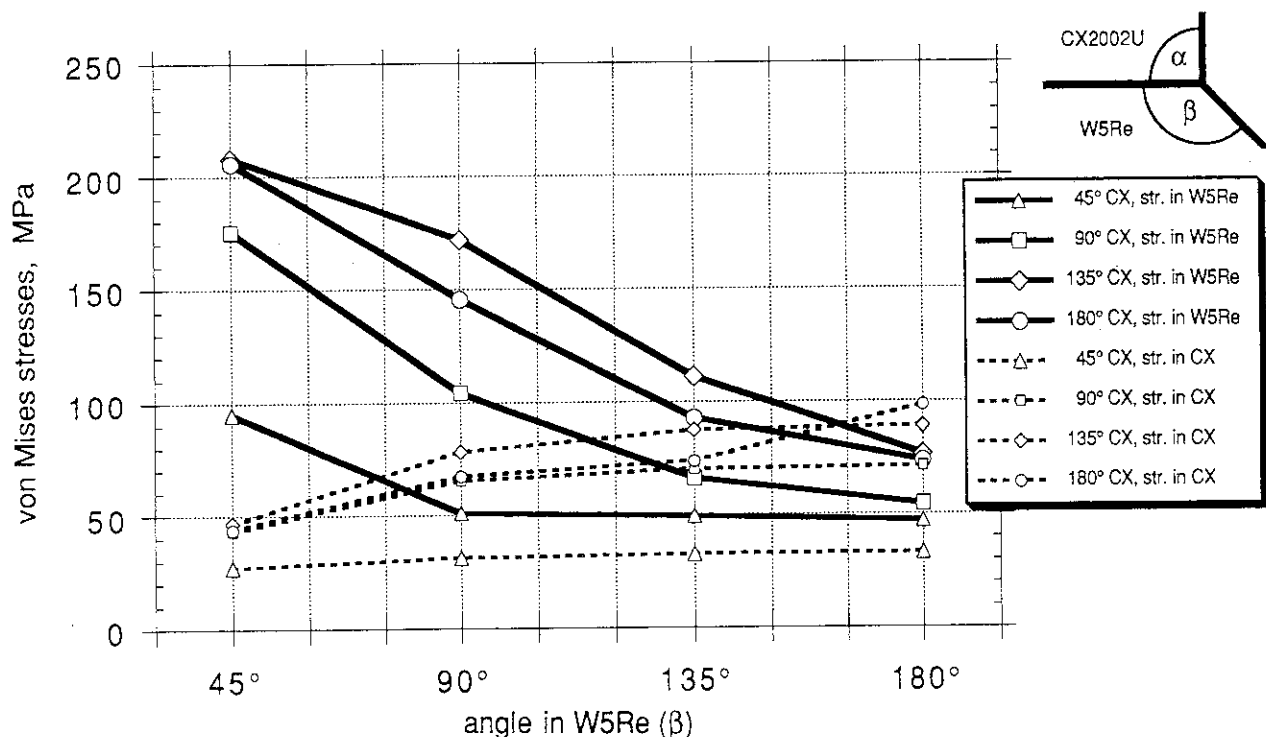


Fig. 5.1.6/II CX2002U Armor + W5Re Substrate Peak Residual Stresses near the Brazing Interface

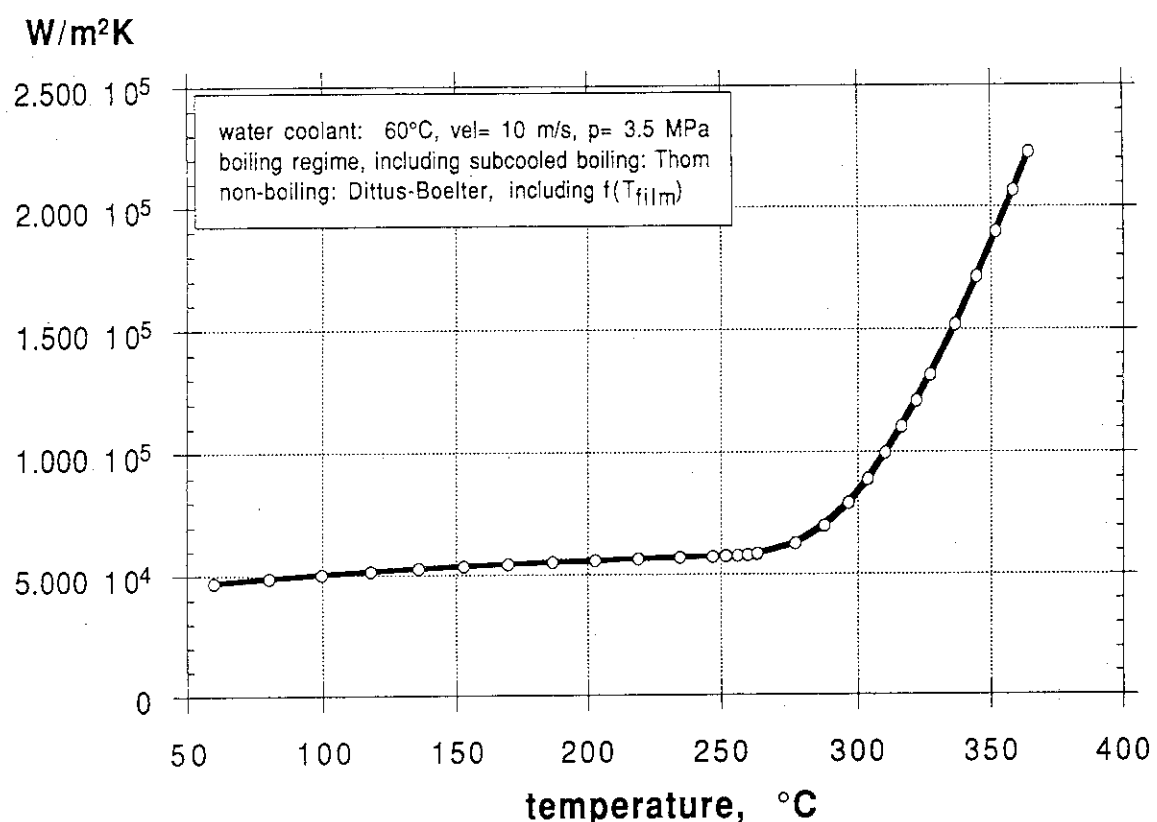


Fig. 6.1 Heat Transfer Coefficient

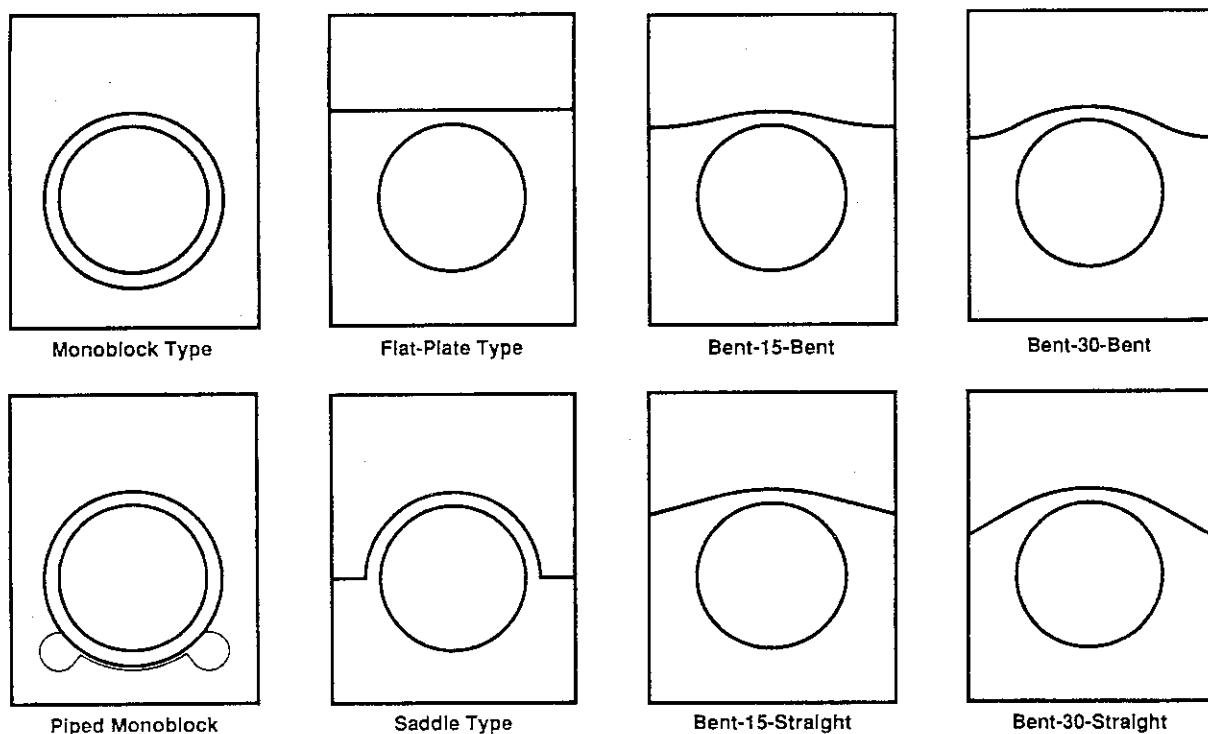


Fig. 7 Cross Sections Through the Considered Designs

Table 7.a Principal Geometry of the FEM Divertor Models

mono-block type	piped mono-block	flat plate type	bent 10-bent	bent 10-straight	bent 15-bent	bent 15-straight	bent 30-bent	bent 30-straight	saddle type	flat* 2-dim.	flat* 3-dim.
										bilinear 4-noded	linear 8-noded
number of nodes	4466	4939	4592	5010	5010	4904	4904	5028	5028	4466	1569
number of elements in the armor	1408	1626	1454	1590	1590	1554	1554	1596	1596	1408	1454
min. armor thickness (mm)	10.0	10.0	10.0	10.0	10.0	10.0	10.0	10.0	10.0	10.0	11632
max. armor thickness (mm)	(32.0)	(32.0)	10.0	11.3	11.7	11.6	12.6	13.3	14.9	19.0	510
length of the braze line in the 2D projection (mm)	56.5	40.1	25.0	25.2	25.3	25.6	26.2	27.3	35.3	25.0	4080
width of the heat sink (mm)	18.0	18.0	25.0	25.0	25.0	25.0	25.0	25.0	25.0	25.0	12.5(x2)

*) all other models: 2-dimensional, biquadratic integration, generalized plain strain, quadrilateral elements (8-noded).

Table 7.b

Comparison	open designs (flat-plate, saddle and bent interface)	closed designs (monoblock and piped monoblock)
de/re-brazing in situ	yes	no
machining & manufacture of divertor-shaped geometries	OK	OK ?
how to apply the brazing pressure	additional high temp. equipment needed	easily achieved
singularities	yes, at the open ends (lateral surfaces)	(no)
heat removal / armor	1D, 2D and 3D C/Cs OK.	only 2D and 3D
thermal fatigue of the joint	OK, if close match in thermal expansion betw. armor and heat sink	a close match in all directions presently is not achievable
neutron activation	higher in any case	favorable

Table 7.1.1 Analysis Summary for the MONOBLOCK TYPE

MFC-1	MFC-1	CX2002U	CX2002U	CX2002U	CX2002U	CX2002U	IG430U	SEP-N112
+ OF-Cu	+ DS-Cu	+ OF-Cu	+ OF&DS-Cu	+ DS-Cu	+ TZM	+ TZM	+ TZM	+ TZM (1mm)
predicted maximum residual stresses (MPa) in the carbon armor:								
x-x	tensile	11.	29.	12.	30.	6.5	7.4	4.6
	compressive	17.	42.	32.	80.	19.	14.	54.
y-y	tensile	21.	201.	12.	35.	9.1	6.8	25.
	compressive	149.	95f.	51.	120.	28.	20.	5.9
z-z	tensile	-	0.23	-	-	.85	3.0	98.
	compressive	4.8	9.5	14.	32.	.70	.85	96.
predicted maximum thermal stresses (MPa) in the carbon armor:								
x-x	tensile	7.0	22.	7.1	24.	5.9	6.6	4.5
	compressive	12.	33.	18.	72.	16.	16.	12.
y-y	tensile	102.	133.	8.6	23.	5.4	5.3	4.7
	compressive	105.	703.	29.	95.	27.	28.	22.
z-z	tensile	-	0.0	1.1	-	.86	1.3	2.3
	compressive	7.6	8.3	14.	33.	.22.	.20.	.23.
predicted maximum stresses (MPa) in the heat sink:								
residual	tensile	88.	507.	82.	40. & 508.	433.	126.	157.
	compressive	46.	228.	-	29. & -	-	21.	49.
thermal	tensile	67.	406.	75.	76. & 406.	365.	316.	283.
	compressive	43.	270.	7.8	24. & .55	44.	198.	191.
thermal response at 15 MW/m ² steady state:								
peak temperature (°C)								
on the top surface								
in the braze & heat sink								
tube inner surface								
peaking factor for the heat flux inside the coolant tube		1.19	1.19	1.48	1.47	1.42	1.39	1.40
corresponding figures:	7.1.1.	a	b	c	d	e	f	g
								h
							i	j
							k	l

Table 7.1.2 Analysis Summary for the PIPED MONOBLOCK TYPE

	CX2002U + OF-Cu	CX2002U + OF&DS-Cu	CX2002U + DS-Cu	CX2002U + TZM (1.5mm)	CX2002U + TZM (1.0mm)	CX2002U + W5Re
predicted maximum residual stresses (MPa) in the carbon armor:						
x-x	tensile compressive	68. 106.	74. 250.	73. 225.	16. 52.	12. 38.
y-y	tensile compressive	67. 49.	132. 104.	135. 114.	31. 27.	30. 22.
z-z	tensile compressive	21.	47.	3.6 45.	3.6 3.2	5.3 -
predicted maximum thermal stresses (MPa) in the carbon armor:						
x-x	tensile compressive	70. 63.	69. 206.	66. 180.	16. 44.	12. 43.
y-y	tensile compressive	47. 34.	114. 75.	116. 88.	31. 22.	29. 22.
z-z	tensile compressive	1.8 16.	41. 39.	1.1 22.	1.3 20.	2.4 23.
predicted maximum stresses (MPa) in the heat sink:						
residual	tensile compressive	90. 80.	116. & 410. 249. & 140.	320. 192.	77. 47.	107. 50.
thermal	tensile compressive	86. 54.	146. & 318. 186. & 122.	287. 141.	334. 156.	296. 156.
thermal response at 15 MW/m ² steady state:						
peak temperature (°C)						
on the top surface						
in the braze & heat sink						
tube inner surface						
peaking factor for the heat flux inside the coolant tube						
corresponding figures:	7.1.2.	a	b	c	d	e
					f	

Table 7.2.1 Analysis Summary for the FLAT-PLATE TYPE

	MFC-1 + OF-Cu	MFC-1 + DS-Cu	MFC-1 + TZM	CX2002U + W-30Cu	CX2002U + OF-Cu	CX2002U + DS-Cu	CX2002U + TZM	CX2002U + W5Re	CX2002U + W-30Cu	IG430U + TZM
predicted maximum residual stresses (MPa) in the carbon armor:										
x-x	tensile	.13	.15	4.5	.33	12.	8.2	1.6	1.2	4.6
	compressive	2.2	3.2	.18	.01	63.	108.	28.	20.	.41
y-y	tensile	5.0	8.0	120.	8.2	27.	17.	4.6	76.	6.5
	compressive	37.	69.	13.	.90	22.	239.	65.	3.4	1.0
z-z	tensile	-	-	4.6	.34	-	-	1.3	3.5	14.
	compressive	2.2	3.3	-	-	23.	49.	5.0	1.1	7.4
predicted maximum thermal stresses (MPa) in the carbon armor:										
x-x	tensile	.06	.04	.18	.38	6.8	3.3	3.9	6.4	4.6
	compressive	5.3	8.2	10.	7.4	32.	44.	13.	15.	29.
y-y	tensile	3.9	9.9	20.	14.	60.	16.	18.	21.	72.
	compressive	14.	10.	26.	8.0	9.5	82.	12.	13.	39.
z-z	tensile	-	-	1.2	.05	-	-	-	-	151.
	compressive	5.9	5.9	8.2	4.7	22.	30.	25.	27.	12.
										138.
predicted maximum stresses (MPa) in the heat sink:										
residual	tensile	21.	34.	139.	9.6	79.	323.	89.	67.	20.
	compressive	46.	82.	57.	4.0	85.	383.	102.	75.	22.
thermal	tensile	51.	203.	456.	278.	61.	286.	503.	799.	630.
	compressive	44.	212.	464.	379.	50.	183.	376.	626.	302.
thermal response at 15 MW/m ² steady state:										
peak temperature (°C)										
on the top surface		940.	1018.	1655.	1067.	1563.	1632.	2097.	2262.	4000.
in the braze & heat sink		457.	511.	964.	546.	443.	489.	858.	1005.	519.
tube inner surface		296.	297.	301.	298.	299.	301.	309.	309.	305.
peaking factor for the heat flux										
inside the coolant tube		1.24	1.27	1.37	1.28	1.32	1.36	1.58	1.62	1.39
corresponding figures:	7.2.1.	a	b	c	d	e	f	g	h	j

Table 7.2.2 Analysis Summary for the SADDLE TYPE

	MFC-1 + OF-Cu	MFC-1 + QE&DS-Cu	MFC-1 + OF&DS-Cu	MFC-1 + DS-Cu	MFC-1 + TZM	MFC-1 + W-30Cu	CX2002U + OF-Cu	CX2002U + QE&DS-Cu	CX2002U + OF&DS-Cu	CX2002U + TZM	CX2002U + OF&TzM
predicted maximum residual stresses (MPa) in the carbon armor:											
x-x	tensile <i>compressive</i>	6.3 8.0	19. 20.	33. 30.	8.2 32.	5.0 11.	6.0 24.	7.1 75.	27. 72.	29. 76.	2.4 26.
y-y	tensile <i>compressive</i>	13. 282.	46. 482.	90. 973.	112. 845.	220. 367.	142. 659.	11. 70.	35. 109.	37. 137.	88. 66.
z-z	tensile <i>compressive</i>	- 3.1	- 6.5	1.2 7.5	- 8.0	4.7 -	.43 3.6	- 27.	- 34.	- 37.	.80 4.9
predicted maximum thermal stresses (MPa) in the carbon armor:											
x-x	tensile <i>compressive</i>	5.6 5.1	17. 15.	28. 21.	5.4 25.	2.9 9.1	3.6 20.	8.7 69.	27. 54.	27. 59.	1.5 20.
y-y	tensile <i>compressive</i>	100. 118.	54. 314.	88. 747.	101. 599.	73. 241.	104. 489.	13. 56.	18. 94.	19. 119.	5.7 68.
z-z	tensile <i>compressive</i>	- 7.5	- 8.3	1.3 8.6	- 8.8	2.5 6.1	.22 6.2	- 20.	- 27.	- 29.	.38 26.
predicted maximum stresses (MPa) in the heat sink:											
residual	tensile <i>compressive</i>	242. 183.	244. & 362. & 42.	503. 173. & 666.	71. & 461.	546. 274.	630. 436.	132. 96.	73. 8 76. 8	469. 3.9	47. 8 76. 8
thermal	tensile <i>compressive</i>	196. 144.	239. & 290. & 88.	425. 102. & 126. & 632.	439. 447. 320.	381. 381. 260.	471. 325.	127. 108.	59. 8 53. 8	413. 53.	392. 73. 8 219.
thermal response at 15 MW/m ² steady state:											
peak temperature (°C)	on the top surface in the braze & heat sink tube inner surface										
	1049. 357. 293.	1056. 367. 293.	1058. 373. 293.	1074. 373. 293.	1311. 505. 293.	1096. 384. 293.	1704. 386. 305.	1722. 399. 304.	1731. 405. 304.	1965. 560. 303.	1944. 556. 303.
peaking factor for the heat flux inside the coolant tube											
corresponding figures:	7.2.2.	a	b	c	d	e	f	g	h	i	j
											k

Table 7.2.3.bb Analysis Summary for the BENT-30-BENT TYPE

	MFC-1 + OF-Cu	MFC-1 + DS-Cu	MFC-1 + TZM	MFC-1 + W-30Cu	CX2002U + OF-Cu	CX2002U + DS-Cu	CX2002U + TZM	CX2002U + W5Re
predicted maximum residual stresses (MPa) in the carbon armor:								
x-x	tensile compressive	.48 .81	.63 .14	4.4 .48	.58 43.	6.1 109.	8.2 109.	2.1 28.
y-y	tensile compressive	26. 31.	30. 41.	182. 30.	76. 38.	19. 39.	33. 288.	21. 55.
z-z	tensile compressive	- 3.1	- 4.3	4.7 -	.42 .45	- 21.	- 51.	3.4 1.5
predicted maximum thermal stresses (MPa) in the carbon armor:								
x-x	tensile compressive	.08 7.6	.07 10.	.70 7.7	.47 7.7	3.8 29.	4.4 59.	.59 9.2
y-y	tensile compressive	15. 23.	20. 32.	7.8 17.	28. 26.	53. 12.	18. 154.	10. 31.
z-z	tensile compressive	- 6.4	- 6.6	1.1 7.0	5.2 7.0	- 19.	- 32.	- 26.
predicted maximum stresses (MPa) in the heat sink:								
residual	tensile compressive	58. 39.	84. 52.	196. 94.	79. 65.	76. 80.	292. 441.	59. 111.
thermal	tensile compressive	50. 49.	174. 171.	300. 360.	248. 279.	56. 47.	237. 243.	10. 317.
thermal response at 15 MW/m ² steady state:								
peak temperature (°C)								
on the top surface	969.	1019.	1458.	1057.	1649.	1695.	2042.	2180.
in the braze & heat sink	367.	391.	678.	416.	379.	400.	592.	683.
tube inner surface	295.	295.	298.	296.	302.	303.	306.	307.
peaking factor for the heat flux inside the coolant tube	1.21	1.22	1.28	1.23.	1.40	1.42	1.52	1.55
corresponding figures:	7.2.3.bb-	a	b	c	d	e	f	g
							h	

Table 7.2.3.bs Analysis Summary for the BENT-30-STRAIGHT TYPE

	MFC-1 + OF-Cu	MFC-1 + DS-Cu	MFC-1 + TZM	MFC-1 + W-30Cu	CX2002U + OF-Cu	CX2002U + DS-Cu	CX2002U + TZM	CX2002U + W5Re
predicted maximum residual stresses (MPa) in the carbon armor:								
x-x	tensile compressive	.05 10.	.10 .24	4.4 6.0	.27 41.	4.7 75.	3.6 18.	.48 13.
y-y	tensile compressive	19. 62.	26. 224.	107. 8.5	17. 81.	13. 89.	32. 291.	.61 49.
z-z	tensile compressive	- 3.4	- 4.6	4.4 -.64	-.31 -.64	- 22.	-.45. 1.1	3.4 - 3.4
predicted maximum thermal stresses (MPa) in the carbon armor:								
x-x	tensile compressive	.37 8.2	.06 11.	.91 7.6	.01 8.2	7.7 31.	1.9 41.	.23 8.8
y-y	tensile compressive	15. 42.	18. 142.	5.2 21.	13. 59.	19. 22.	18. 178.	9.7 30.
z-z	tensile compressive	- 6.5	- 6.9	1.0 6.5	5.2 5.2	- 19.	-.33. 33.	- 26. 27.
predicted maximum stresses (MPa) in the heat sink:								
residual	tensile compressive	60. 66.	125. 196.	91. 39.	69. 72.	77. 97.	294. 276.	79. 65.
thermal	tensile compressive	50. 52.	177. 138.	300. 326.	251. 236.	57. 47.	235. 174.	311. 240.
thermal response at 15 MW/m ² steady state:								
peak temperature (°C)								
on the top surface								
in the braze & heat sink								
tube inner surface								
peaking factor for the heat flux inside the coolant tube								
corresponding figures:	7.2.3.bs-	a	b	c	d	e	f	g h

Table 7.2.4 Analysis Summary for the Materials Combination MFC-1 (1992) & DS-Cu

	flat	bent-10-bent	bent-10-straight	bent-15-bent	bent-15-straight	bent-30-bent	bent-30-straight	saddle
predicted maximum residual stresses (MPa) in the carbon armor:								
x-x	tensile compressive	.15 3.2	.49 5.8	.11 6.2	.58 6.9	.10 8.0	.63 10.	.10 13.
y-y	tensile compressive	8.0 69.	10. 45.	6.5 92.	15. 42.	9.4 113.	30. 41.	32. 112.
z-z	tensile compressive	- 3.3	- 3.6	- 3.6	- 3.7	- 3.9	- 4.3	- 4.6
predicted maximum thermal stresses (MPa) in the carbon armor:								
x-x	tensile compressive	.04 8.2	.05 8.7	.05 8.8	.05 8.9	.05 9.4	.07 10.	.06 11.
y-y	tensile compressive	9.9 10.	9.8 15.	8.7 25.	13. 16.	9.6 44.	20. 32.	25. 101.
z-z	tensile compressive	- 5.9	- 6.2	- 6.2	- 6.3	- 6.4	- 6.6	- 6.9
predicted maximum stresses (MPa) in the heat sink:								
residual	tensile compressive	34. 82.	52. 56.	48. 97.	67. 53.	58. 113.	84. 52.	54. 461.
thermal	tensile compressive	203. 212.	191. 202.	190. 194.	187. 197.	183. 178.	174. 171.	125. 196.
thermal response at 15 MW/m ² steady state:								
peak temperature (°C)								
on the top surface								
in the braze & heat sink								
tube inner surface								
peaking factor for the heat flux inside the coolant tube								
corresponding figures:	7.2.1.b	7.2.4.a	7.2.4.b	7.2.4.c	7.2.4.d	7.2.3.bb-b	7.2.3.bs-d	7.2.2.d

Table 7.2.5 Analysis Summary for the Materials Combination MFC-1 (1992) & W-30Cu

	flat	bent-10-bent	bent-10-straight	bent-15-bent	bent-15-straight	bent-30-bent	bent-30-straight	saddle
predicted maximum residual stresses (MPa) in the carbon armor:								
x-x	tensile	.33	.73	.38	.94	.39	.58	.27
	compressive	.01	1.7	1.8	2.4	3.1	4.8	6.0
y-y	tensile	8.2	34.	4.2	38.	6.5	76.	24.
	compressive	.90	12.	2.7	13.	8.4	38.	142.
z-z	tensile	.34	3.9	.34	.42	.34	.42	669.
	compressive	-	-	-	.09	.19	.45	.31
								.43
								3.6
predicted maximum thermal stresses (MPa) in the carbon armor:								
x-x	tensile	.38	.41	.27	.41	.15	.47	.01
	compressive	7.4	7.4	7.5	7.4	7.6	7.7	3.6
y-y	tensile	14.	20.	8.9	20.	7.6	28.	20.
	compressive	8.0	12.	10.	13.	12.	26.	104.
z-z	tensile	.05	-	-	-	-	-	489.
	compressive	4.7	4.9	4.9	5.0	5.0	5.2	.22
								6.2
predicted maximum stresses (MPa) in the heat sink:								
residual	tensile	9.6	36.	15.	40.	23.	79.	69.
	compressive	4.0	29.	7.9	40.	12.	65.	72.
thermal	tensile	278.	259.	257.	255.	248.	251.	636.
	compressive	379.	338.	325.	330.	301.	279.	436.
thermal response at 15 MW/m ² steady state:								
peak temperature (°C)								
on the top surface		1067.	1063.	1060.	1057.	1057.	1047.	1096.
in the braze & heat sink		546.	493.	475.	480.	416.	405.	384.
tube inner surface		298.	297.	297.	296.	296.	296.	293.
peaking factor for the heat flux								
inside the coolant tube		1.28	1.26	1.26	1.25	1.25	1.23	1.18
corresponding figures:		7.2.1.d	7.2.5.a	7.2.5.b	7.2.5.c	7.2.5.d	7.2.3.bb-d	7.2.3.bs-d
								7.2.2.f

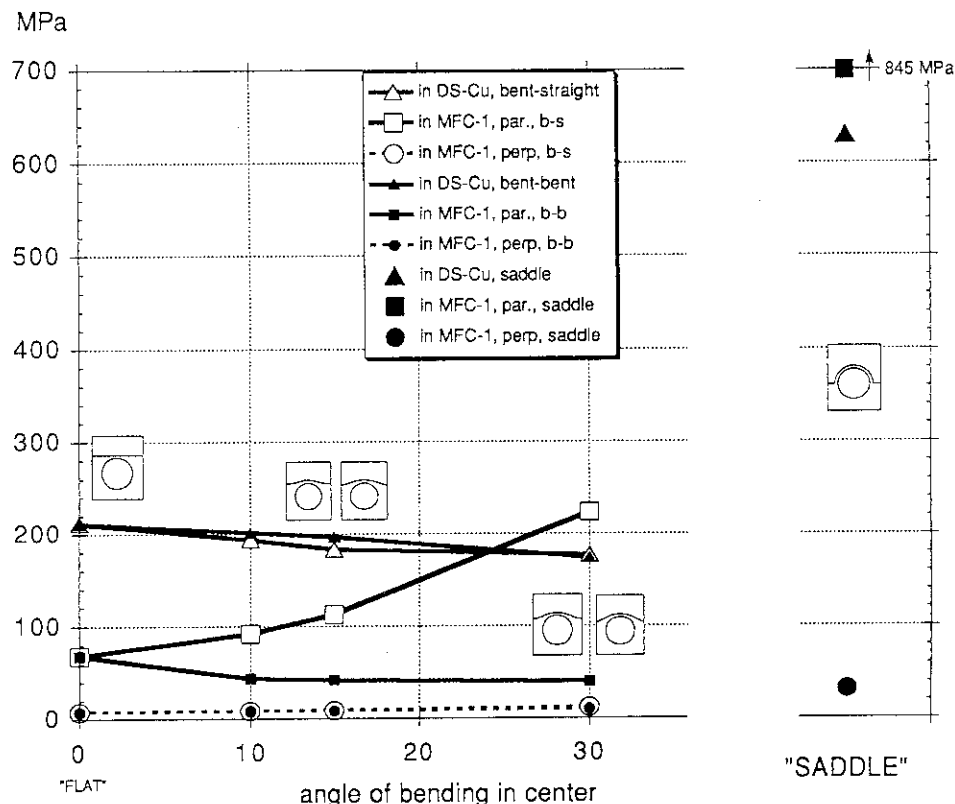


Fig. 7.2.4 Peak Residual and/or Thermal Stresses in (MFC-1 Armor/DS-Cu Heat-Sink) Combinations

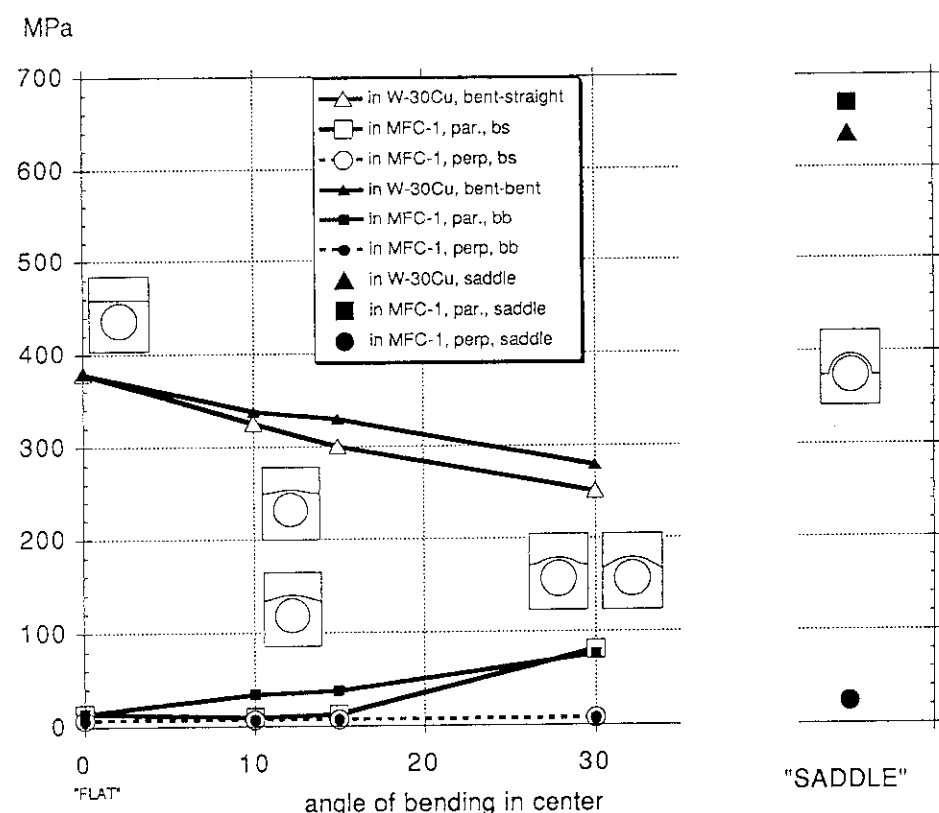


Fig. 7.2.5 Peak Residual and/or Thermal Stresses in (MFC-1 Armor/W-30Cu Heat-Sink) Combinations

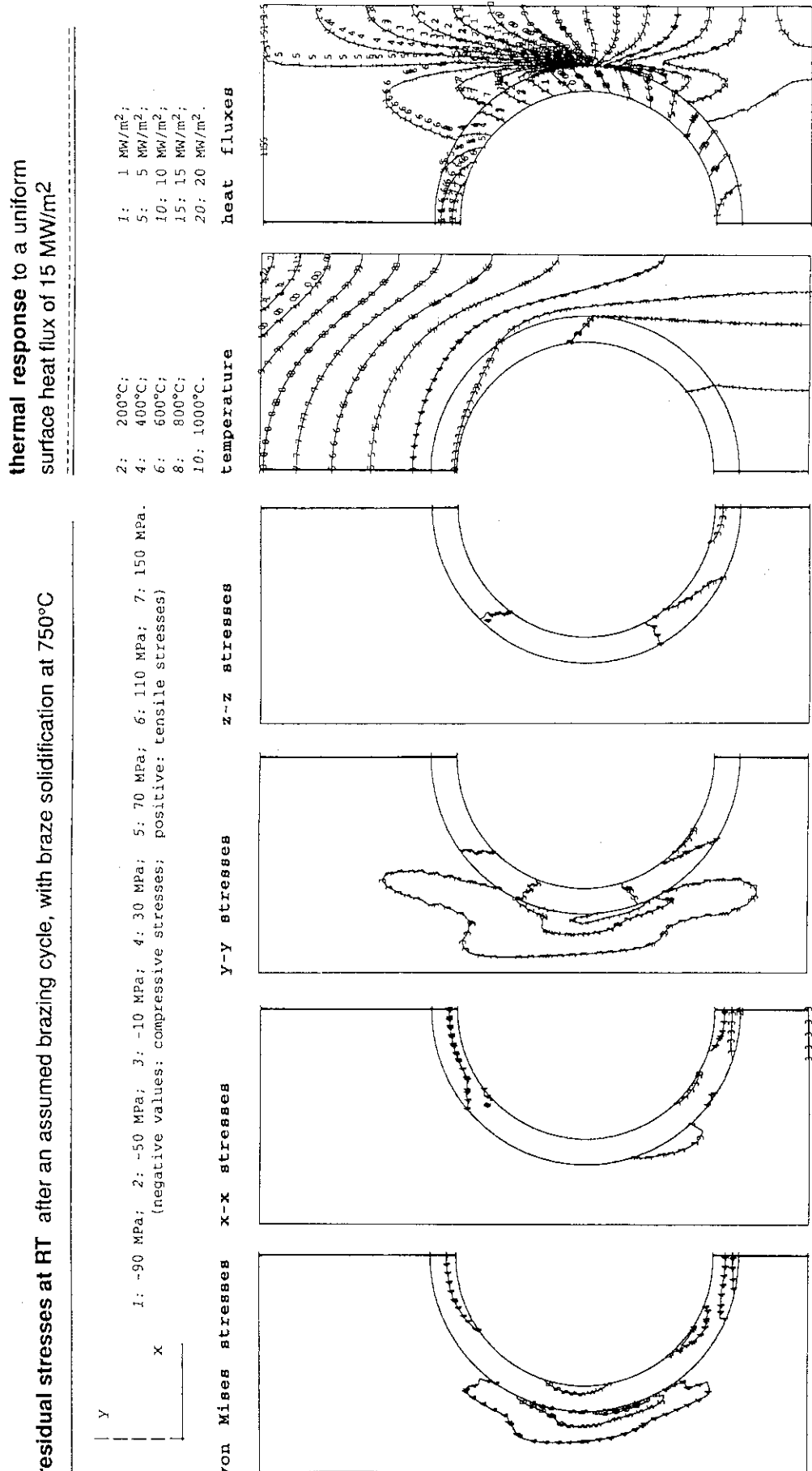


Fig. 7.1.1.a/I Monoblock Type, Armor: MFC-1 (1992), Heat Sink: OF-Cu

stress distribution and displacement at a uniform steady state surface heat flux of 15 MW/m²

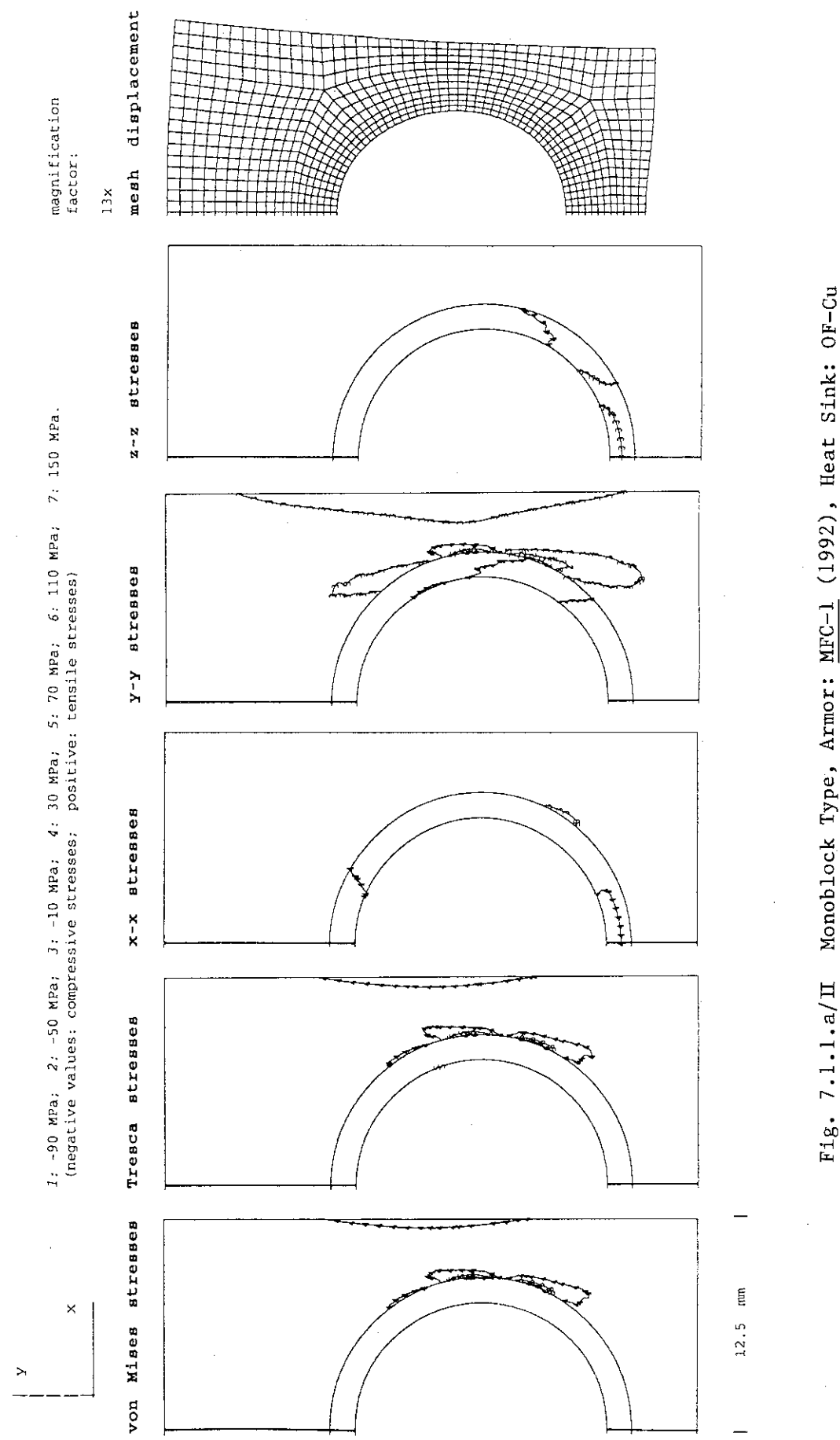
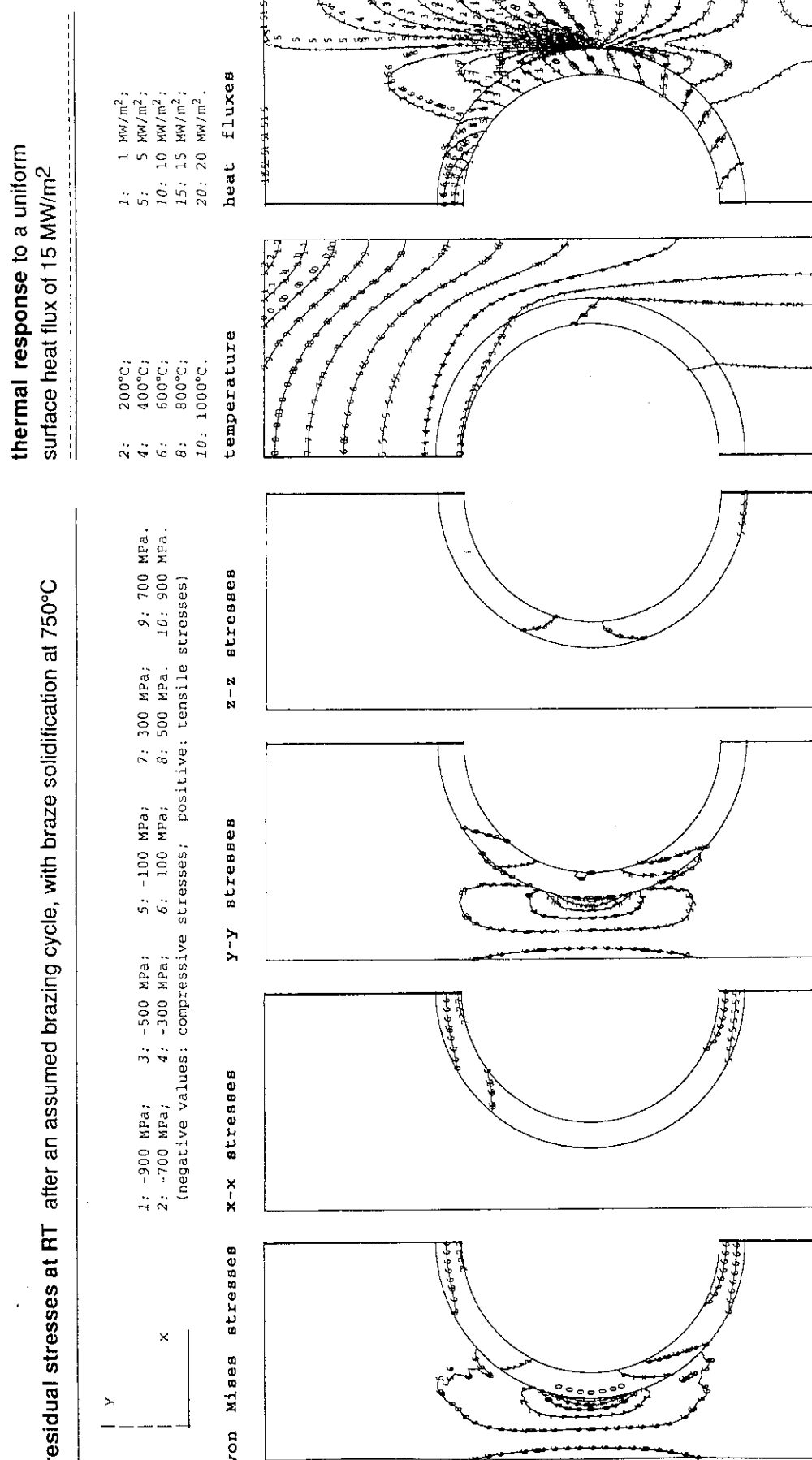


Fig. 7.1.1.a/II Monoblock Type, Armor: MFC-1 (1992), Heat Sink: OF-Cu



12.5 mm

Fig. 7.1.1.b/I Monoblock Type, Armor: MFC-1 (1992), Heat Sink: DS-Cu

stress distribution and displacement at a uniform steady state surface heat flux of 15 MW/m²

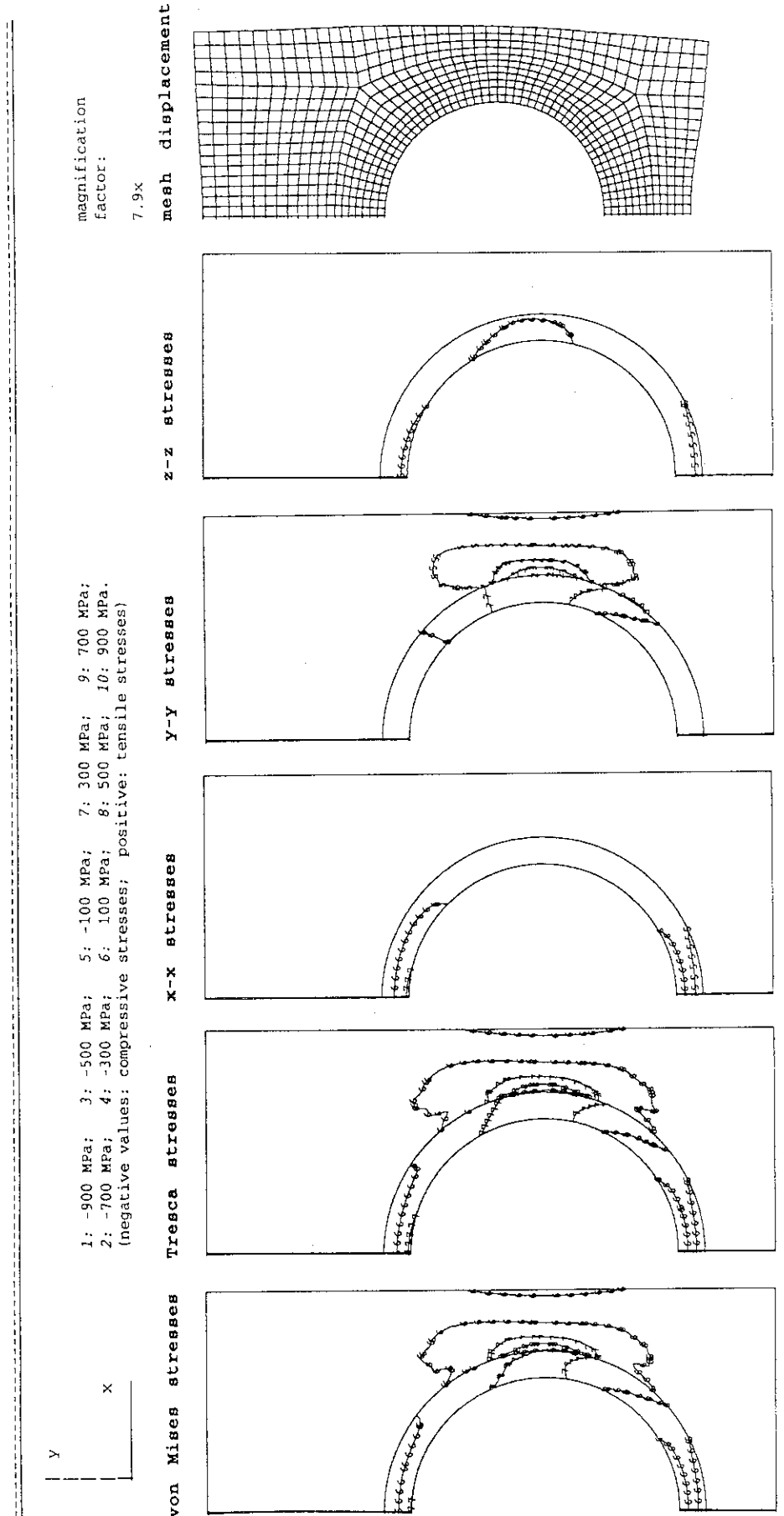


Fig. 7.1.1.b/II Monoblock Type, Armor: MFC-1 (1992), Heat Sink: DS-Cu

residual stresses at RT after an assumed brazing cycle, with braze solidification at 750°C

thermal response to a uniform surface heat flux of 15 MW/m²

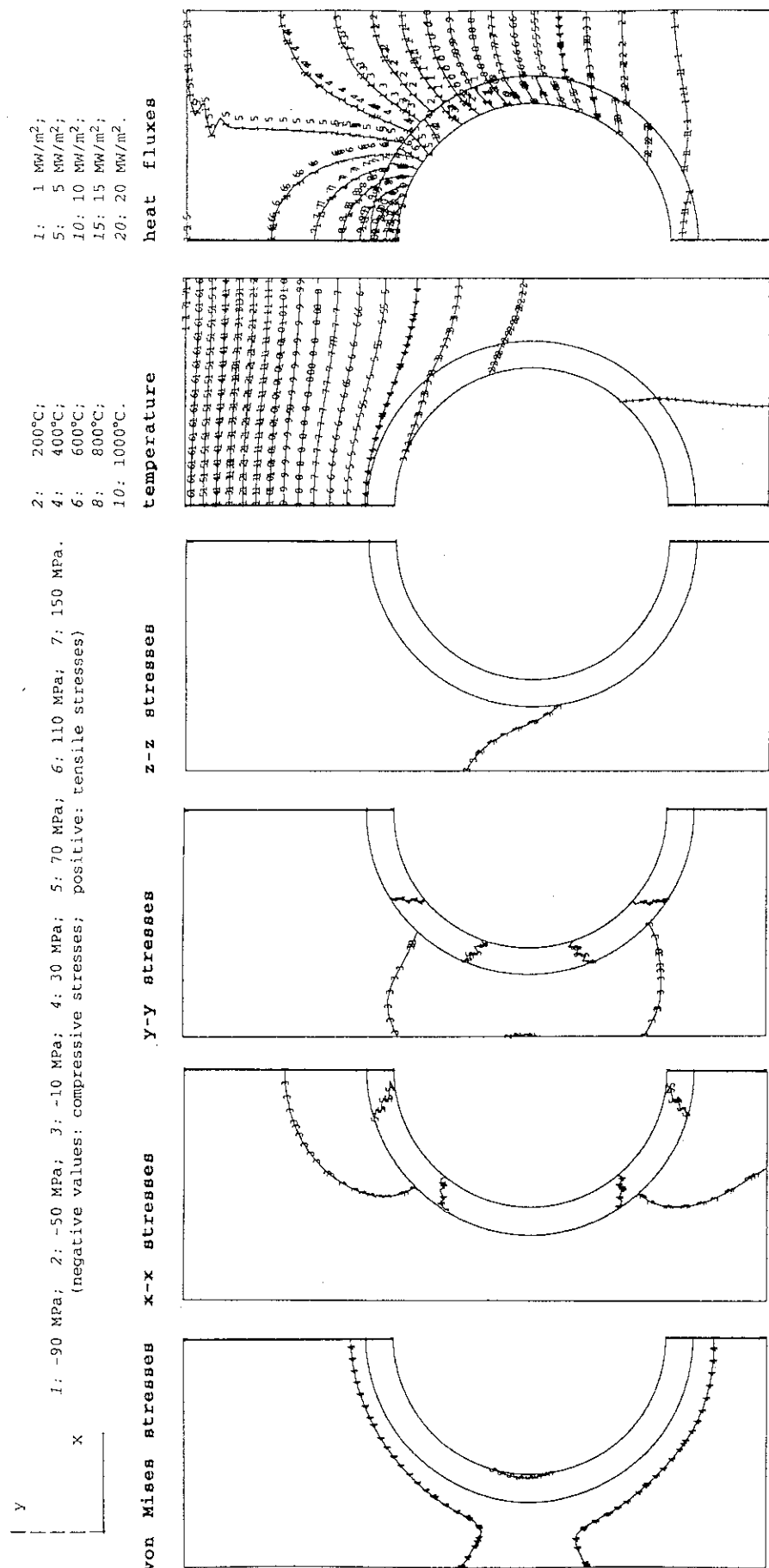


Fig. 7.1.1.c/I Monoblock Type, Armor: CX2002U, Heat Sink: OF-Cu

stress distribution and displacement at a uniform steady state surface heat flux of 15 MW/m²

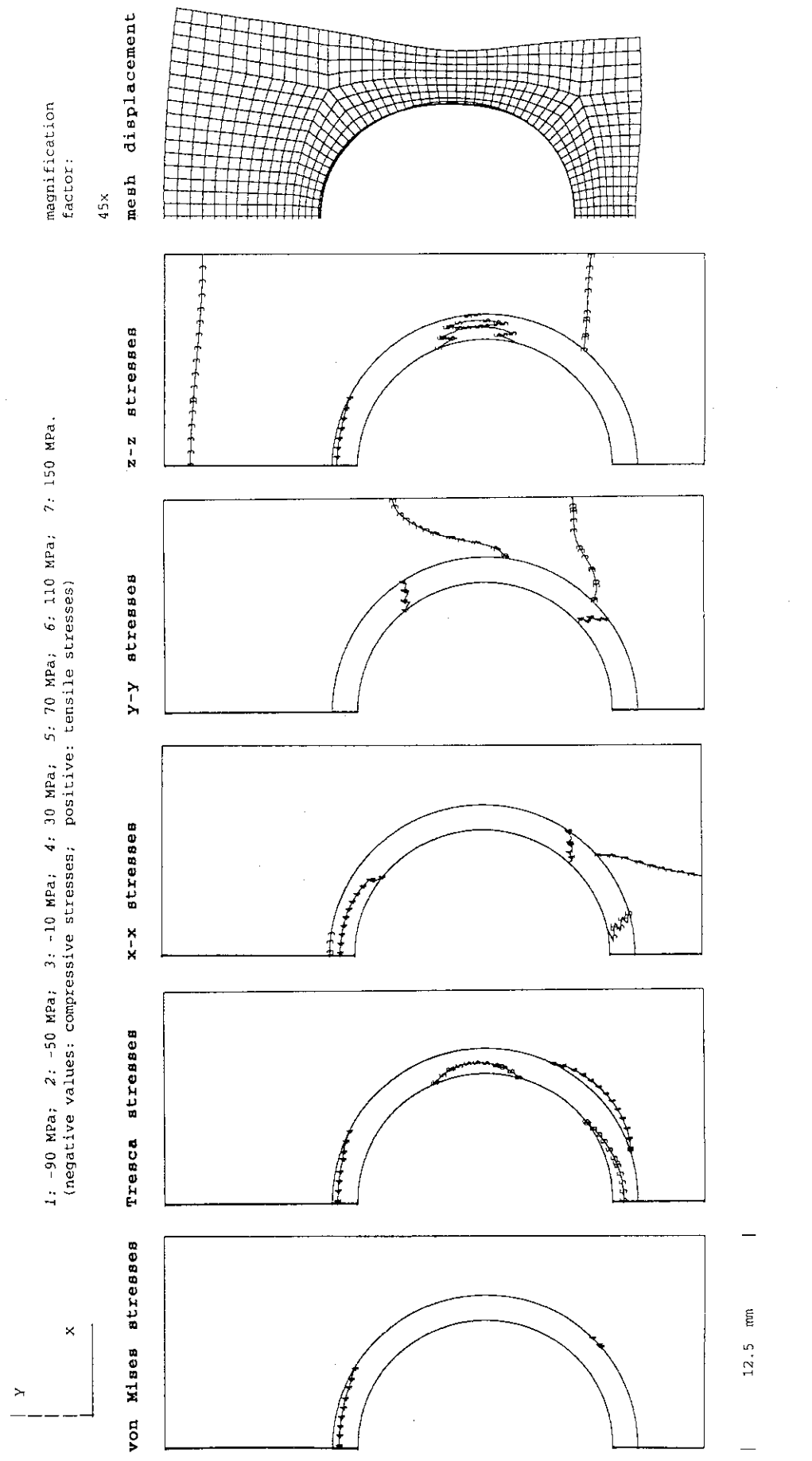


Fig. 7.1.1.c/II Monoblock Type, Armor: CX2002U, Heat Sink: OF-Cu

residual stresses at RT after an assumed brazing cycle, with braze solidification at 750°C

thermal response to a uniform surface heat flux of 15 MW/m²

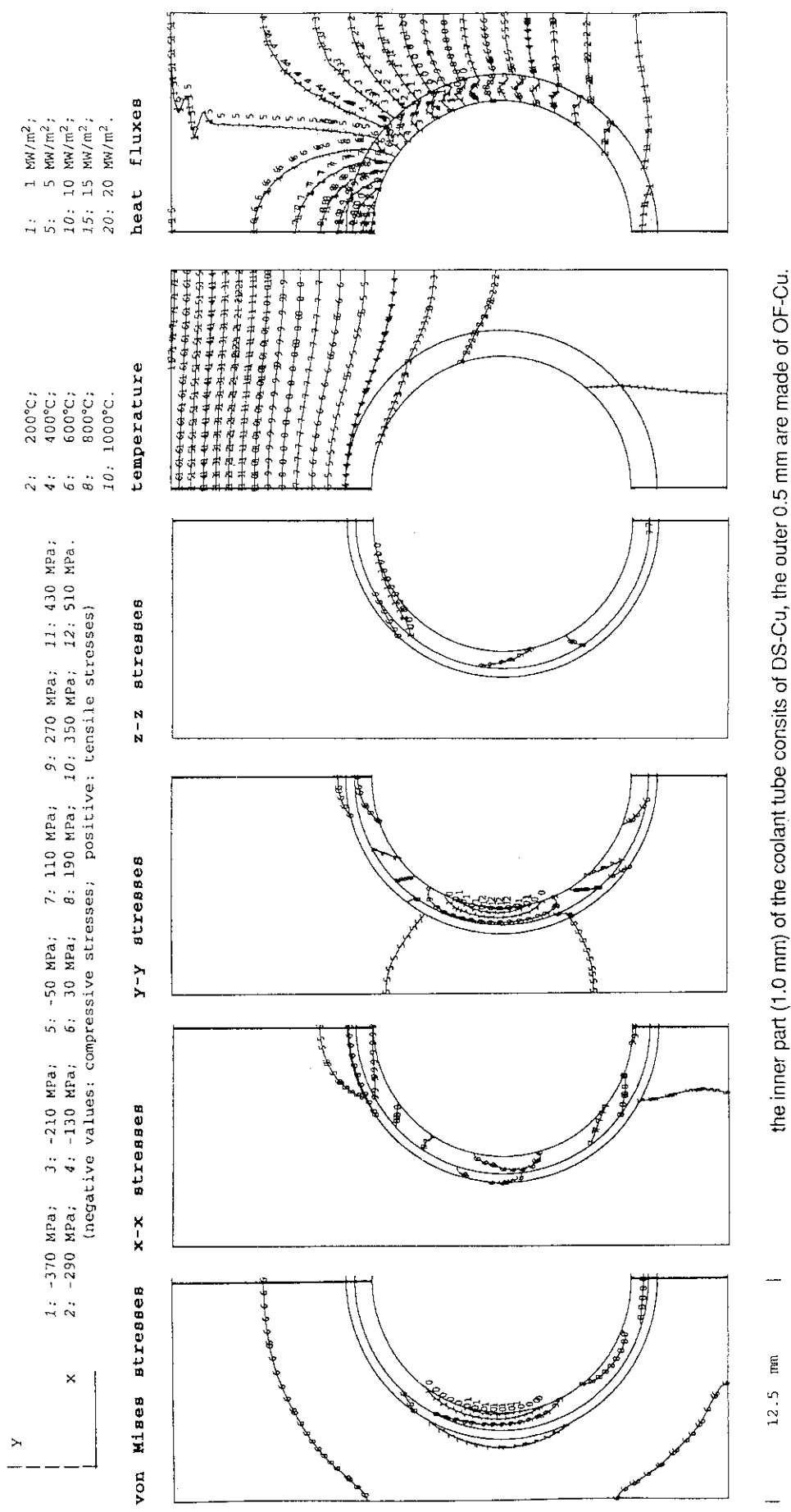
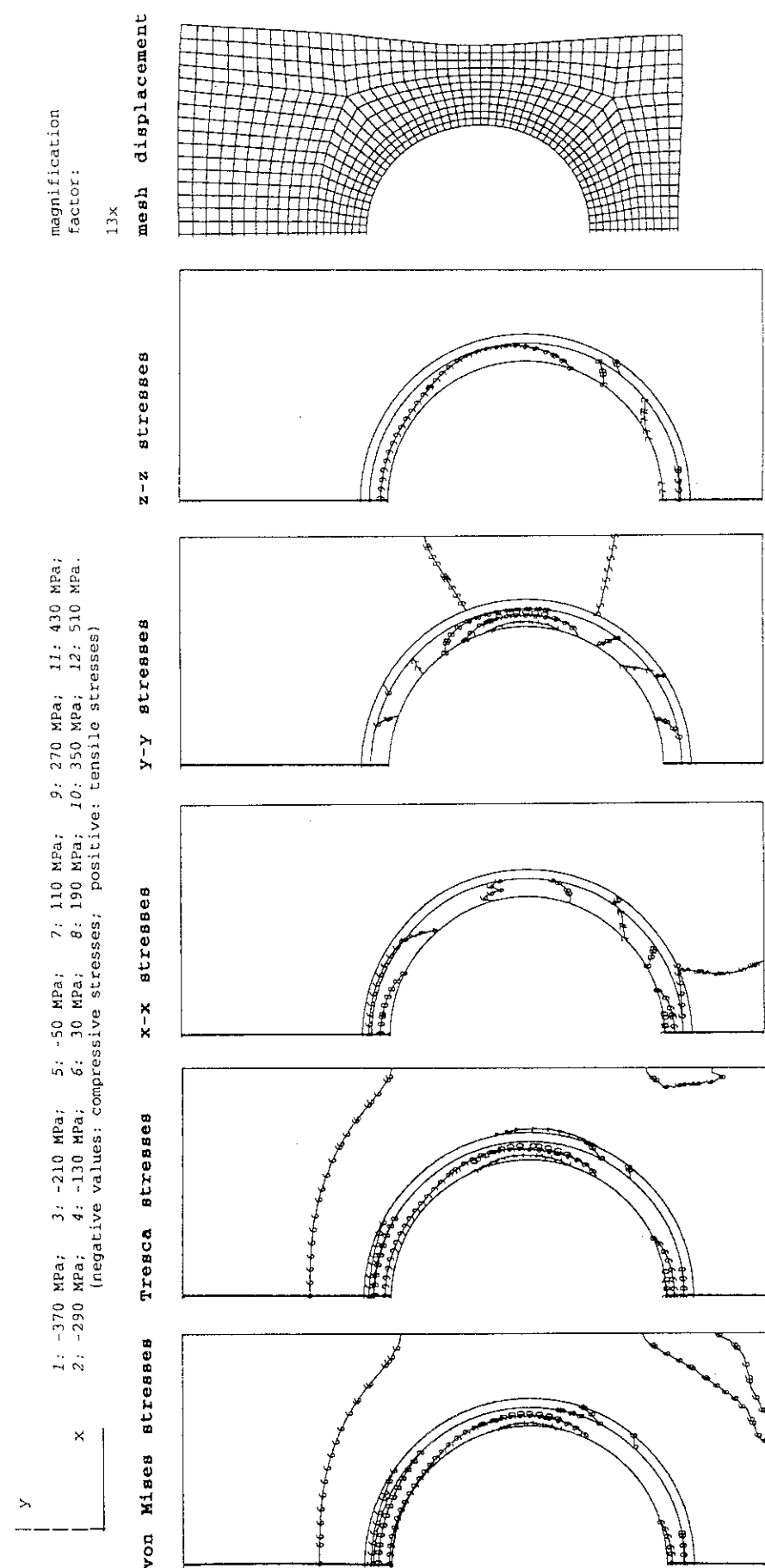


Fig. 7.1.1.d/I Monoblock Type, Armor: CX2002U, Tube: OF(0.5)&DS(1.0mm)-Cu
the inner part (1.0 mm) of the coolant tube consists of DS-Cu, the outer 0.5 mm are made of OF-Cu.

stress distribution and displacement at a uniform steady state surface heat flux of 15 MW/m²



the inner part (1.0 mm) of the coolant tube consists of DS-Cu, the outer 0.5 mm are made of OF-Cu.

Fig. 7.1.1.d/II Monoblock Type, Armor: CX2002U, Tube: OF(0.5)&DS(1.0 mm)-Cu

residual stresses at RT after an assumed brazing cycle, with braze solidification at 750°C

thermal response to a uniform surface heat flux of 15 MW/m²

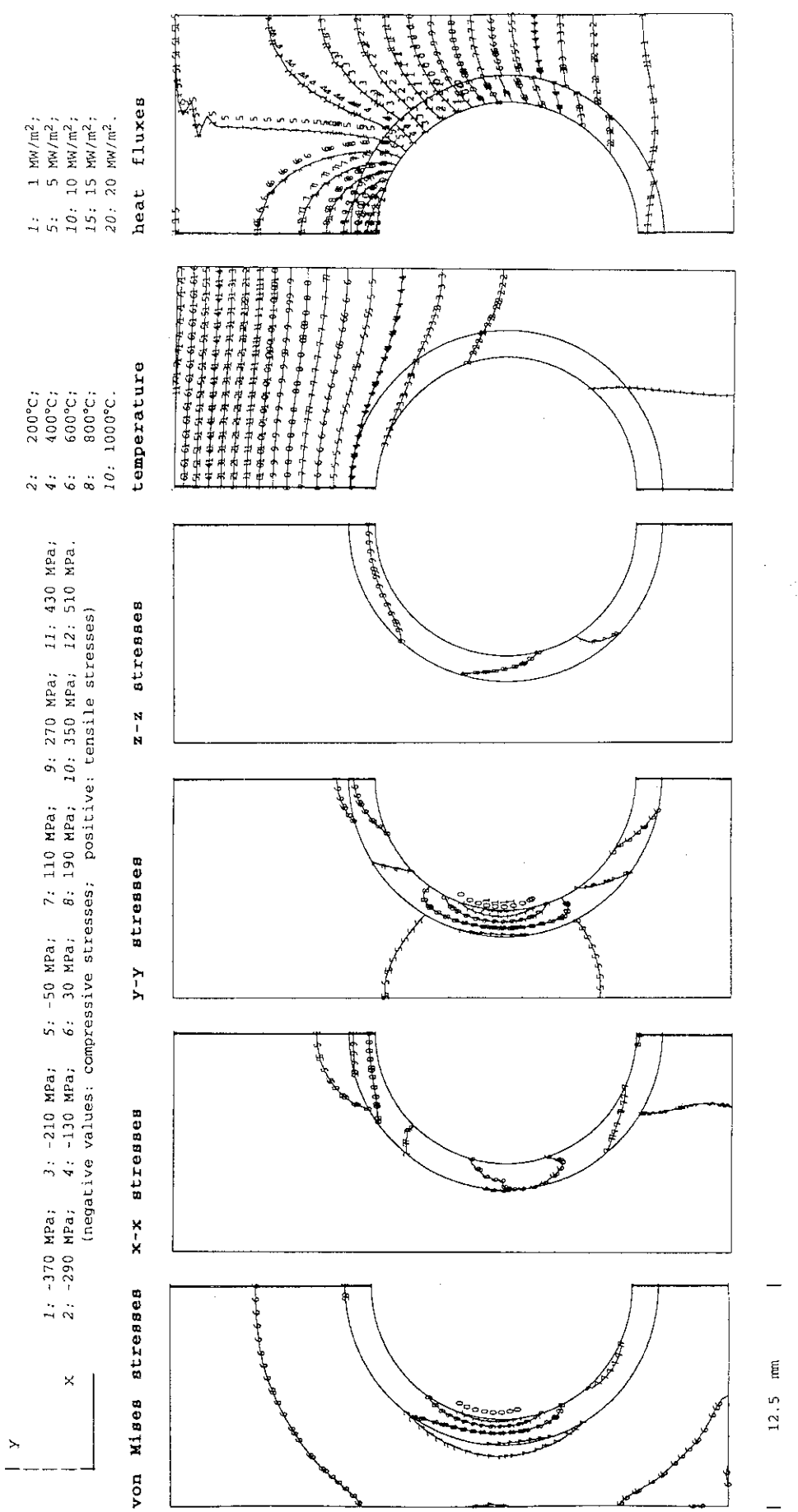


Fig. 7.1.1.e/I Monoblock Type, Armor: CX2002U, Heat Sink: DS-Cu

12.5 mm

stress distribution and displacement at a uniform steady state surface heat flux of 15 MW/m²

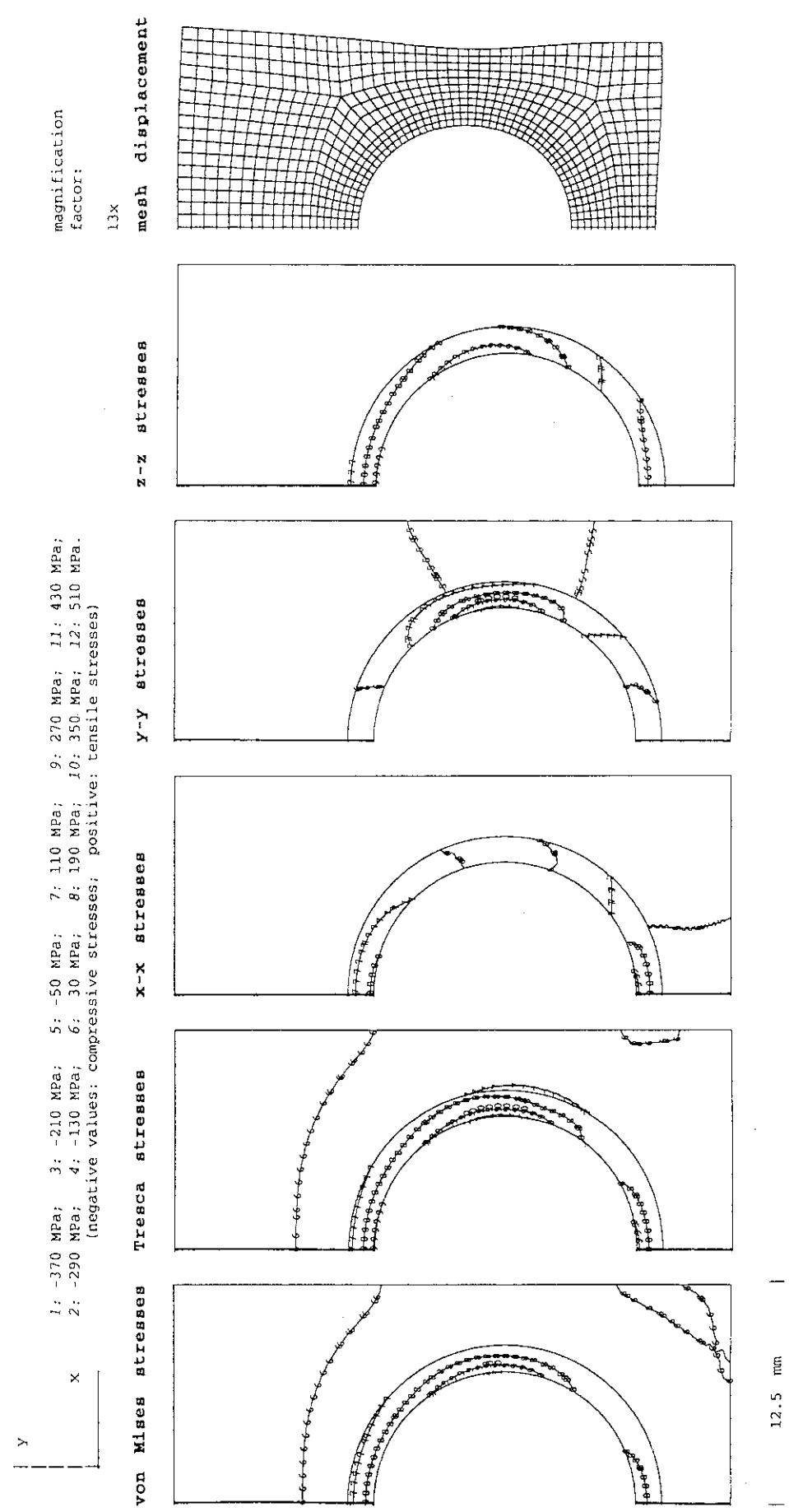


Fig. 7.1.1.e/II Monoblock Type, Armor: CX2002U, Heat Sink: DS-Cu

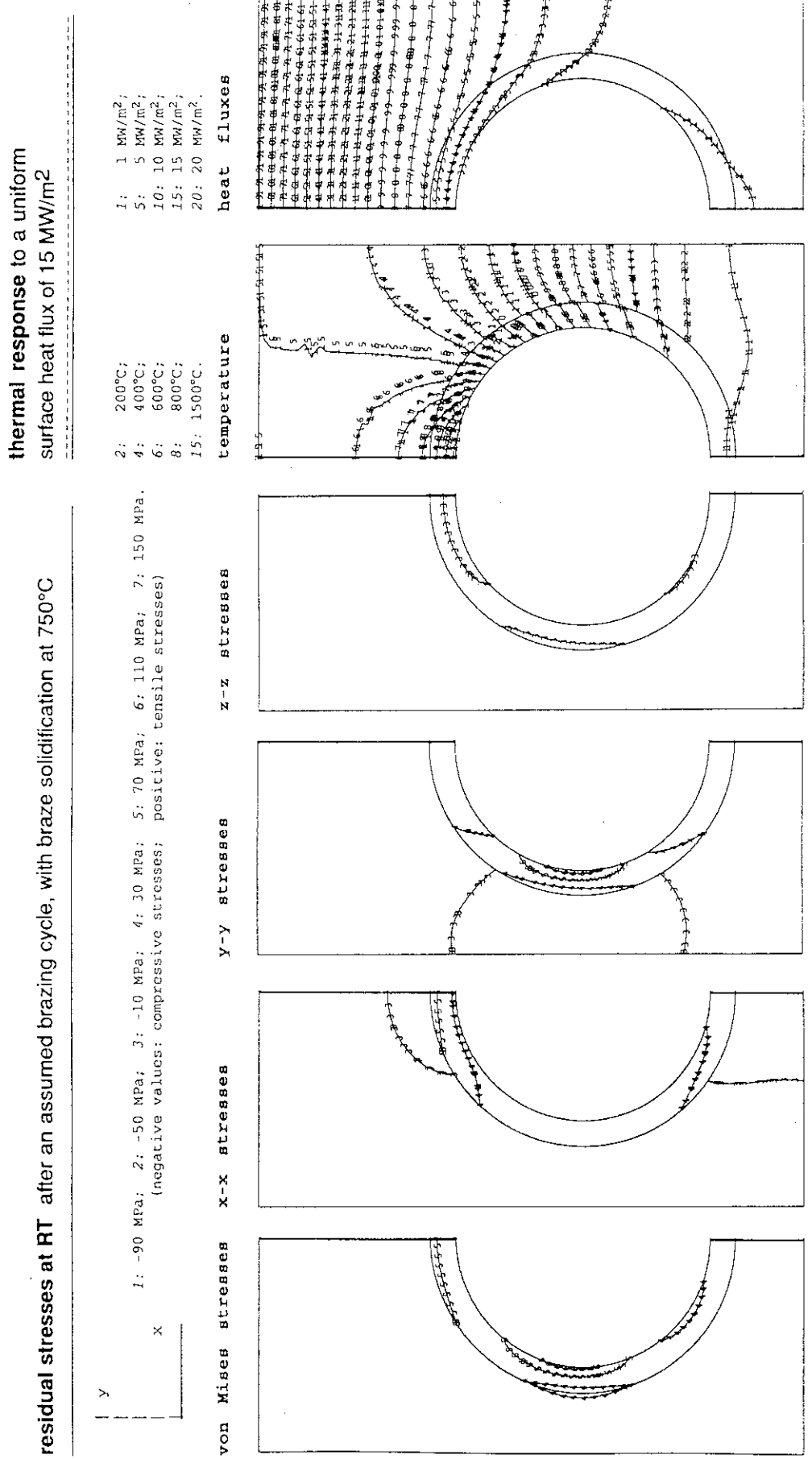


Fig. 7.1.1.f/I Monoblock Type, Armor: CX2002U, Heat Sink: TZM (1.5 mm)

stress distribution and displacement at a uniform steady state heat flux of 15 MW/m²

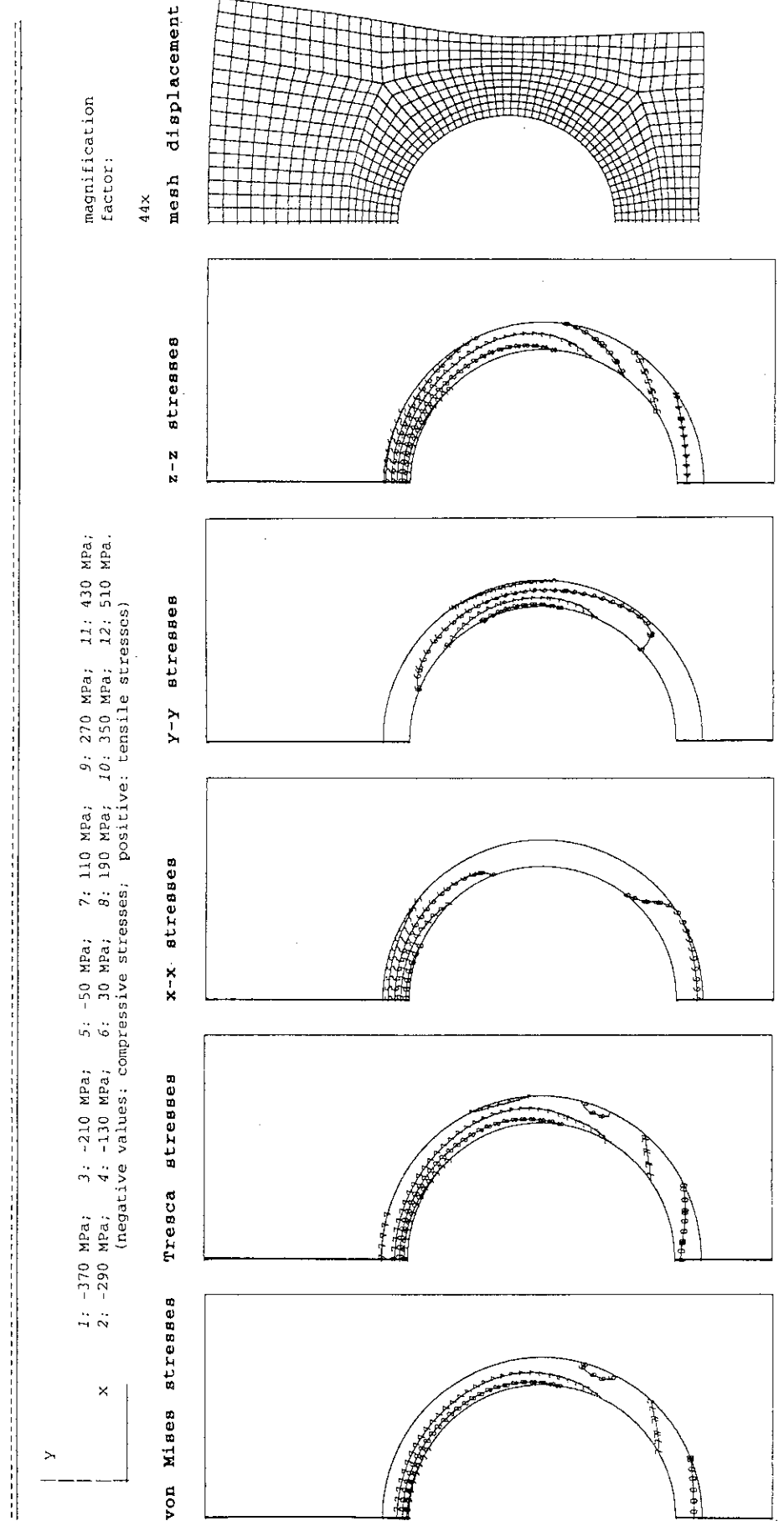


Fig. 7.1.1.f/II Monoblock Type, Armor: CX2002U, Heat Sink: TZM (1.5 mm)

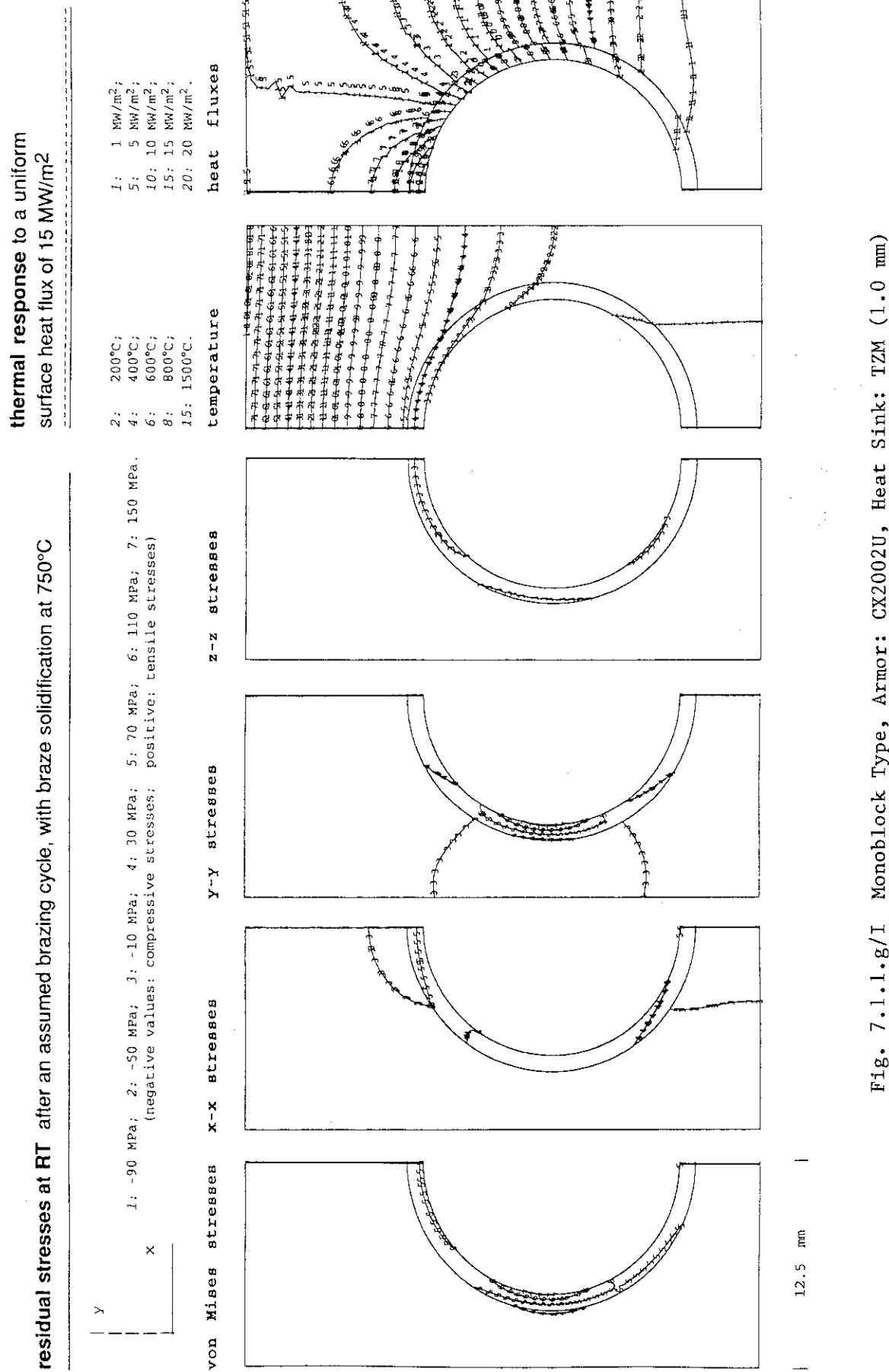
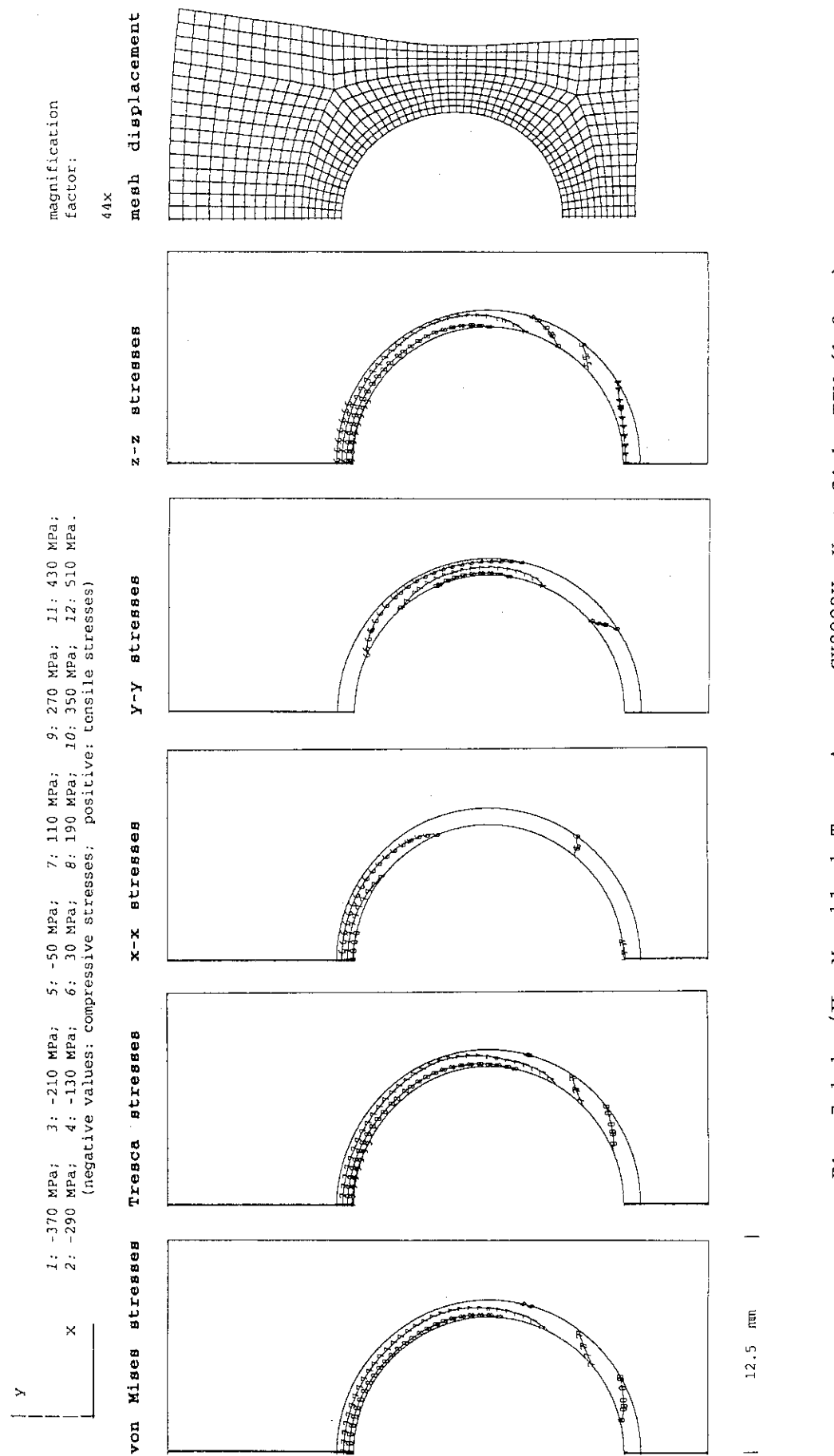


Fig. 7.1.1.g/I Monoblock Type, Armor: CX2002U, Heat Sink: TZM (1.0 mm)

stress distribution and displacement at a uniform steady state surface heat flux of 15 MW/m²



residual stresses at RT after an assumed brazing cycle, with braze solidification at 750°C

thermal response to a uniform surface heat flux of 15 MW/m²

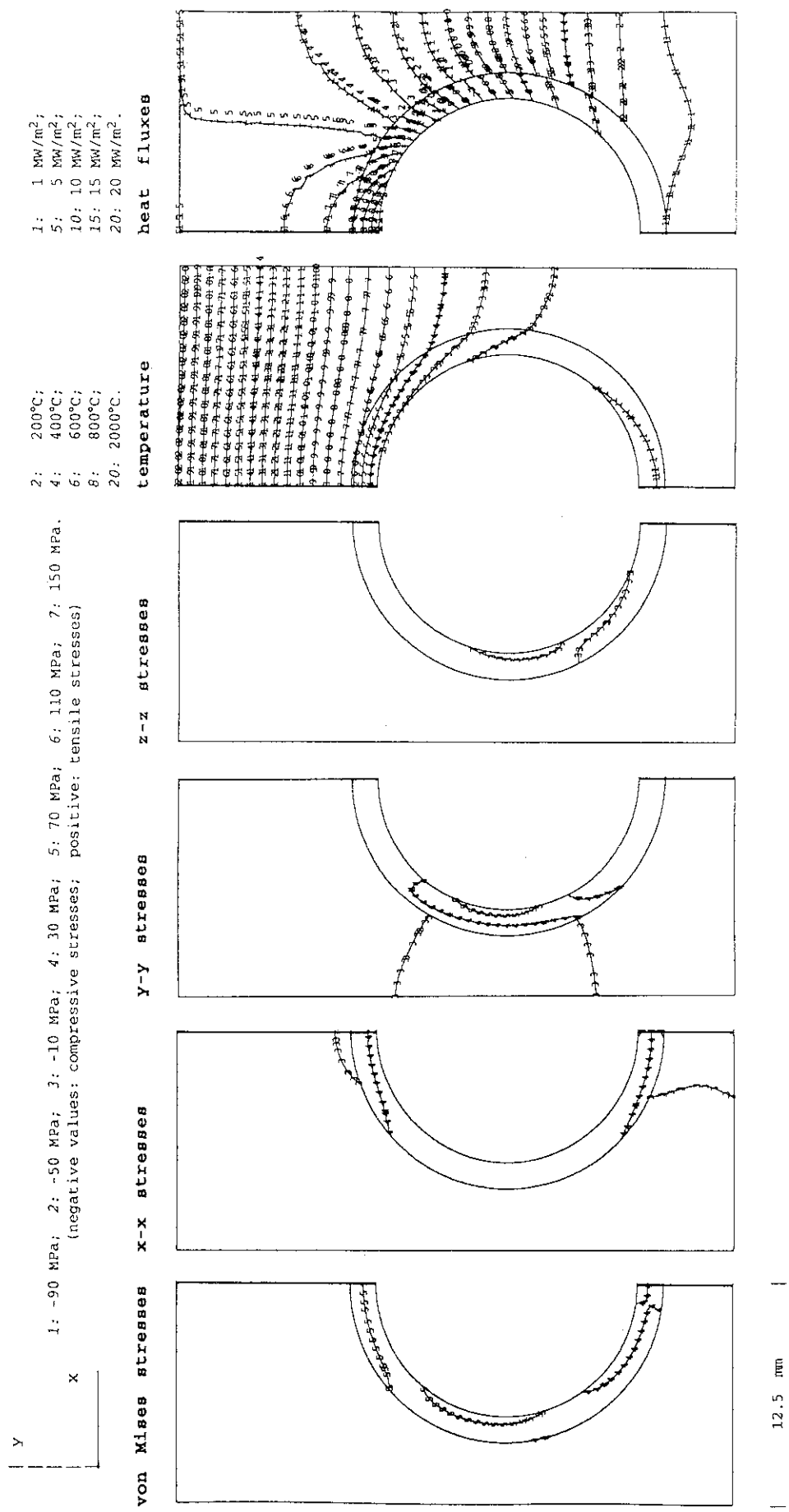


Fig. 7.1.1.h/I Monoblock Type, Armor: CX2002U, Heat Sink: W5Re

stress distribution and displacement at a uniform steady state surface heat flux of 15 MW/m²

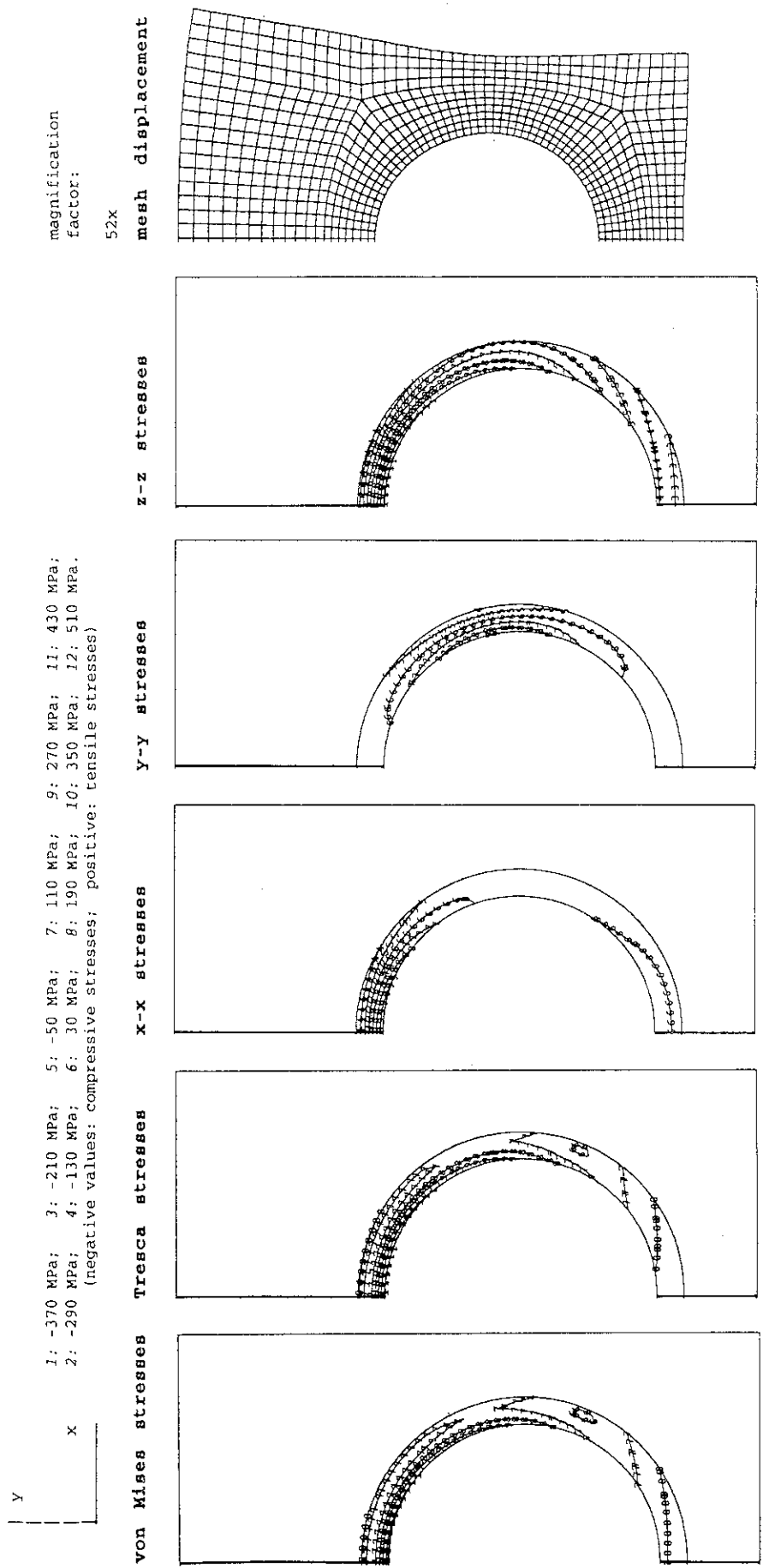


Fig. 7.1.1.h/II Monoblock Type, Armor: CX2002U, Heat Sink: W5Re

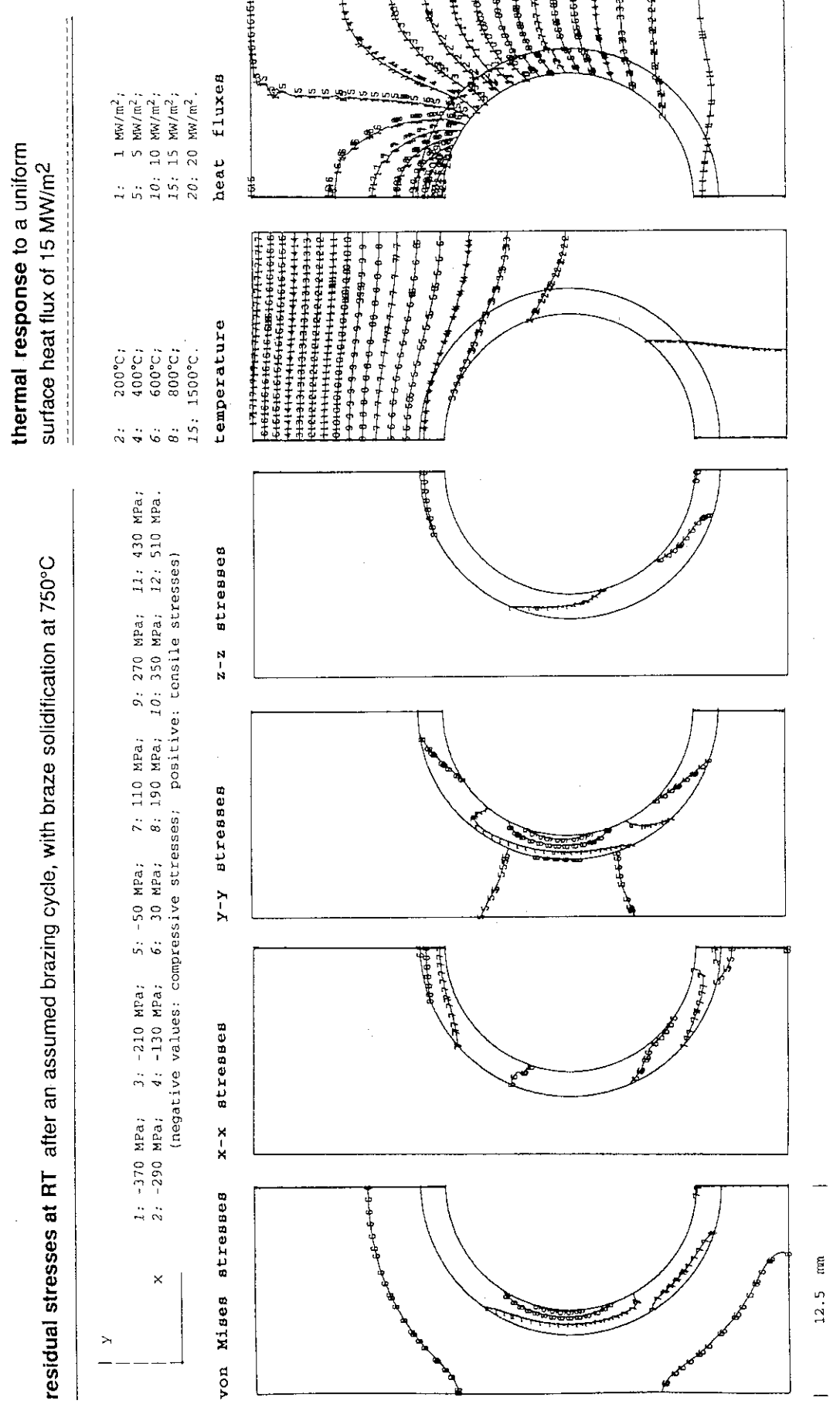


Fig. 7.1.1.i/I Monoblock Type, Armor: Cx2002U, Heat Sink: W-30Cu

stress distribution and displacement at a uniform steady state surface heat flux of 15 MW/m²

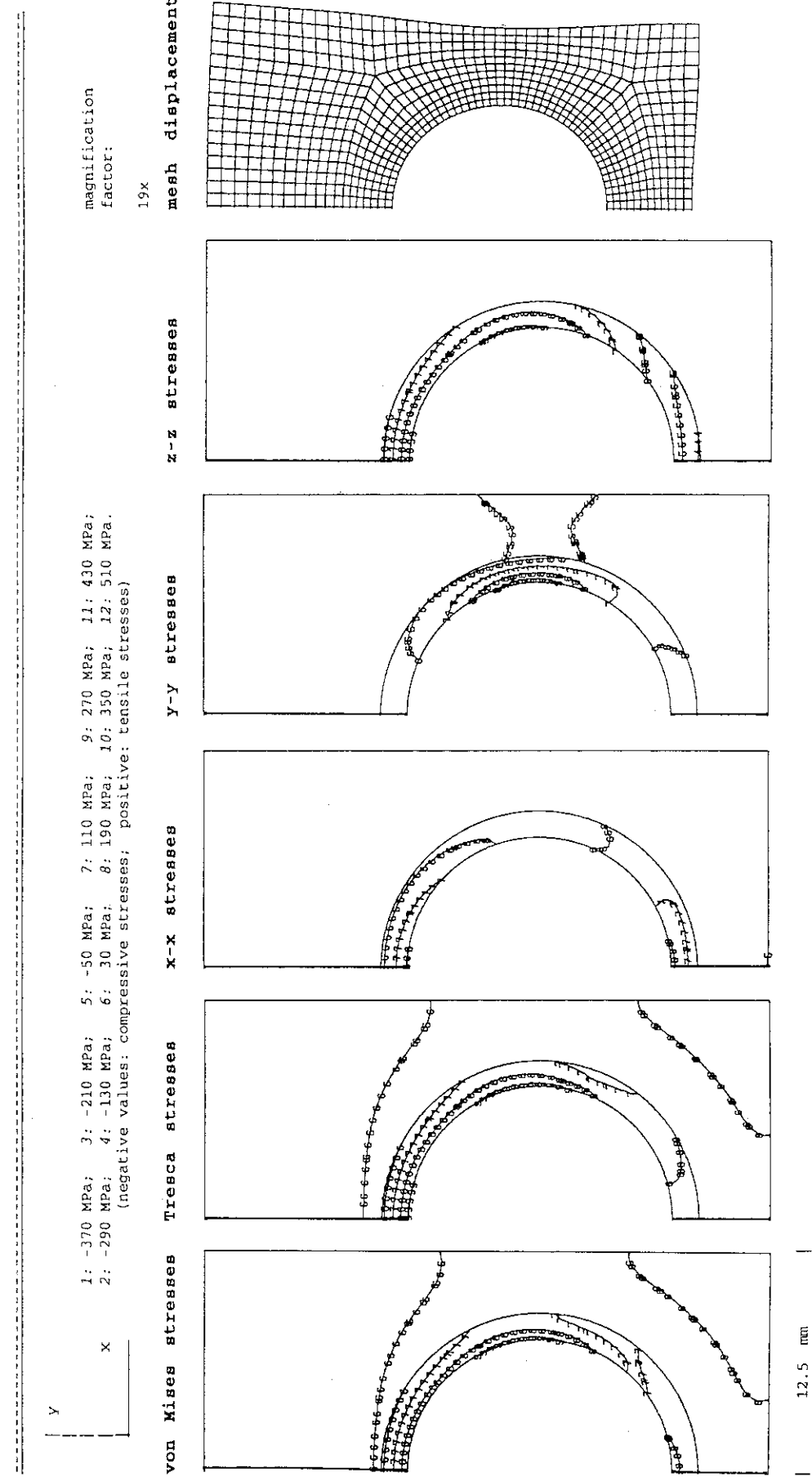


Fig. 7.1.1.i/II Monoblock Type, Armor: CX2002U, Heat Sink: W-30Cu

residual stresses at RT after an assumed brazing cycle, with braze solidification at 750°C

thermal response to a uniform surface heat flux of 15 MW/m²

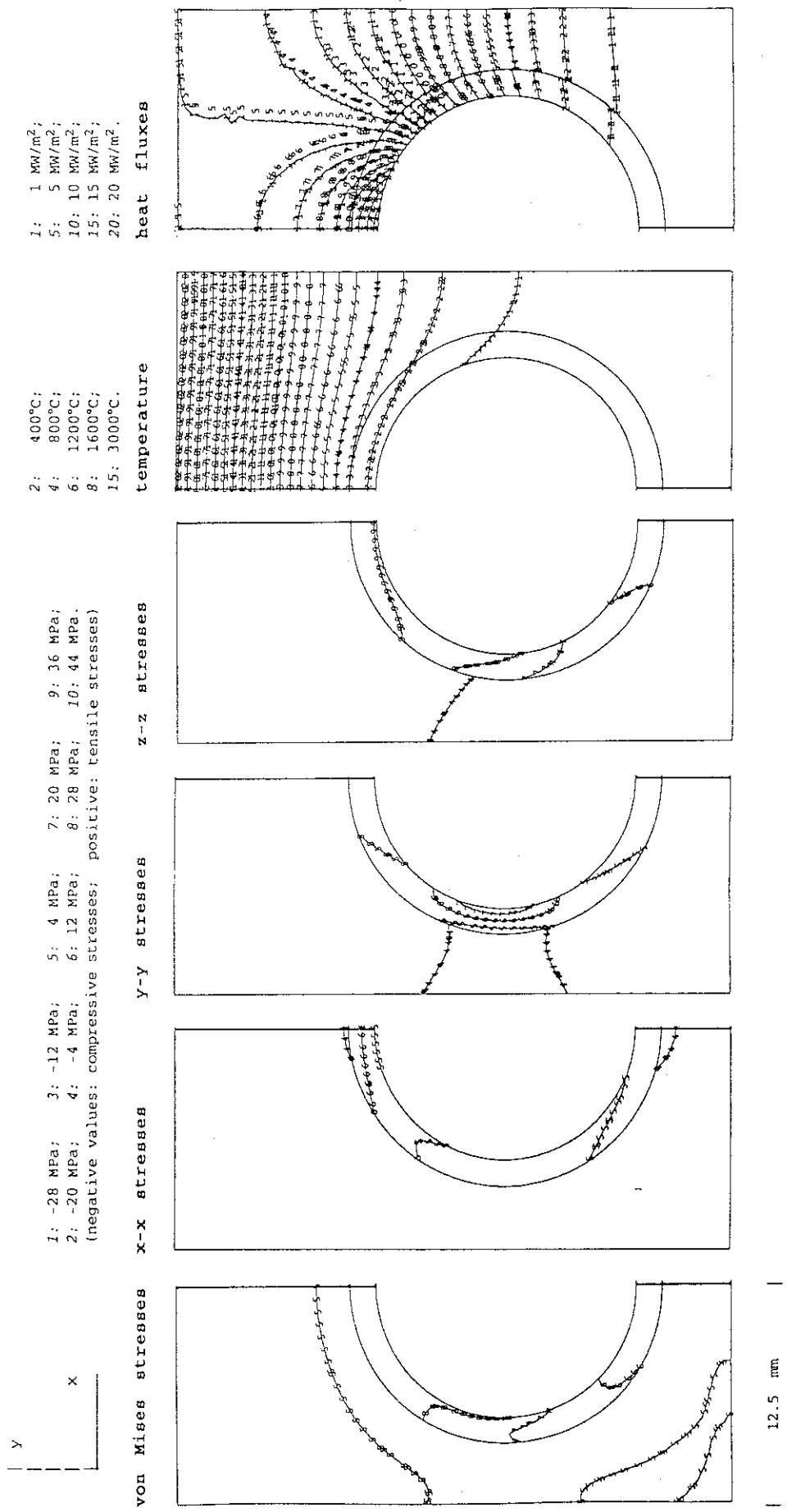
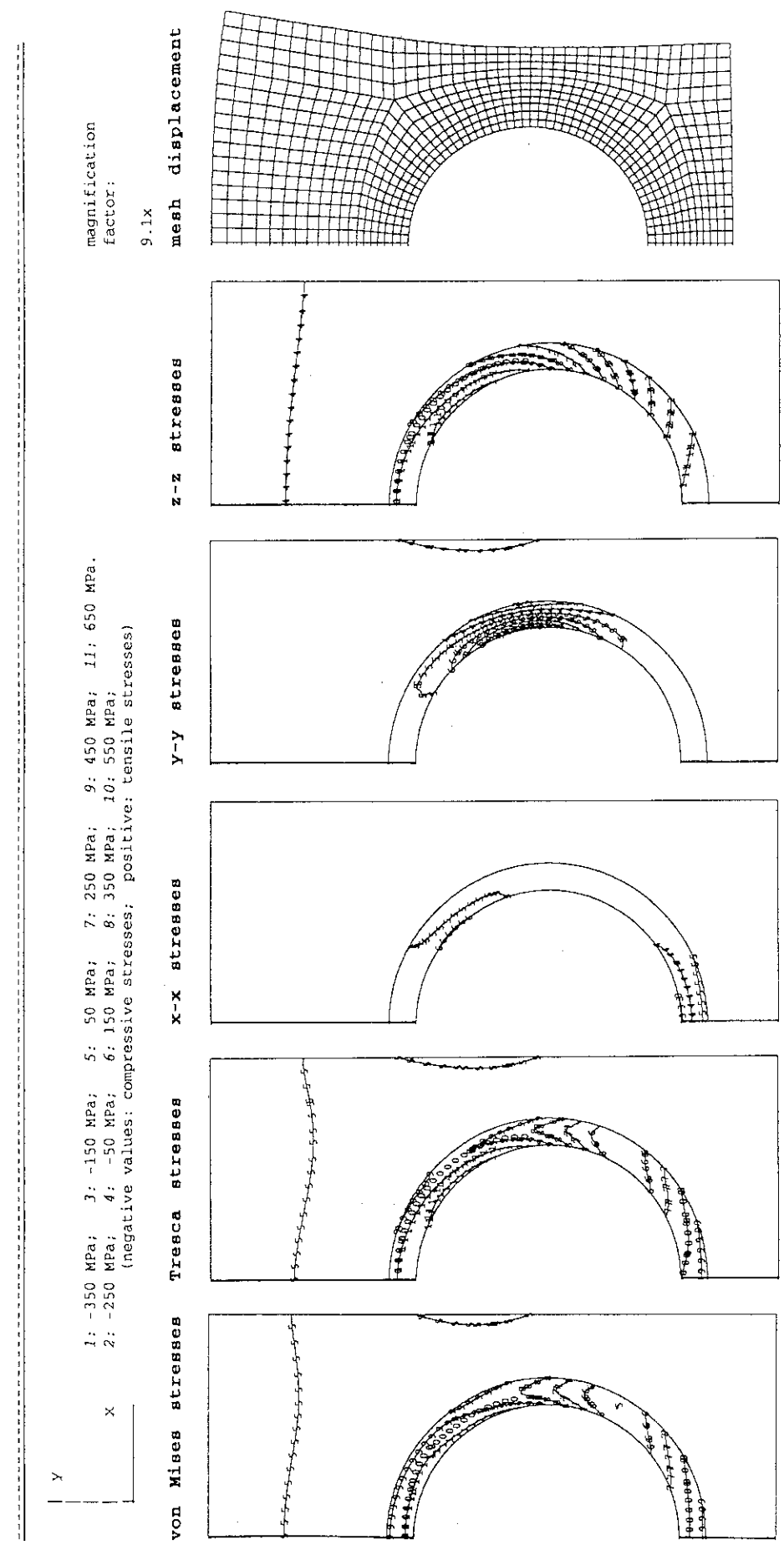


Fig. 7.1.1.j/I Monoblock Type, Armor: IG430U, Heat Sink: TZM

stress distribution and displacement at a uniform steady state surface heat flux of 15 MW/m²



12.5 mm

Fig. 7.1.1.j/II Monoblock Type, Armor: IG430U, Heat Sink: TZM

residual stresses at RT after an assumed brazing cycle, with braze solidification at 750°C

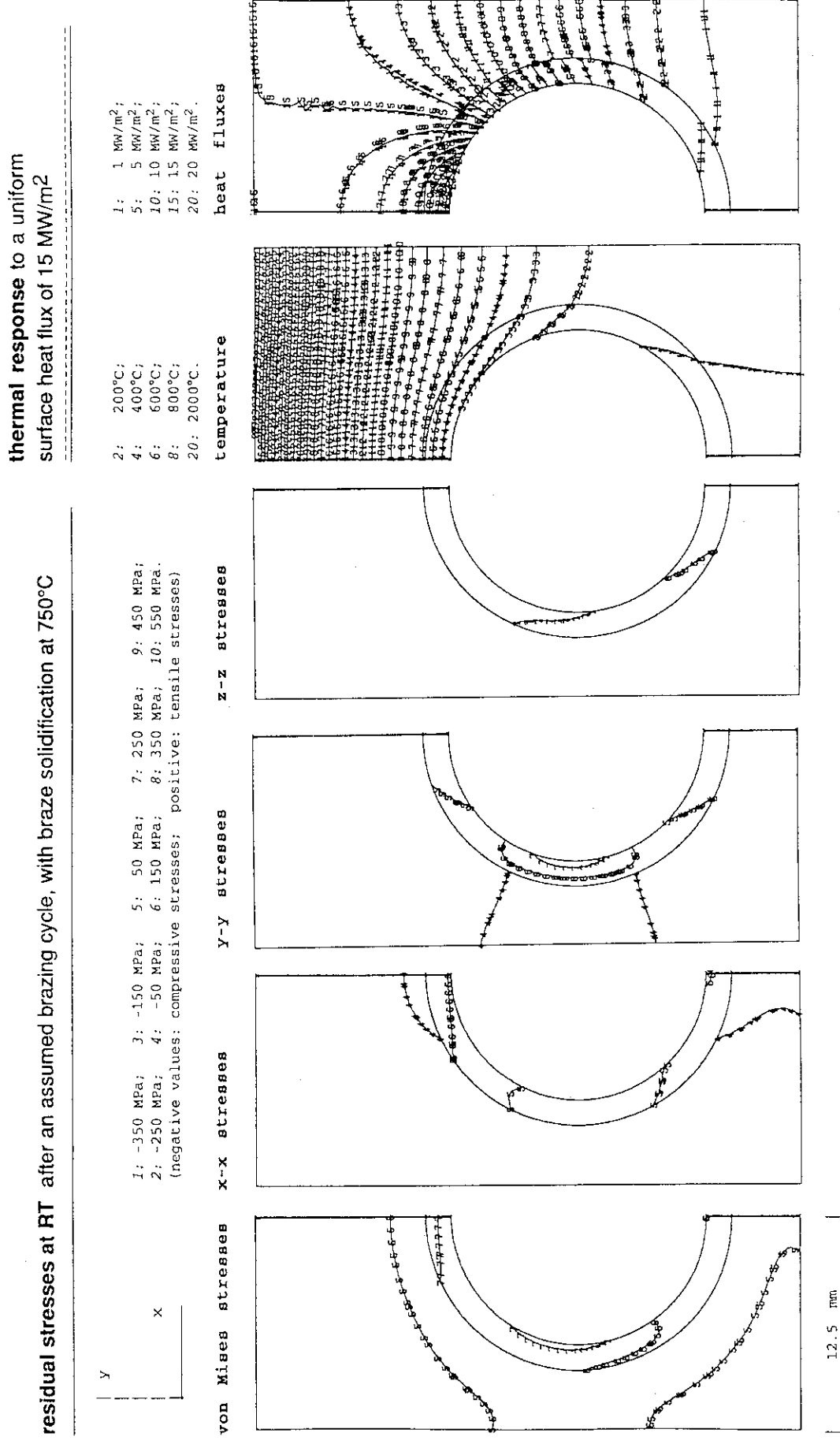


Fig. 7.1.1.k/I Monoblock Type, Armor: SEP-NI12, Heat Sink: TZM (1.5 mm)

stress distribution and displacement at a uniform steady state surface heat flux of 15 MW/m²

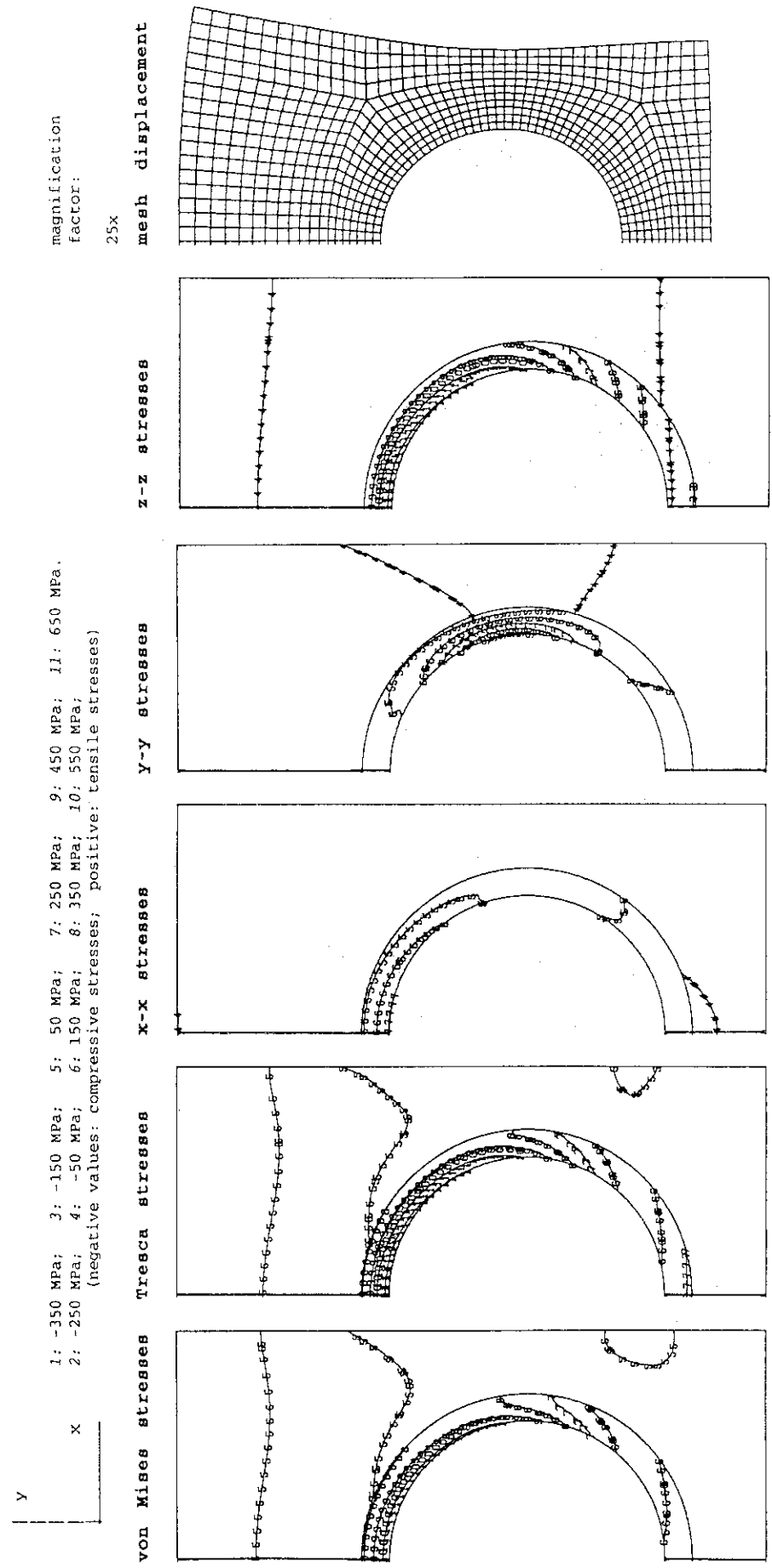


Fig. 7.1.1.k/II Monoblock Type, Armor: SEP-N112, Heat Sink: TZM (1.5 mm)

12.5 mm

residual stresses at RT after an assumed brazing cycle, with braze solidification at 750°C

thermal response to a uniform surface heat flux of 15 MW/m²

Y
 |
 | 1: -350 MPa; 3: -150 MPa; 5: 50 MPa; 7: 250 MPa; 9: 450 MPa;
 | 2: -250 MPa; 4: -50 MPa; 6: 150 MPa; 8: 350 MPa; 10: 550 MPa.
 | (negative values: compressive stresses; positive: tensile stresses)

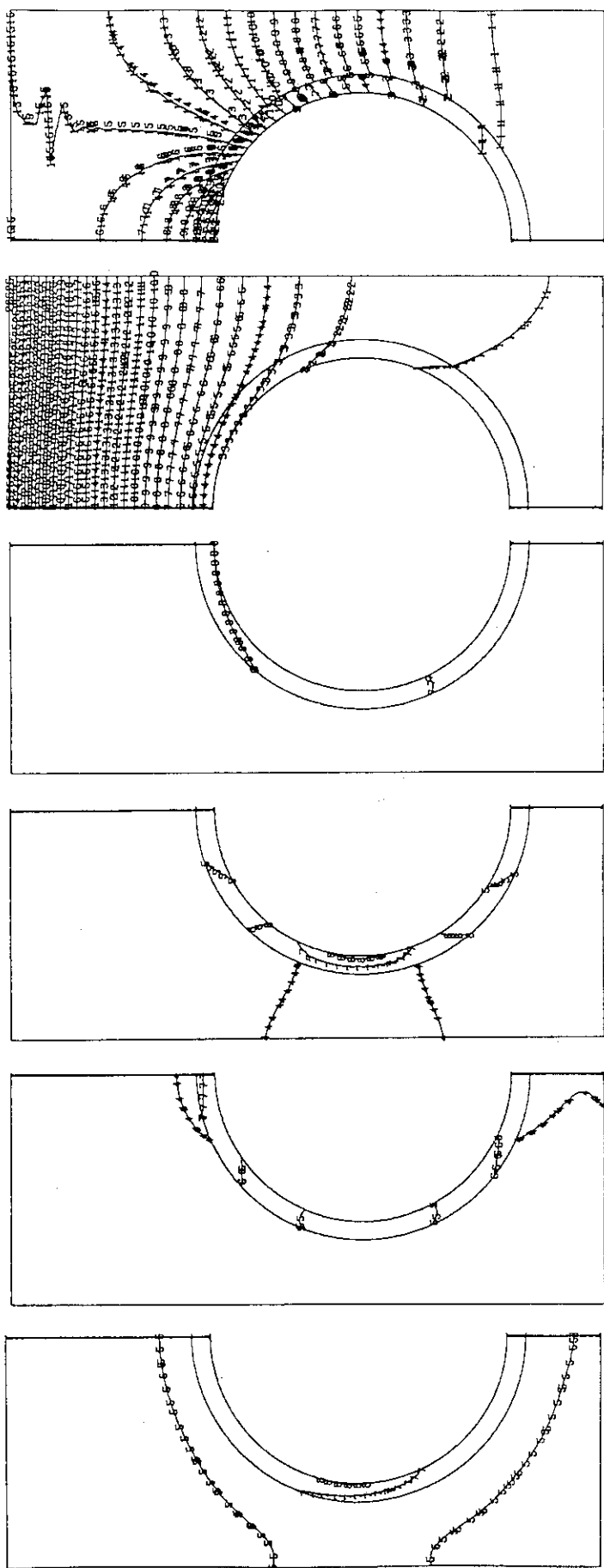
X
 |
 | 2: 200°C; 4: 400°C; 6: 600°C; 8: 800°C; 20: 2000°C.
 | 1: 1 MW/m²; 5: 5 MW/m²; 10: 10 MW/m²; 15: 15 MW/m²; 20: 20 MW/m².

von Mises stresses

x-x stresses

y-y stresses

z-z stresses



12.5 mm

Fig. 7.1.1.1/I Monoblock Type, Armor: SEP-N112, Heat Sink: TZM (1.0 mm)

stress distribution and displacement at a uniform steady state surface heat flux of 15 MW/m²

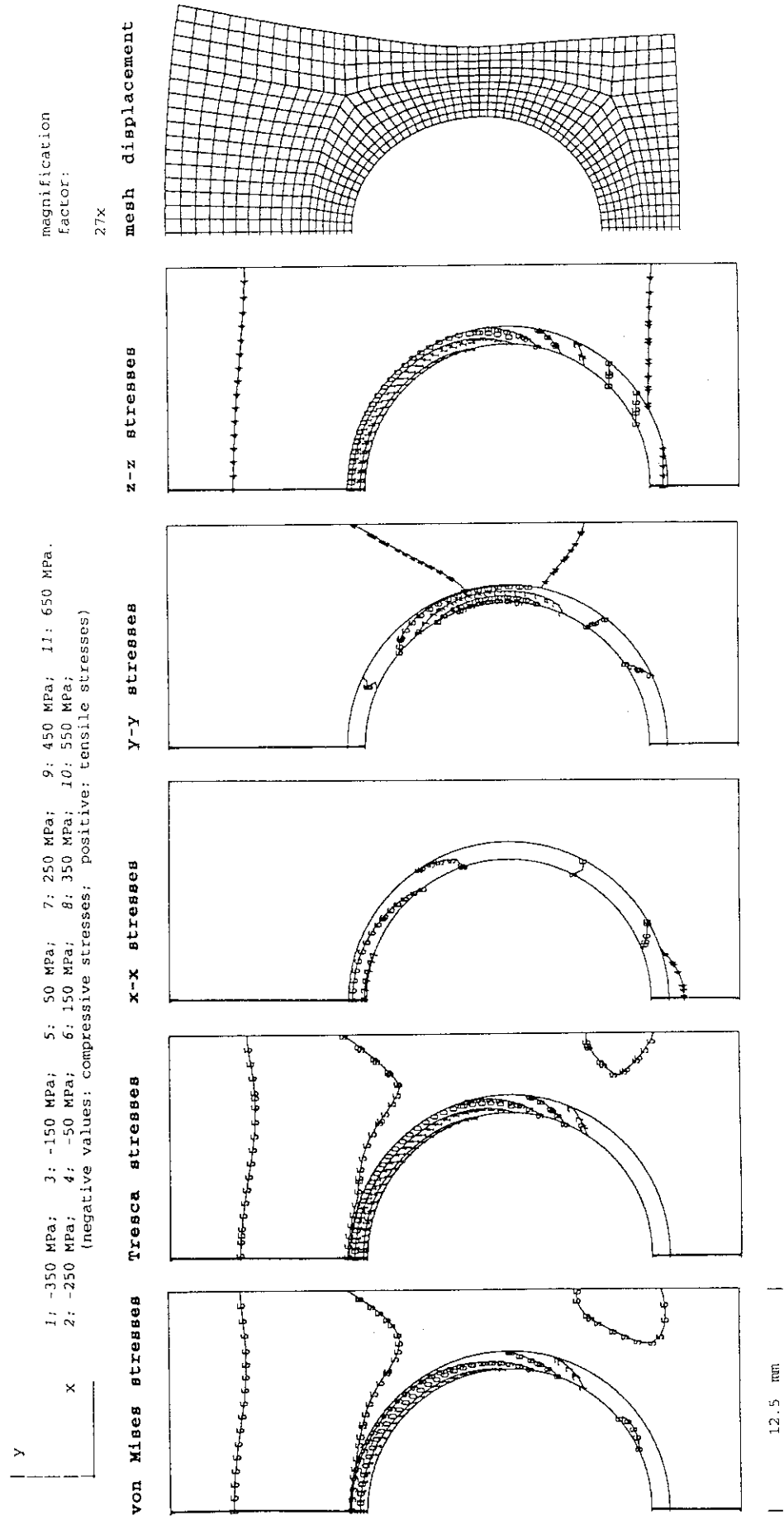


Fig. 7.1.1.1/II Monoblock Type, Armor: SEP-N112, Heat Sink: TZM (1.0 mm)

residual stresses at RT after an assumed brazing cycle, with braze solidification at 750°C

thermal response to a uniform surface heat flux of 15 MW/m²

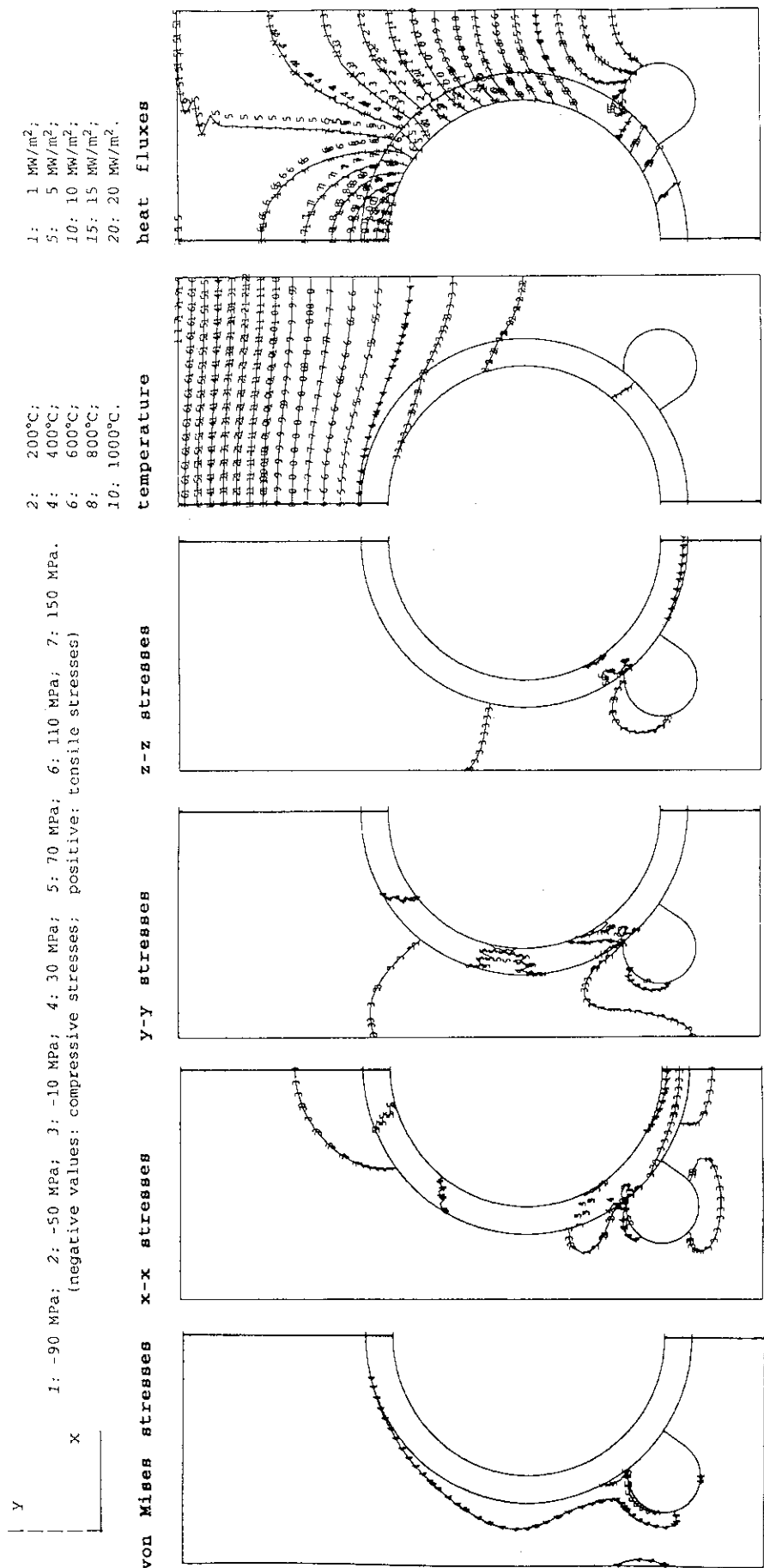


Fig. 7.1.2.a/I Piped Monoblock, Armor: CX2002U, Heat Sink: OF-Cu

stress distribution and displacement at a uniform steady state surface heat flux of 15 MW/m²

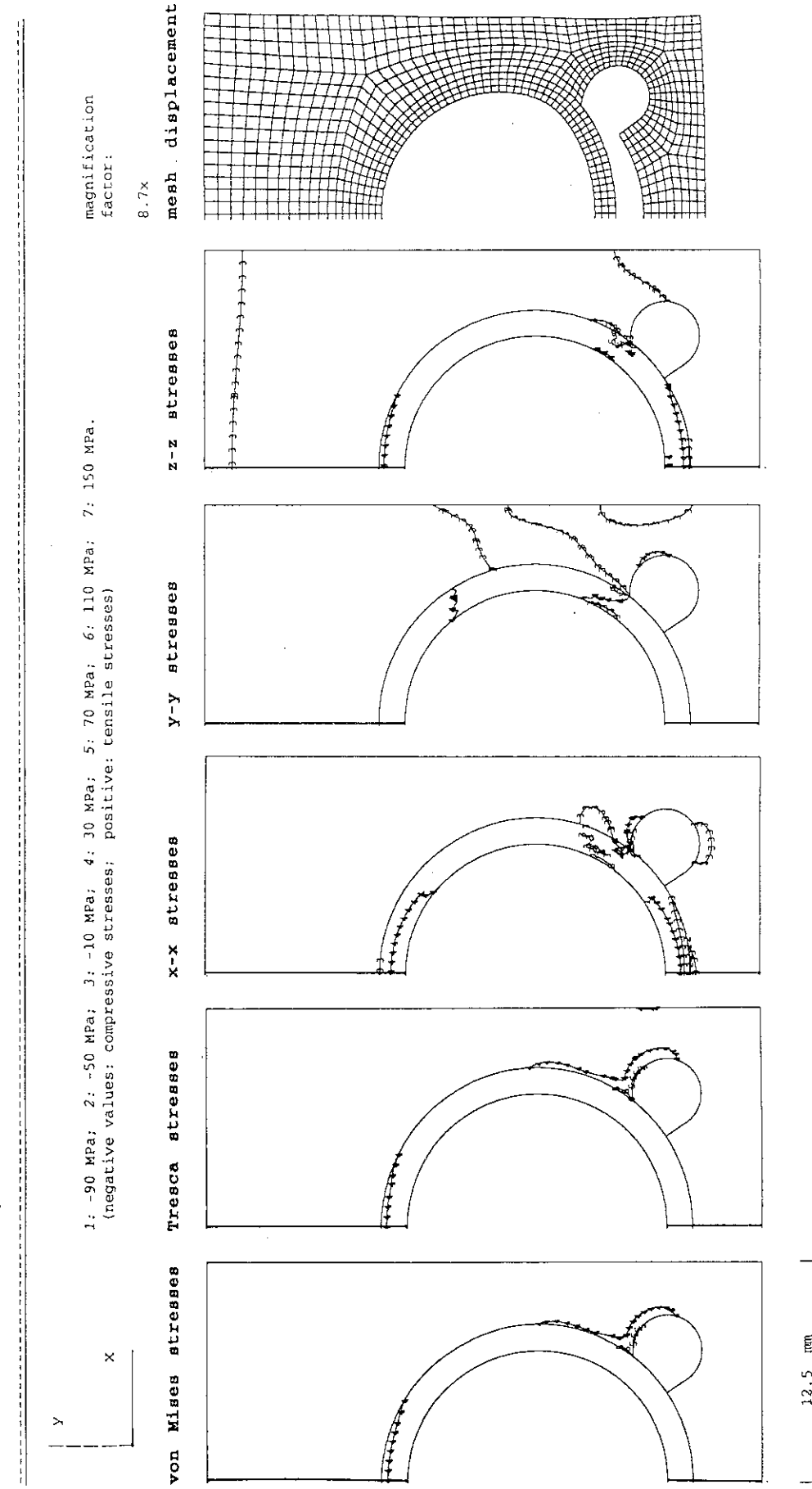
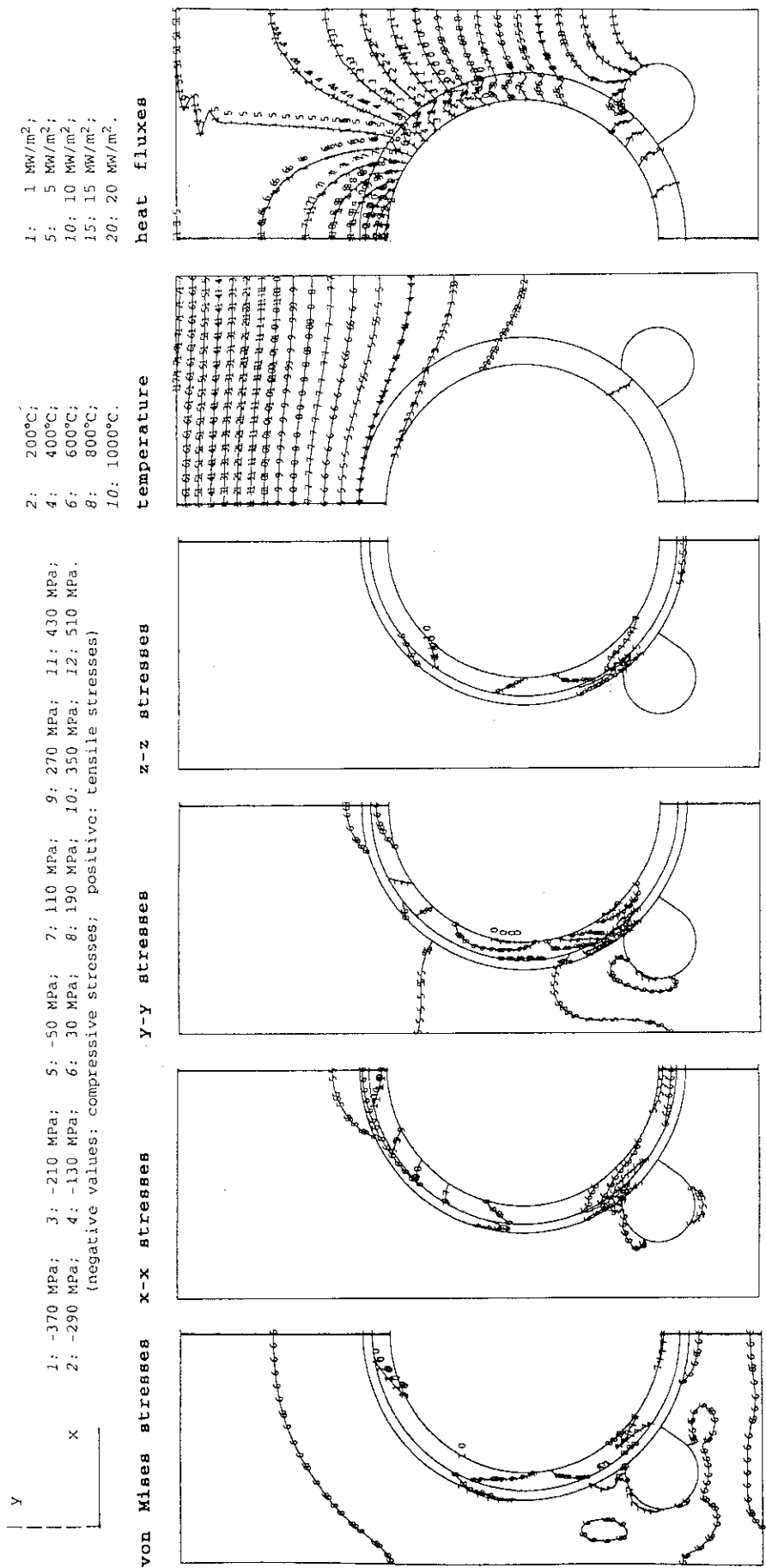


Fig. 7.1.2.a/II Piped Monoblock, Armor: CX2002U, Heat Sink: OF-Cu

thermal response to a uniform
surface heat flux of 15 MW/m²

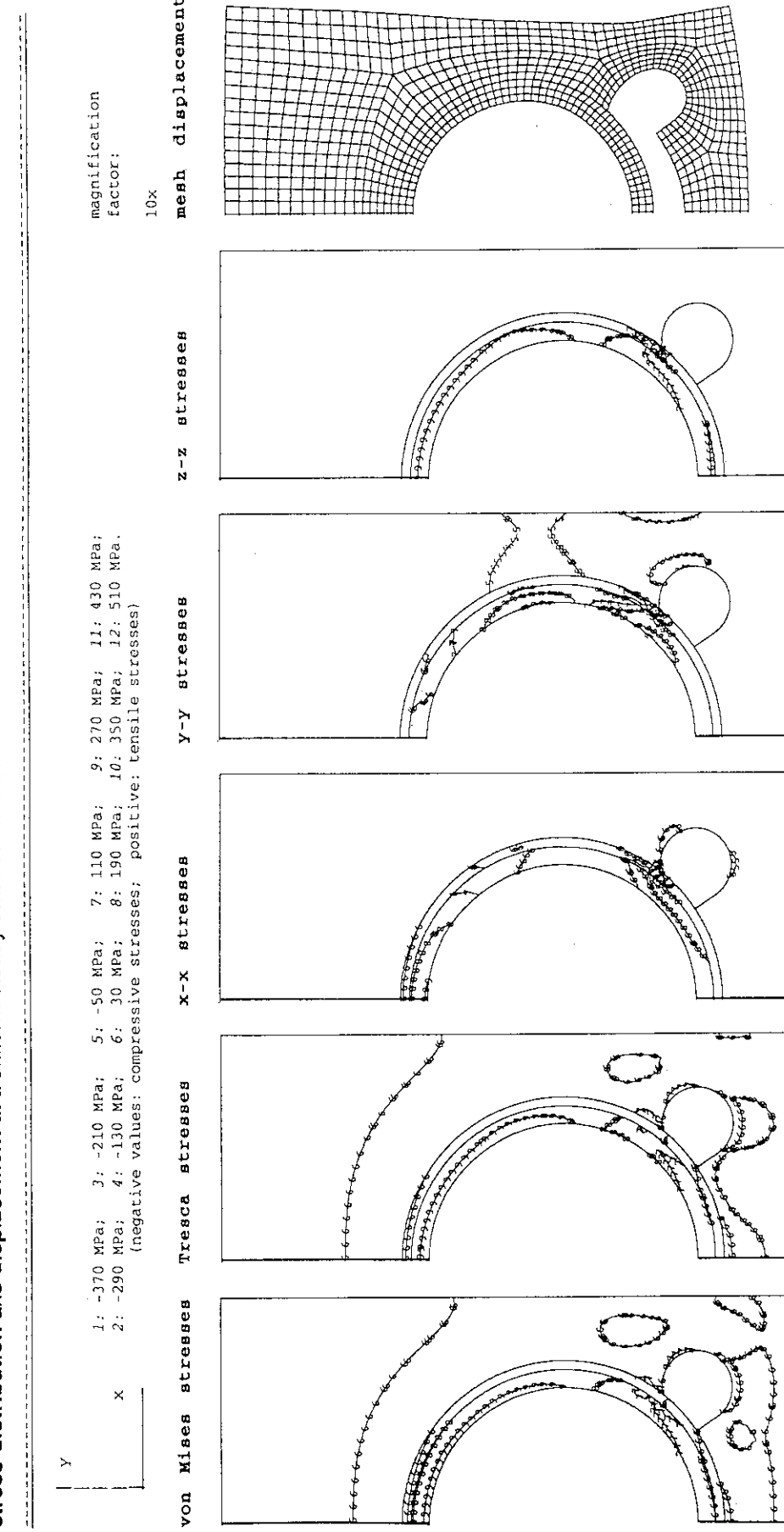
residual stresses at RT after an assumed brazing cycle, with braze solidification at 750°C



the inner part (1.0 mm) of the coolant tube consists of DS-Cu, the outer 0.5 mm are made of OF-Cu.

Fig. 7.1.2.b/I Piped Monoblock, Armor: CX2002U, Tube: OF(0.5)&DS(1.0mm)-Cu

stress distribution and displacement at a uniform steady state surface heat flux of 15 MW/m²



the inner part (1.0 mm) of the coolant tube consists of DS-Cu, the outer 0.5 mm are made of OF-Cu.

Fig. 7.1.2.b/II Piped Monoblock, Armor: CX2002U, Tube: OF(0.5)&DS(1.0 mm)-Cu

residual stresses at RT after an assumed brazing cycle, with braze solidification at 750°C

thermal response to a uniform surface heat flux of 15 MW/m²

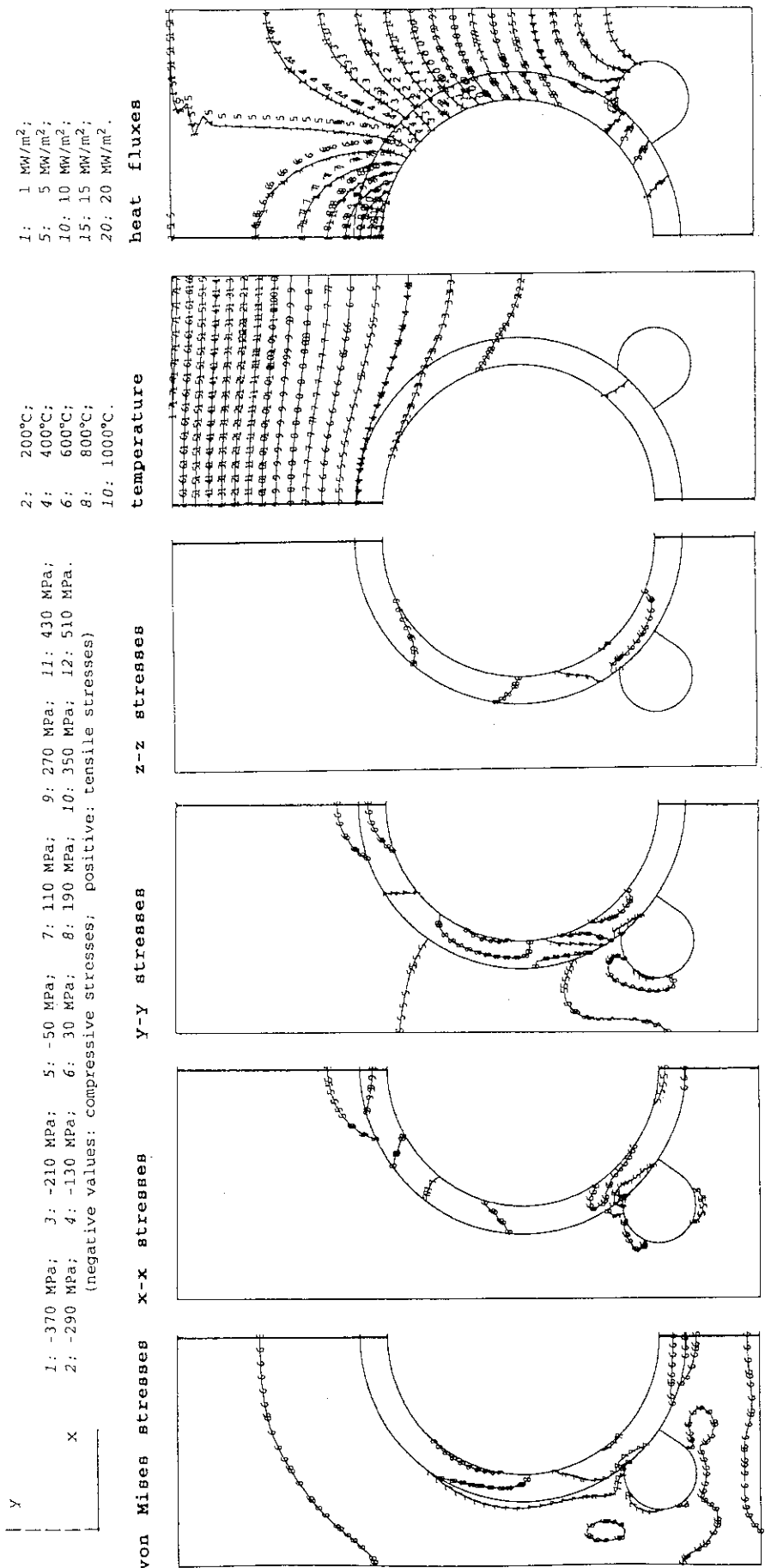


Fig. 7.1.2.c/I Piped Monoblock, Armor: CX2002U, Heat Sink: DS-Cu

stress distribution and displacement at a uniform steady state surface heat flux of 15 MW/m²

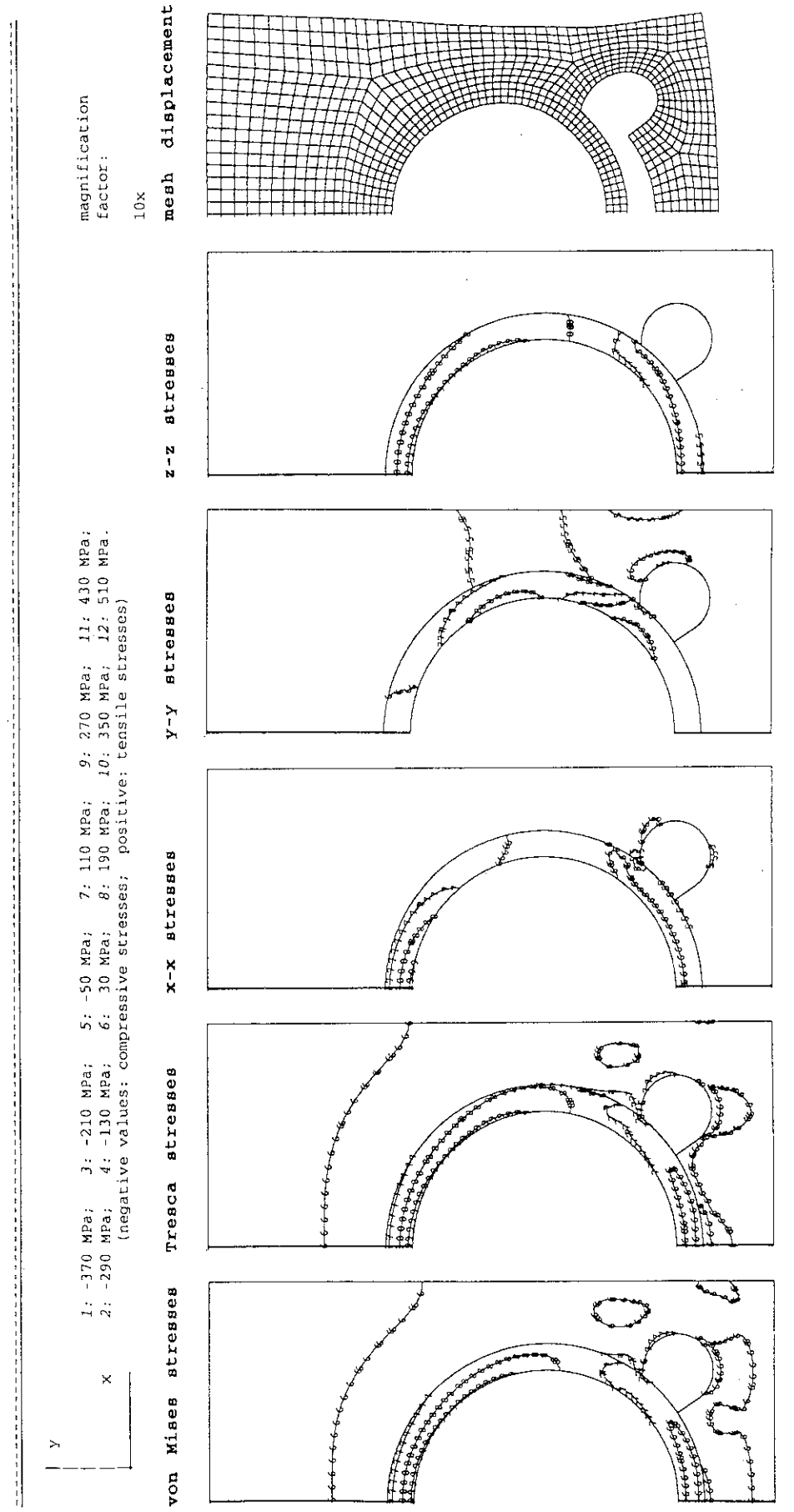


Fig. 7.1.2.c/II Piped Monoblock, Armor: CX2002U, Heat Sink: DS-Cu

residual stresses at RT after an assumed brazing cycle, with braze solidification at 750°C

thermal response to a uniform surface heat flux of 15 MW/m²

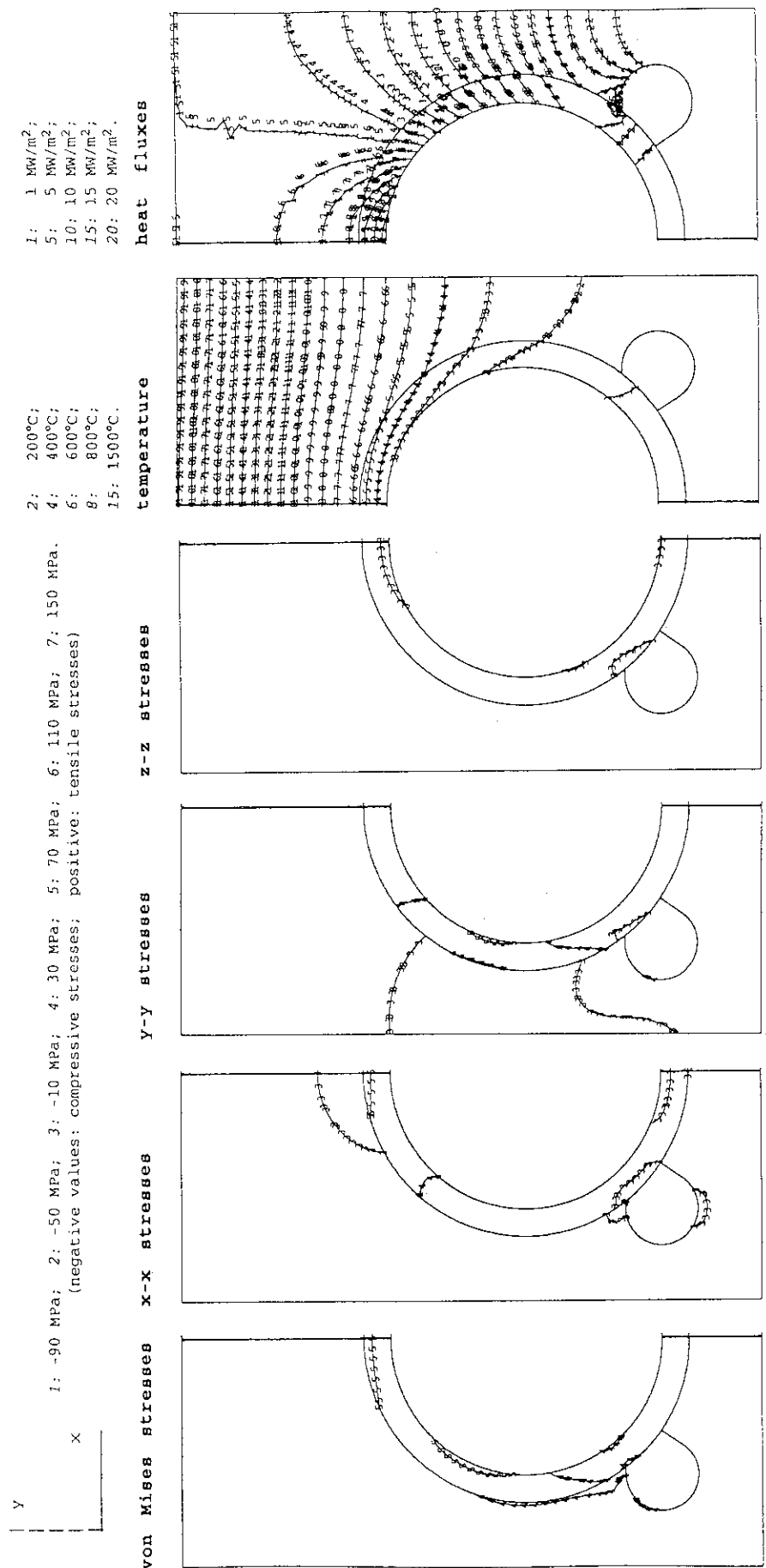


Fig. 7.1.2.d/I Piped Monoblock, Armor: CX2002U, Heat Sink: TZM (1.5 mm)

stress distribution and displacement at a uniform steady state surface heat flux of 15 MW/m²

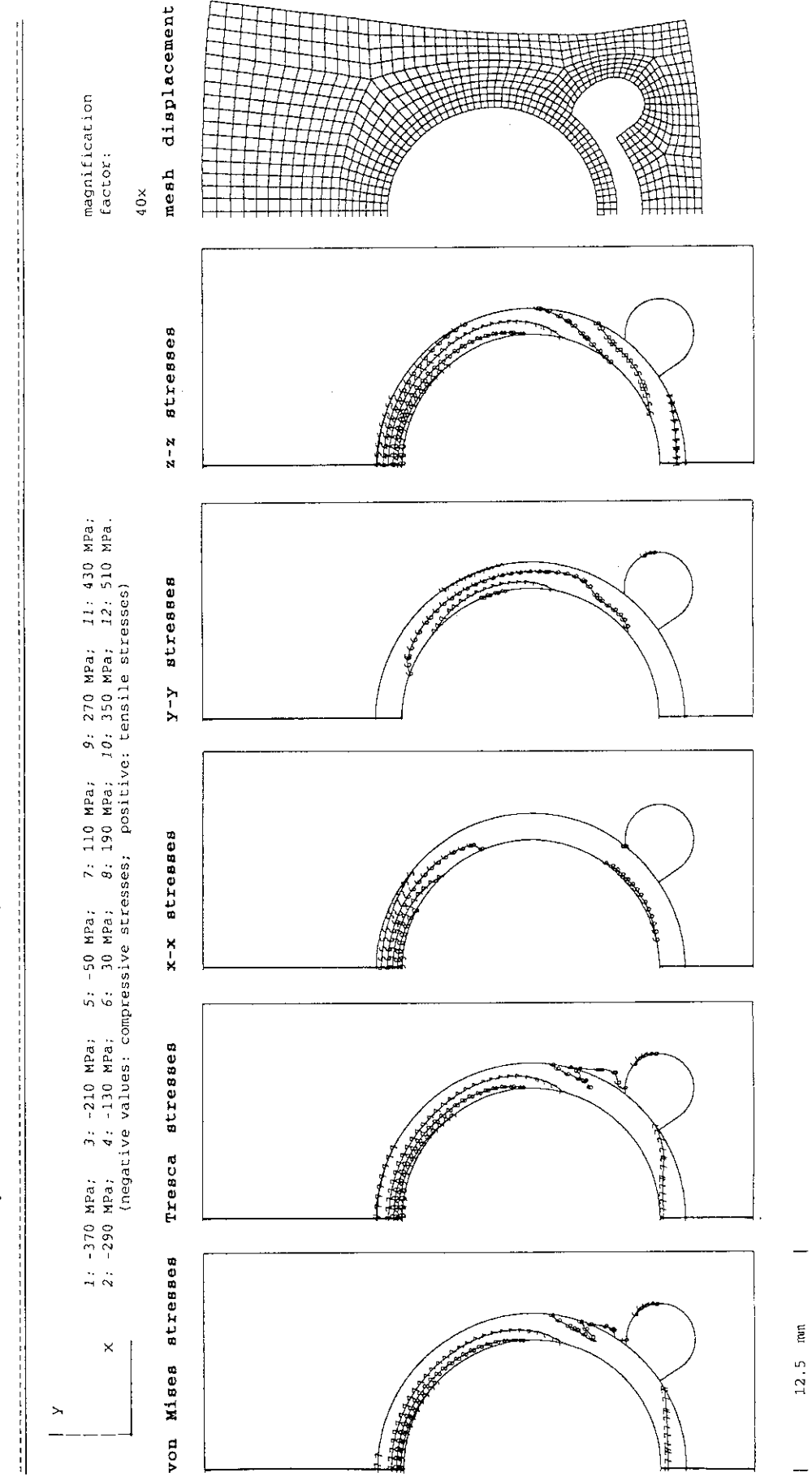


Fig. 7.1.2.d/II Piped Monoblock, Armor: CX2002U, Heat Sink: TZM (1.5 mm)

residual stresses at RT after an assumed brazing cycle, with braze solidification at 750°C

thermal response to a uniform surface heat flux of 15 MW/m²

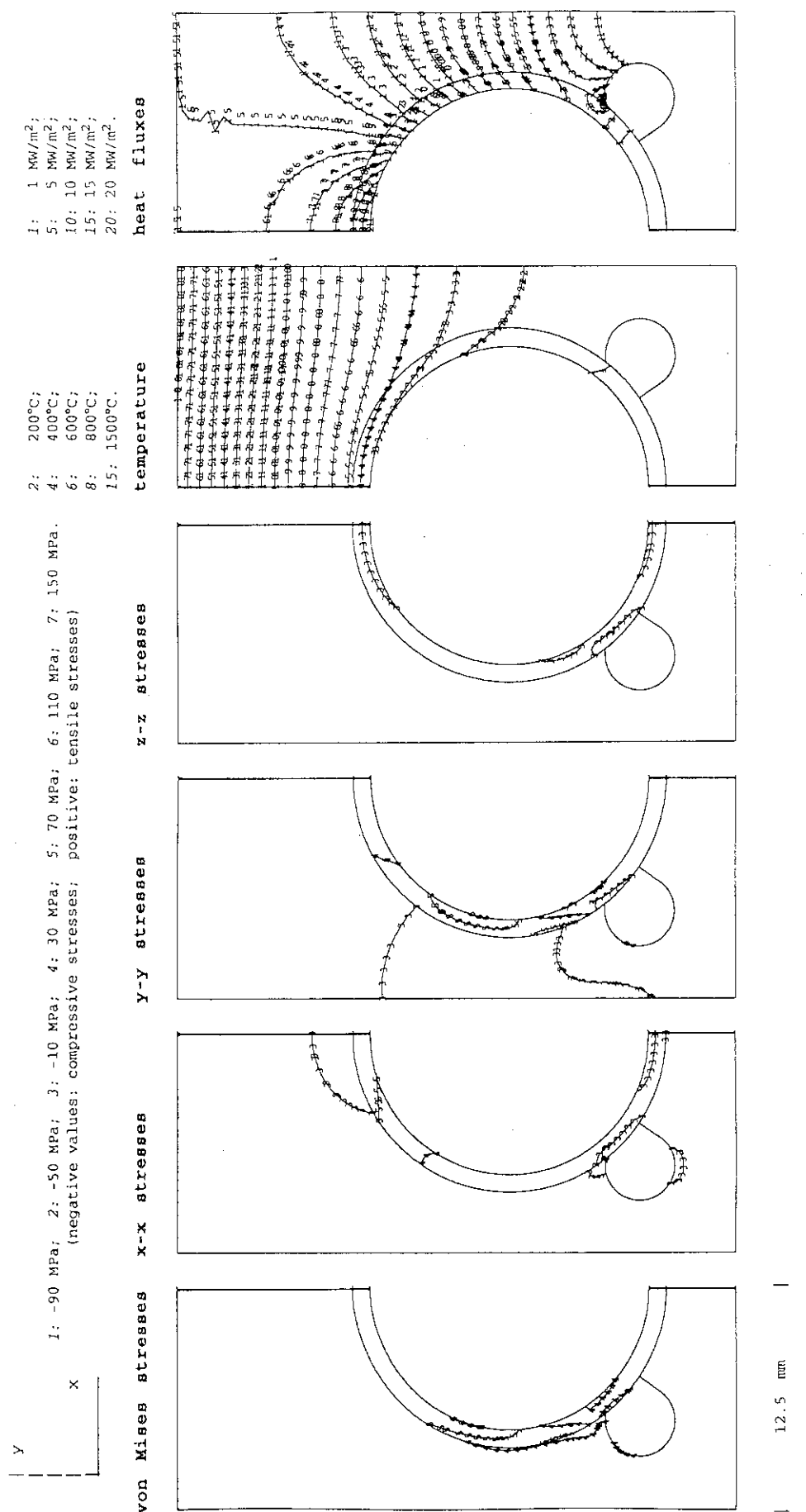


Fig. 7.1.2.e/I Piped Monoblock, Armor: CX2002U, Heat Sink: TZM (1.0 mm)

12.5 mm

stress distribution and displacement at a uniform steady state surface heat flux of 15 MW/m²

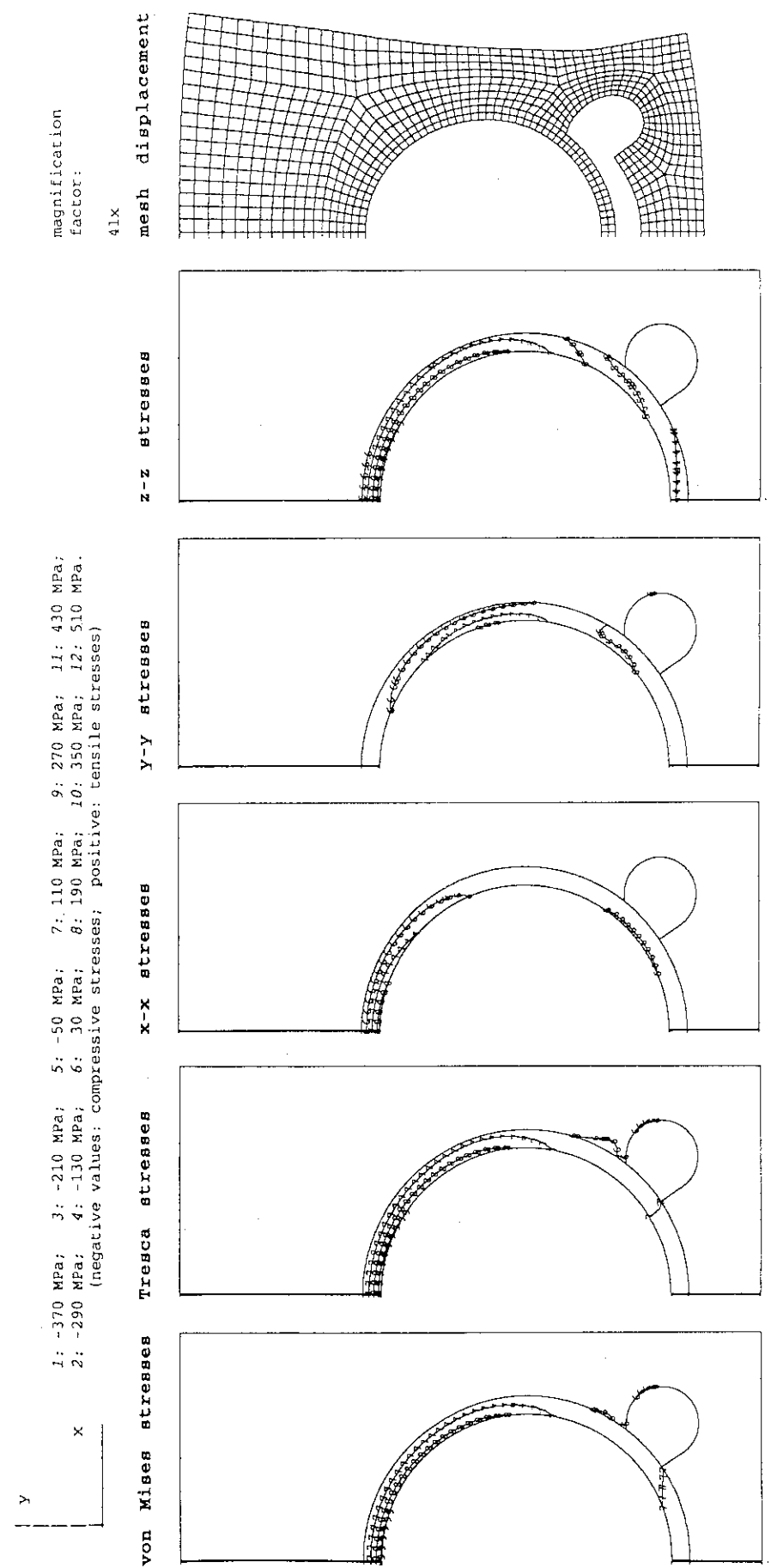


Fig. 7.1.2.e/II Piped Monoblock, Armor: CX2002U, Heat Sink: TZM (1.0 mm)

thermal response to a uniform surface heat flux of 15 MW/m²

residual stresses at RT after an assumed brazing cycle, with braze solidification at 750°C

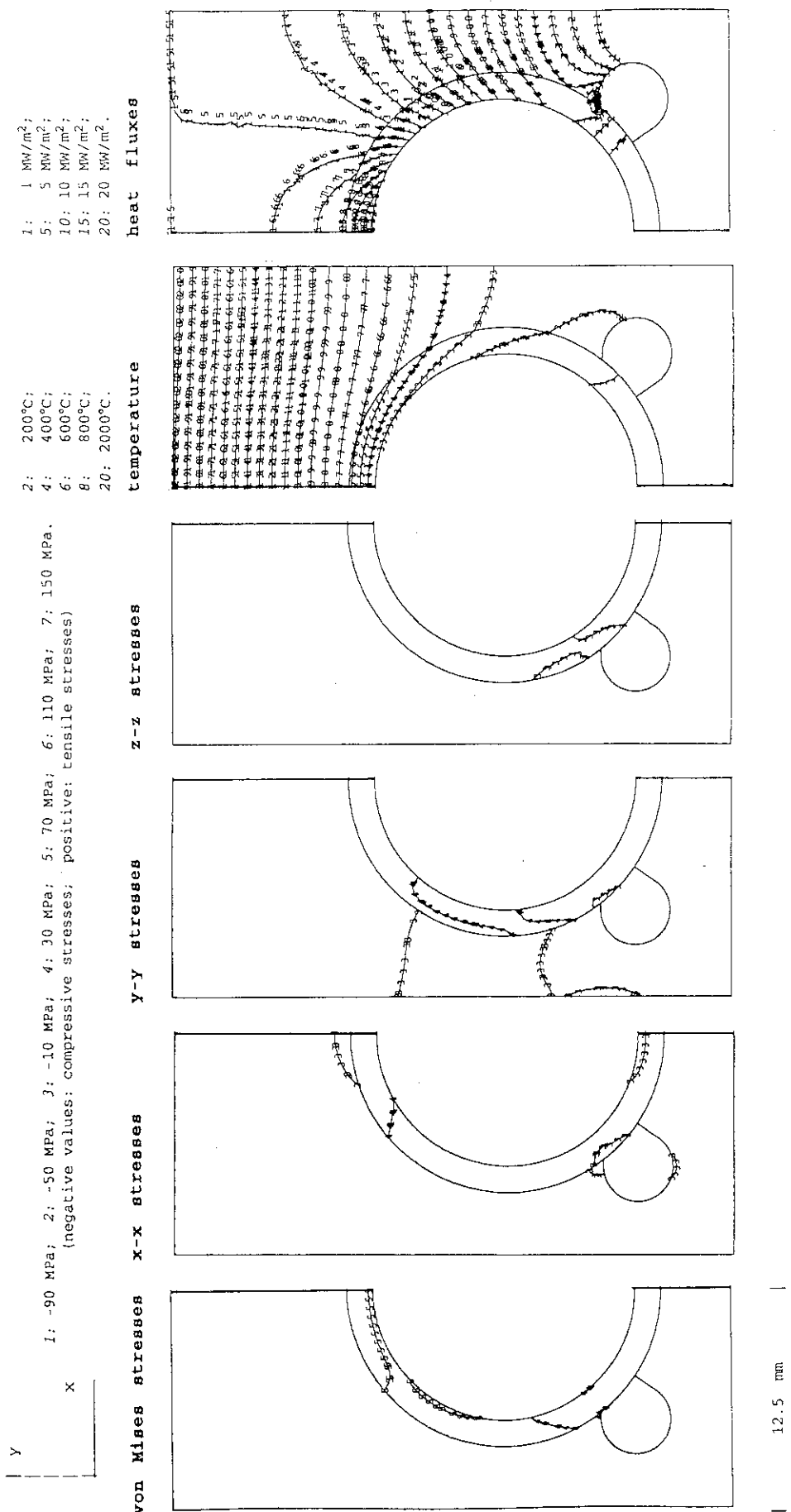


Fig. 7.1.1.f/I Piped Monoblock, Armor: CX2002U, Heat Sink: W5Re

stress distribution and displacement at a uniform steady state surface heat flux of 15 MW/m²

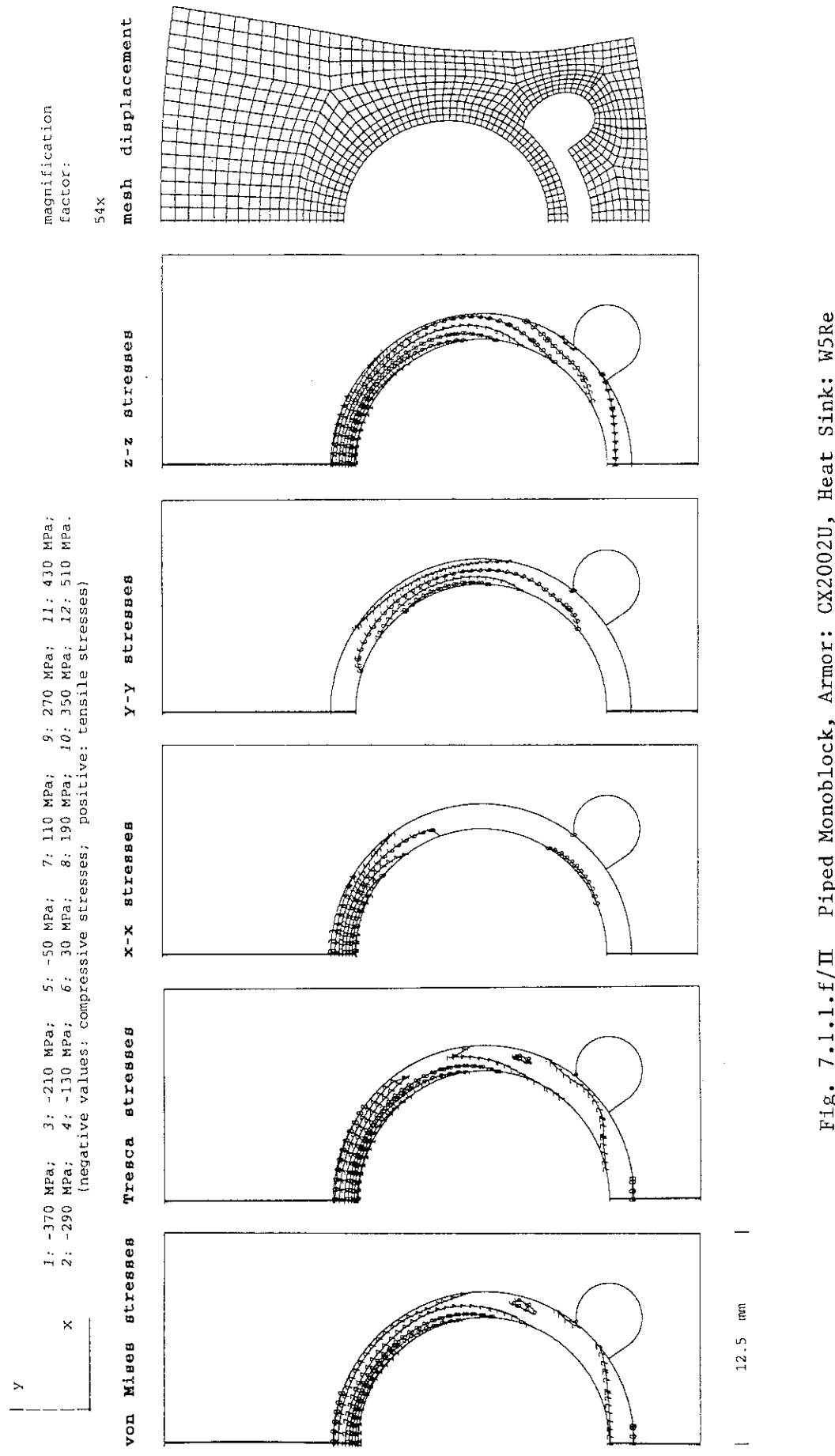


Fig. 7.1.1.f/II Piped Monoblock, Armor: CX2002U, Heat Sink: W5Re

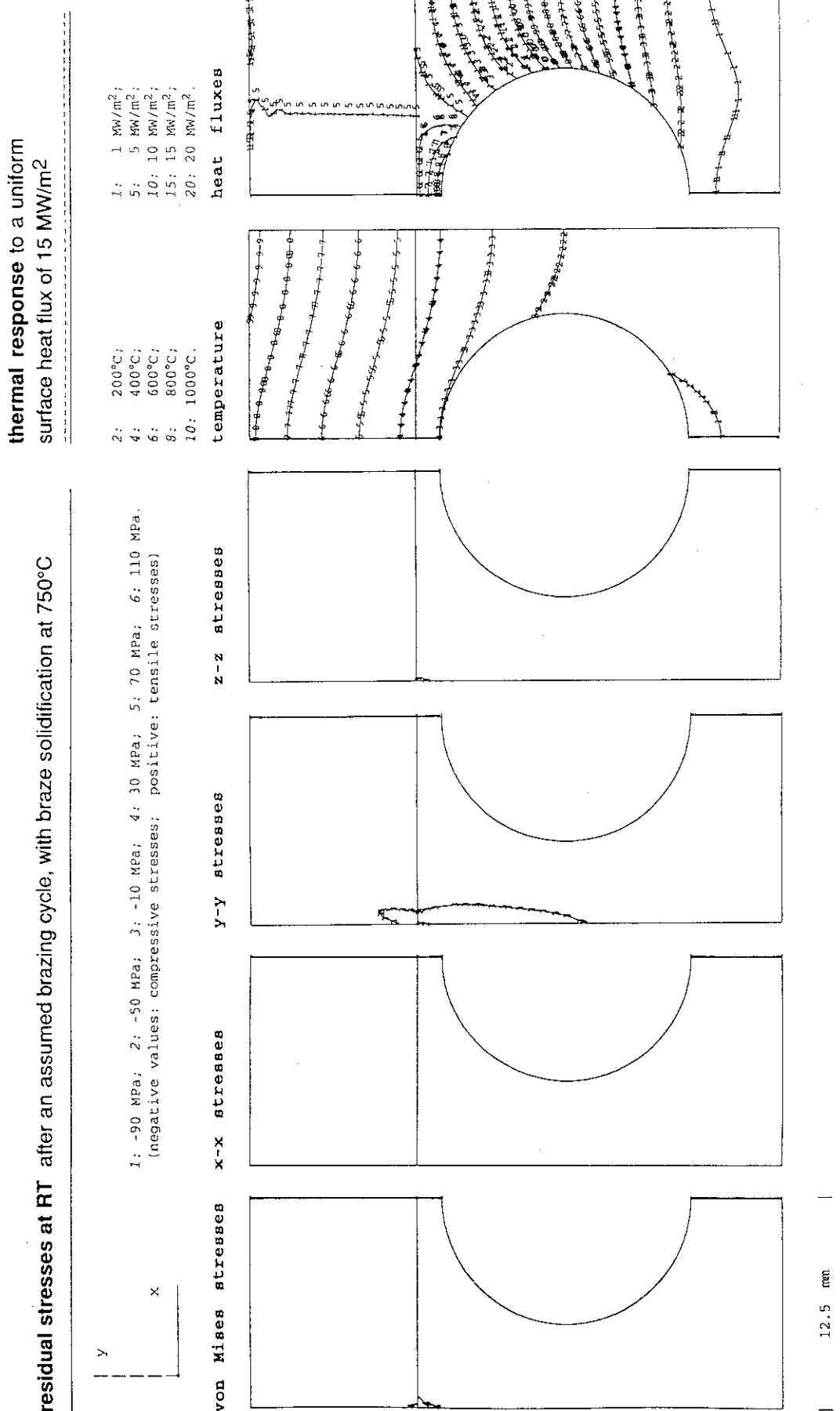


Fig. 7.2.1.a/I Flat-Plate Type, Armor: MFC-1 (1992), Heat Sink: OF-Cu

stress distribution and displacement at a uniform steady state surface heat flux of 15 MW/m²

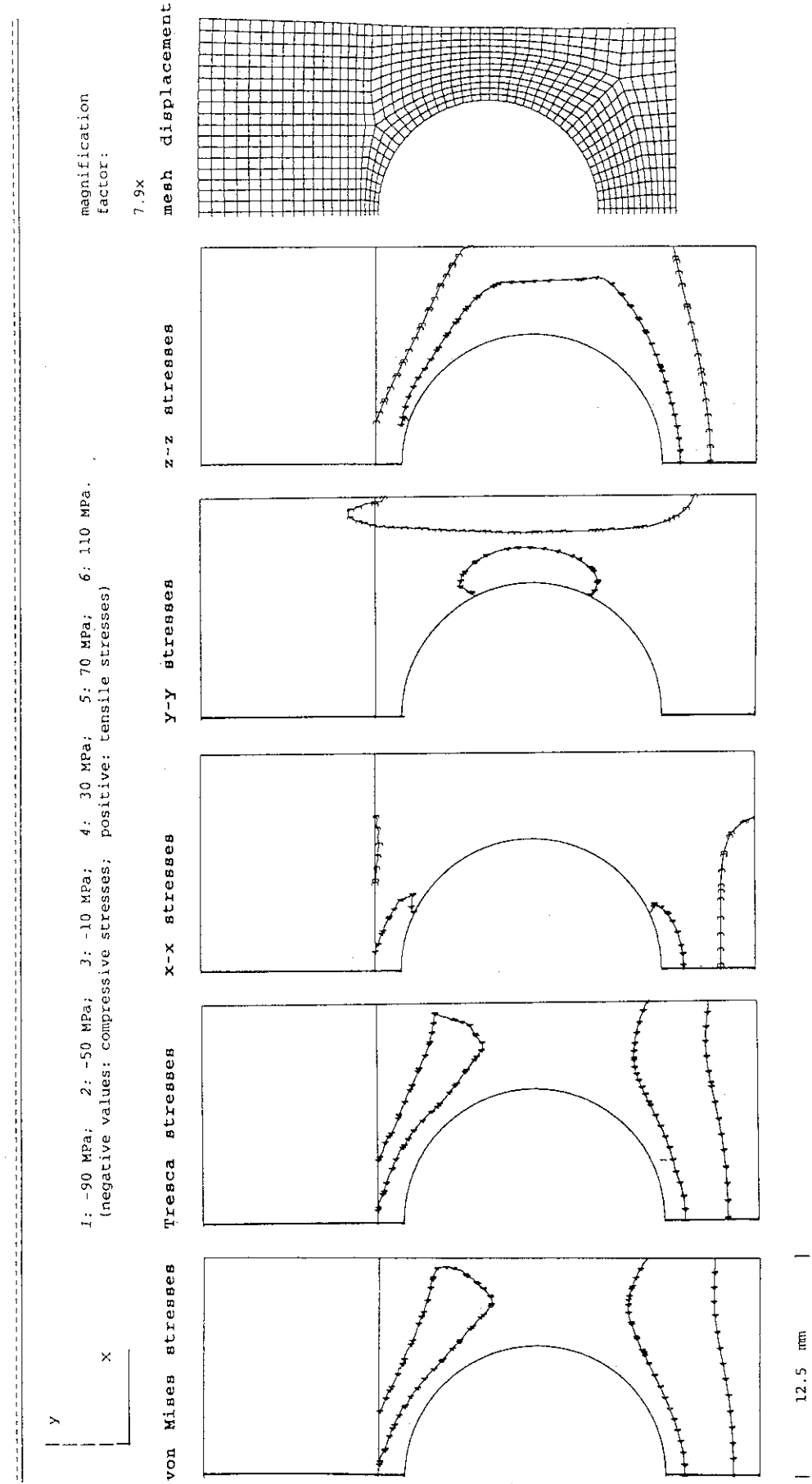


Fig. 7.2.1.a/II Flat-Plate Type, Armor: MFC-1 (1992), Heat Sink: OF-Cu

residual stresses at RT after an assumed brazing cycle, with braze solidification at 750°C

thermal response to a uniform surface heat flux of 15 MW/m²

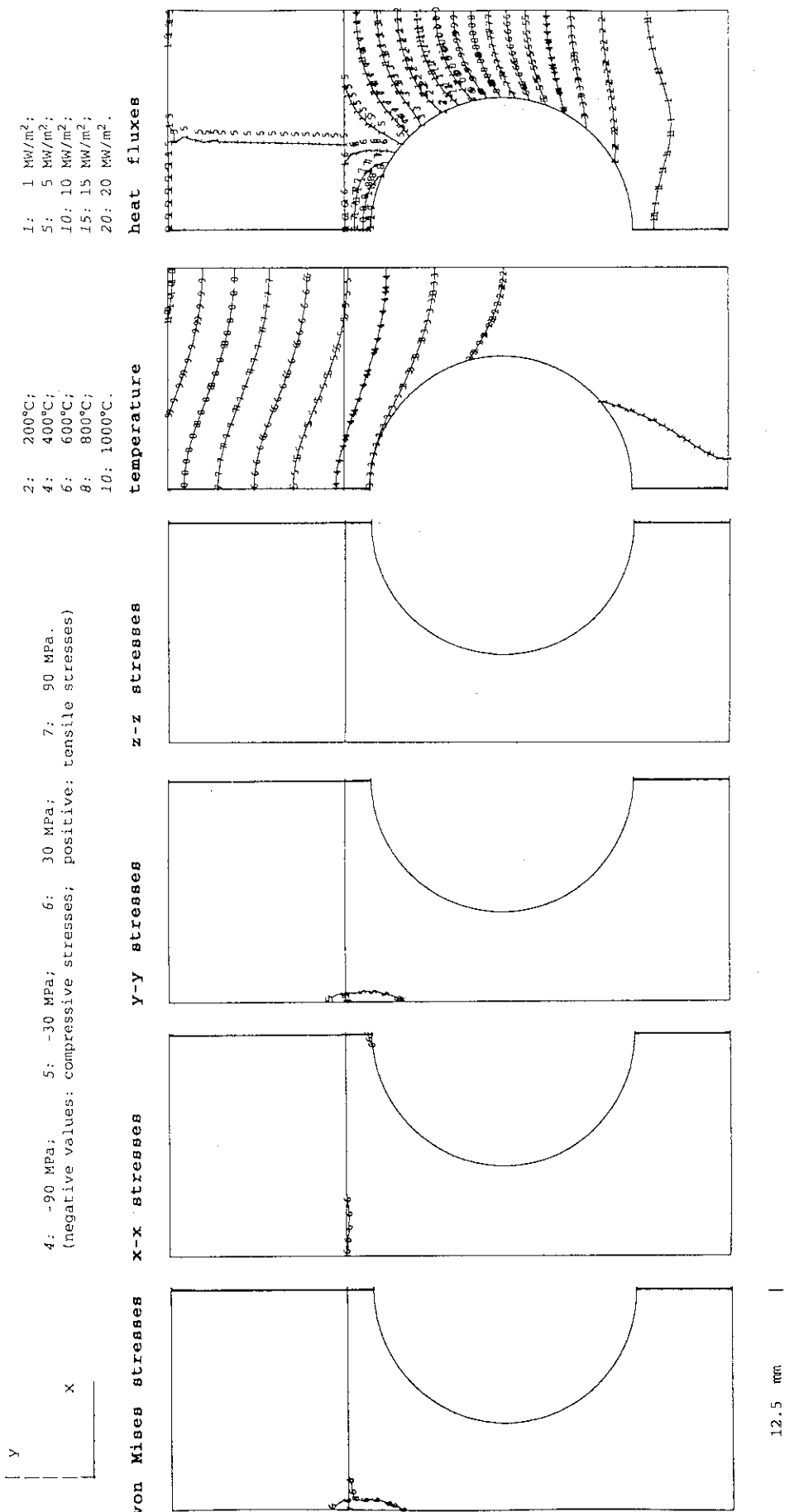
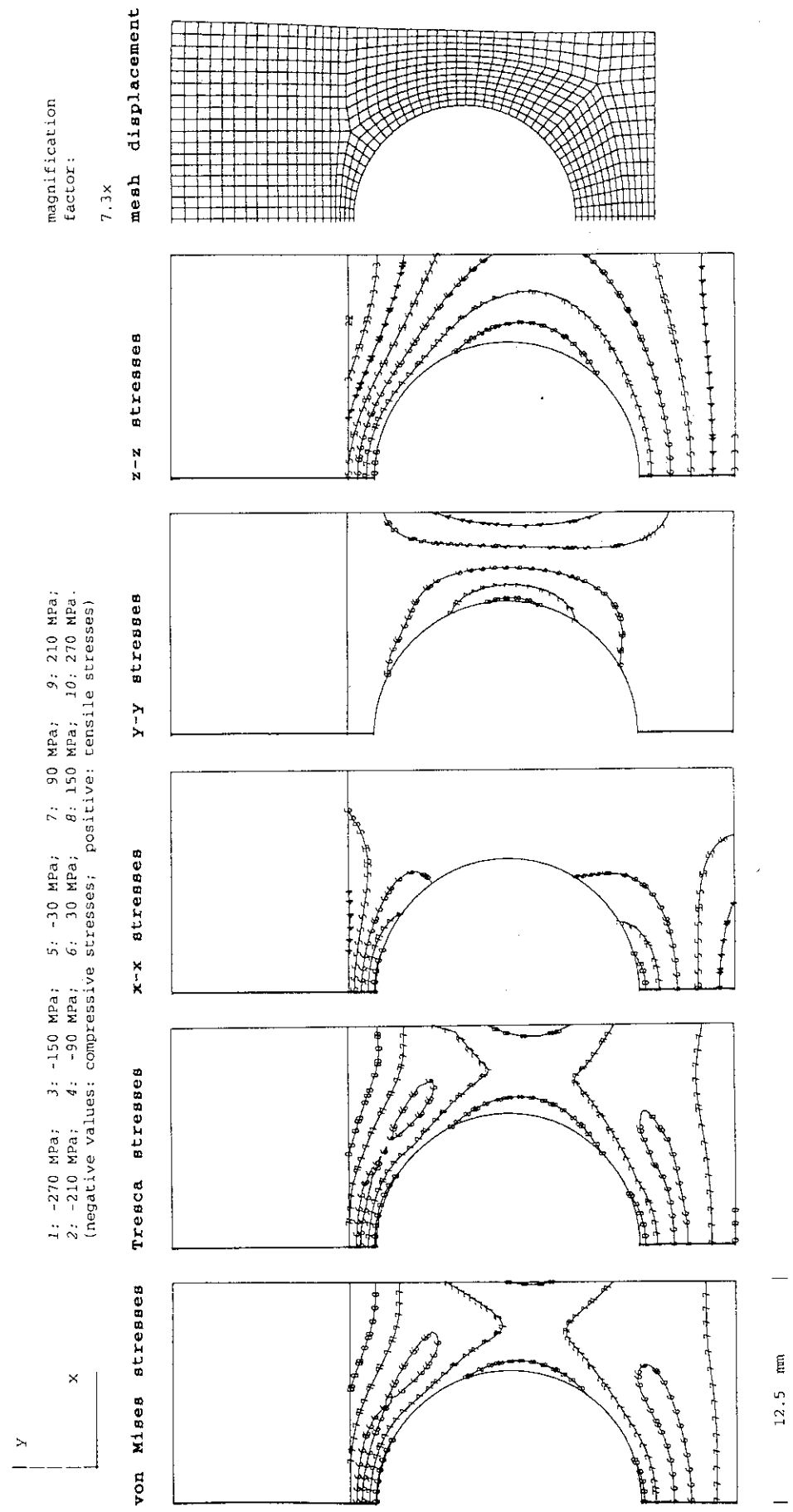


Fig. 7.2.1.b/I Flat-Plate Type, Armor: MFC-1 (1992), Heat Sink: DS-Cu

12.5 mm

stress distribution and displacement at a uniform steady state surface heat flux of 15 MW/m²



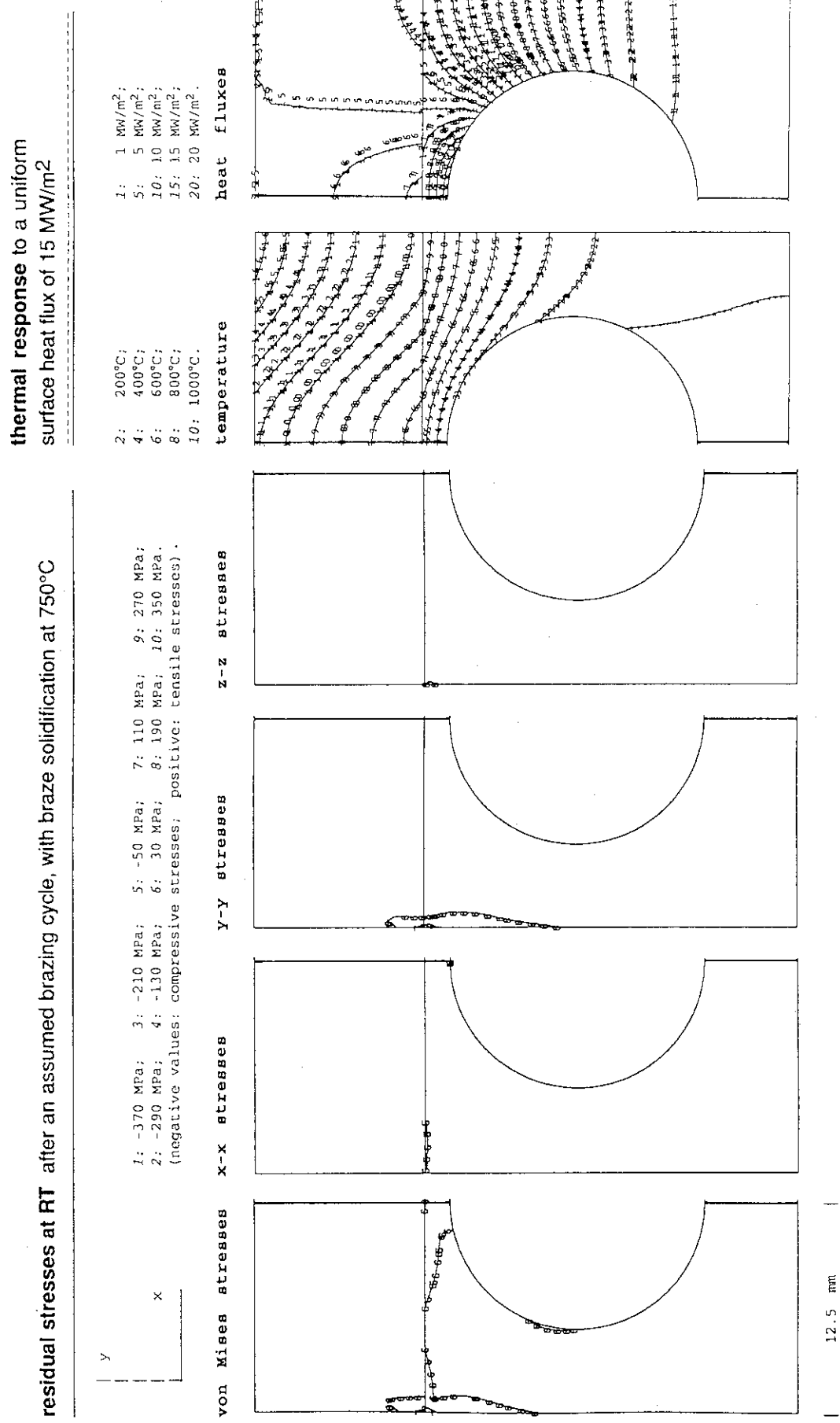


Fig. 7.2.1.c/I Flat-Plate Type, Armor: MFC-1 (1992), Heat Sink: TZM

stress distribution and displacement at a uniform steady state surface heat flux of 15 MW/m²

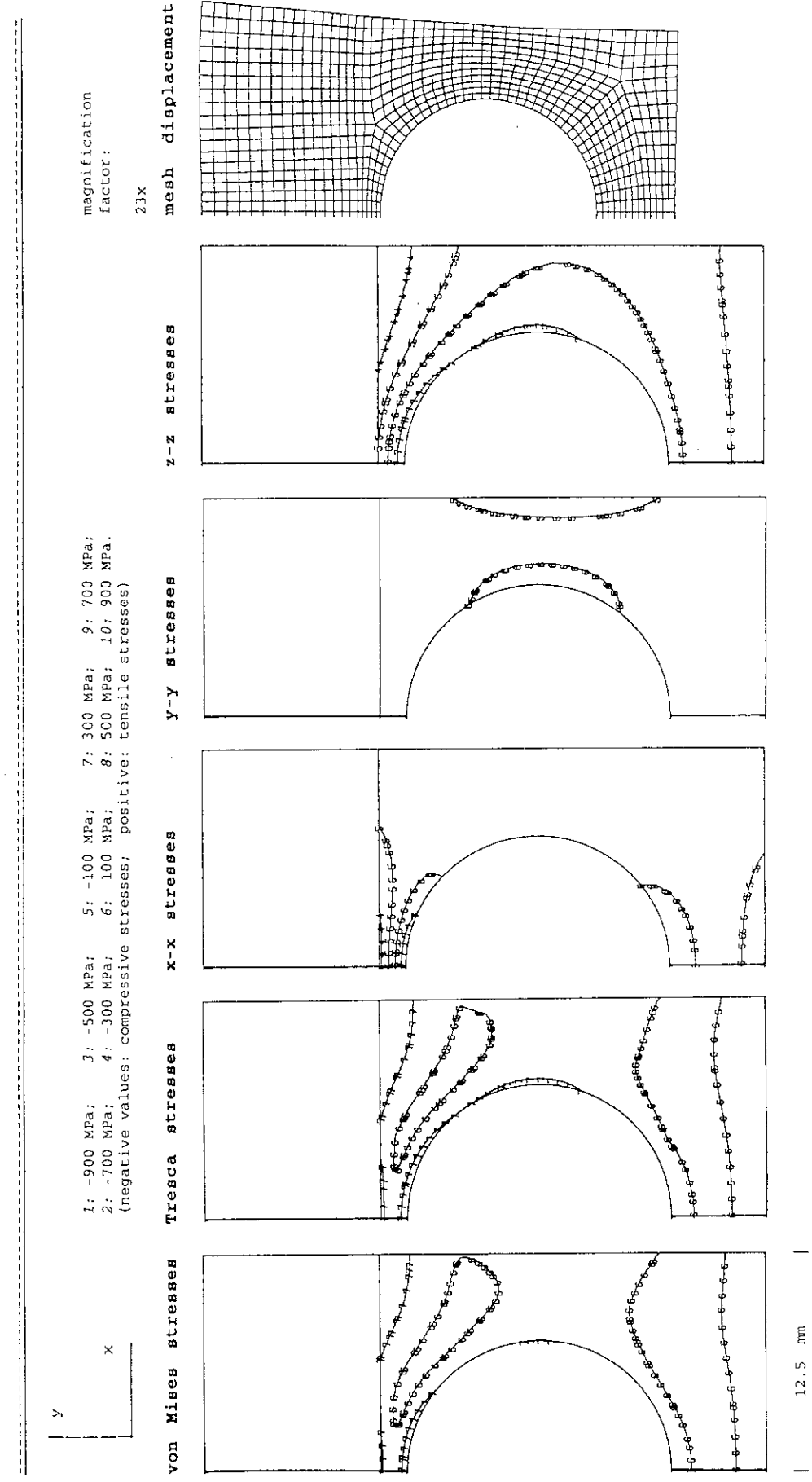


Fig. 7.2.1.c/II Flat-Plate Type, Armor: MFC-1 (1992), Heat Sink: TZM

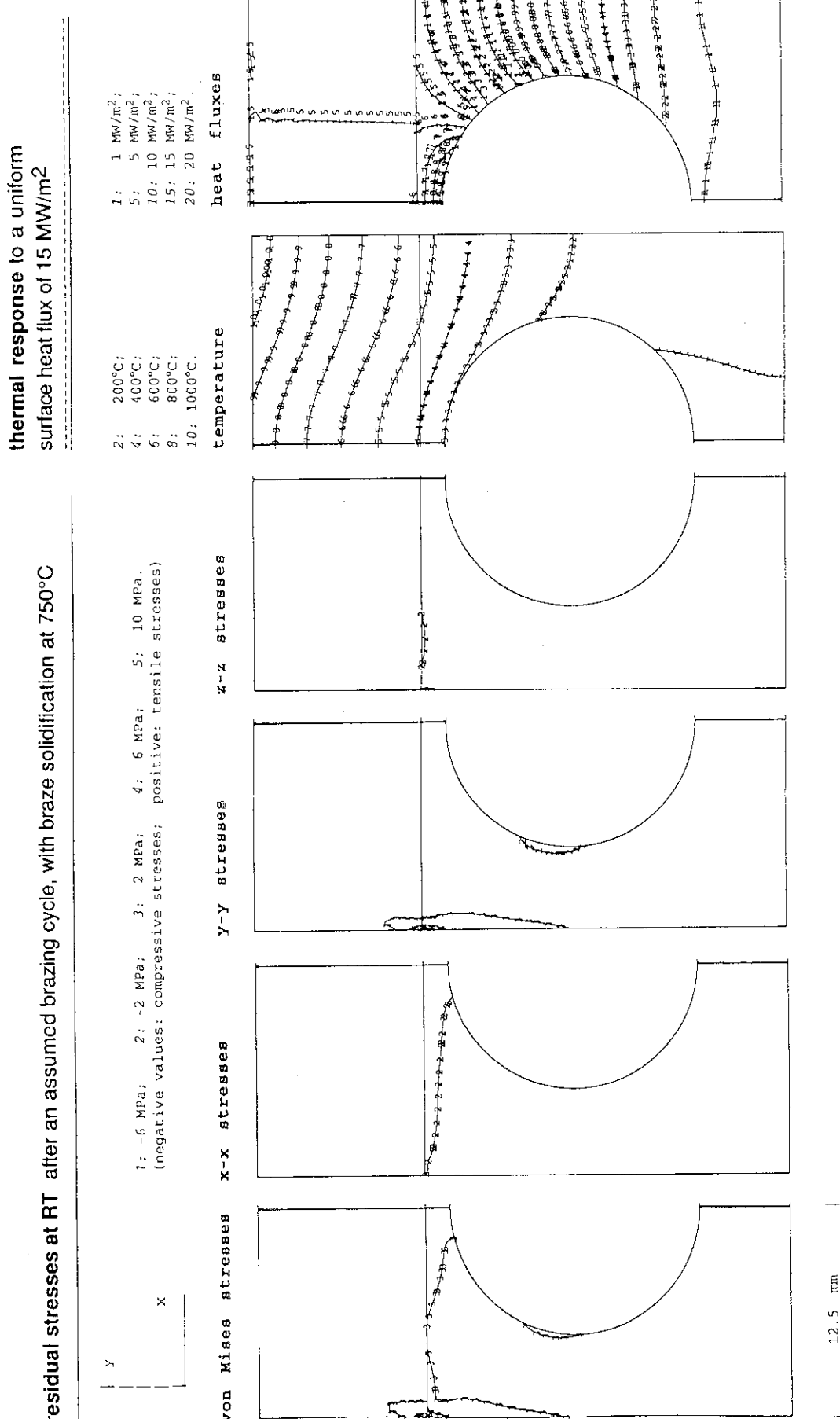


Fig. 7.2.1.d/I Flat-Plate Type, Armor: MFC-1 (1992), Heat Sink: W-30Cu

stress distribution and displacement at a uniform steady state surface heat flux of 15 MW/m²

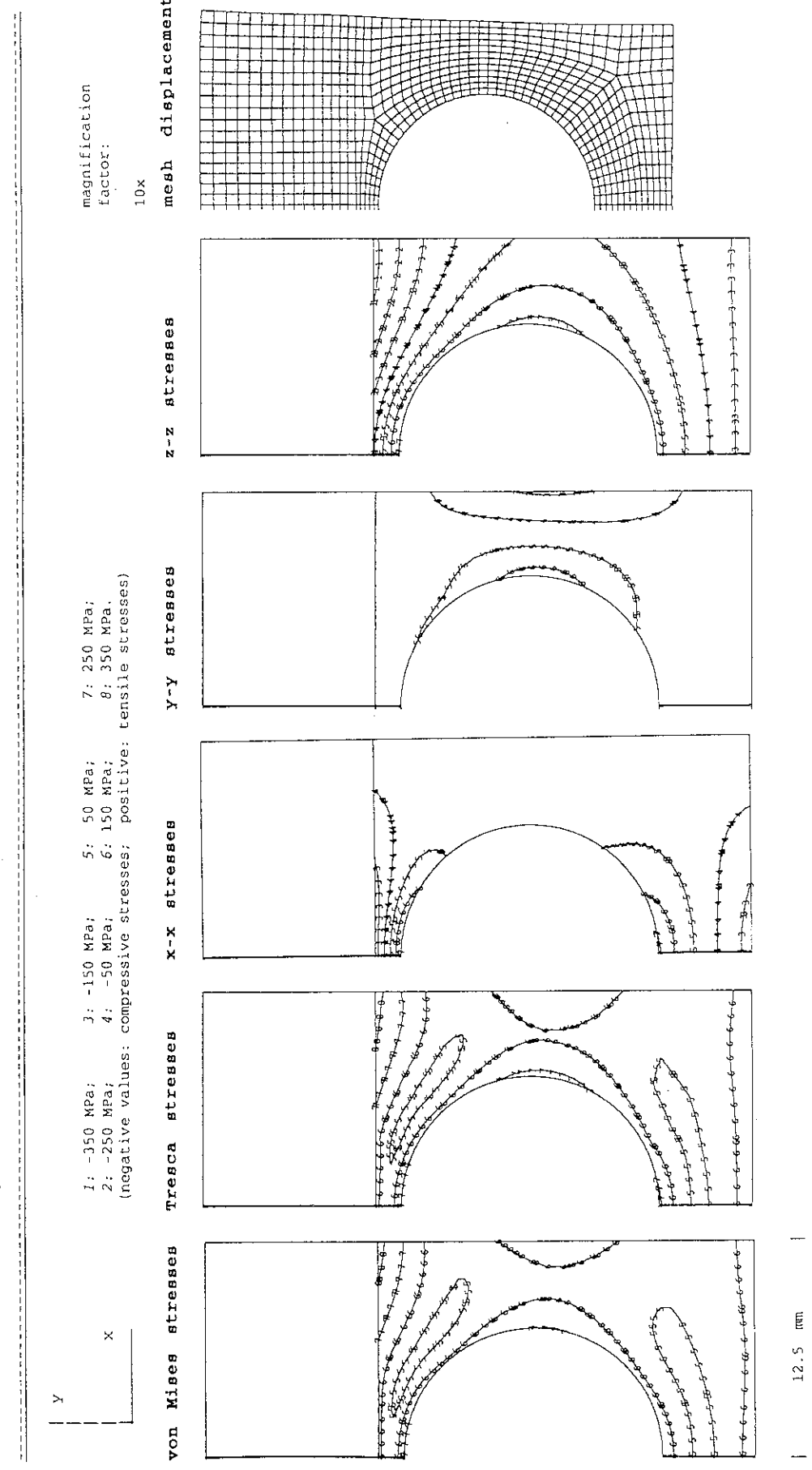
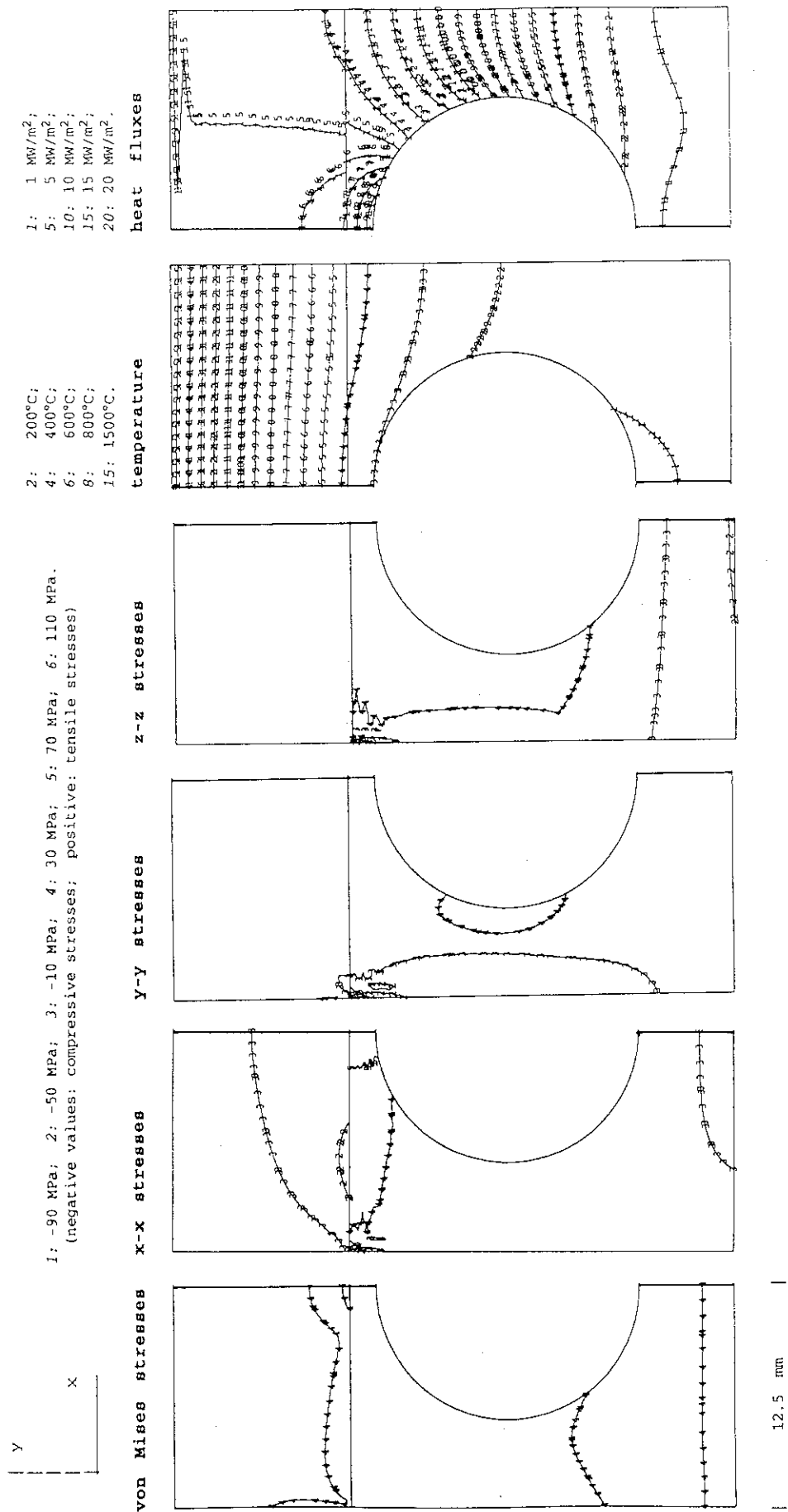


Fig. 7.2.1.d/II Flat-Plate Type, Armor: MFC-1 (1992), Heat Sink: W-30Cu

residual stresses at RT after an assumed brazing cycle, with braze solidification at 750°C

thermal response to a uniform surface heat flux of 15 MW/m²



stress distribution and displacement at a uniform steady state surface heat flux of 15 MW/m²

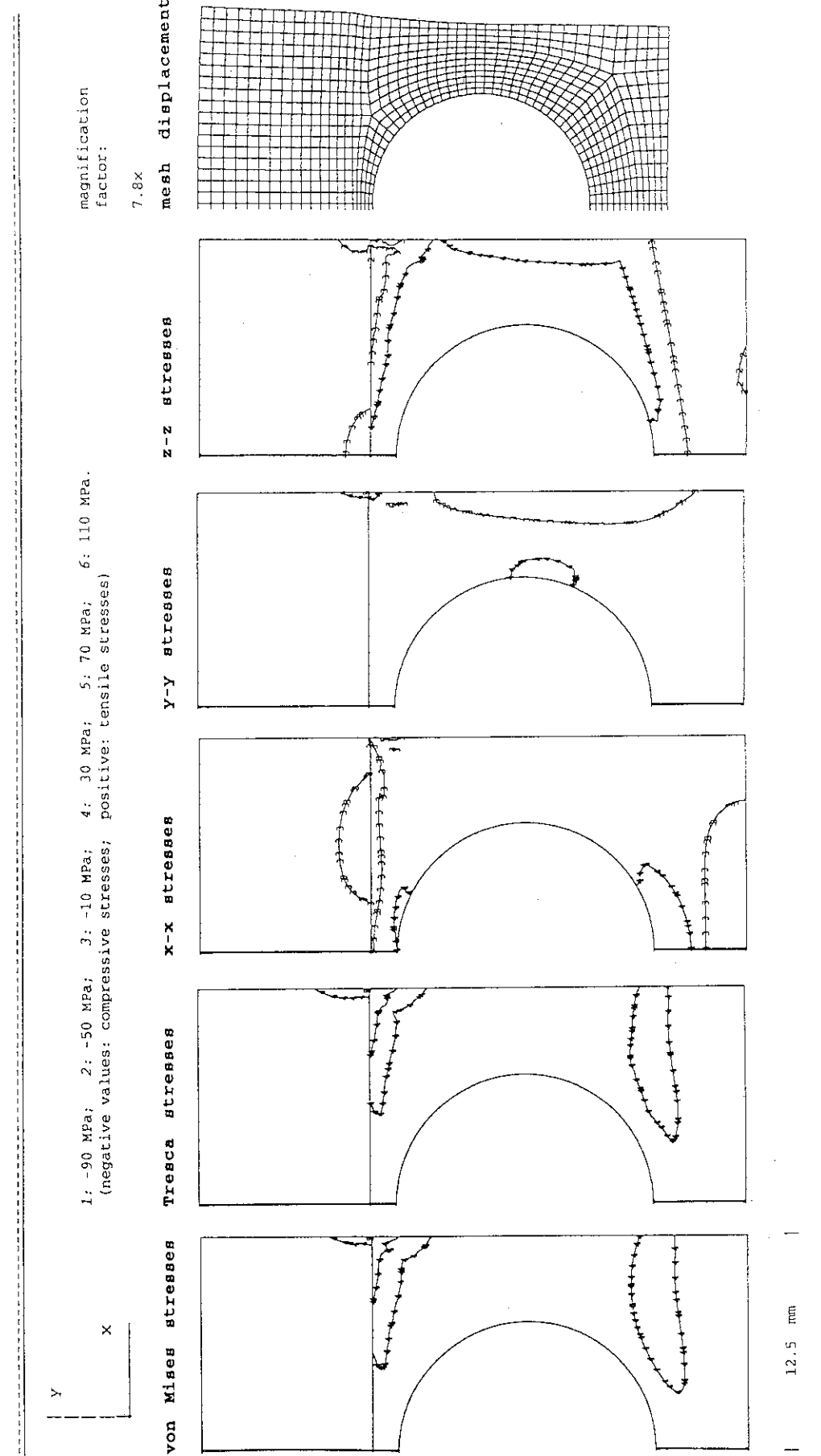


Fig. 7.2.1.e/II Flat-Plate Type, Armor: CX2002U, Heat Sink: OF-Cu

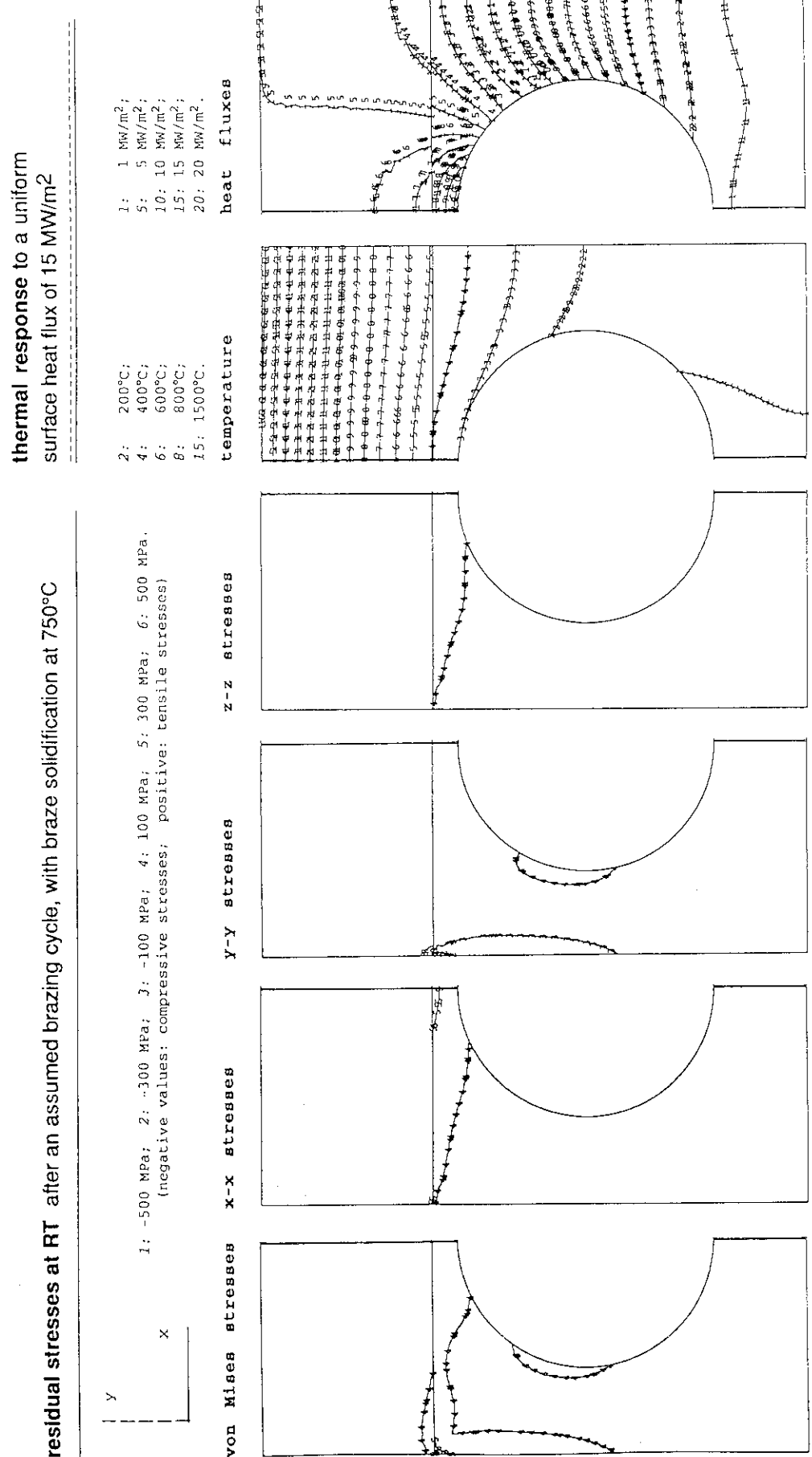


Fig. 7.2.1.f/I Flat-Plate Type, Armor: CX2002U, Heat Sink: DS-Cu

stress distribution and displacement at a uniform steady state surface heat flux of 15 MW/m²

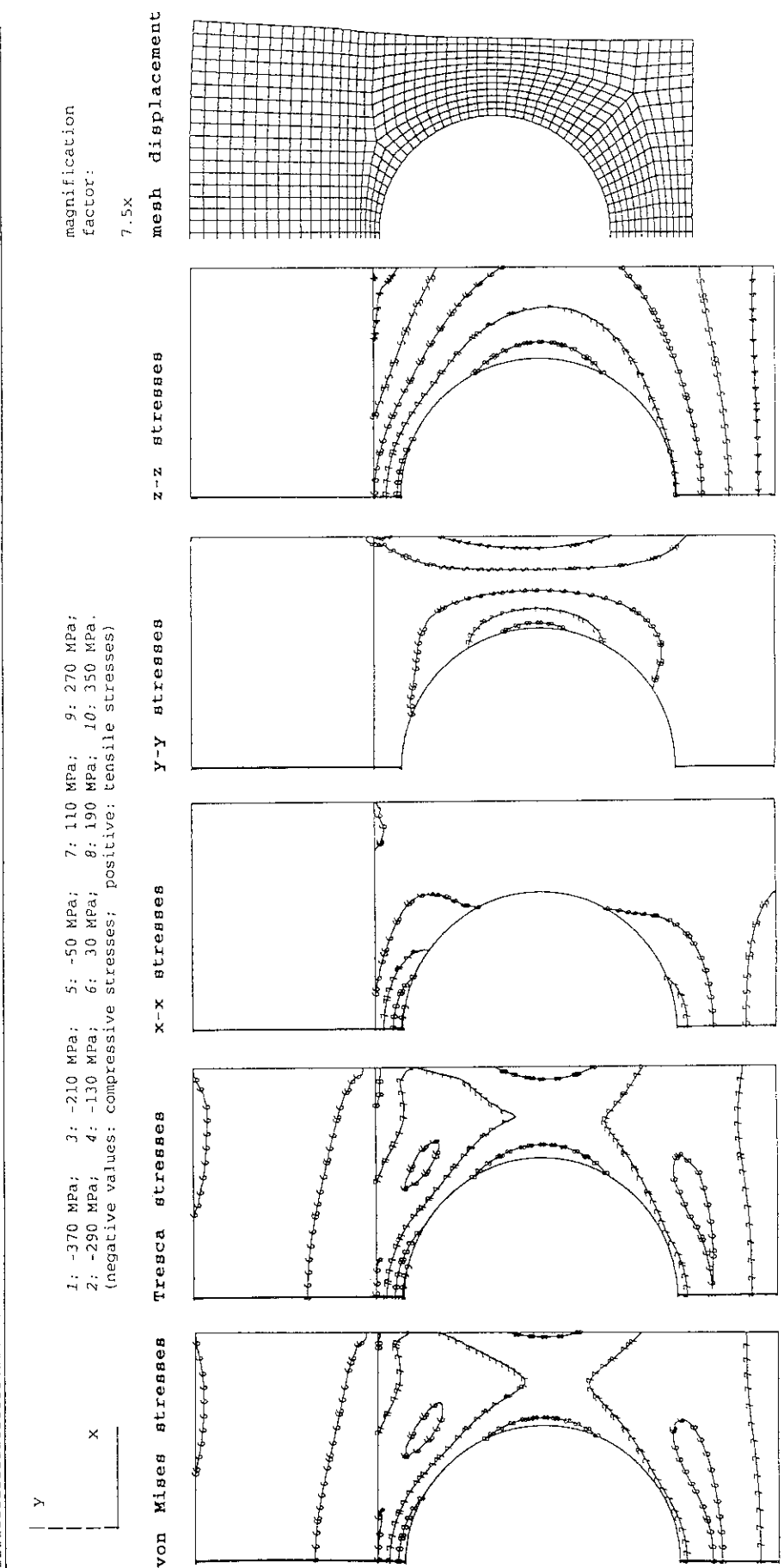
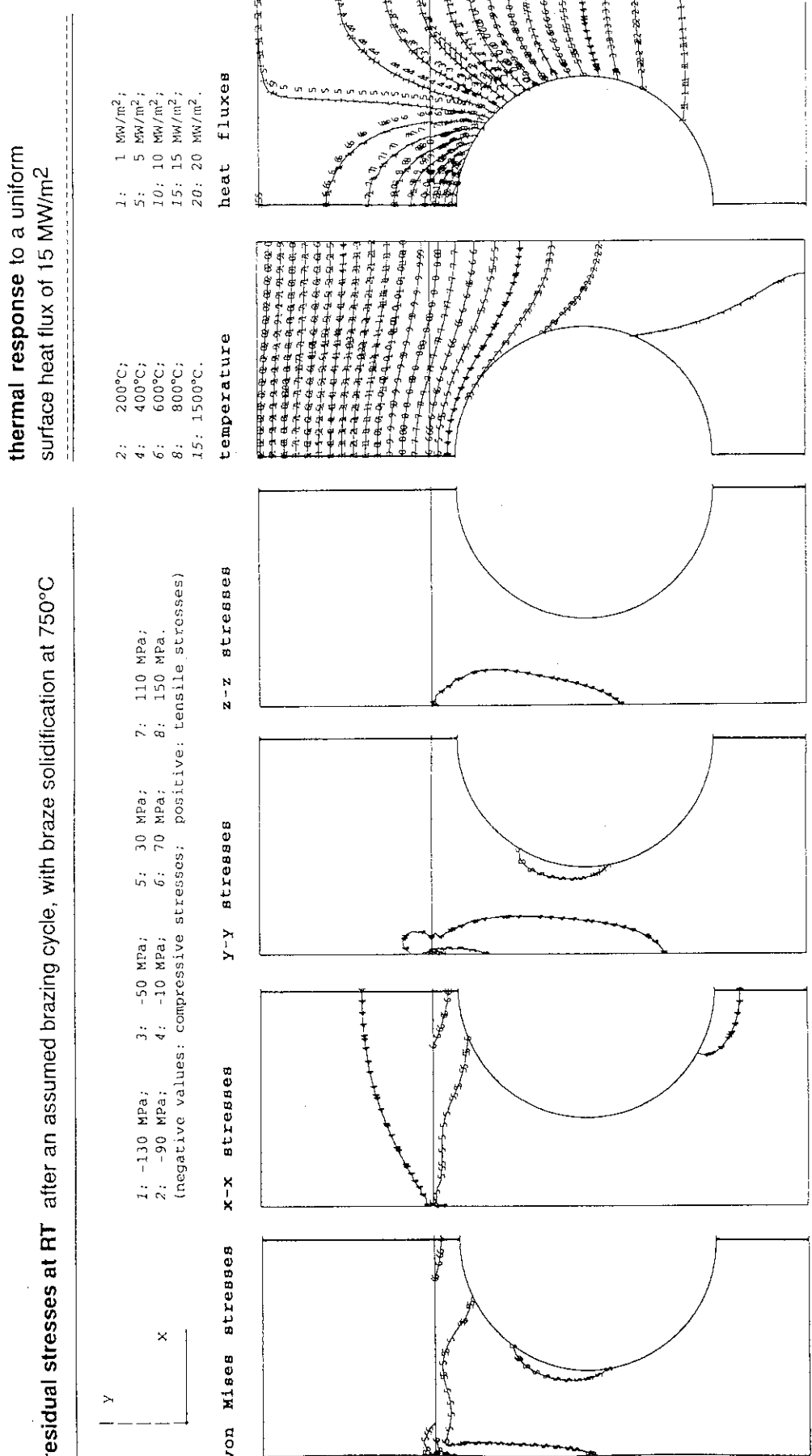


Fig. 7.2.1.f/II Flat-Plate Type, Armor: CX2002U, Heat Sink: DS-Cu



12.5 item

Fig. 7.2.1.8/I Flat-Plate Type, Armor: CX2002U, Heat Sink: TZM

stress distribution and displacement at a uniform steady state heat flux of 15 MW/m²

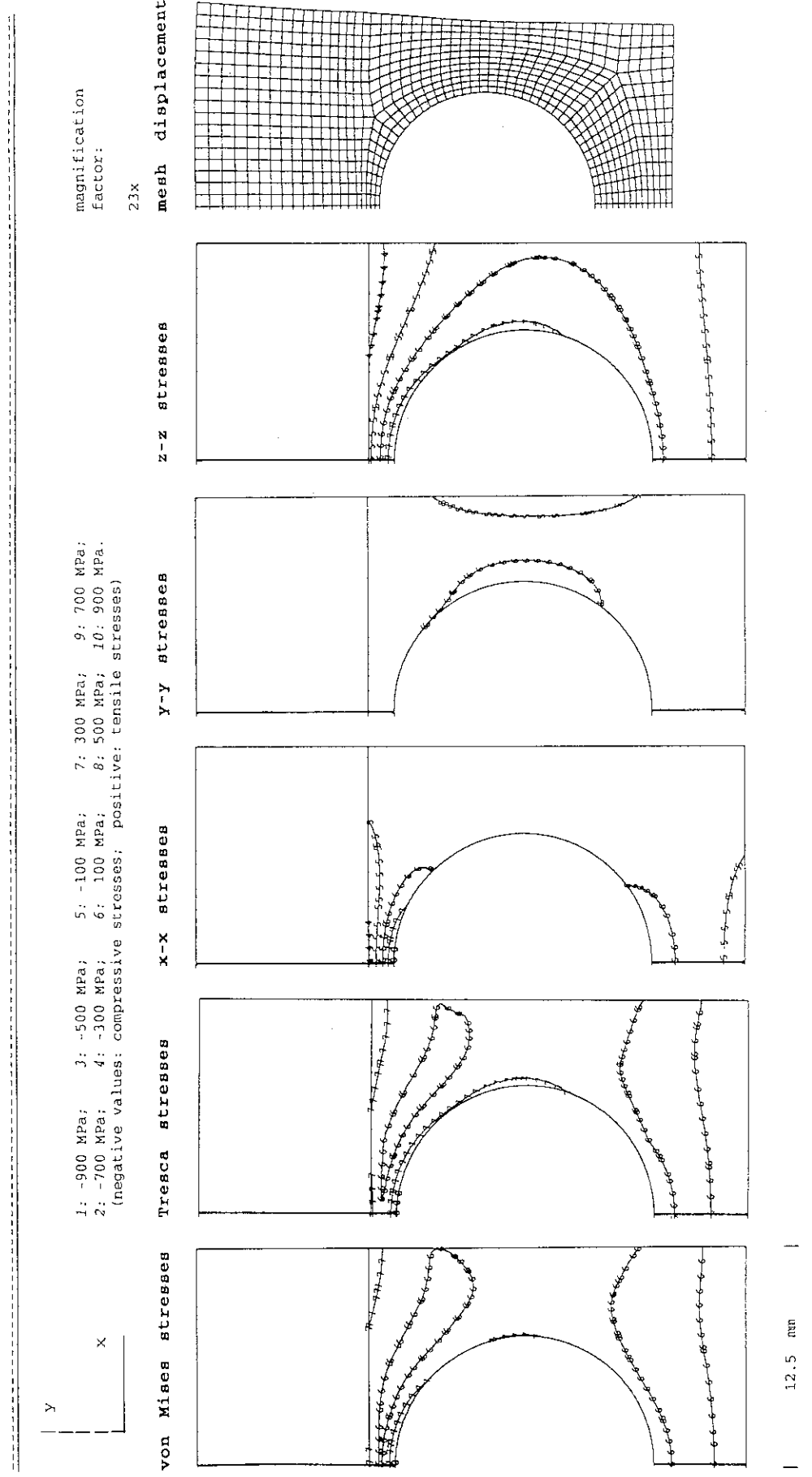


Fig. 7.2.1.g/II Flat-Plate Type, Armor: CX2002U, Heat Sink: TZM

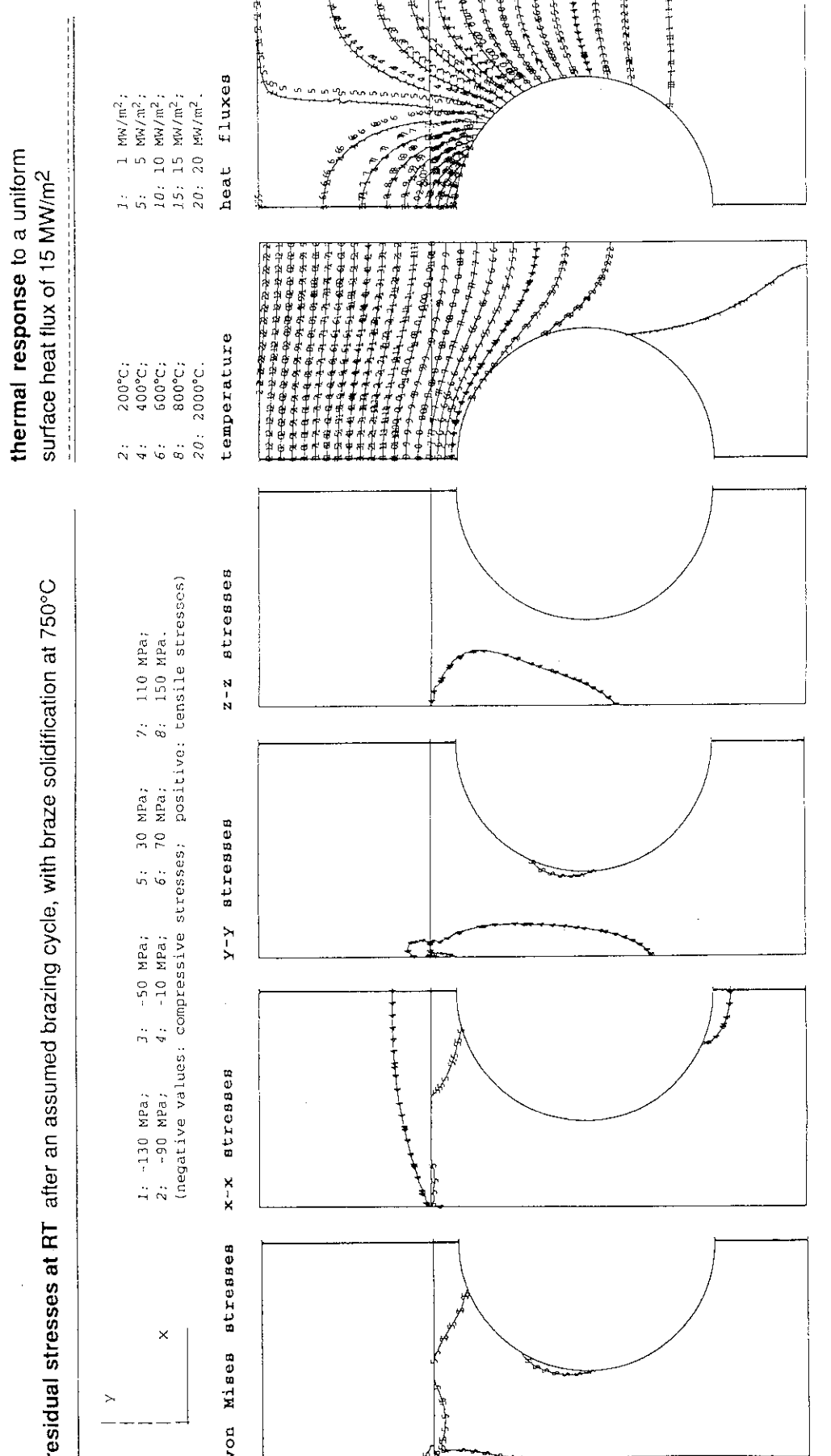


Fig. 7.2.1.h/I Flat-Plate Type, Armor: GX2002U, Heat Sink: W5Re

stress distribution and displacement at a uniform steady state surface heat flux of 15 MW/m²

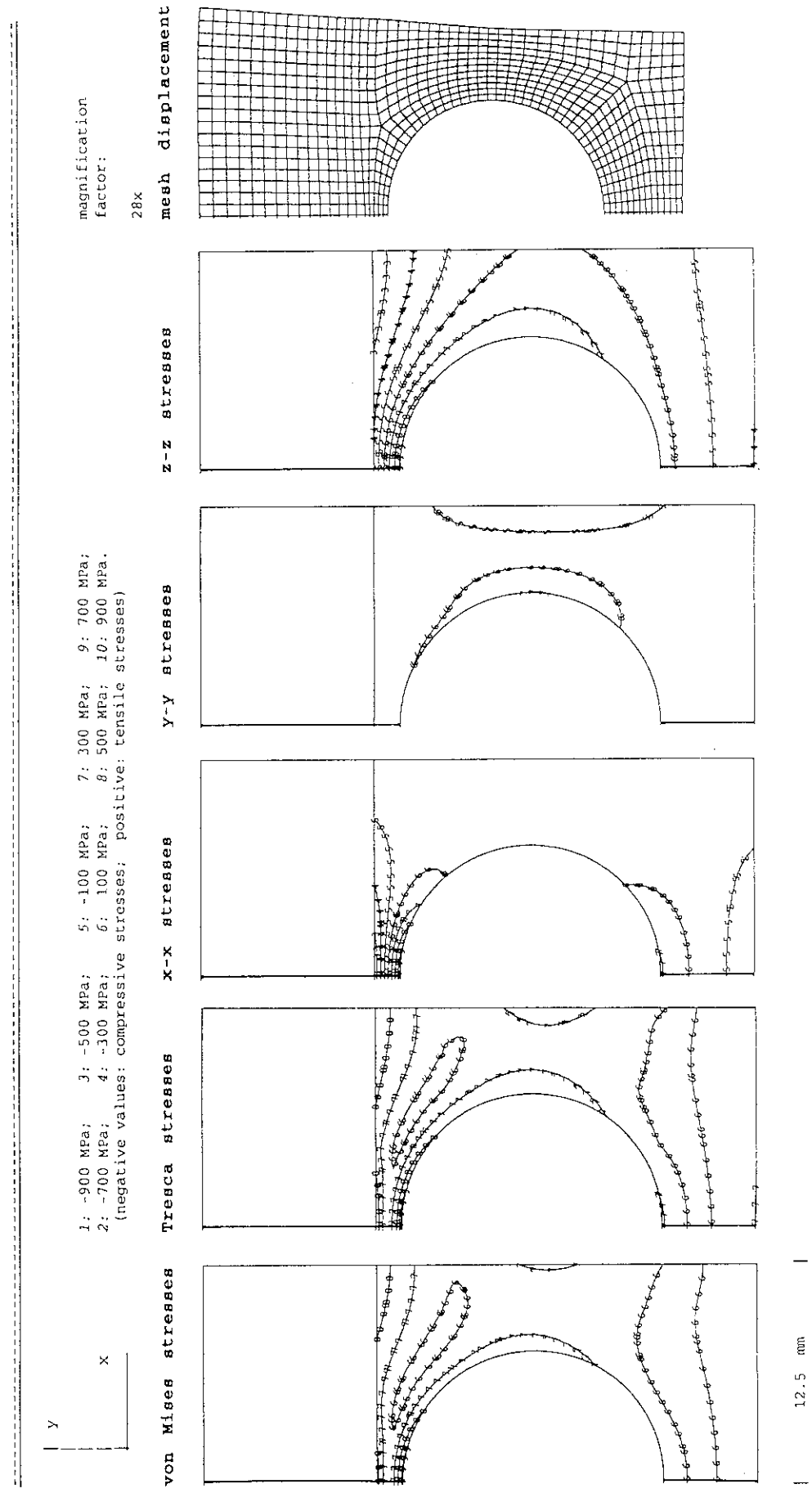


Fig. 7.2.1.h/II Flat-Plate Type, Armor: CX2002U, Heat Sink: W5Re

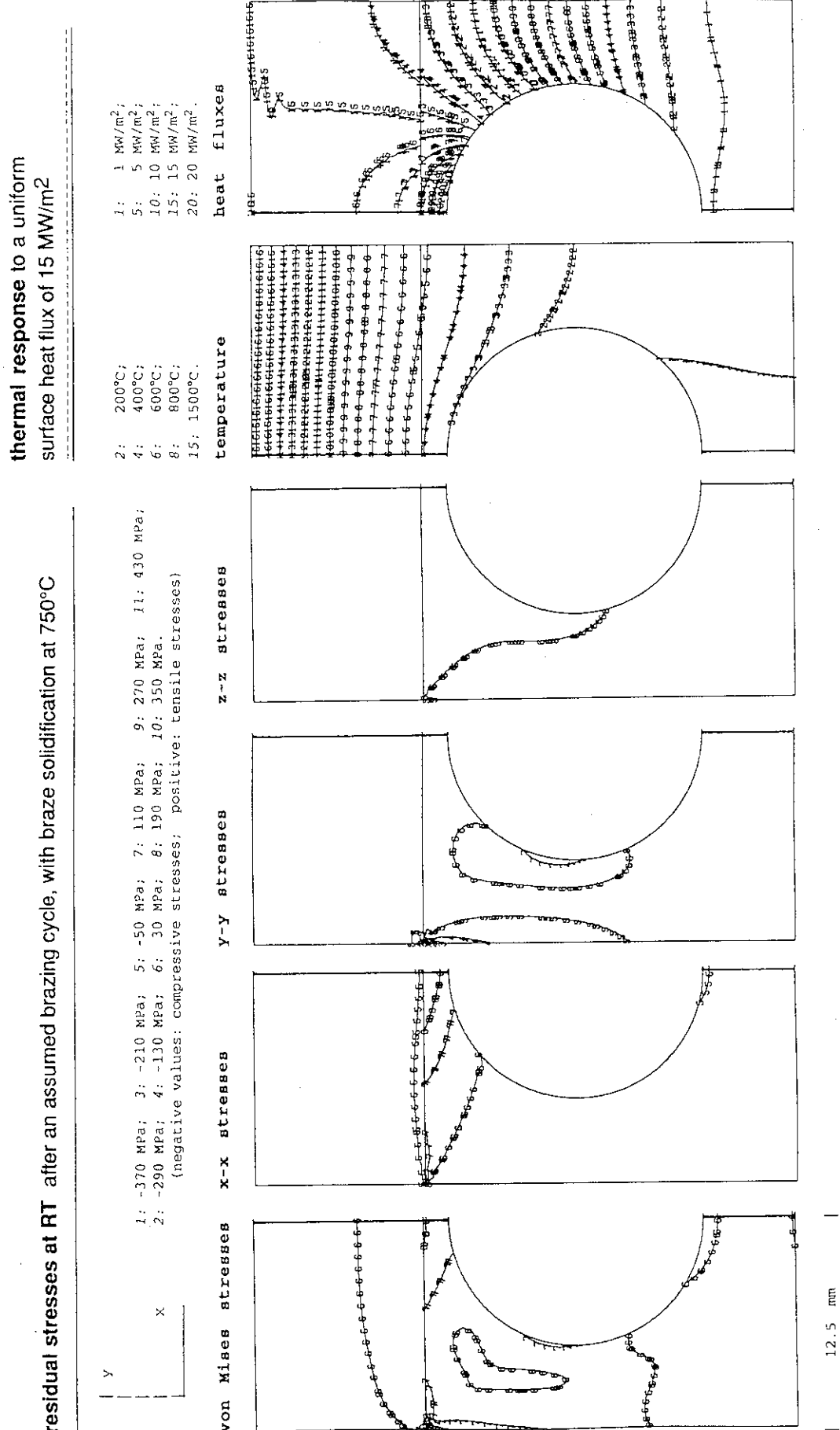


Fig. 7.2.1.1/I Flat-Plate Type, Armor: CX2002U, Heat Sink: W-30Cu

stress distribution and displacement at a uniform steady state surface heat flux of 15 MW/m²

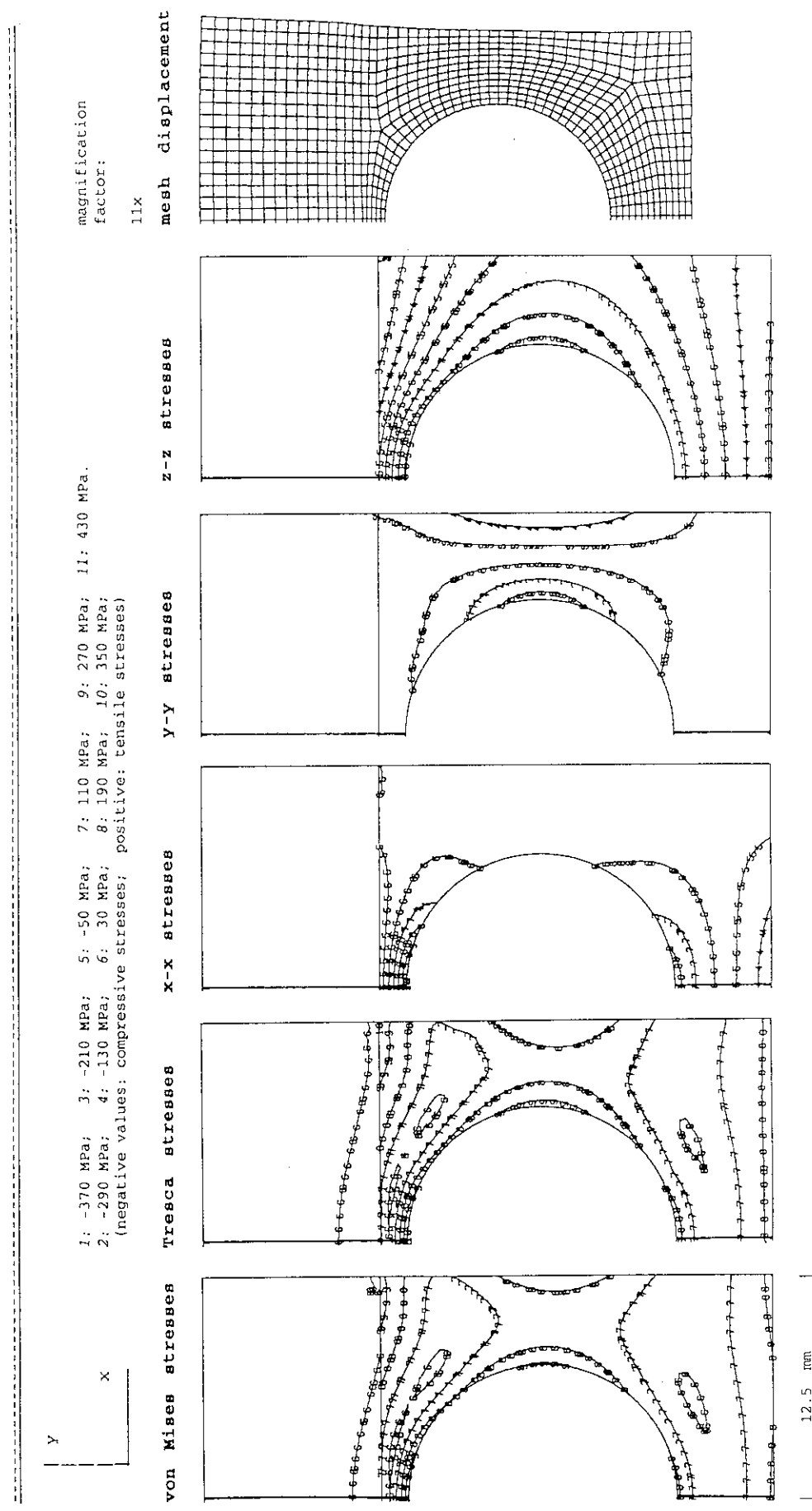


Fig. 7.2.1.i/II Flat-Plate Type, Armor: CX2002U, Heat Sink: W-30Cu

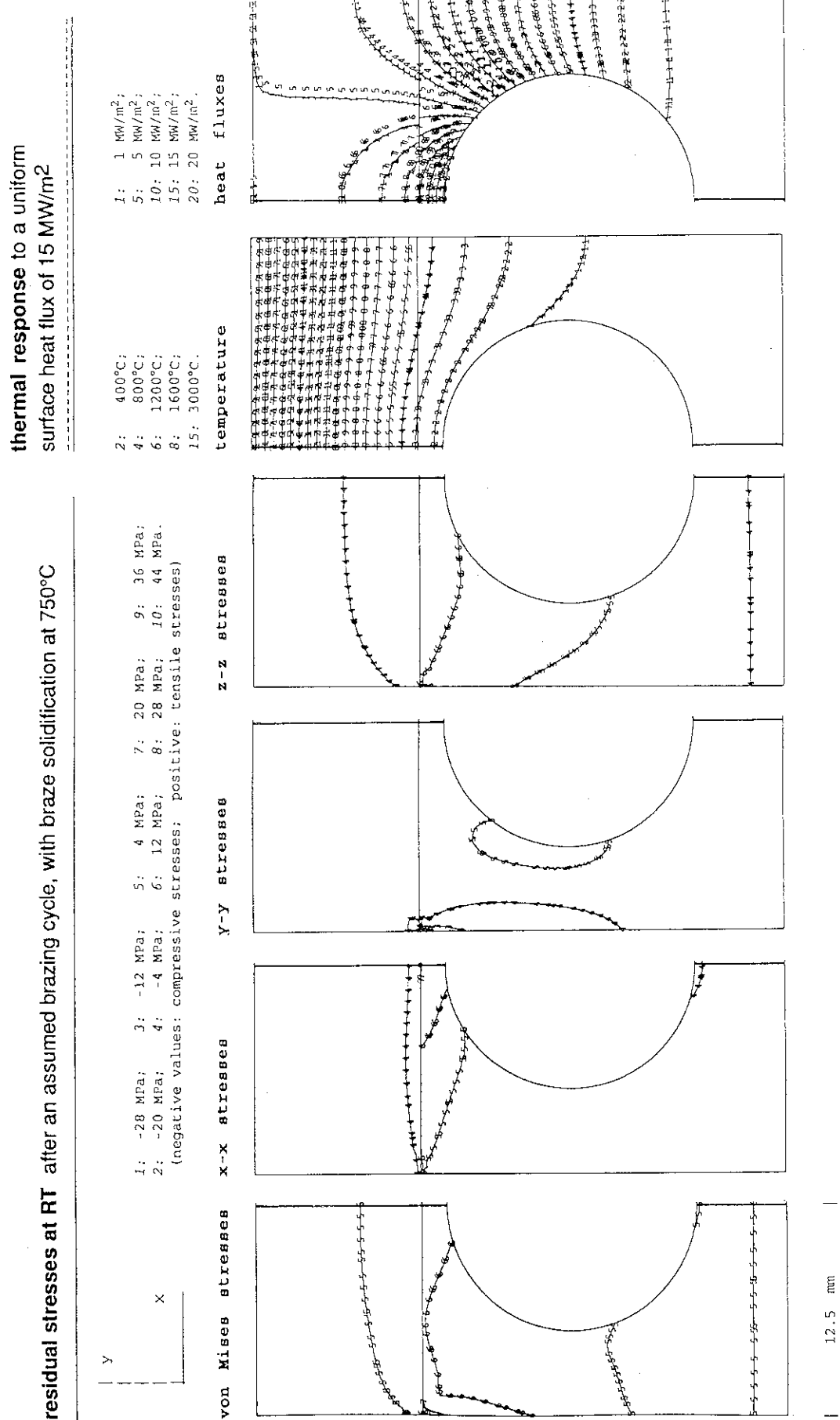


Fig. 7.2.1.j/I Flat-Plate Type, Armor: IG430U, Heat Sink: TZM

stress distribution and displacement at a uniform steady state surface heat flux of 15 MW/m²

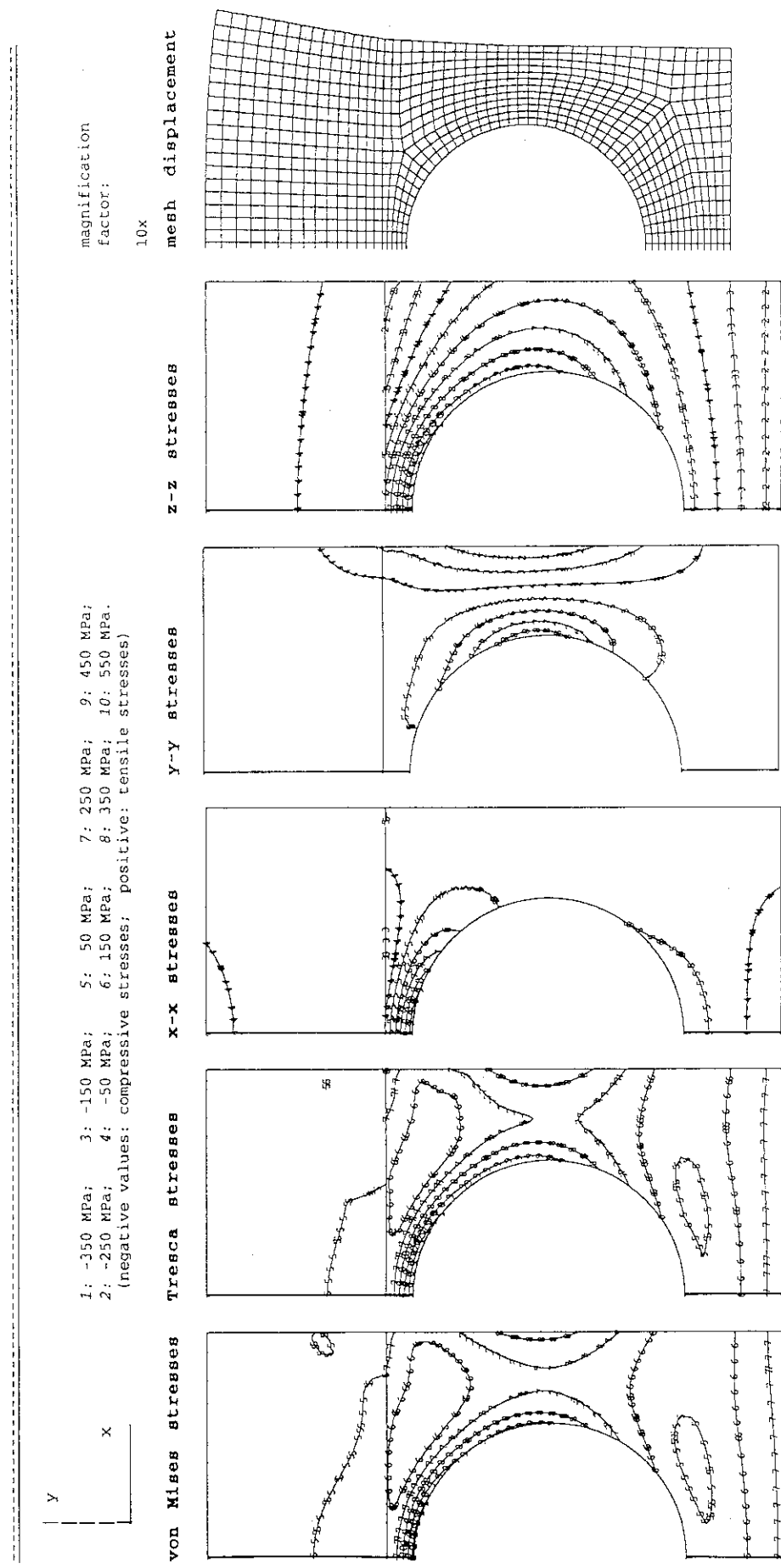
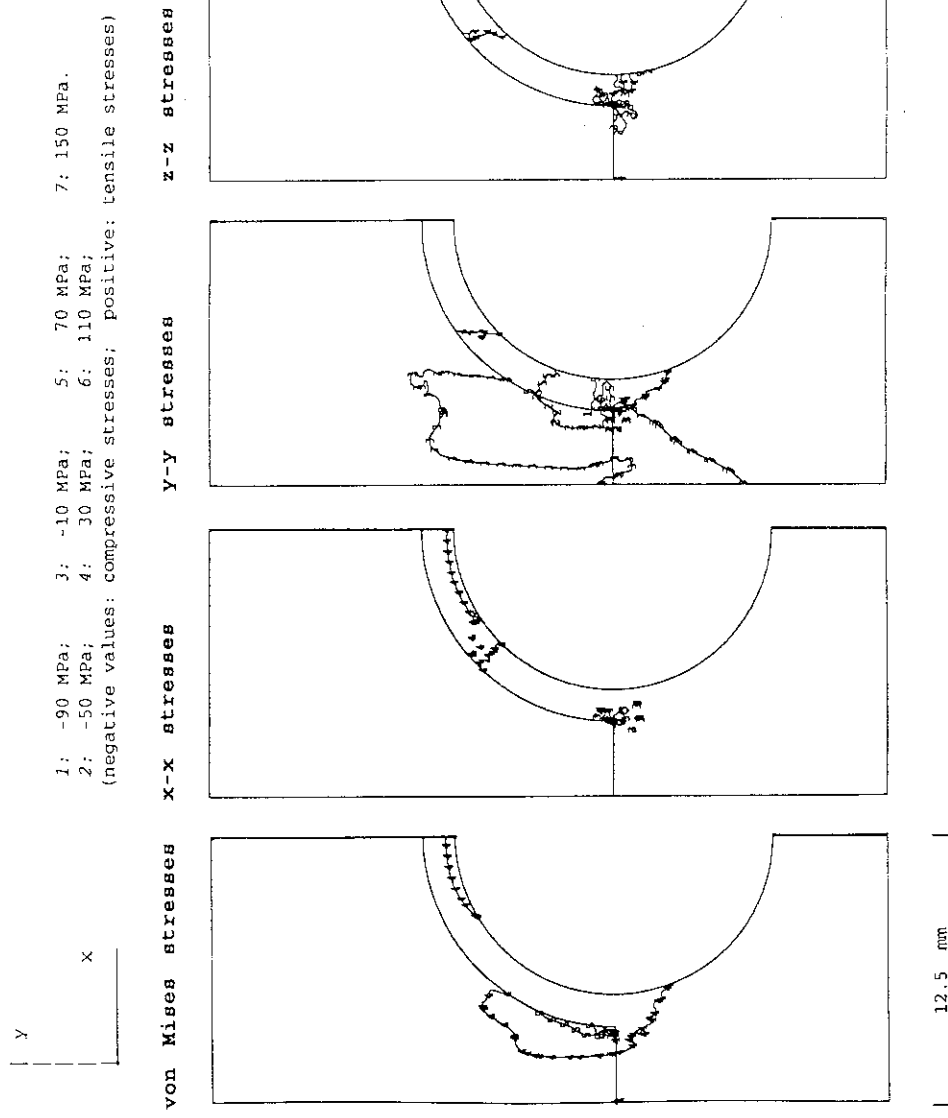


Fig. 7.2.1.j/II Flat-Plate Type, Armor: IG430U, Heat Sink: TZM

residual stresses at RT after an assumed brazing cycle, with braze solidification at 750°C

thermal response to a uniform surface heat flux of 15 MW/m²



12.5 mm

Fig. 7.2.2.a/I Saddle Type, Armor: MFC-1 (1992), Heat Sink: OF-Cu

stress distribution and displacement at a uniform steady state surface heat flux of 15 MW/m²

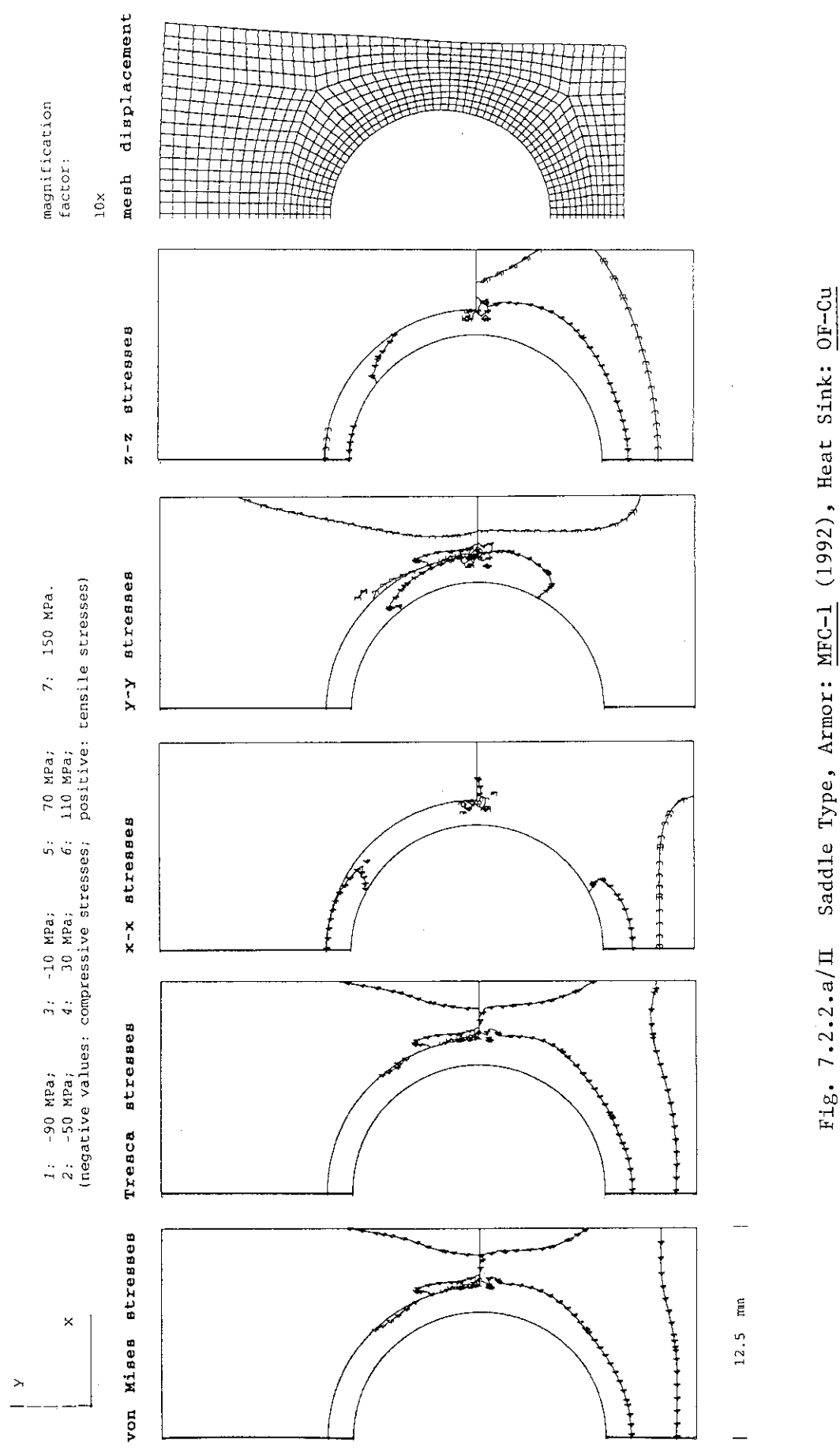
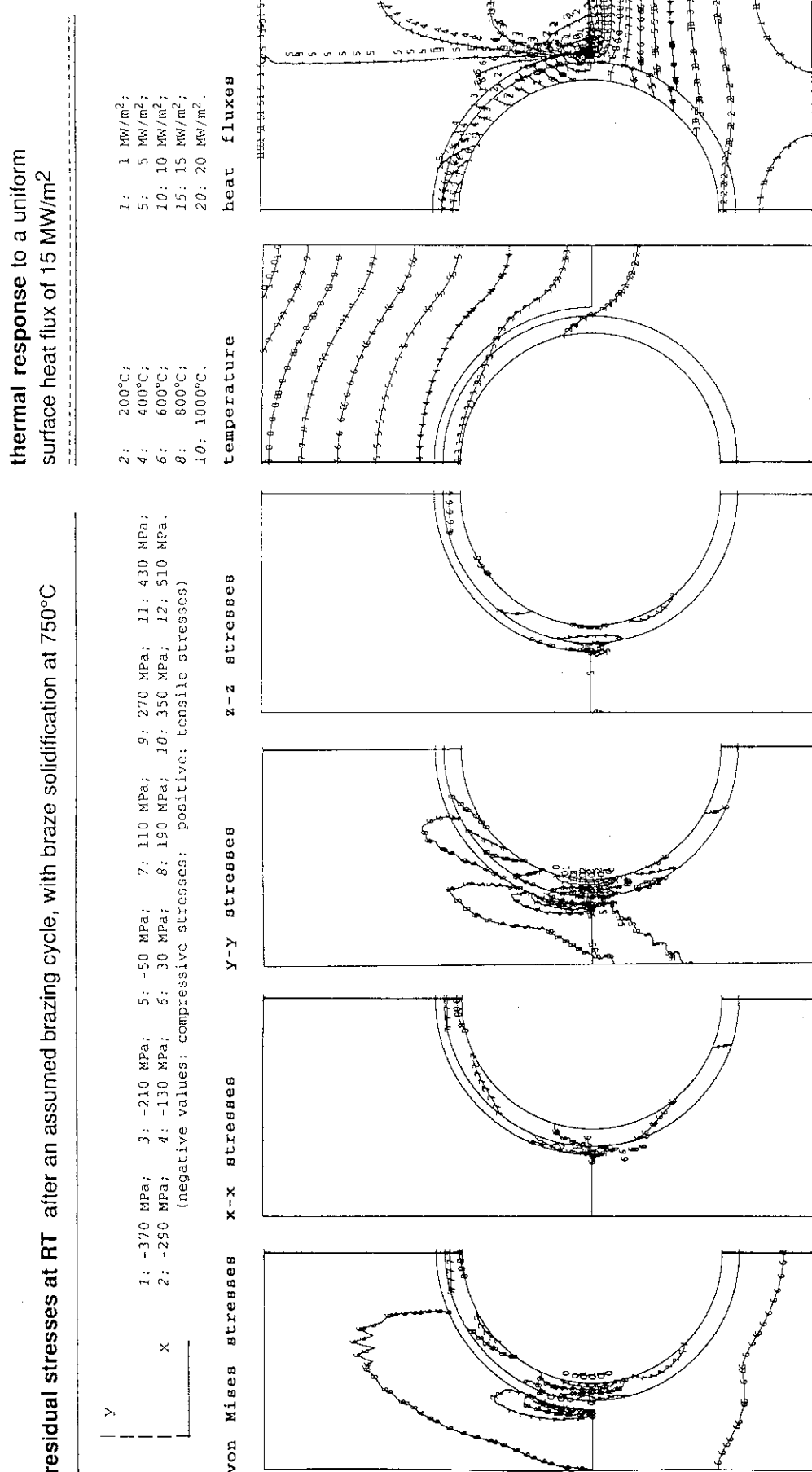


Fig. 7.2.2.a/II Saddle Type, Armor: MFC-1 (1992), Heat Sink: OF-Cu

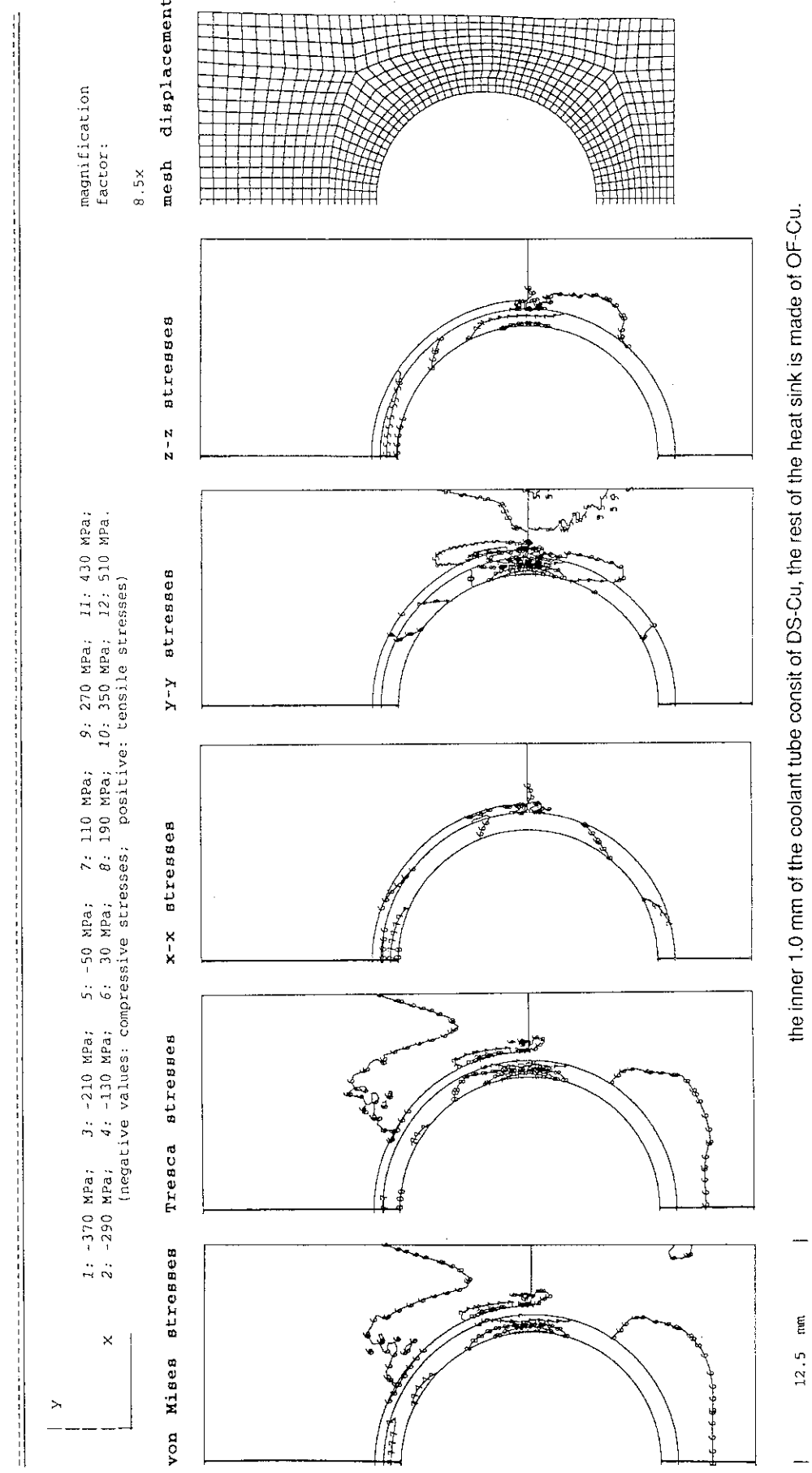


the inner 1.0 mm of the coolant tube consist of DS-Cu, the rest of the heat sink is made of OF-Cu.

Fig. 7.2.2.b/I Saddle Type, Armor: MFC-1 (1992), Heat Sink: OF&DS-Cu

12.5 mm

stress distribution and displacement at a uniform steady state surface heat flux of 15 MW/m²

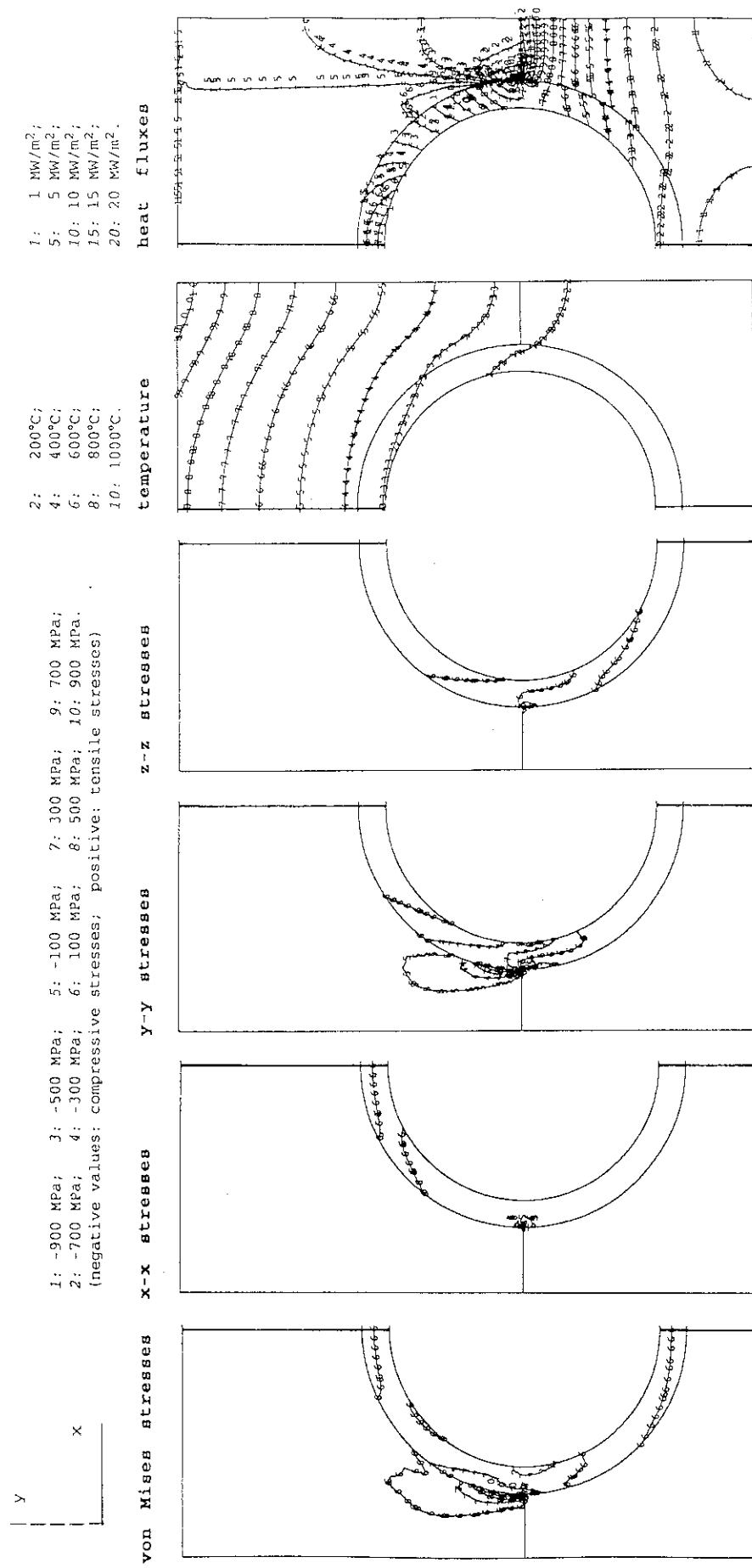


the inner 1.0 mm of the coolant tube consist of DS-Cu, the rest of the heat sink is made of OF-Cu.

Fig. 7.2.2.b/II Saddle Type, Armor: MFC-1 (1992), Heat Sink: OF&DS-Cu

residual stresses at RT after an assumed brazing cycle, with braze solidification at 750°C

thermal response to a uniform surface heat flux of 15 MW/m²

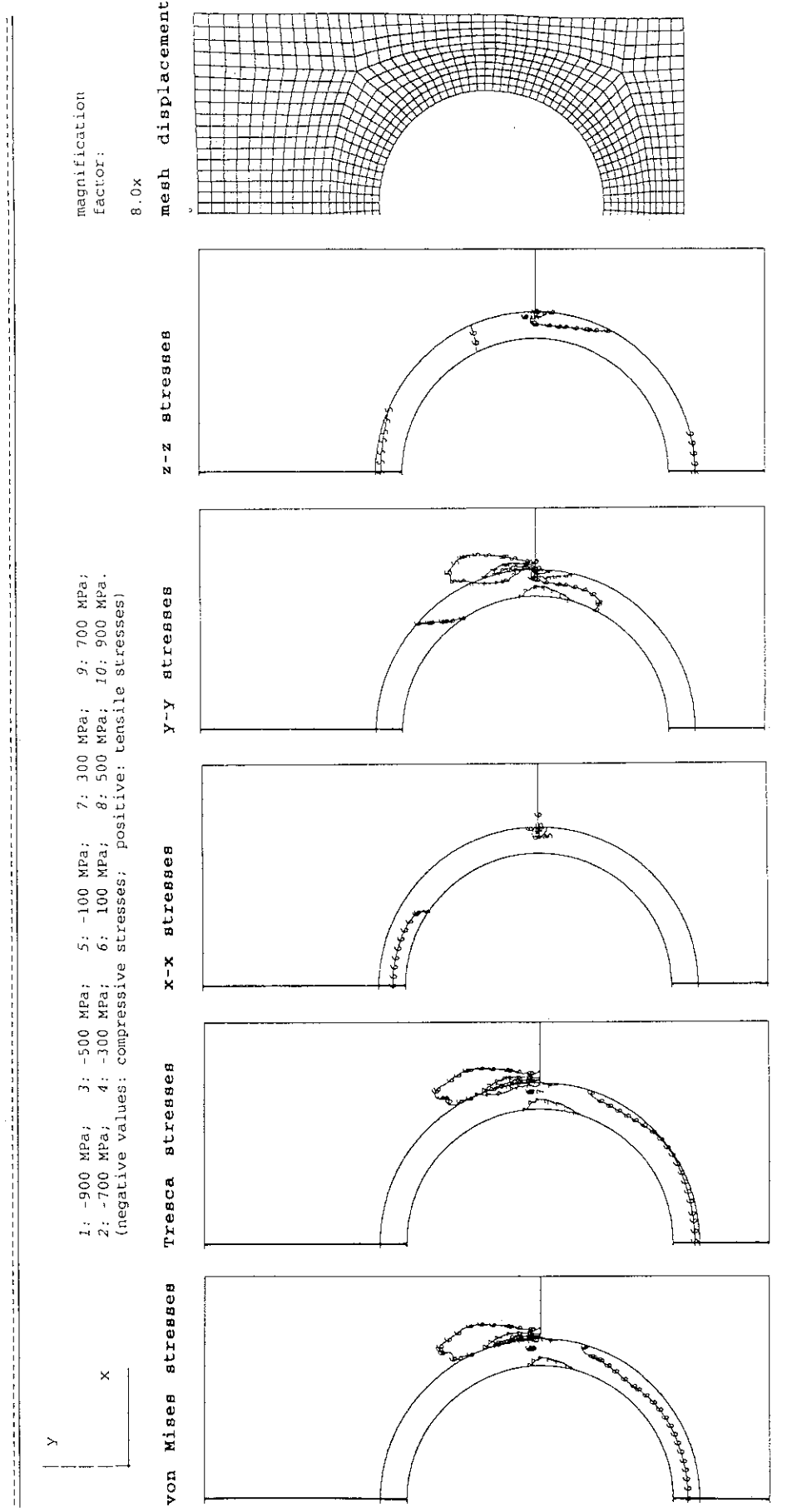


12.5 mm

the coolant tube consists of DS-Cu, the rest of the heat sink is made of OF-Cu.

Fig. 7.2.2.c/I Saddle Type, Armor: MFC-1 (1992), Heat Sink: OF&DS-Cu

stress distribution and displacement at a uniform steady state surface heat flux of 15 MW/m²



the coolant tube consists of DS-Cu, the rest of the heat sink is made of OF-Cu.

Fig. 7.2.2.c/II Saddle Type, Armor: MFC-1 (1992), Heat Sink: OF&DS-Cu

residual stresses at RT after an assumed brazing cycle, with braze solidification at 750°C

thermal response to a uniform surface heat flux of 15 MW/m²

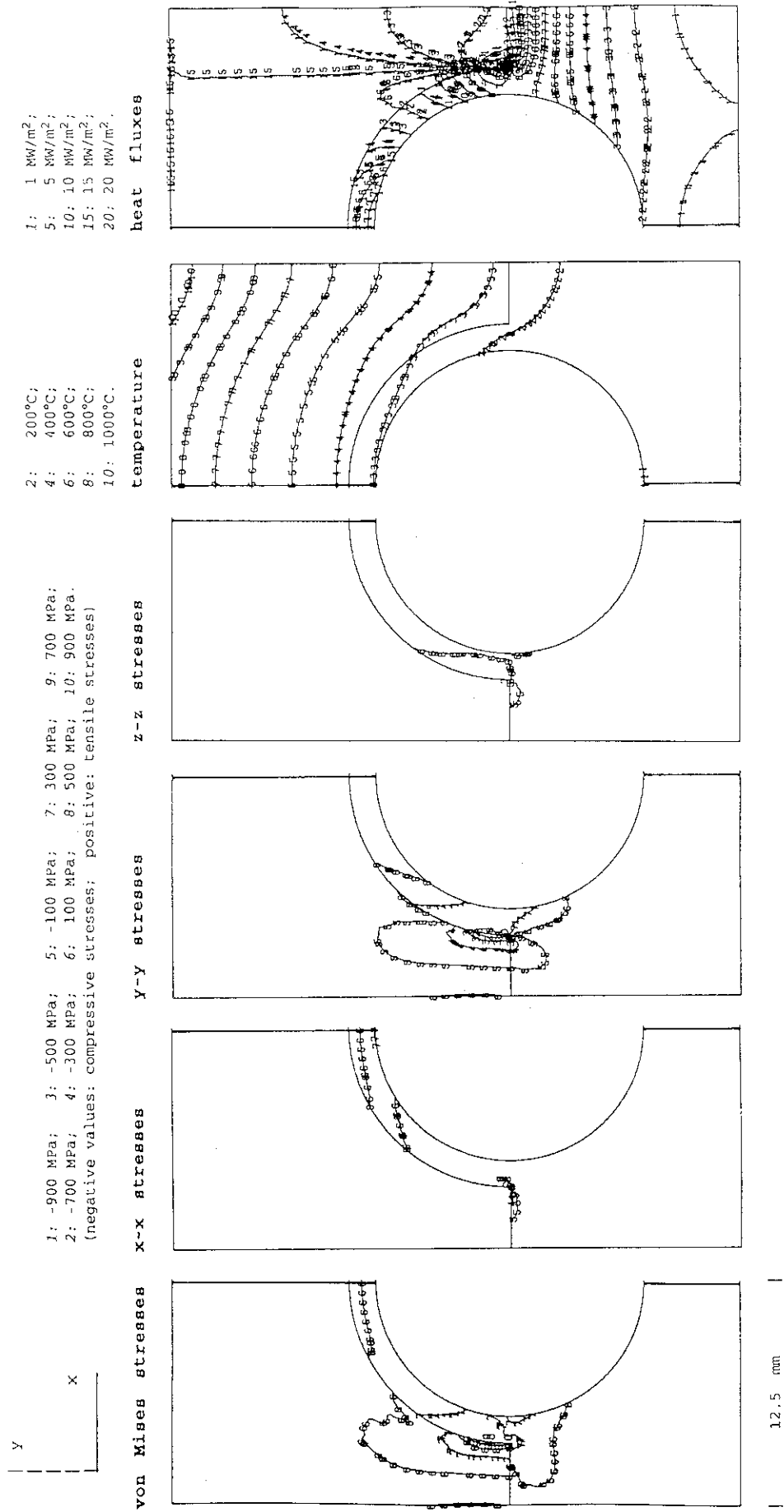


Fig. 7.2.2.d/I Saddle Type, Armor: MFC-1 (1992), Heat Sink: DS-Cu

stress distribution and displacement at a uniform steady state heat flux of 15 MW/m²

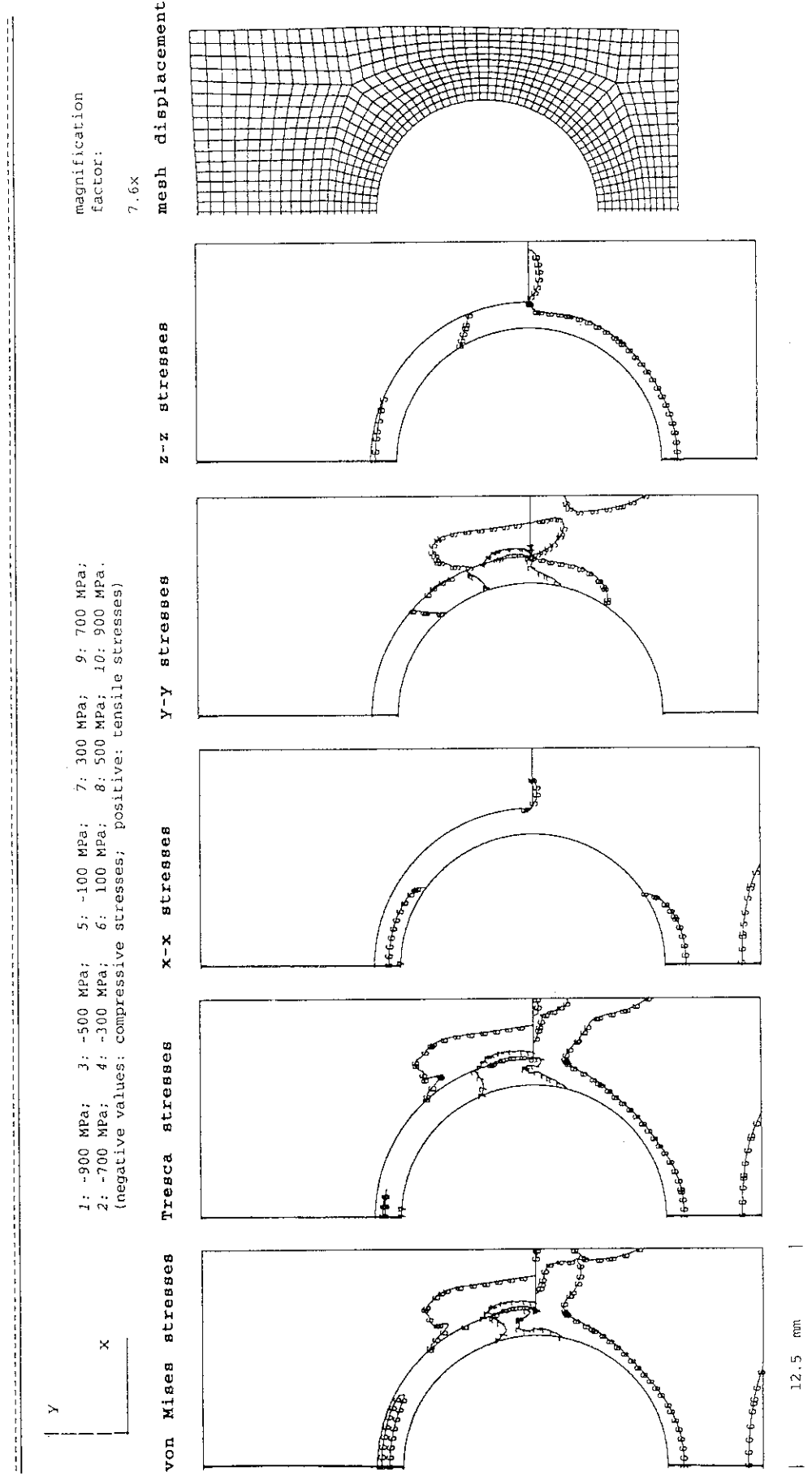


Fig. 7.2.2.d/II Saddle Type, Armor: MFC-1 (1992), Heat Sink: DS-Cu

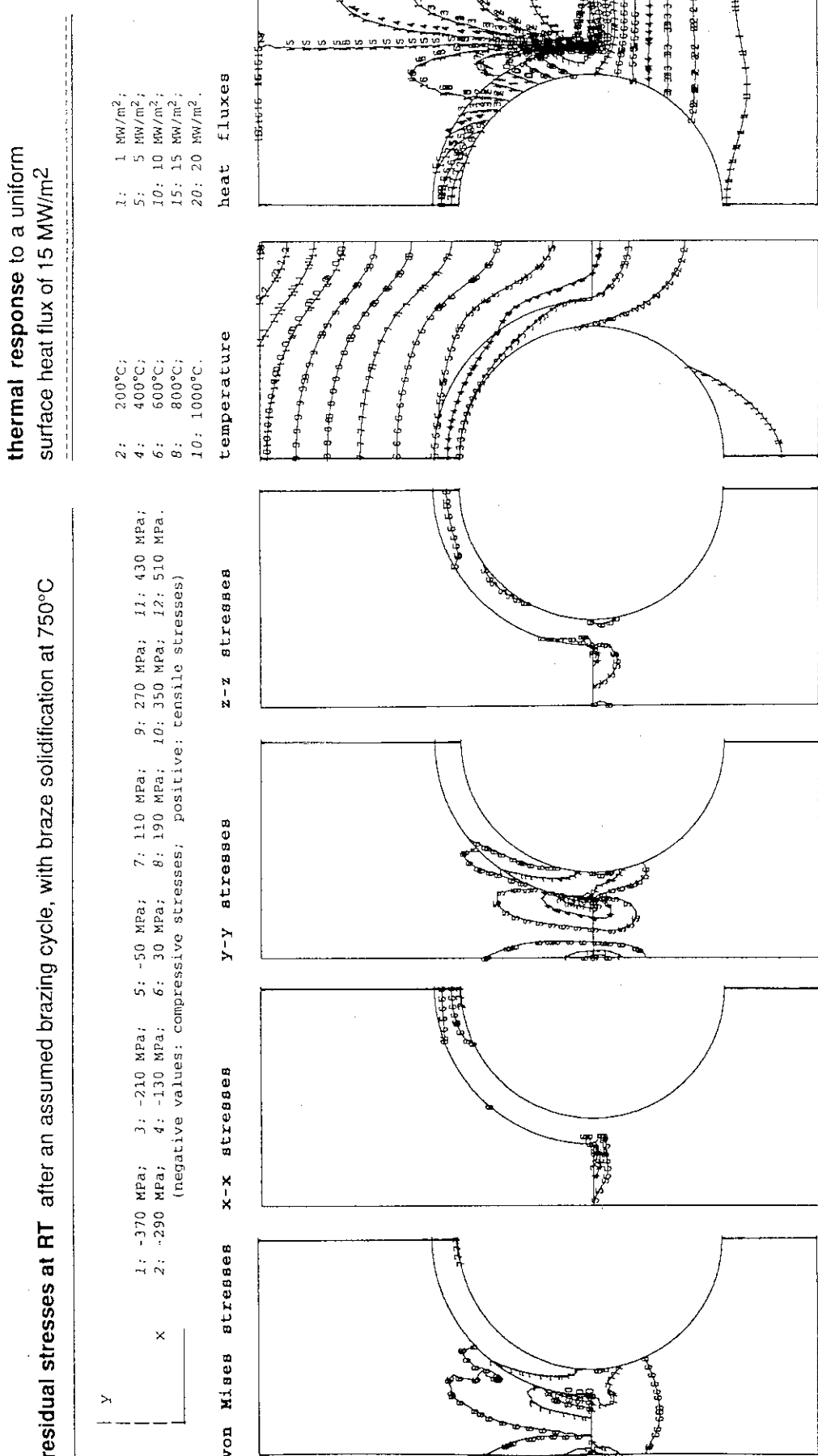


Fig. 7.2.2.e/I Saddle Type, Armor: MFC-1 (1992), Heat Sink: TZM

stress distribution and displacement at a uniform steady state surface heat flux of 15 MW/m²

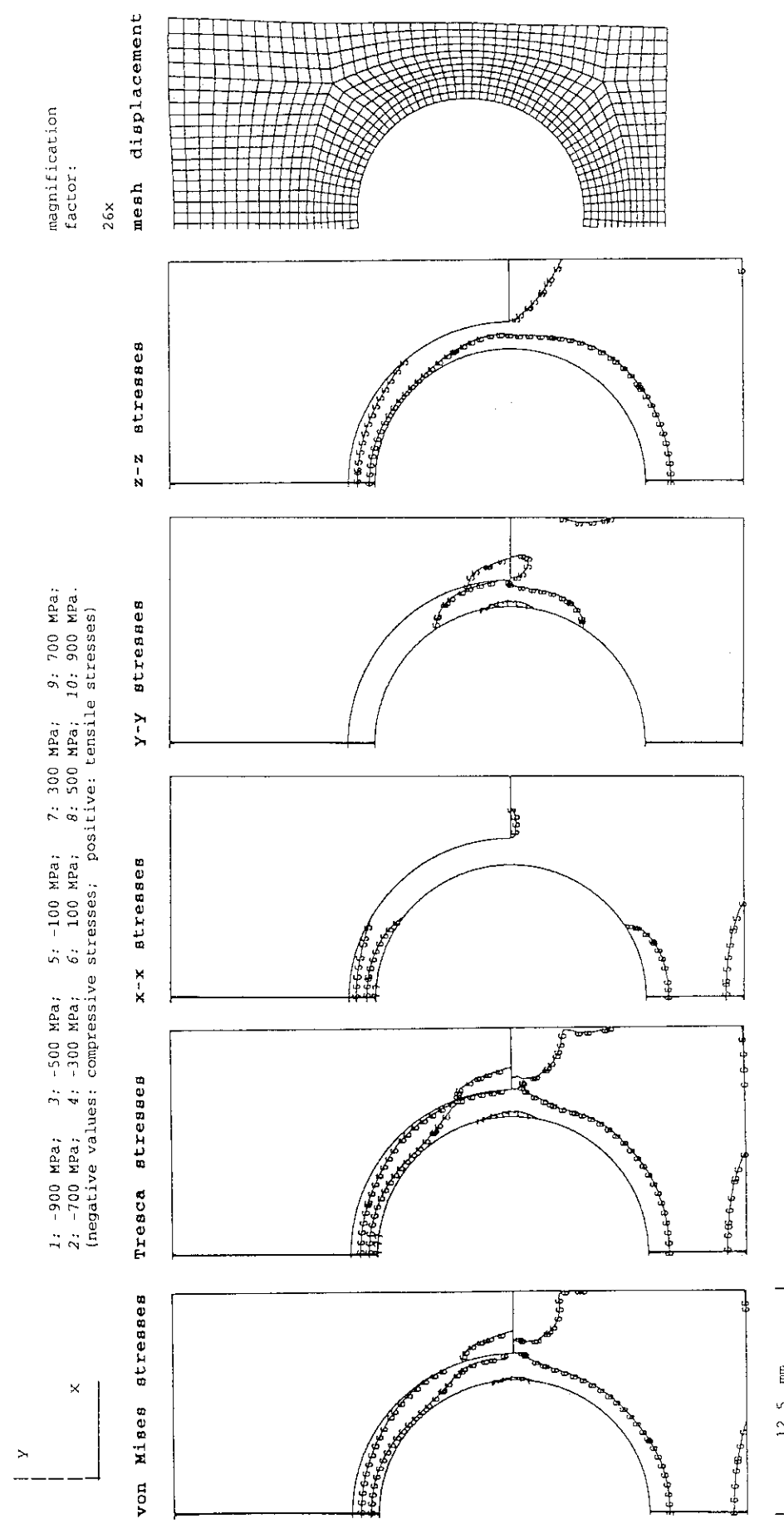


Fig. 7.2.2.e/II Saddle Type, Armor: MFC-1 (1992), Heat Sink: TZM

thermal response to a uniform
surface heat flux of 15 MW/m²

residual stresses at RT after an assumed brazing cycle, with braze solidification at 750°C

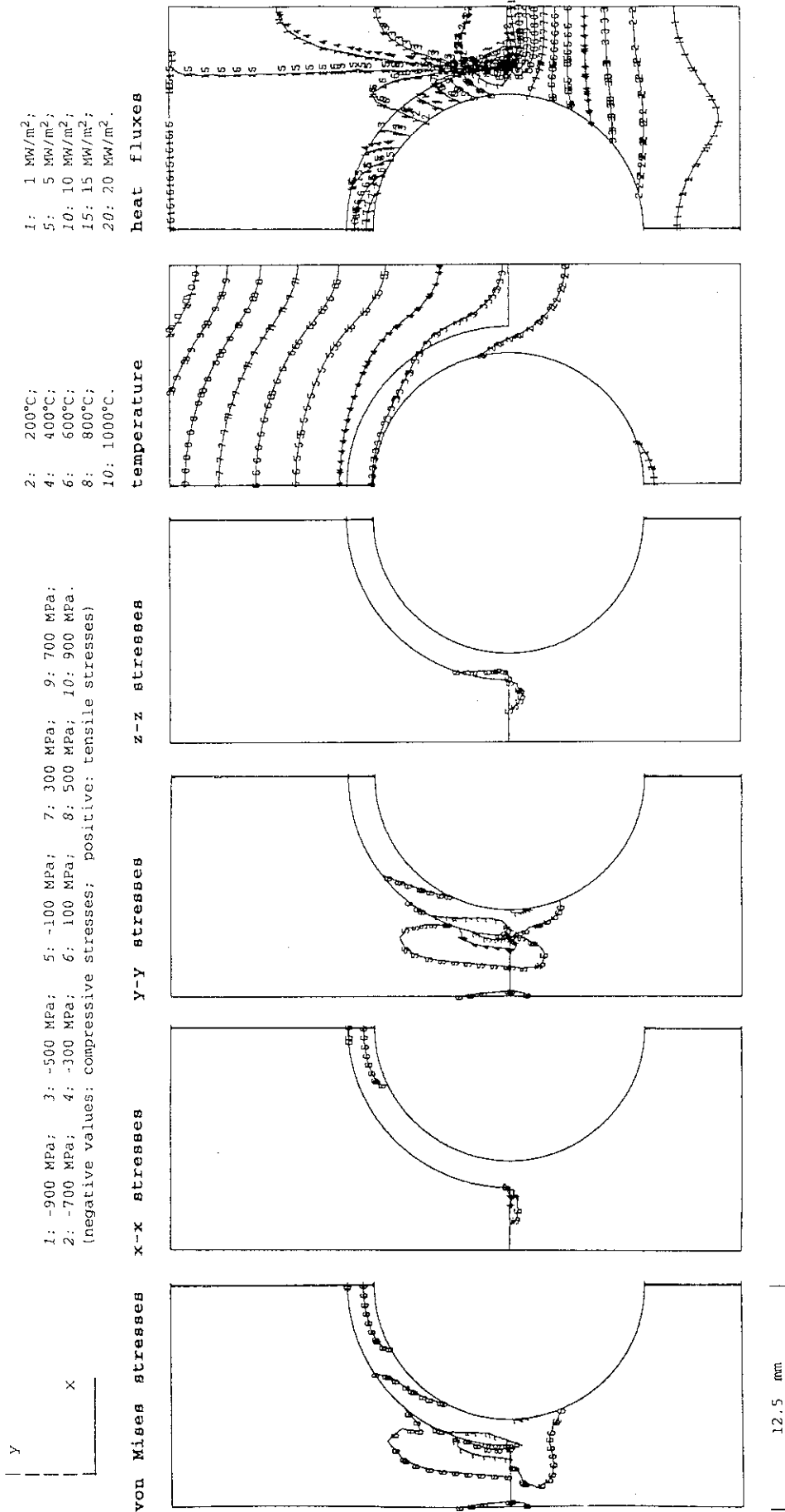


Fig. 7.2.2.f/I Saddle Type, Armor: MFC-1 (1992), Heat Sink: W-30Cu

stress distribution and displacement at a uniform steady state heat flux of 15 MW/m²

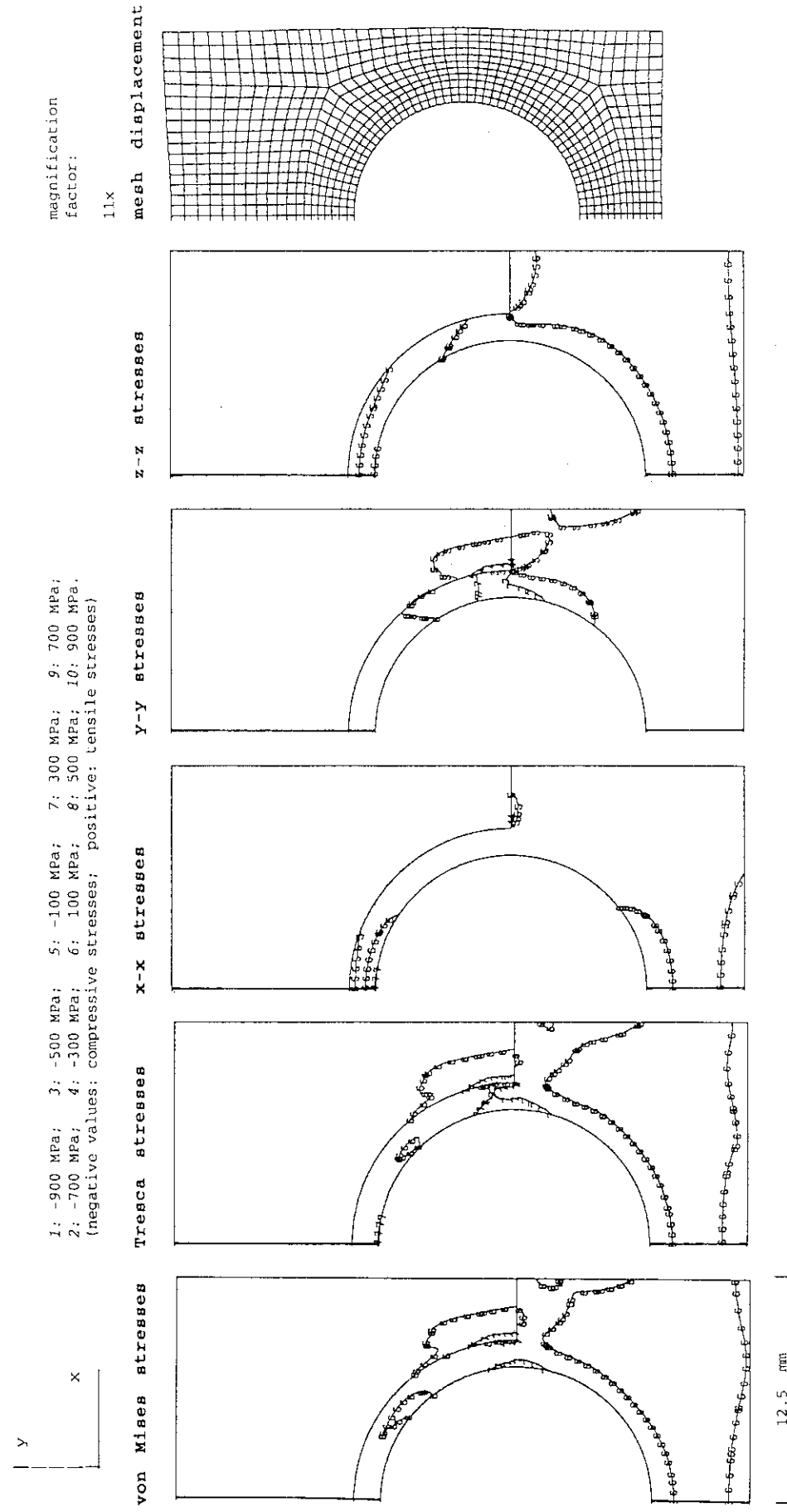


Fig. 7.2.2.f/II Saddle Type, Armor: MFC-1 (1992), Heat Sink: W-30Cu

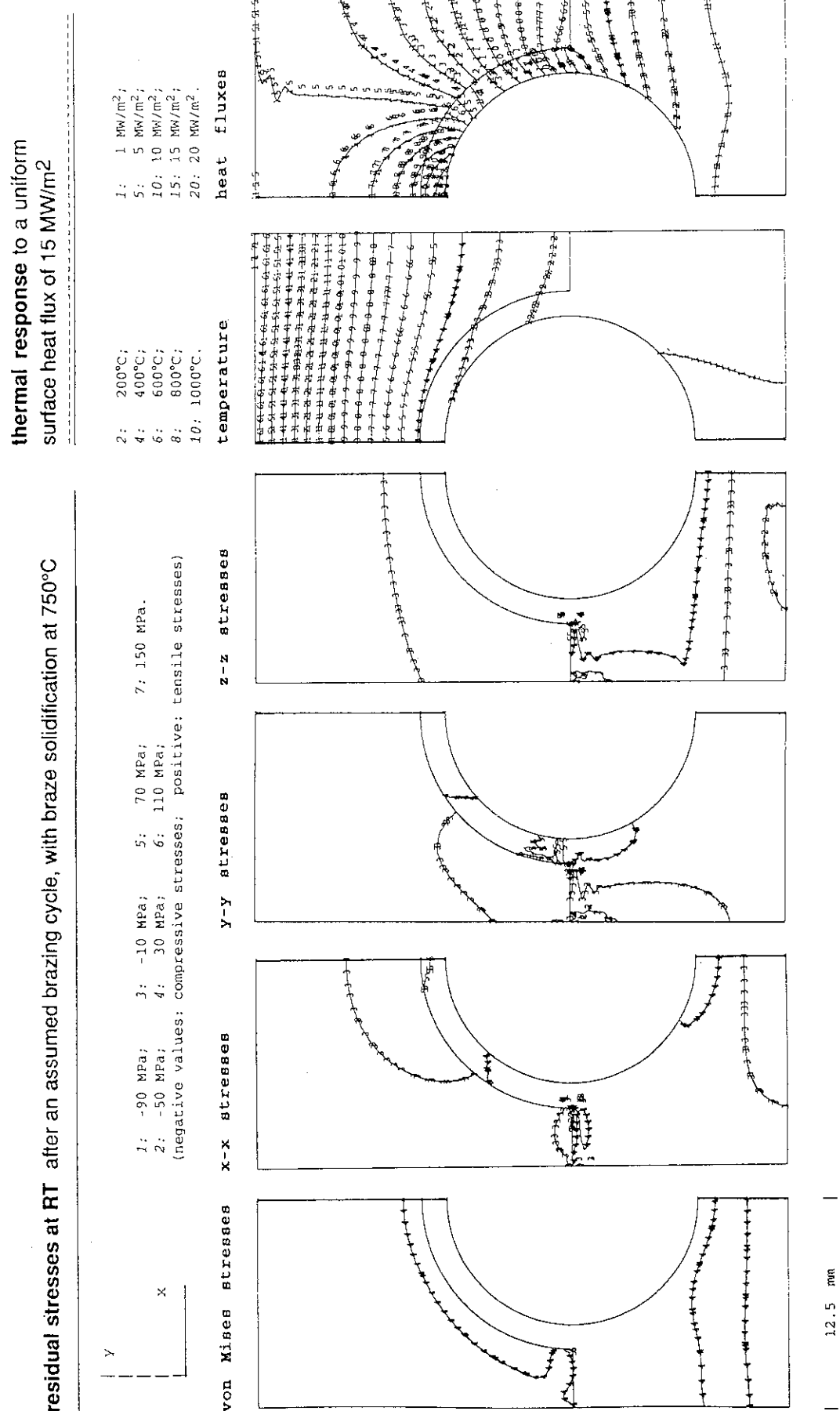


Fig. 7.2.2.g/I Saddle Type, Armor: CX2002U, Heat Sink: OF-Cu

stress distribution and displacement at a uniform steady state surface heat flux of 15 MW/m²

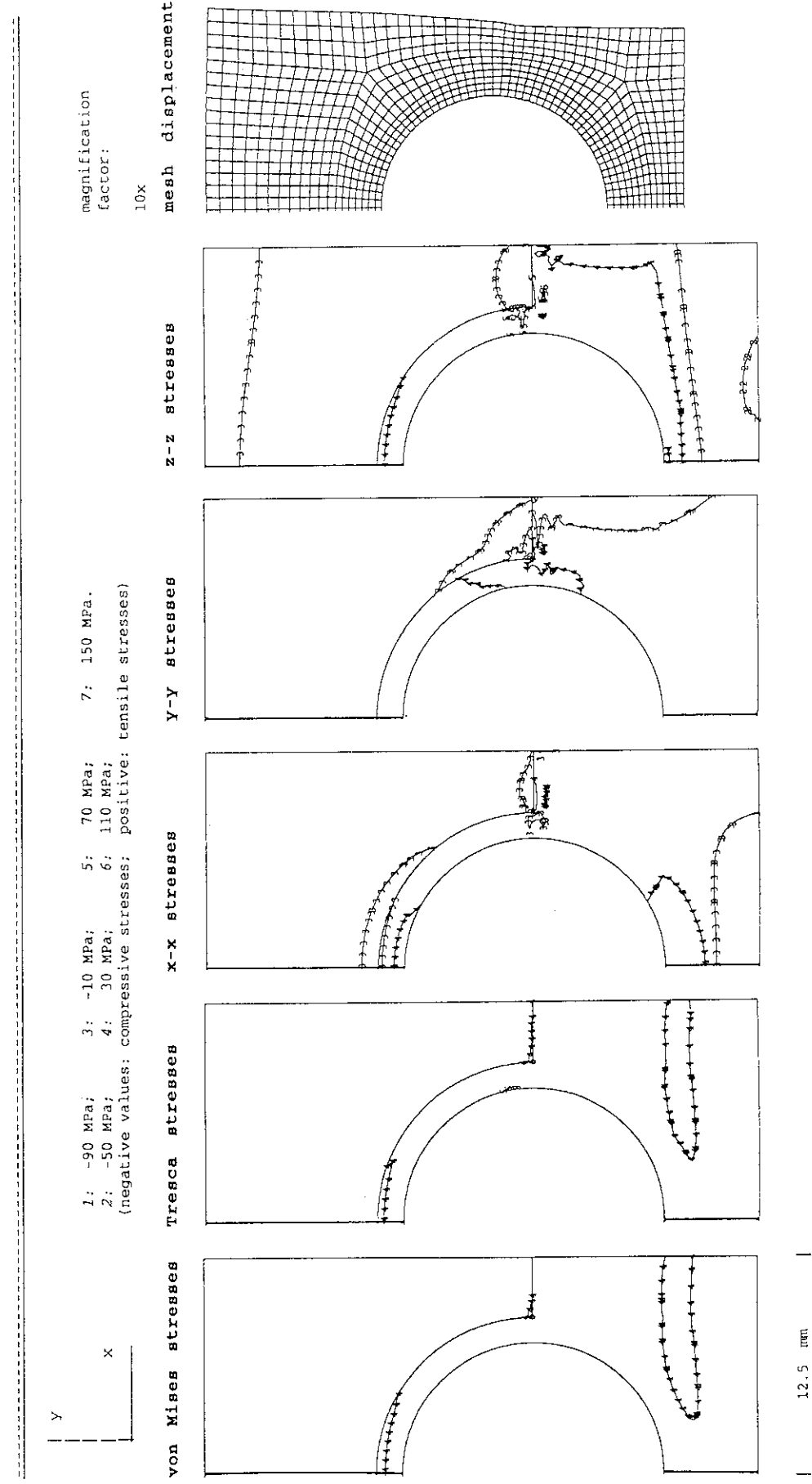
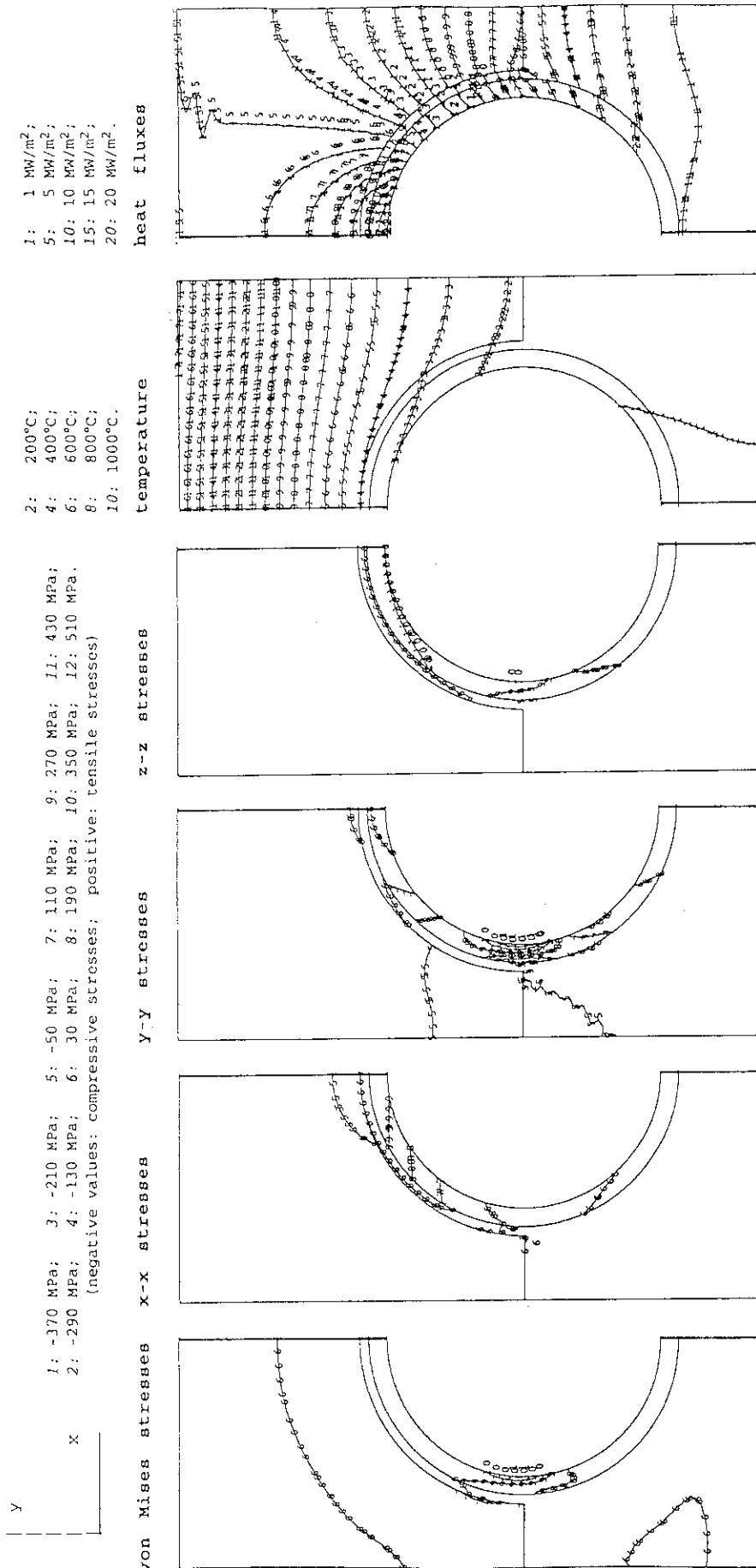


Fig. 7.2.2.g/II Saddle Type, Armor: CX2002U, Heat Sink: OF-Cu

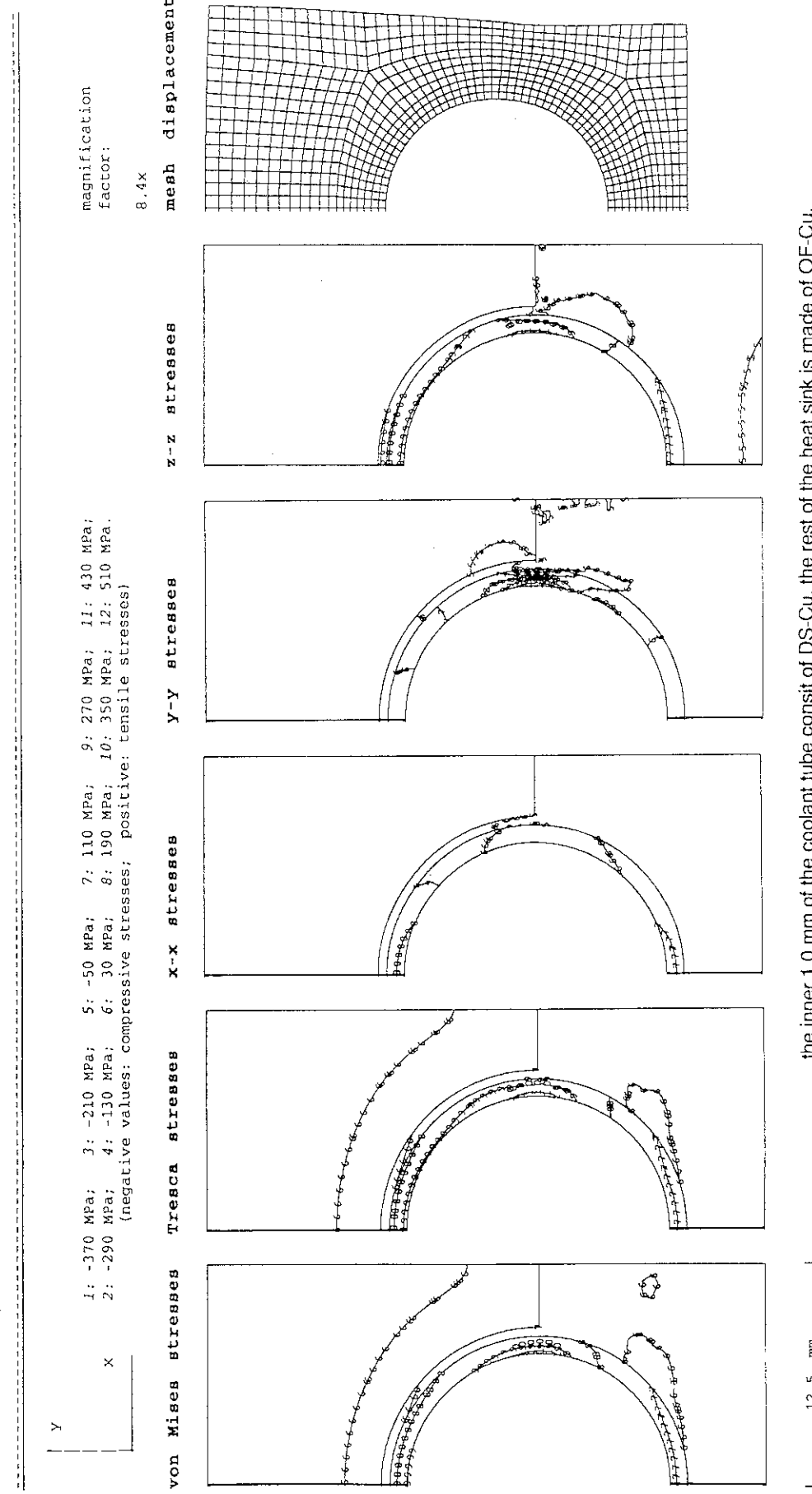
residual stresses at RT after an assumed brazing cycle, with braze solidification at 750°C
thermal response to a uniform surface heat flux of 15 MW/m²



the inner 1.0 mm of the coolant tube consist of DS-Cu, the rest of the heat sink is made of OF-Cu.

Fig. 7.2.2.h/I Saddle Type, Armor: CX2002U, Heat Sink: OF&DS-Cu

stress distribution and displacement at a uniform steady state surface heat flux of 15 MW/m²

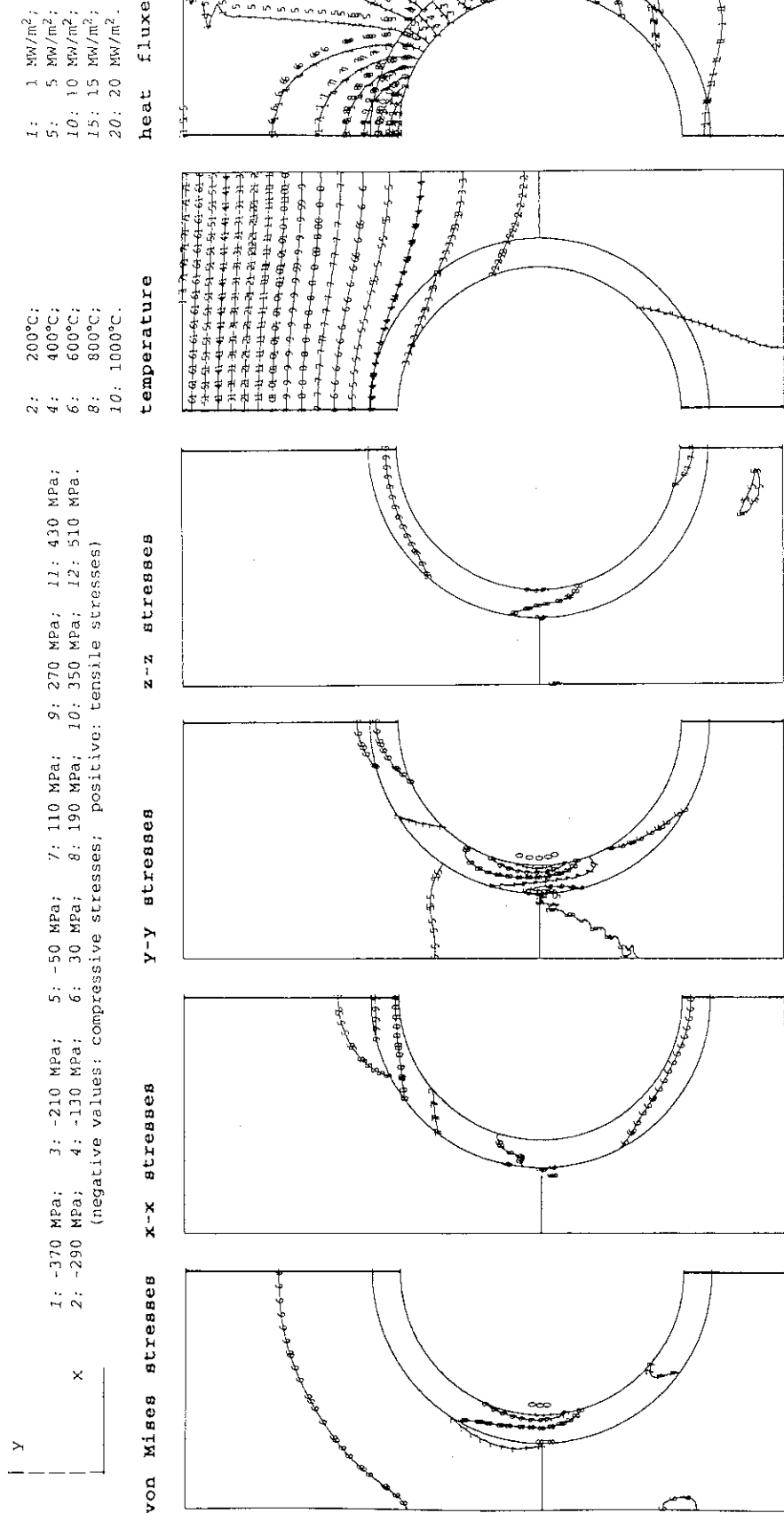


the inner 1.0 mm of the coolant tube consist of DS-Cu, the rest of the heat sink is made of OF-Cu.

Fig. 7.2.2.h/II Saddle Type, Armor: CX2002U, Heat Sink: OF&DS-Cu

residual stresses at RT after an assumed brazing cycle, with braze solidification at 750°C

thermal response to a uniform surface heat flux of 15 MW/m²

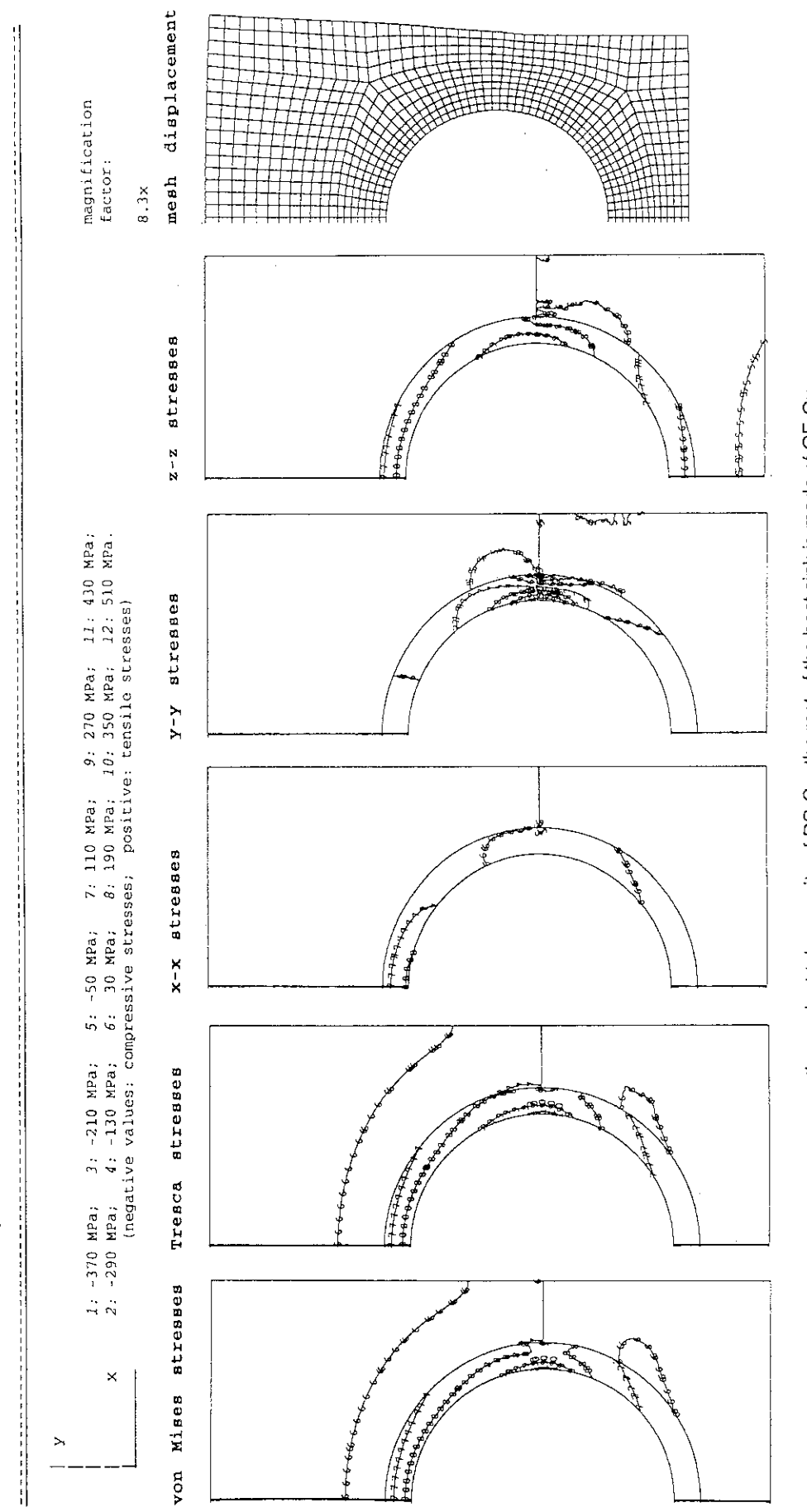


12.5 mm

the coolant tube consists of DS-Cu, the rest of the heat sink is made of OF&DS-Cu.

Fig. 7.2.2.i/I Saddle Type, Armor: CX2002U, Heat Sink: OF&DS-Cu

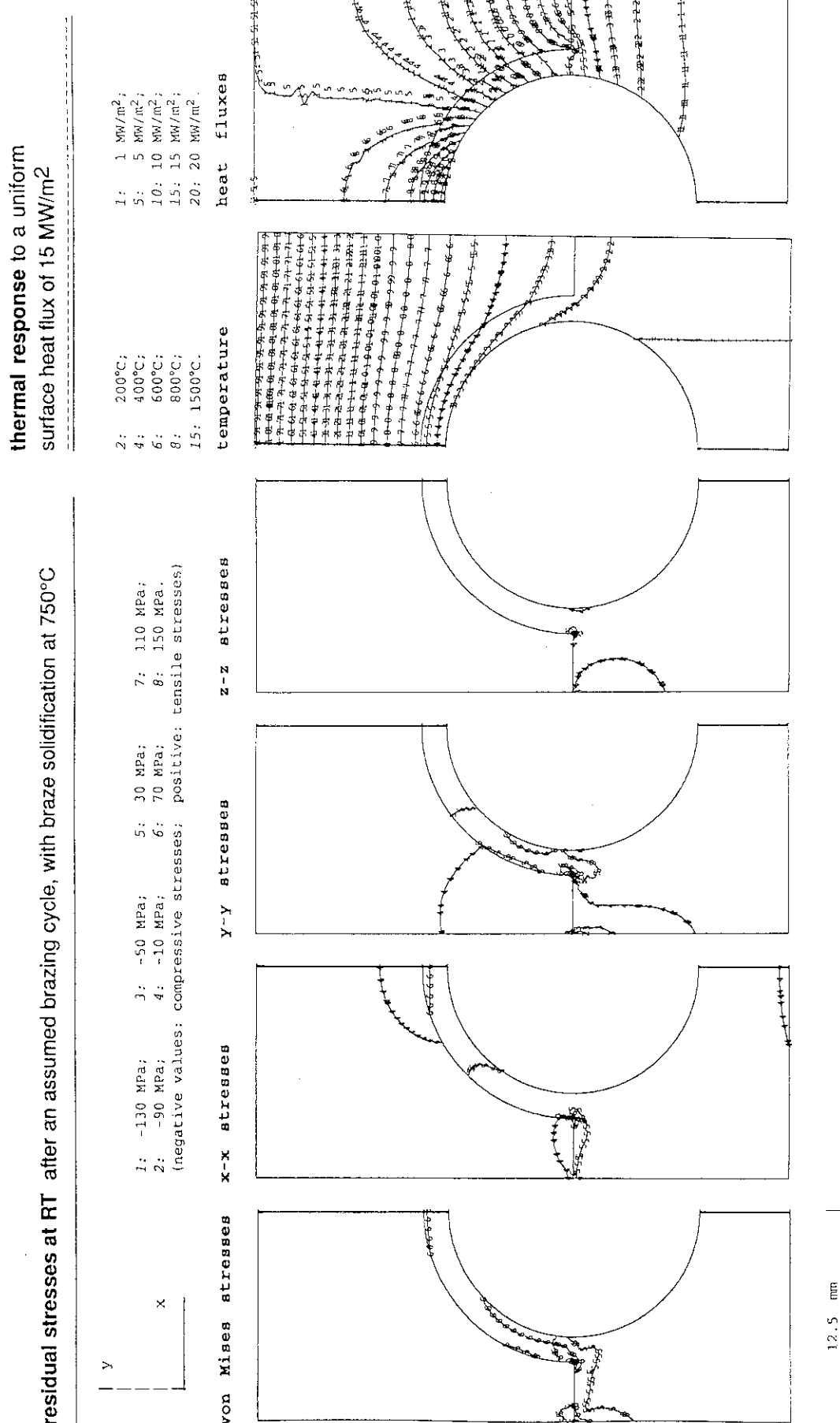
stress distribution and displacement at a uniform steady state surface heat flux of 15 MW/m²



12.5 mm

the coolant tube consists of DS-Cu, the rest of the heat sink is made of OF-Cu.

Fig. 7.2.2.i/II Saddle Type, Armor: CX2002U, Heat Sink: OF&DS-Cu

Fig. 7.2.2.j/I Saddle Type, Armor: CX2002U, Heat Sink: TZM

stress distribution and displacement at a uniform steady state surface heat flux of 15 MW/m²

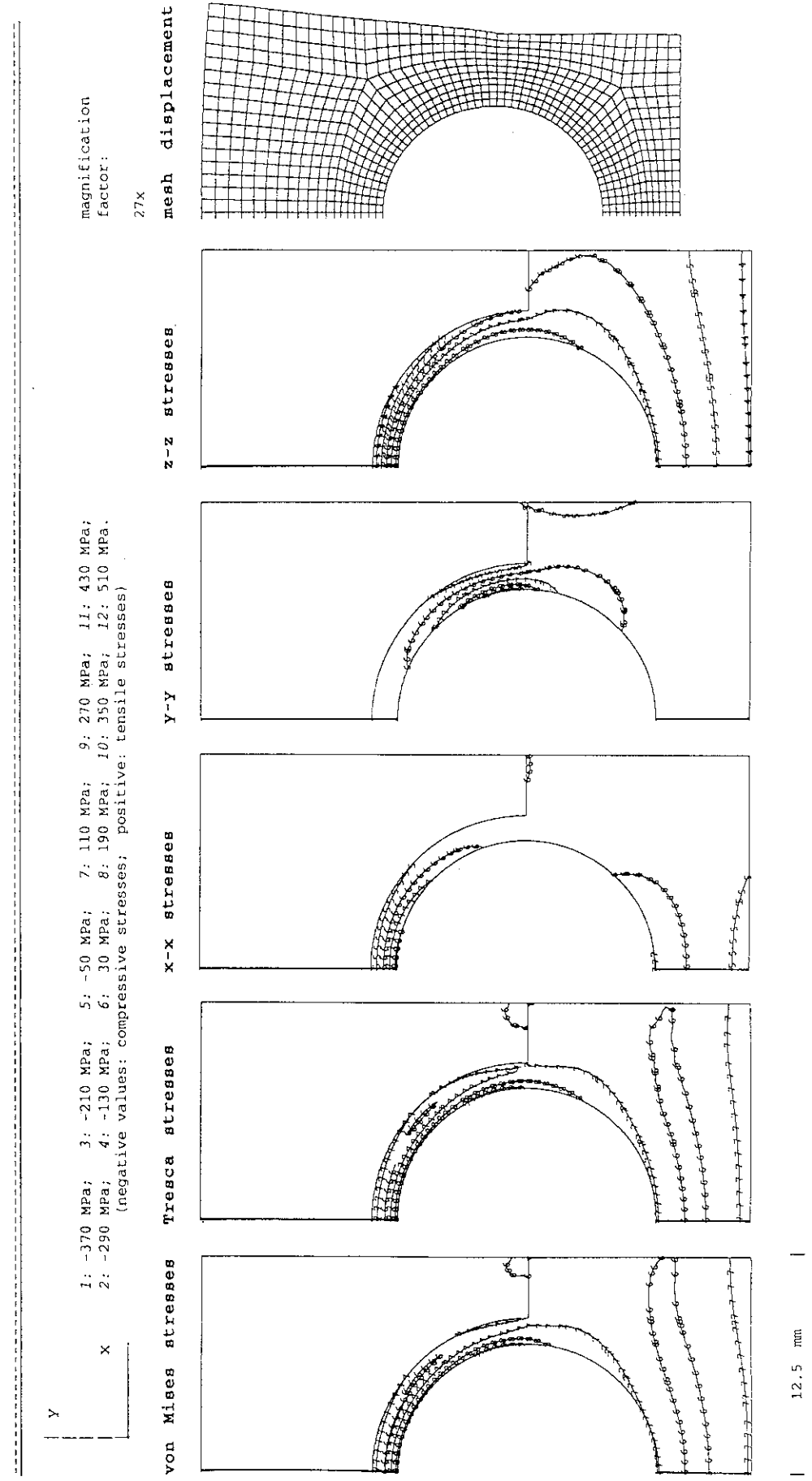
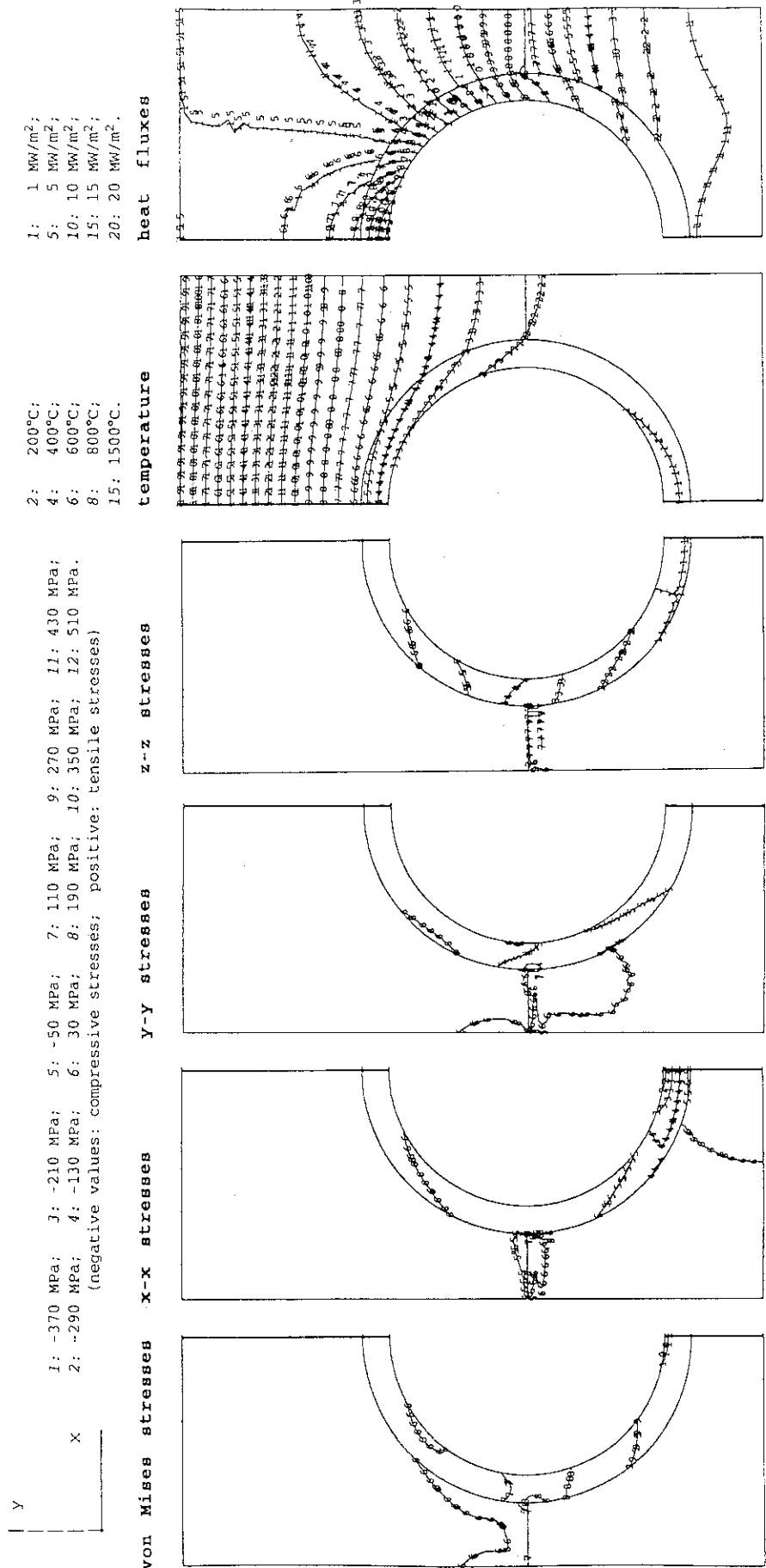


Fig. 7.2.2-j / II Saddle Type, Armor: CX2002U, Heat Sink: TZM

thermal response to a uniform surface heat flux of 15 MW/m²

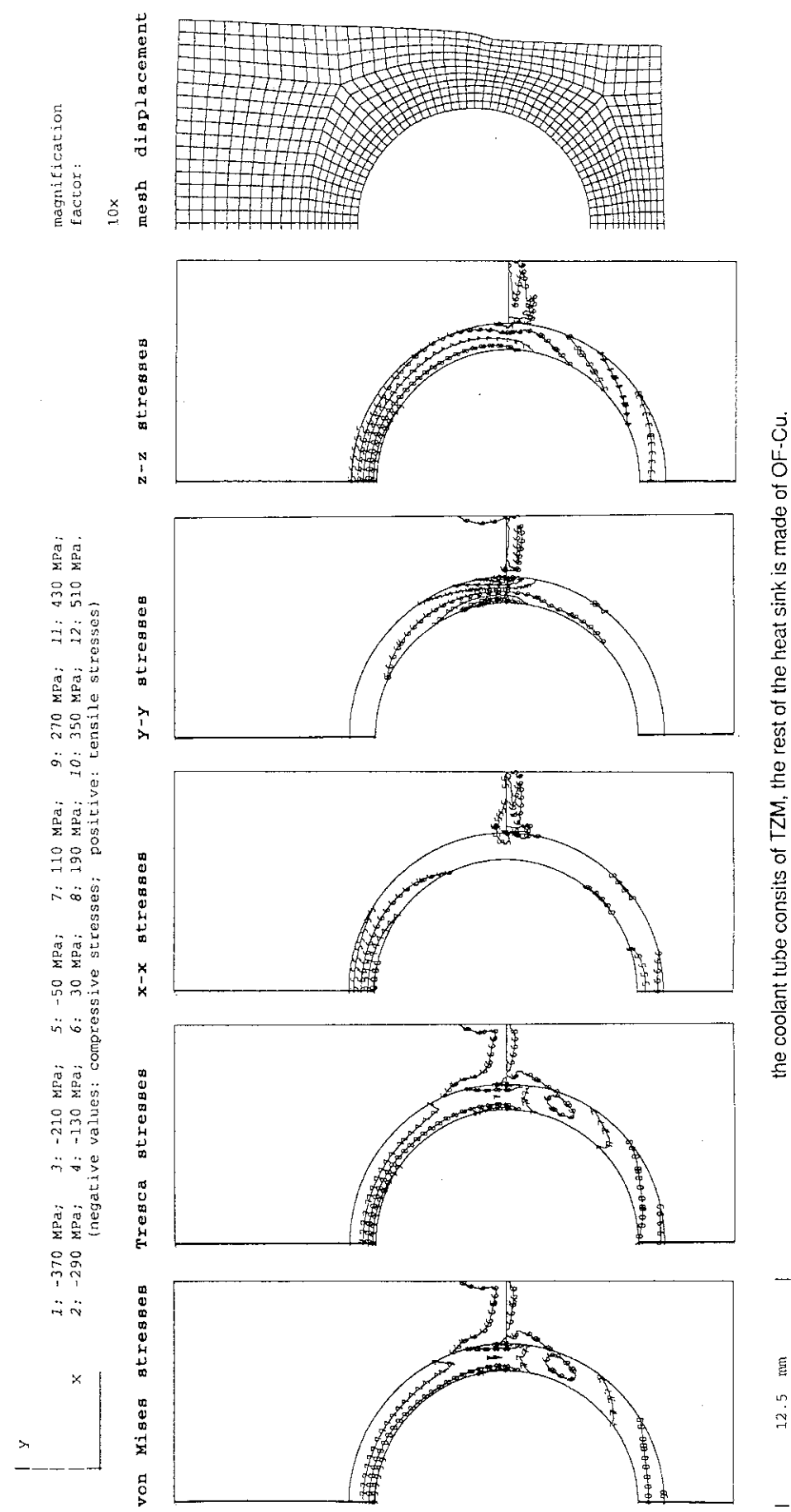
residual stresses at RT after an assumed brazing cycle, with braze solidification at 750°C



the coolant tube consists of TZM, the rest of the heat sink is made of OF-Cu.

Fig. 7.2.2.k/I Saddle Type, Armor: CX2002U, Heat Sink: OF-Cu&TZM

stress distribution and displacement at a uniform steady state heat flux of 15 MW/m²



the coolant tube consists of TZM, the rest of the heat sink is made of OF-Cu.

Fig. 7.2.2.k/II Saddle Type, Armor: CX2002U, Heat Sink: OF-Cu&TZM

thermal response to a uniform surface heat flux of 15 MW/m²

residual stresses at RT after an assumed brazing cycle, with braze solidification at 750°C

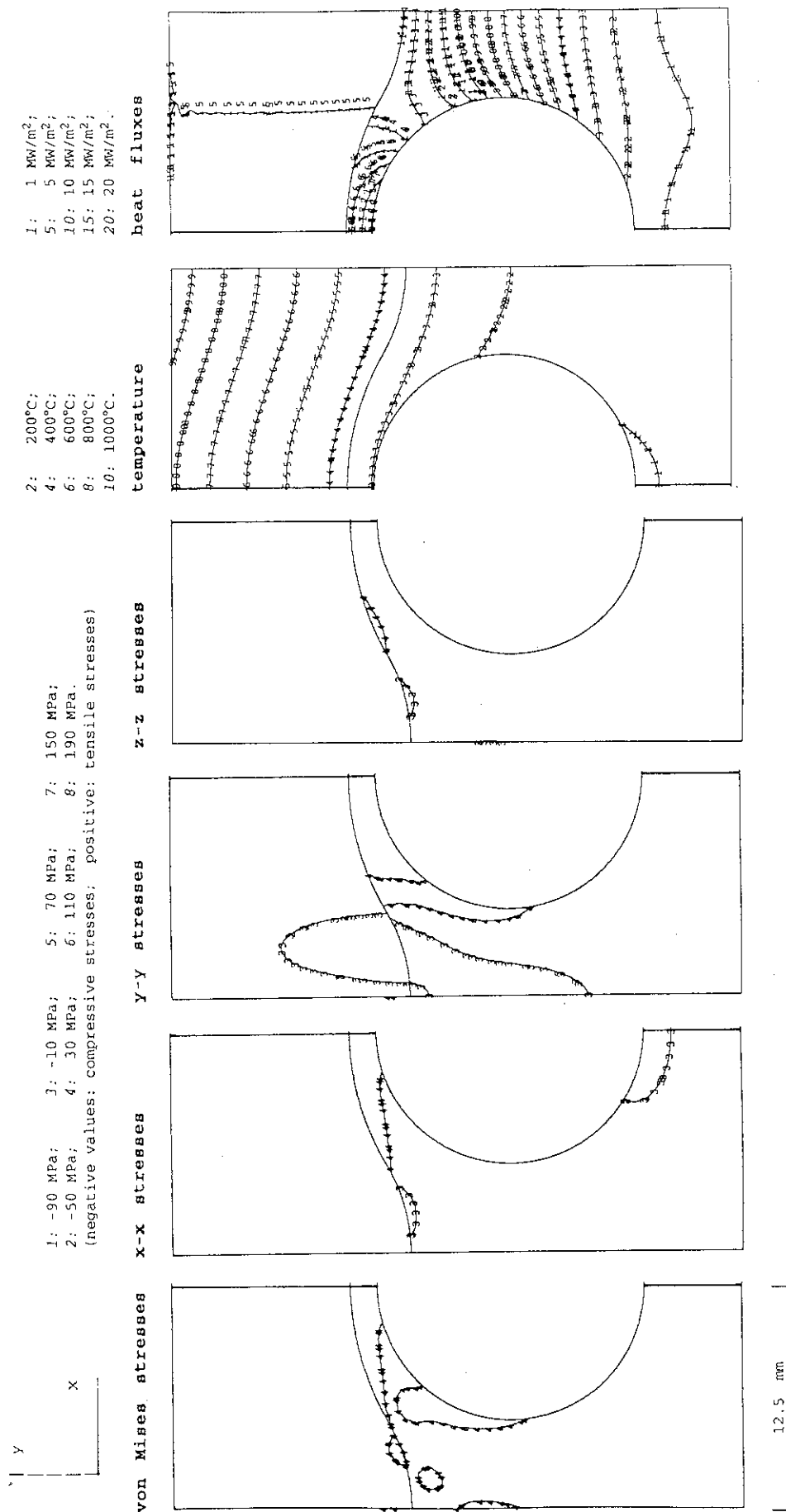


Fig. 7.2.3.bb-a/I Bent-30-Bent, Armor: MFC-1 (1992), Heat Sink: OF-Cu

stress distribution and displacement at a uniform steady state surface heat flux of 15 MW/m²

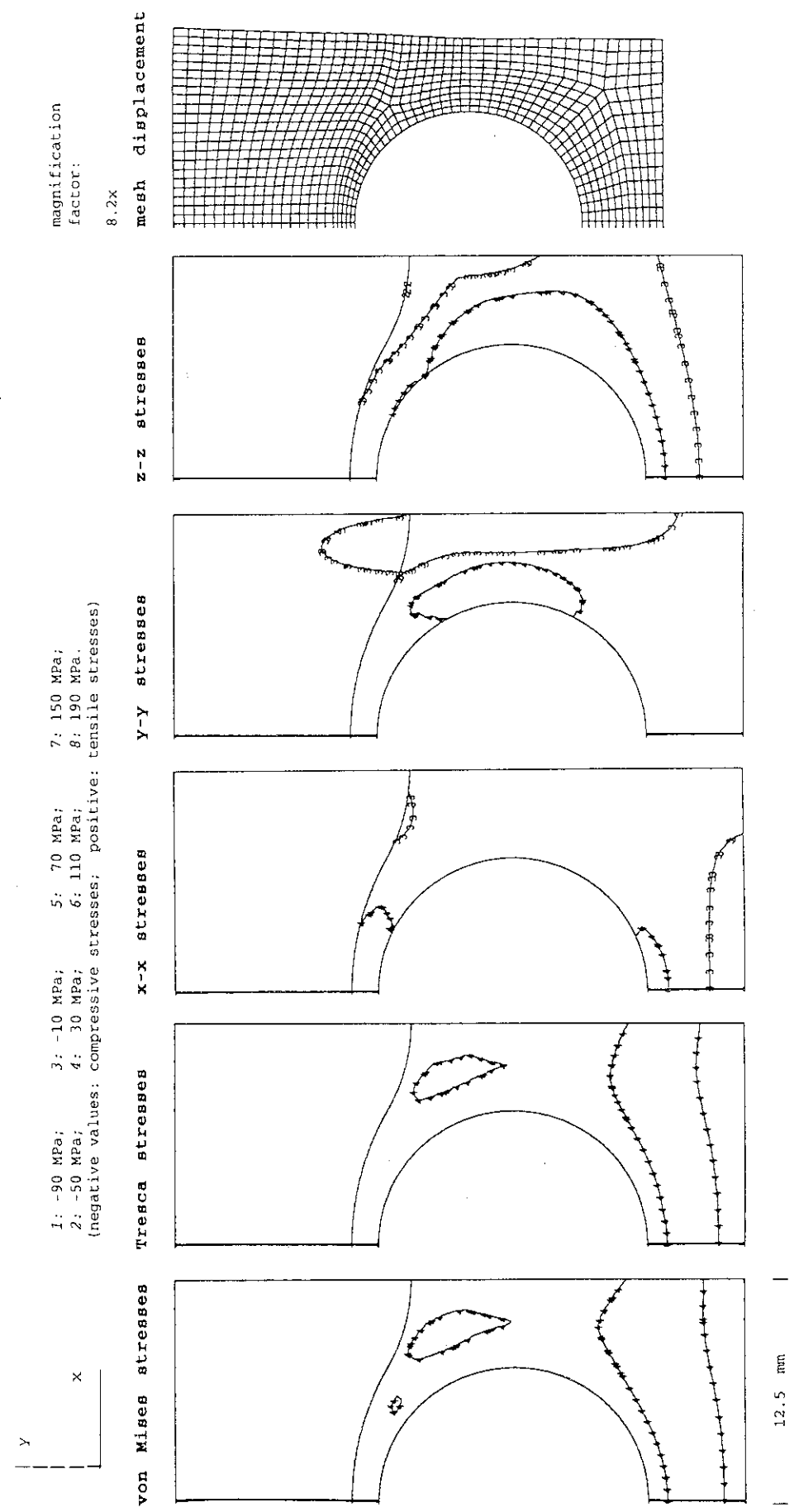


Fig. 7.2.3.bb-a/II Bent-30-Bent, Armor: MFC-1 (1992), Heat Sink: OF-Cu

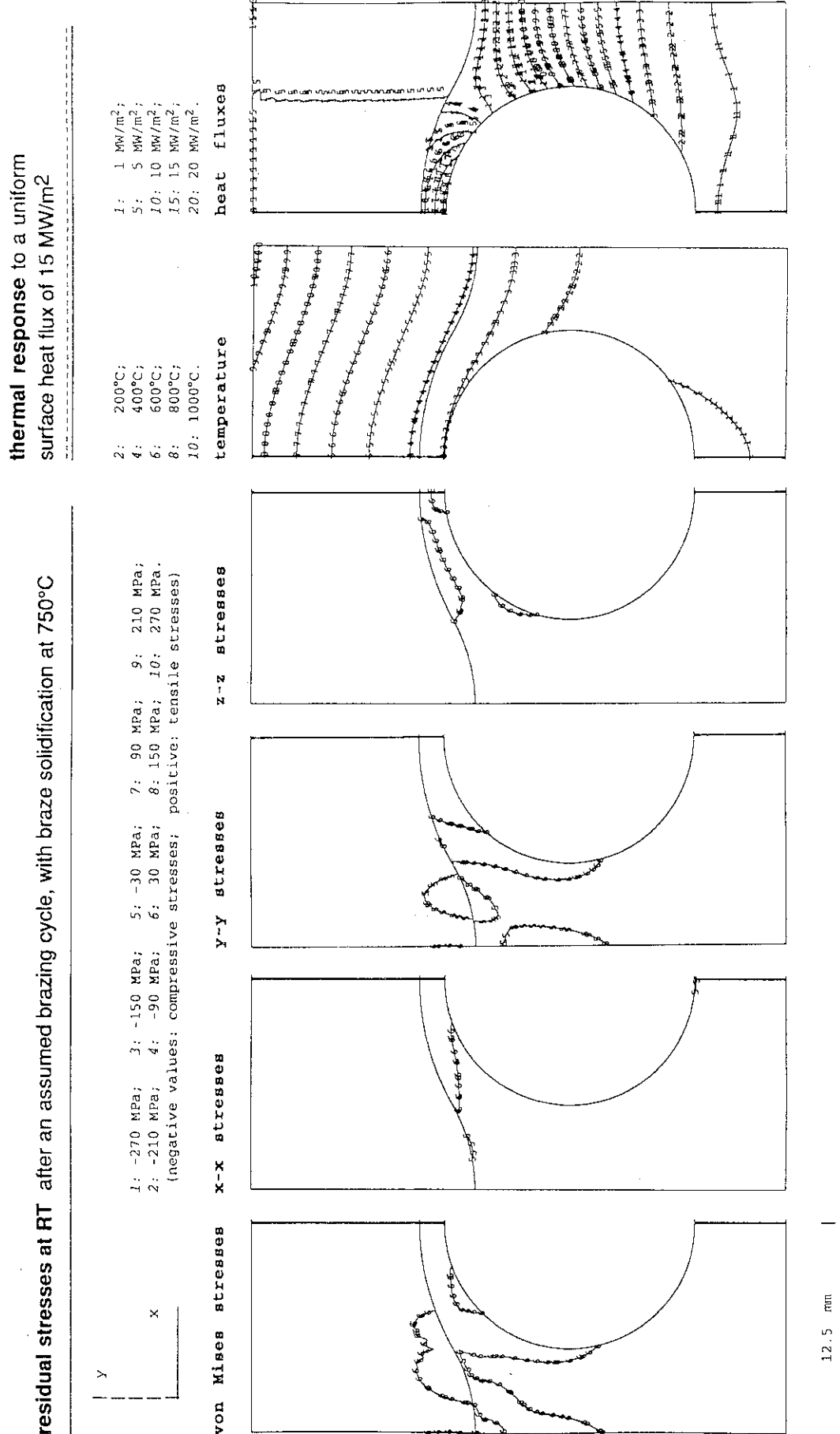


Fig. 7.2.3.bb-b1 Bent-30-Bent, Armor: MFC-1 (1992), Heat Sink: DS-Cu

stress distribution and displacement at a uniform steady state surface heat flux of 15 MW/m²

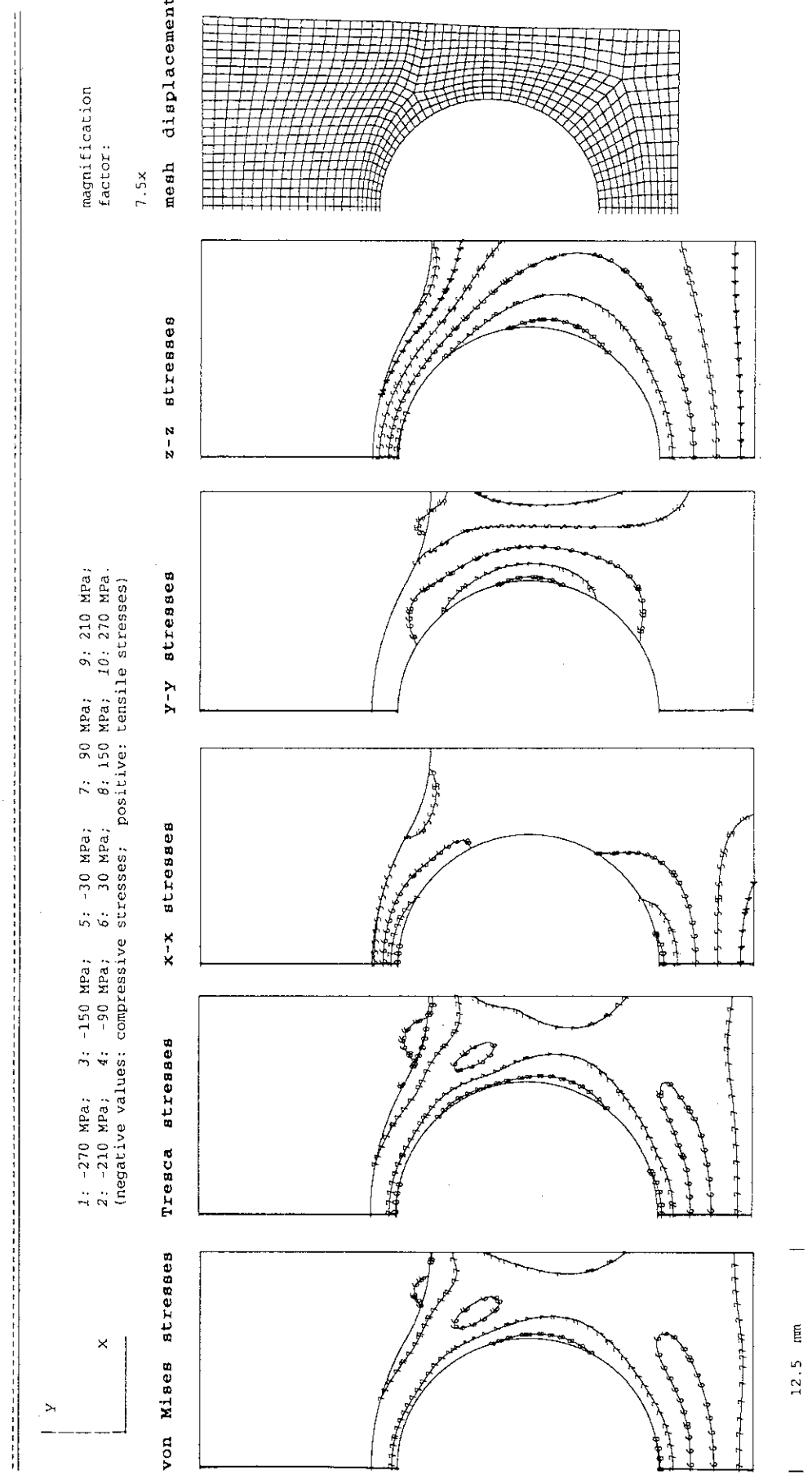


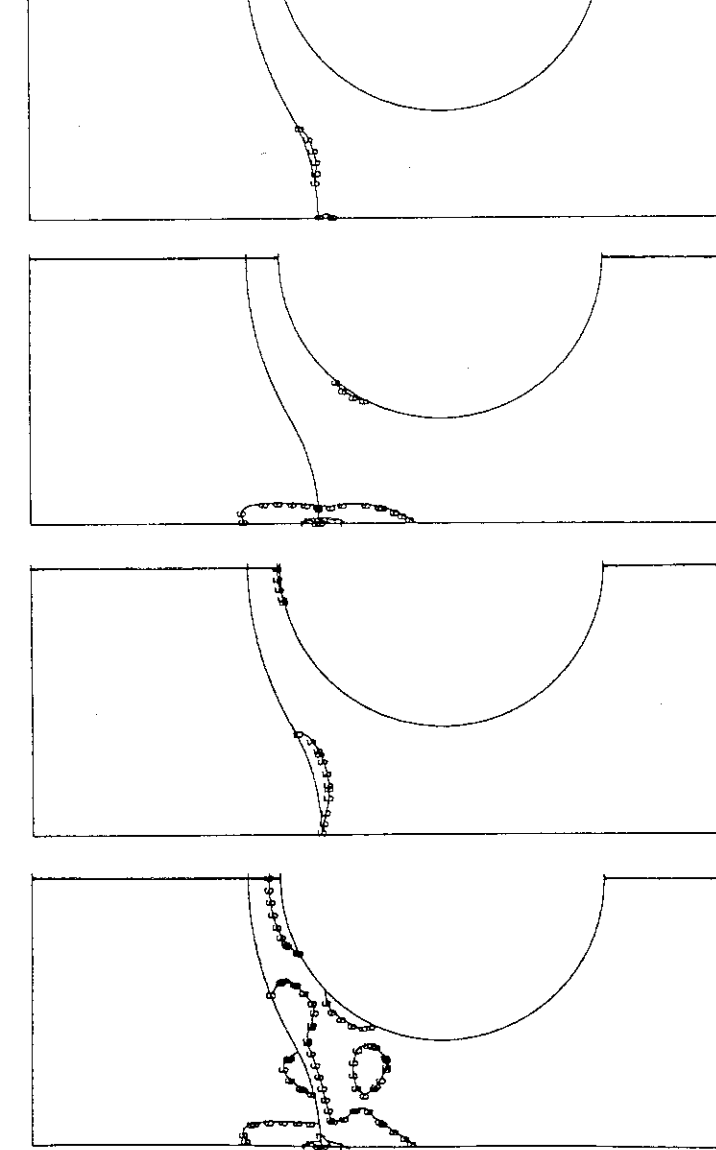
Fig. 7.2.3.bb-b/II Bent-30-Bent, Armor: MFC-1 (1992), Heat Sink: DS-Cu

residual stresses at RT after an assumed brazing cycle, with braze solidification at 750°C

thermal response to a uniform
surface heat flux of 15 MW/m²

Y
x
1: -370 MPa; 3: -210 MPa; 5: -50 MPa; 7: 110 MPa; 9: 270 MPa;
2: -290 MPa; 4: -130 MPa; 6: -30 MPa; 8: 190 MPa; 10: 350 MPa.
(negative values: compressive stresses; positive: tensile stresses)

von Mises stresses



12.5 mm

Y
x
1: 200°C; 2: 400°C; 4: 600°C; 6: 800°C; 8: 1000°C.
5: 1 MW/m²; 5: 5 MW/m²; 10: 10 MW/m²; 15: 15 MW/m²; 20: 20 MW/m².

heat fluxes

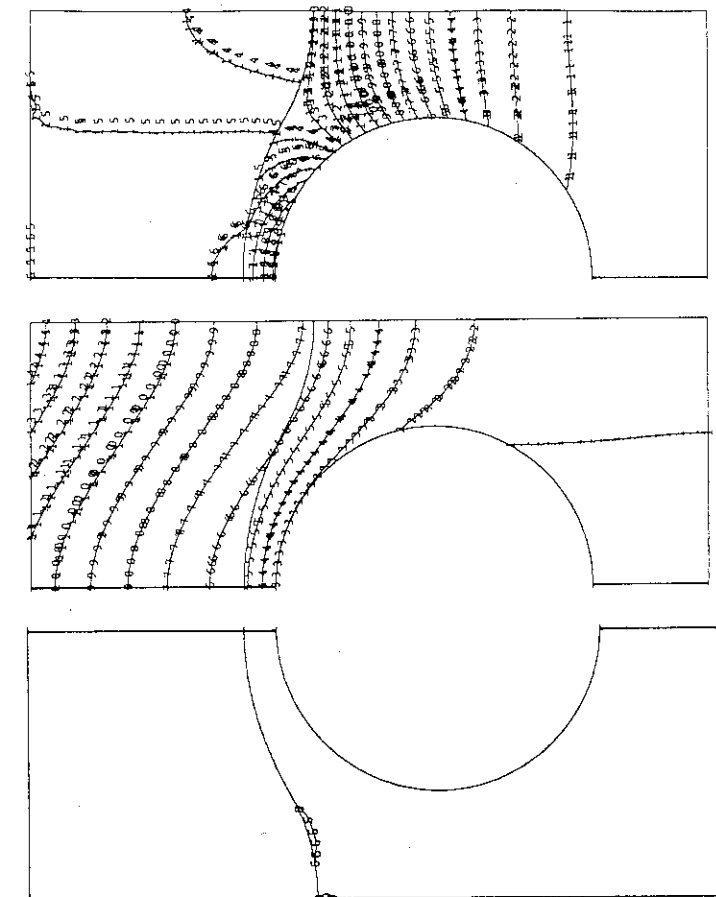


Fig. 7.2.3.bb-c/I Bent-30-Bent, Armor: MFC-1 (1992), Heat Sink: TZM

stress distribution and displacement at a uniform steady state heat flux of 15 MW/m²

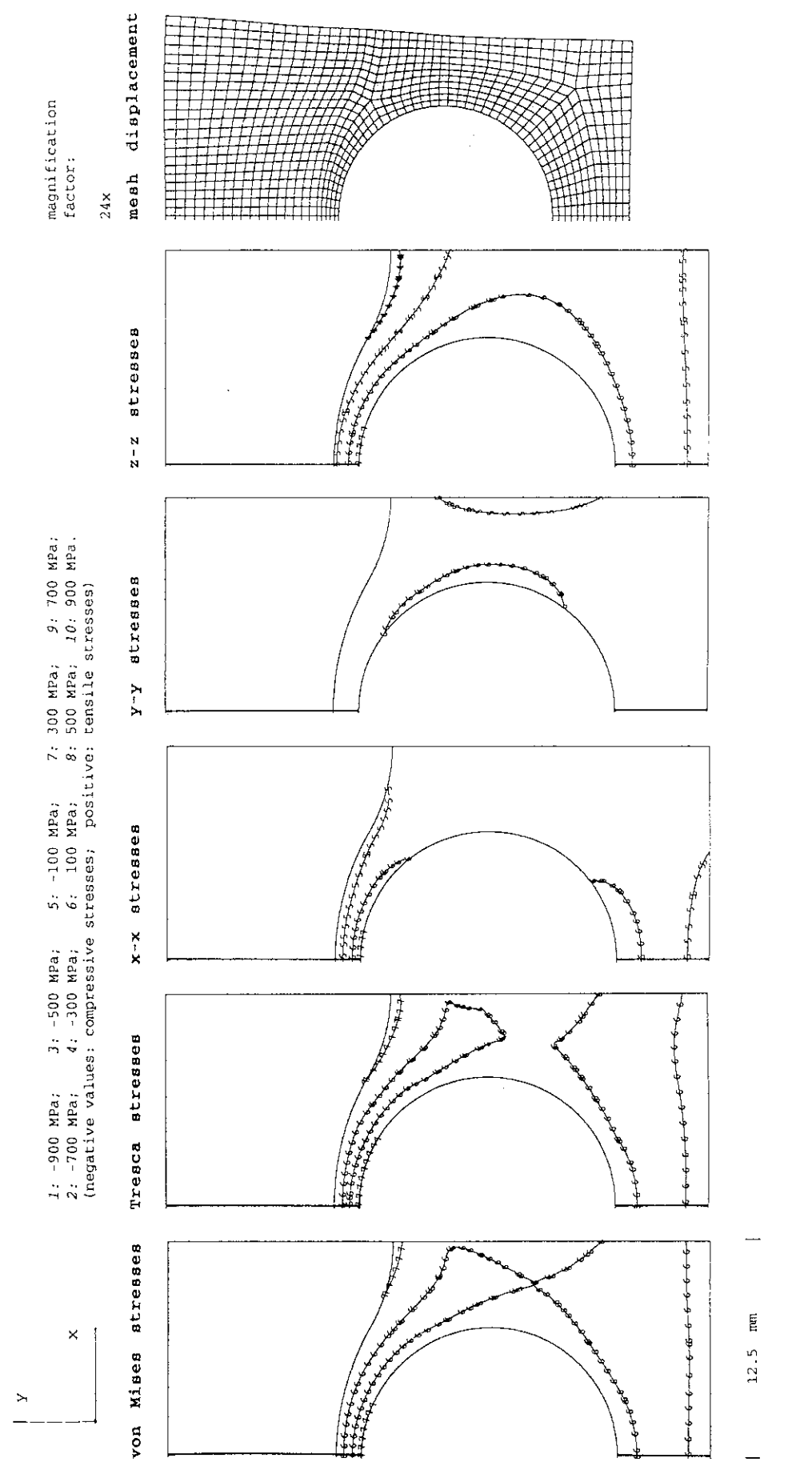


Fig. 7.2.3.bb-c/II Bent-30-Bent, Armor: MFC-1 (1992), Heat Sink: TZM

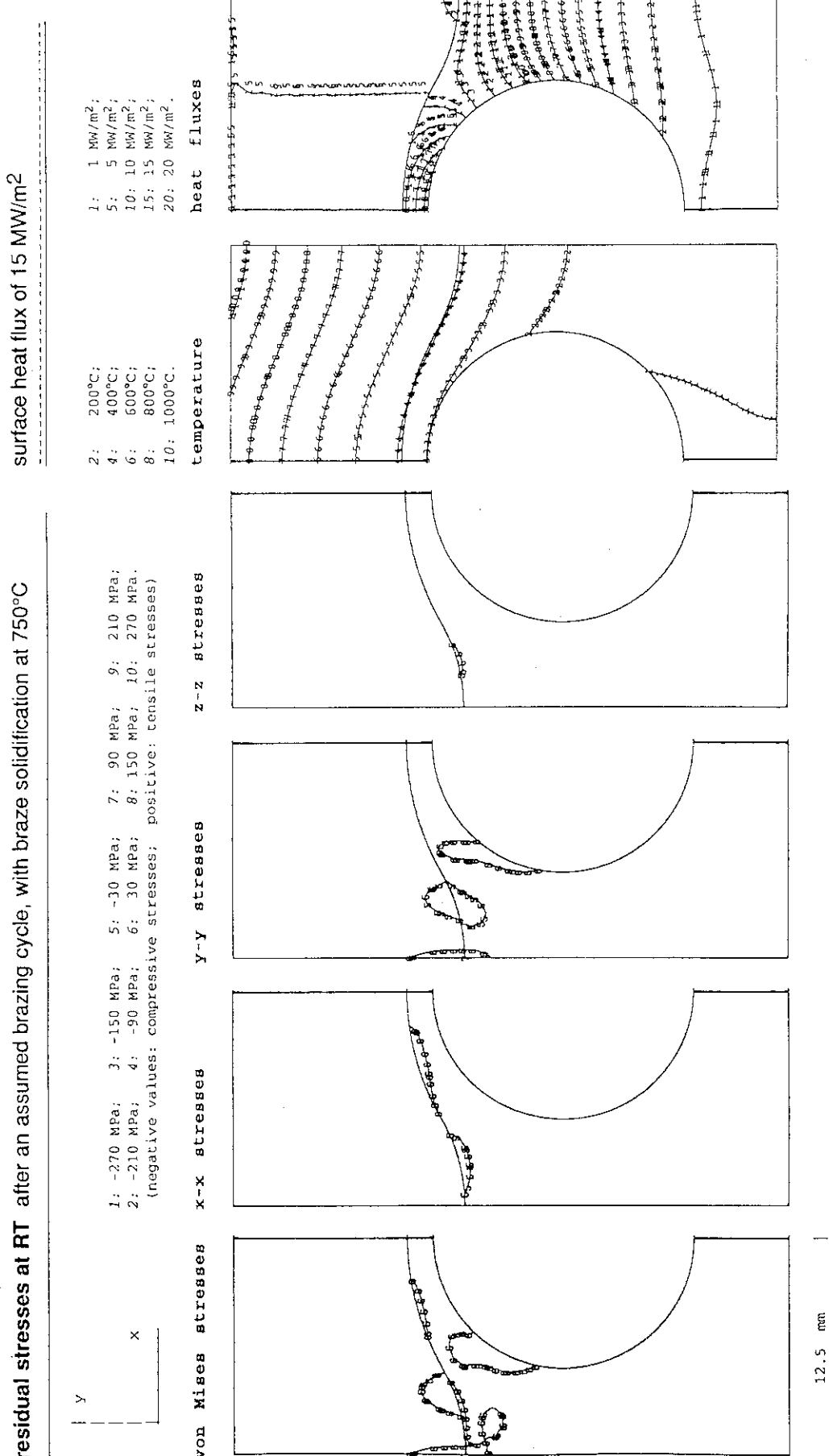


Fig. 7.2.3.bb-d/I Bent-30-Bent, Armor: MFC-1 (1992), Heat Sink: W-30Cu

stress distribution and displacement at a uniform steady state surface heat flux of 15 MW/m²

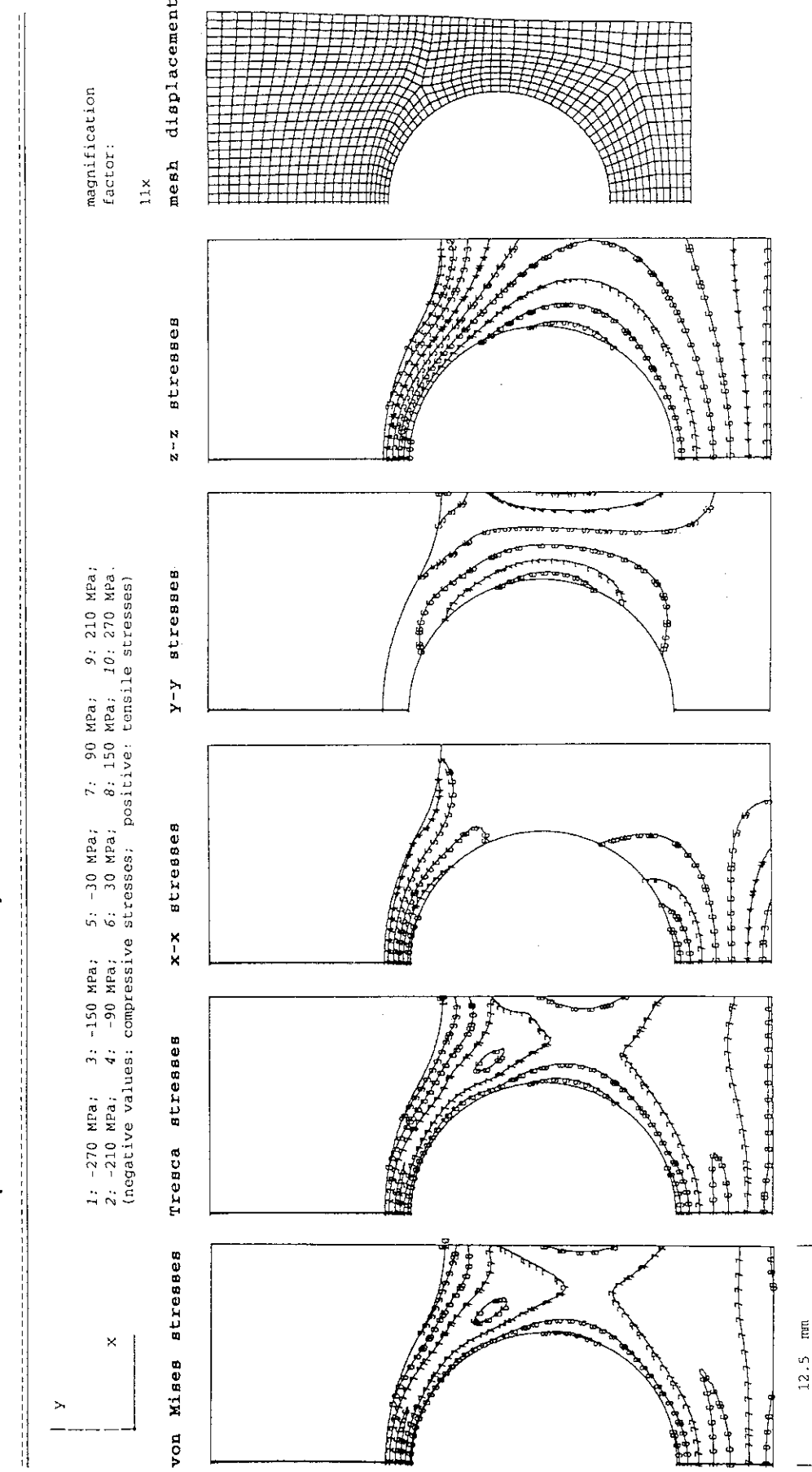


Fig. 7.2.3.bb-d/II Bent-30-Bent, Armor: MFC-1 (1992), Heat Sink: W-30Cu

residual stresses at RT after an assumed brazing cycle, with braze solidification at 750°C

thermal response to a uniform surface heat flux of 15 MW/m²

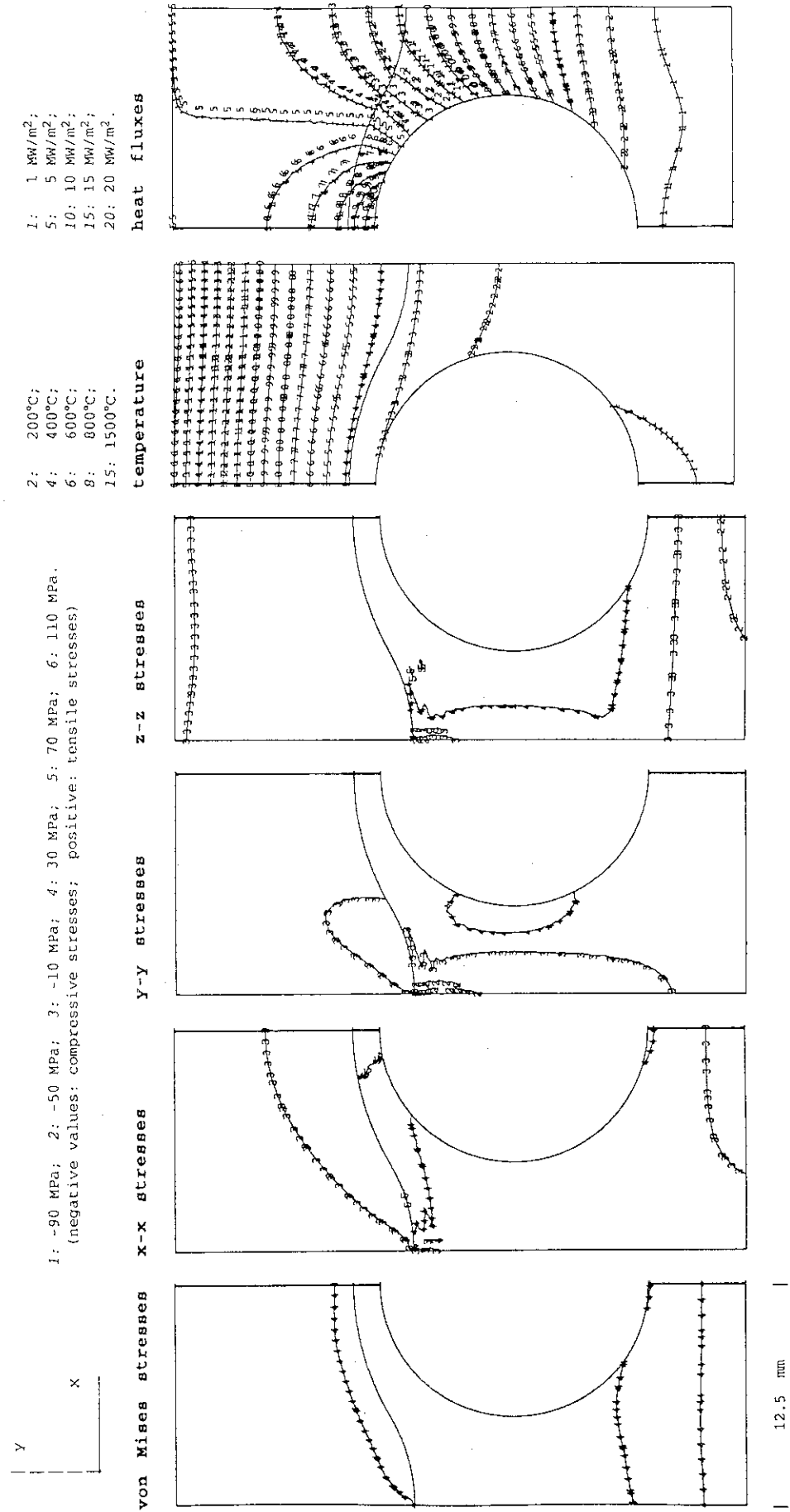


Fig. 7.2.3.bb-e/I Bent-30-Bent, Armor: CX2002U, Heat Sink: OF-Cu

stress distribution and displacement at a uniform steady state surface heat flux of 15 MW/m²

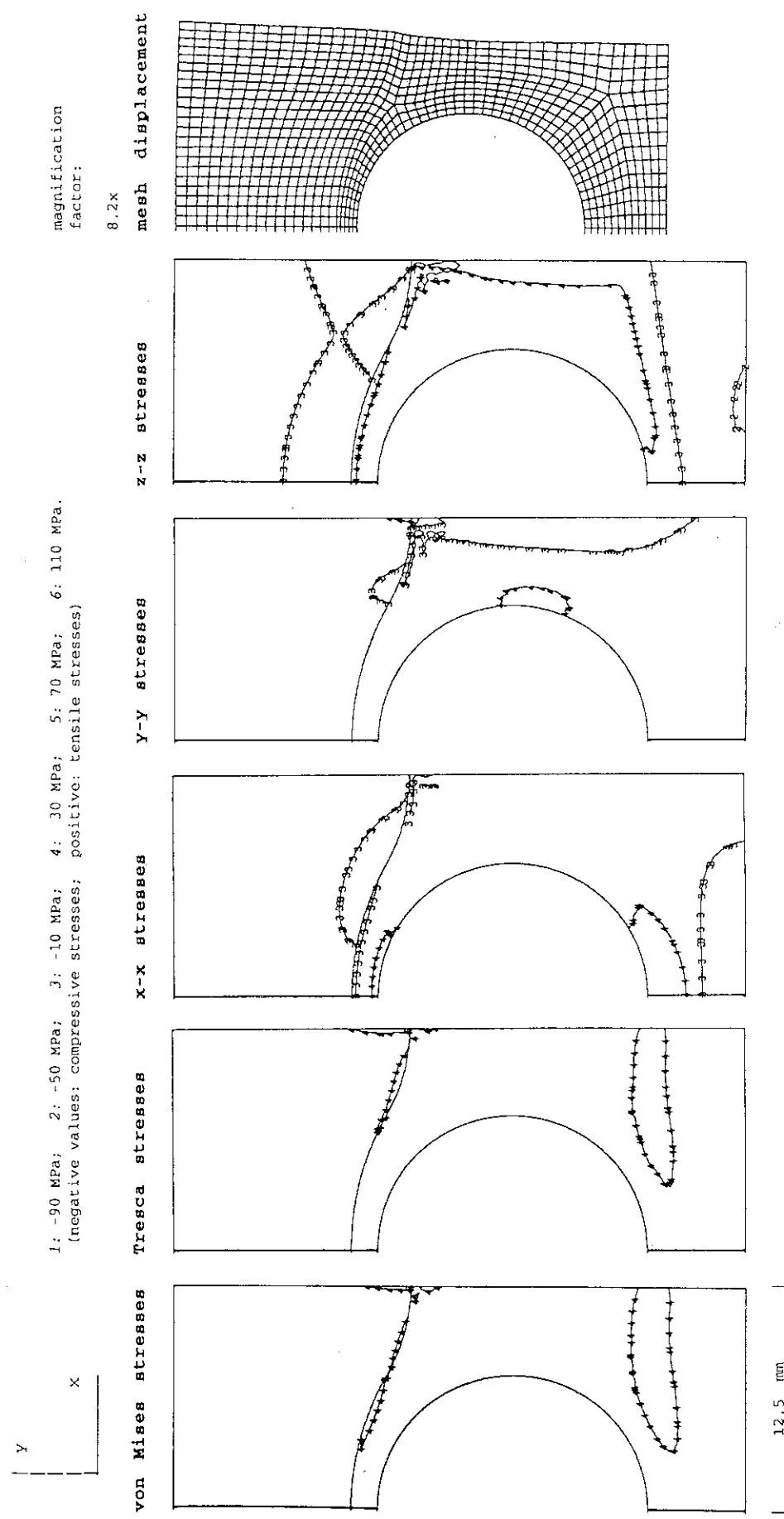
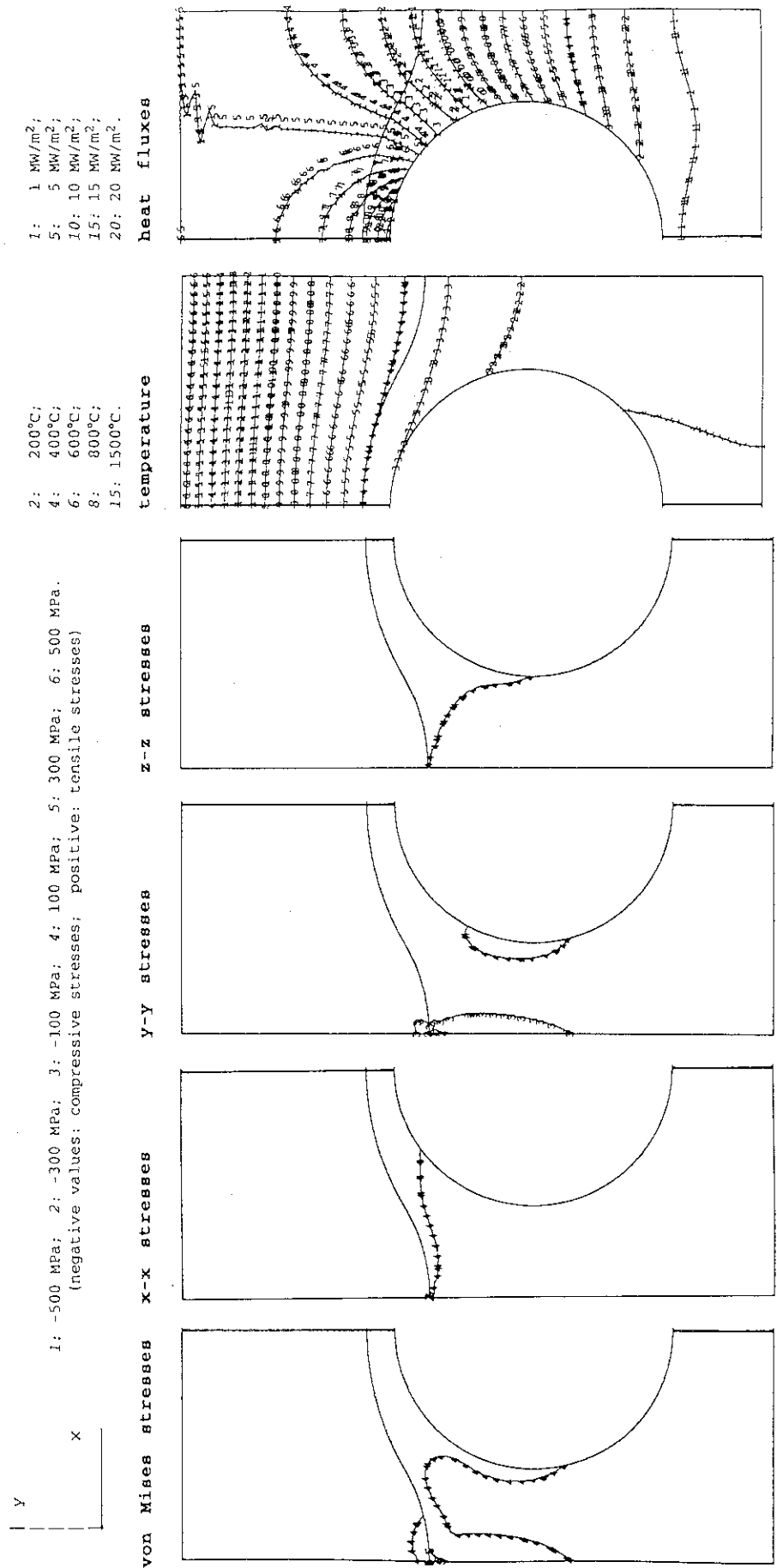


Fig. 7.2.3.bb-e/II Bent-30-Bent, Armor: CX2002U, Heat Sink: OF-Cu

residual stresses at RT after an assumed brazing cycle, with braze solidification at 750°C

thermal response to a uniform surface heat flux of 15 MW/m²



12.5 mm

Fig. 7.2.3.bb-f/I Bent-30-Bent, Armor: CX2002U, Heat Sink: DS-Cu

stress distribution and displacement at a uniform steady state surface heat flux of 15 MW/m²

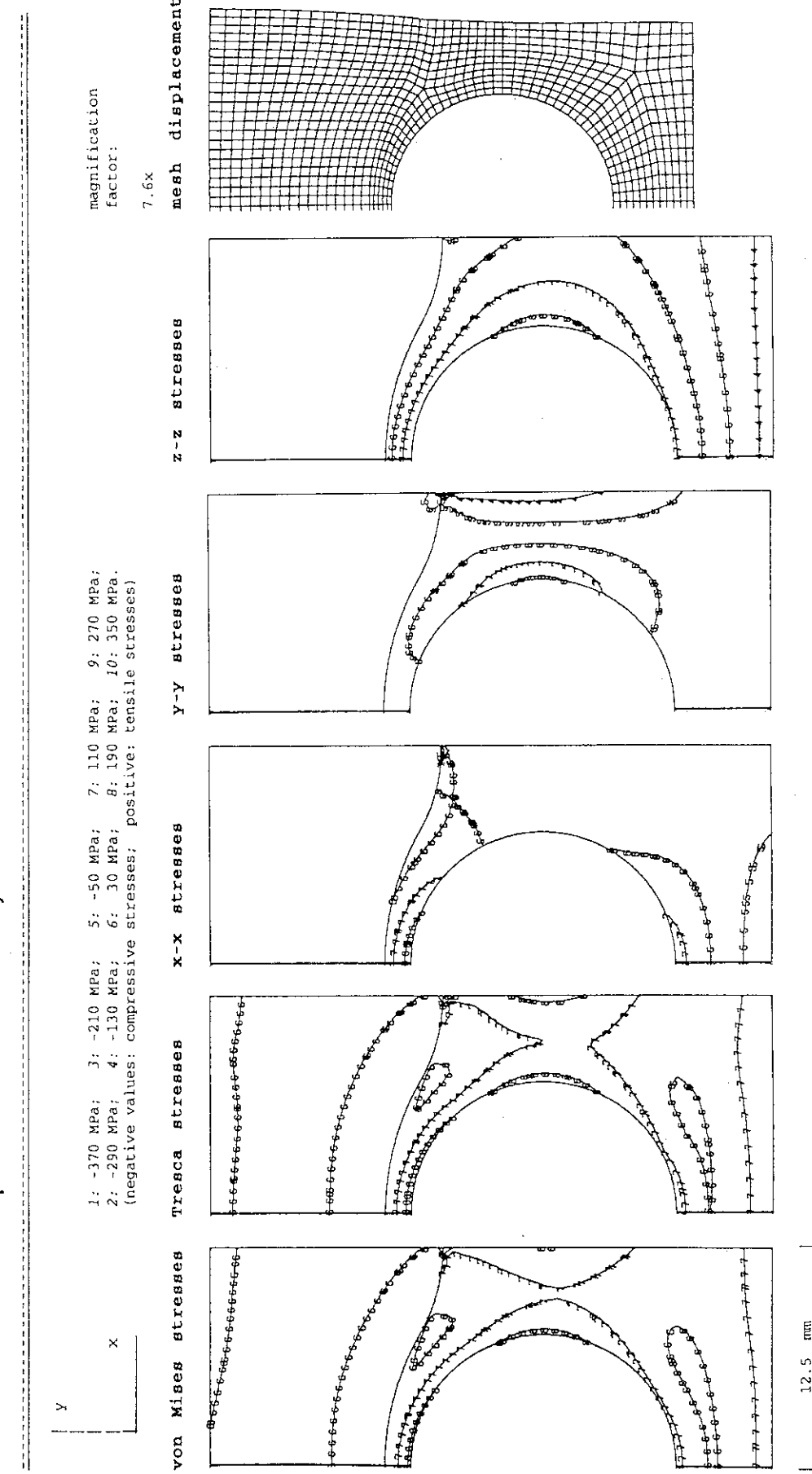
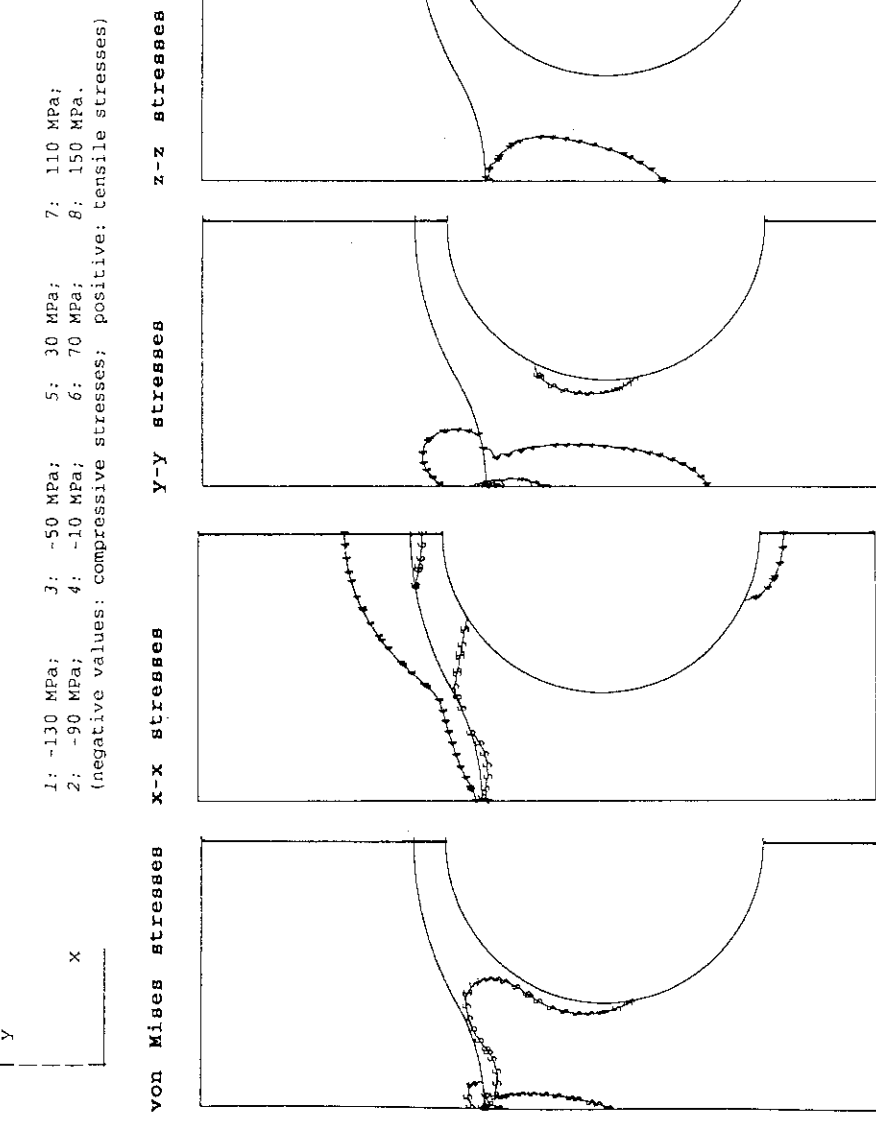


Fig. 7.2.3.bb-f/II Bent-30-Bent, Armor: CX2002U, Heat Sink: Ds-Cu

residual stresses at RT after an assumed brazing cycle, with braze solidification at 750°C



12.5 mm

Fig. 7.2.3.bb-g/I Bent-30-Bent, Armor: CX2002U, Heat Sink: TZM

stress distribution and displacement at a uniform steady state surface heat flux of 15 MW/m²

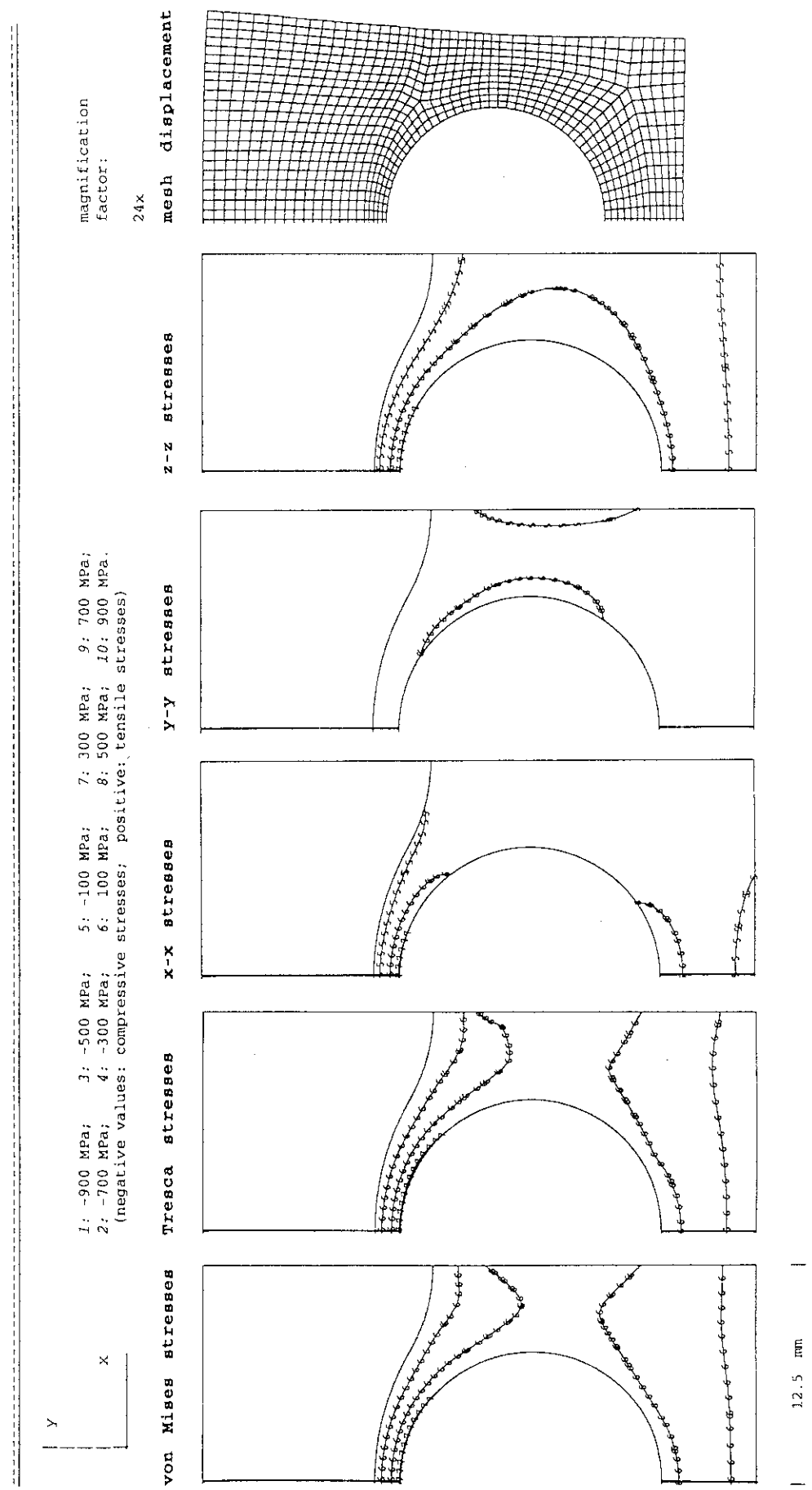


Fig. 7.2.3.bb-g/II Bent-30-Bent, Armor: CX2002U, Heat Sink: TZM

residual stresses at RT after an assumed brazing cycle, with braze solidification at 750°C

thermal response to a uniform surface heat flux of 15 MW/m²

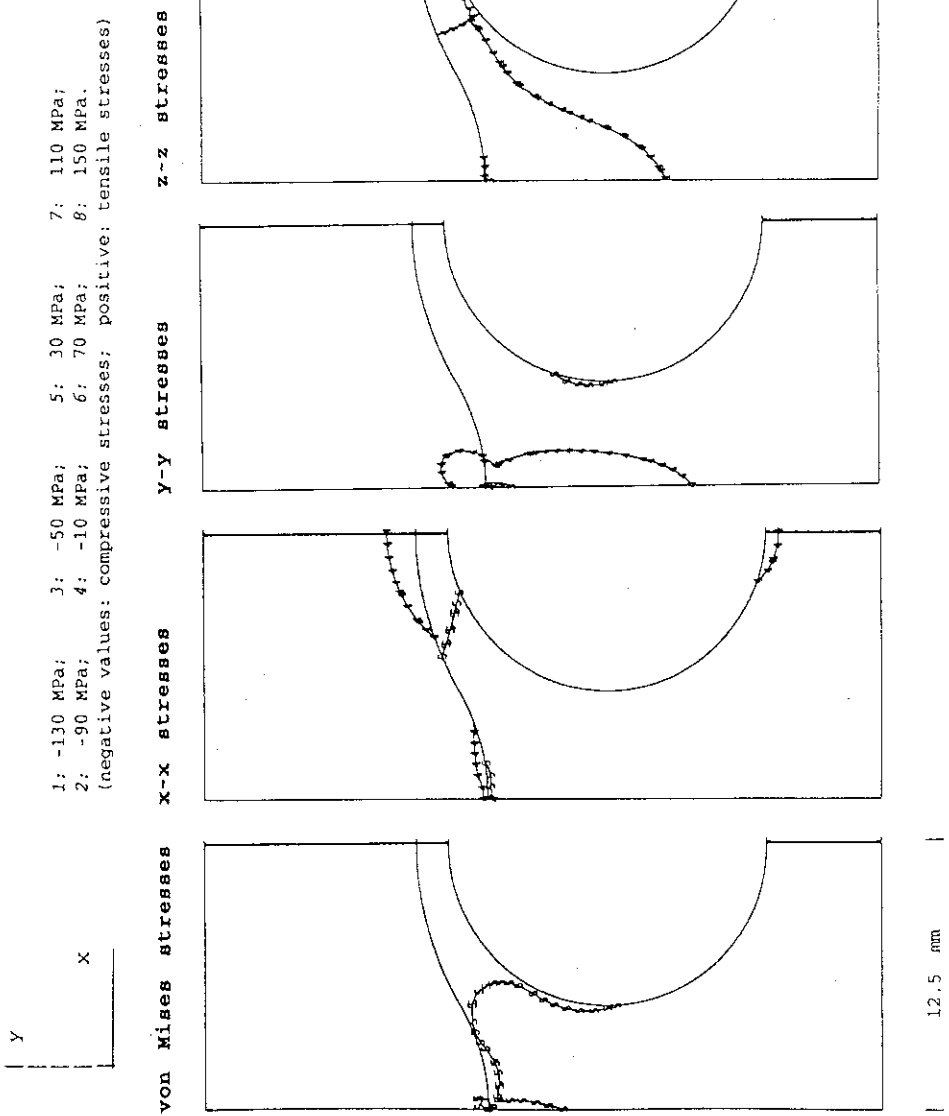


Fig. 7.2.3.bb-h/I Bent-30-Bent, Armor: CX2002U, Heat Sink: W5Re

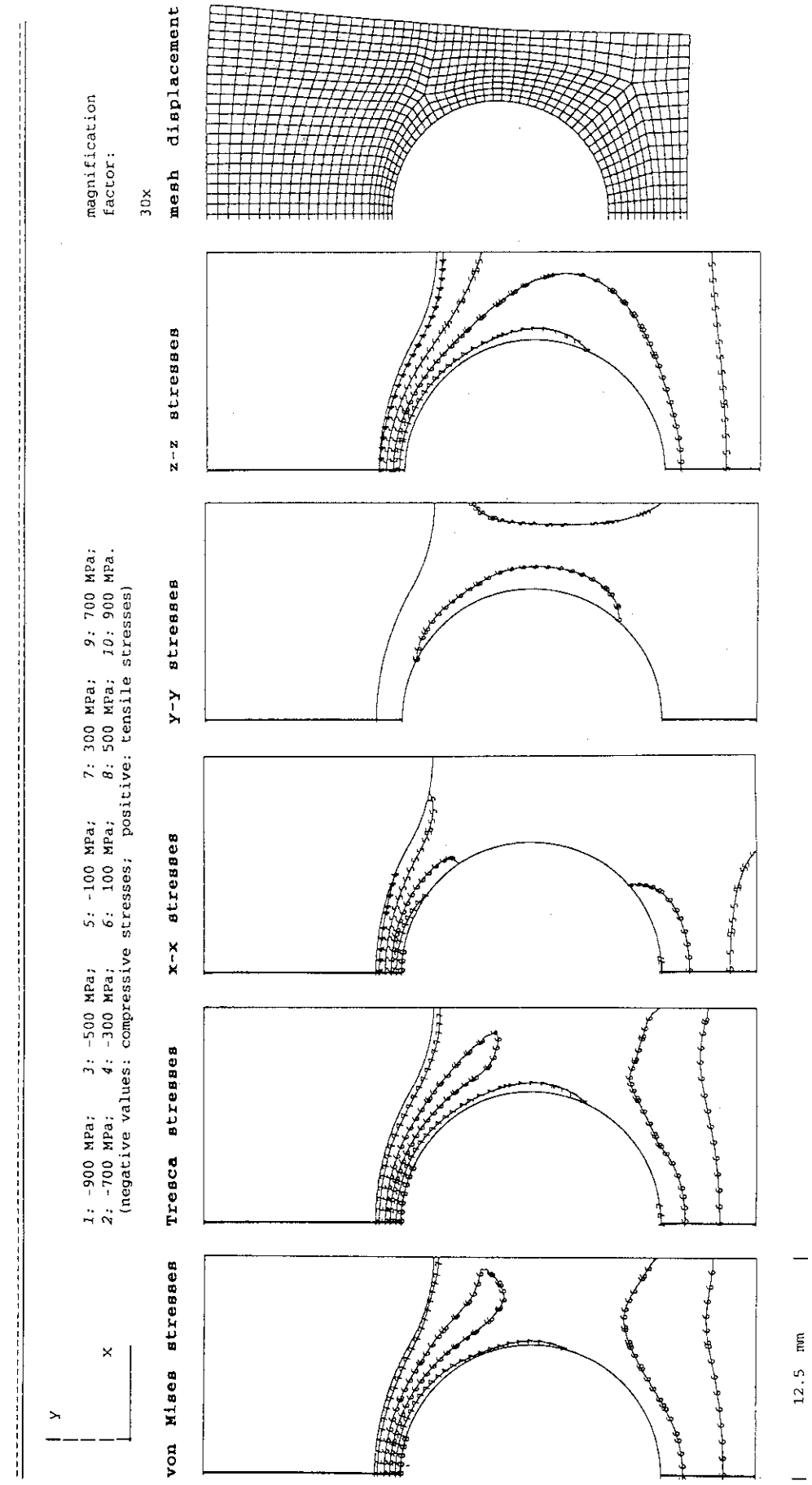
stress distribution and displacement at a uniform steady state heat flux of 15 MW/m²

Fig. 7.2.3.bb-h/II Bent-30-Bent, Armor: CX2002U, Heat Sink: W5Re

residual stresses at RT after an assumed brazing cycle, with braze solidification at 750°C

thermal response to a uniform surface heat flux of 15 MW/m²

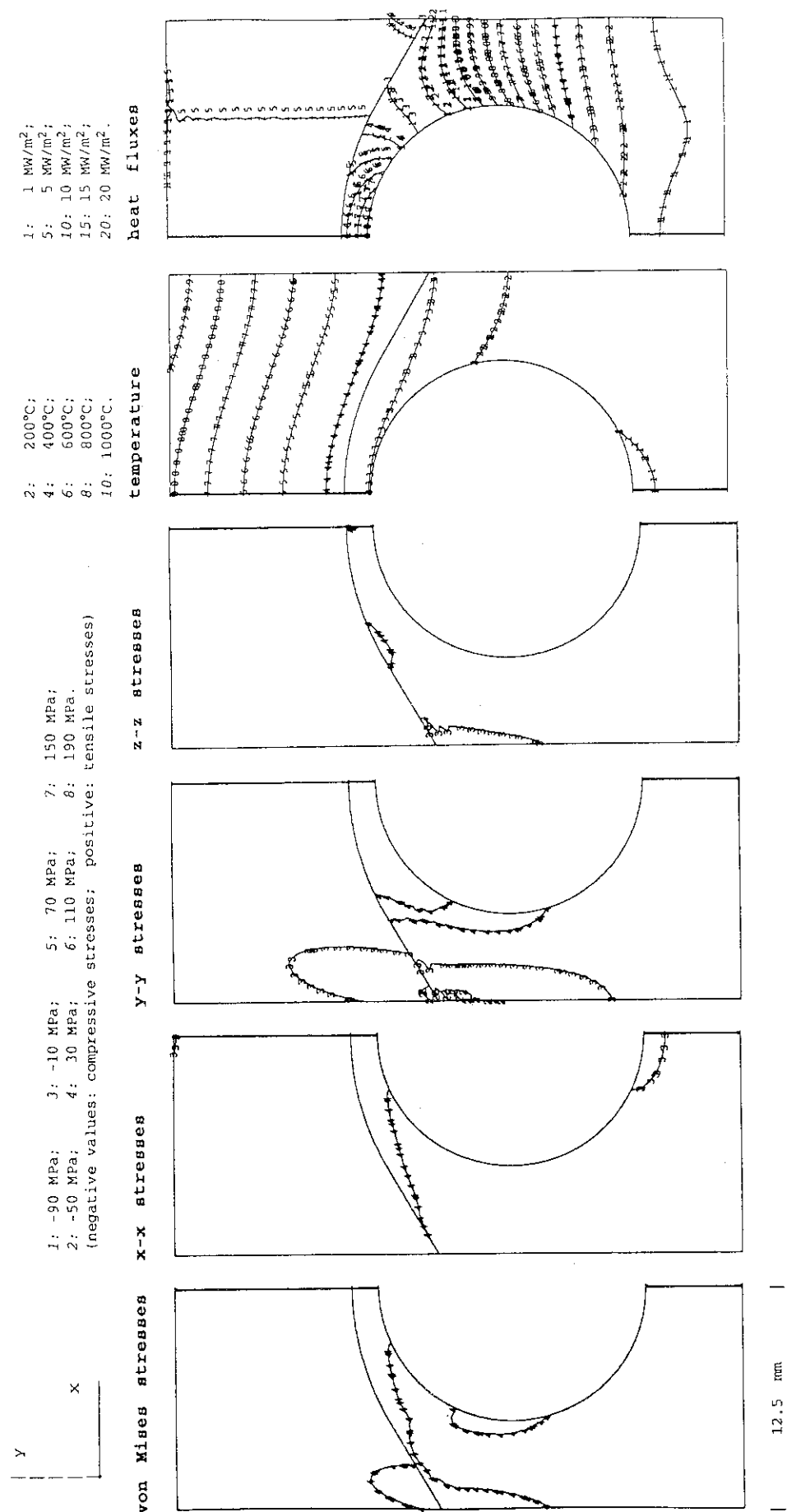


Fig. 7.2.3.bs-a/I Bent-30-Straight, Armor: MFC-1 (1992), Heat Sink: OF-Cu

stress distribution and displacement at a uniform steady state surface heat flux of 15 MW/m²

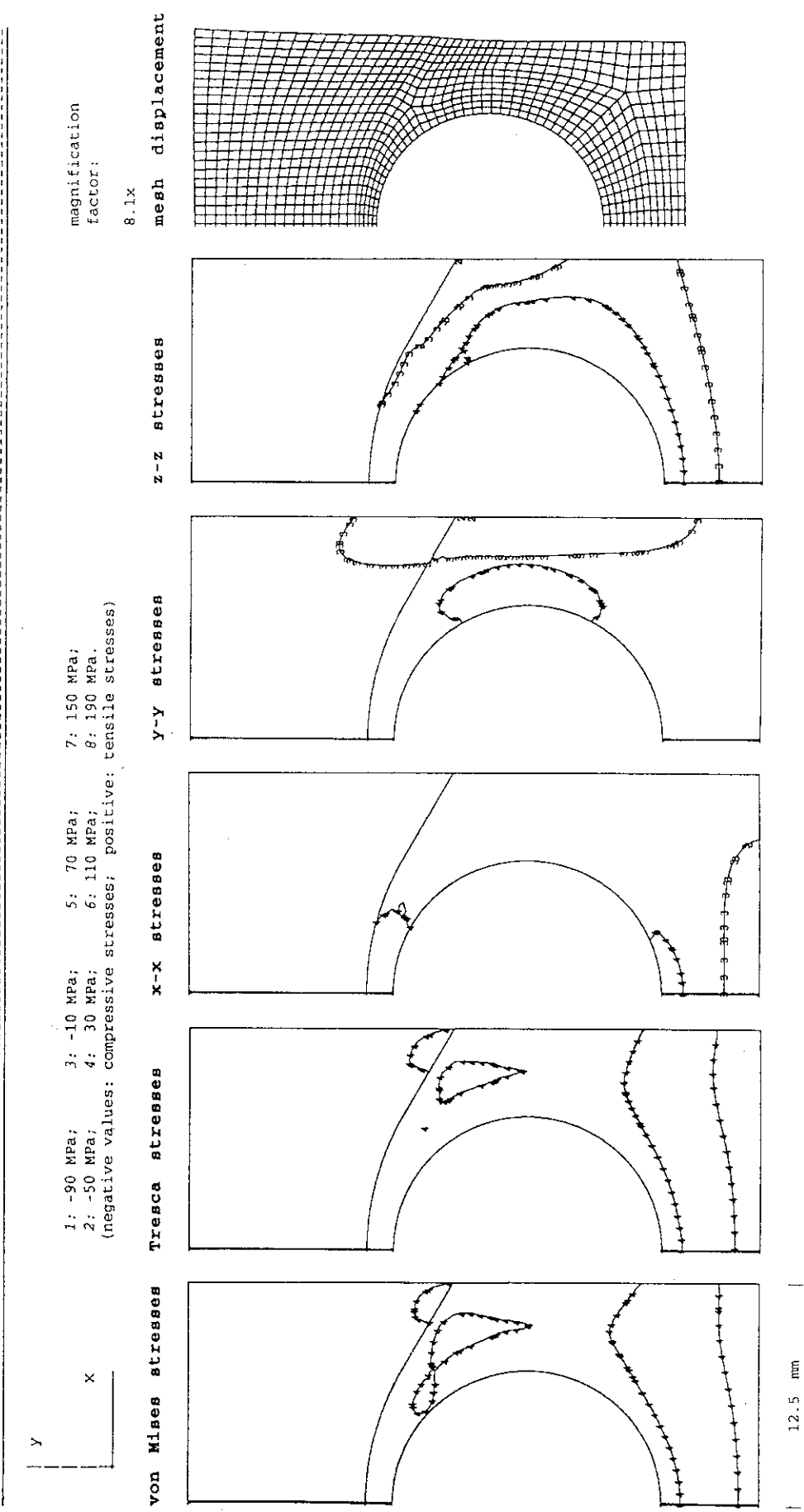


Fig. 7.2.3.bs-a/II Bent-30-Straight, Armor: MFC-1 (1992), Heat Sink: OF-Cu

residual stresses at RT after an assumed brazing cycle, with braze solidification at 750°C

thermal response to a uniform surface heat flux of 15 MW/m²

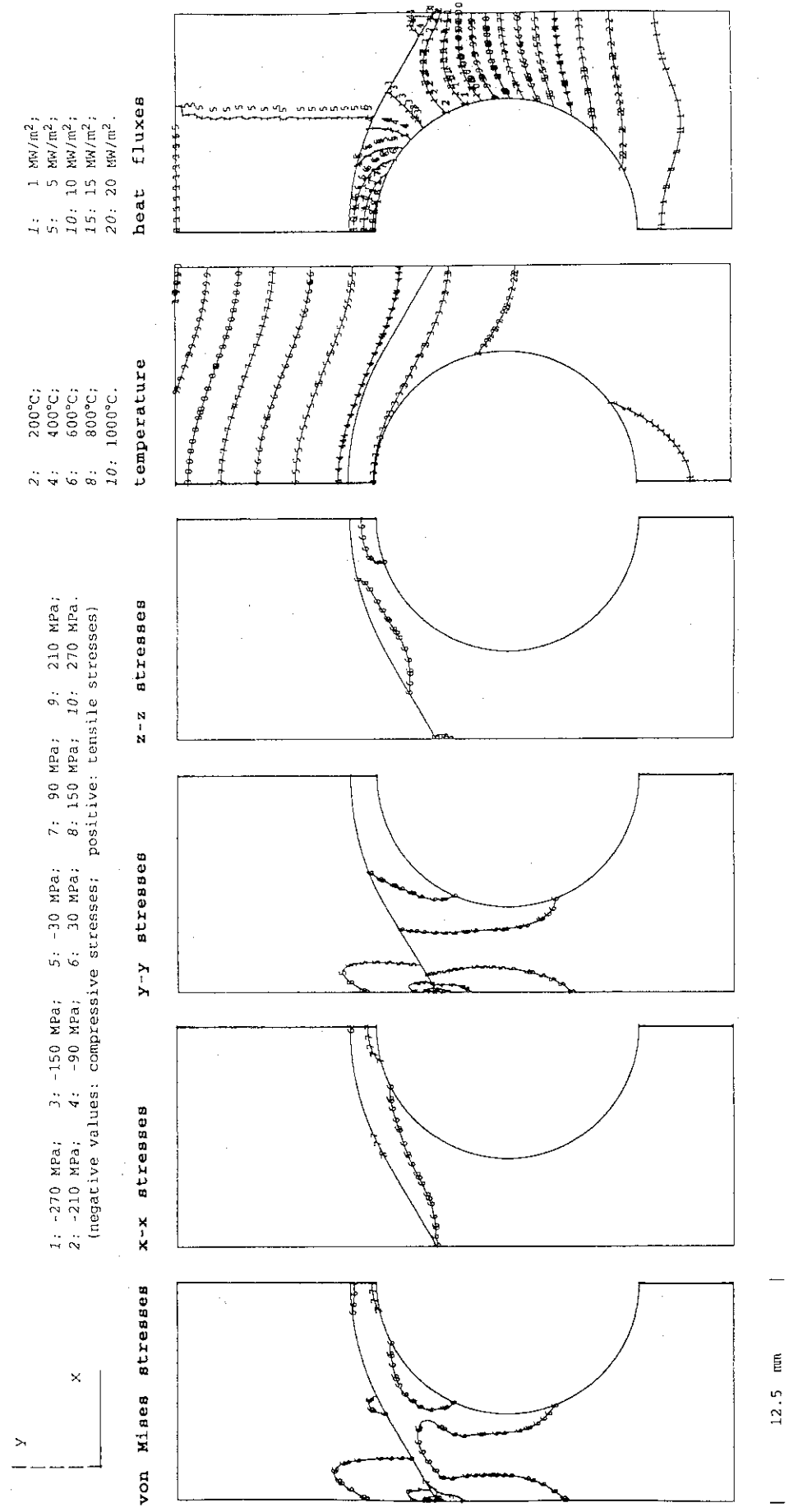


Fig. 7.2.3.bs-b/I Bent-30-Straight, Armor: MFC-1 (1992), Heat Sink: DS-Cu

stress distribution and displacement at a uniform steady state heat flux of 15 MW/m²

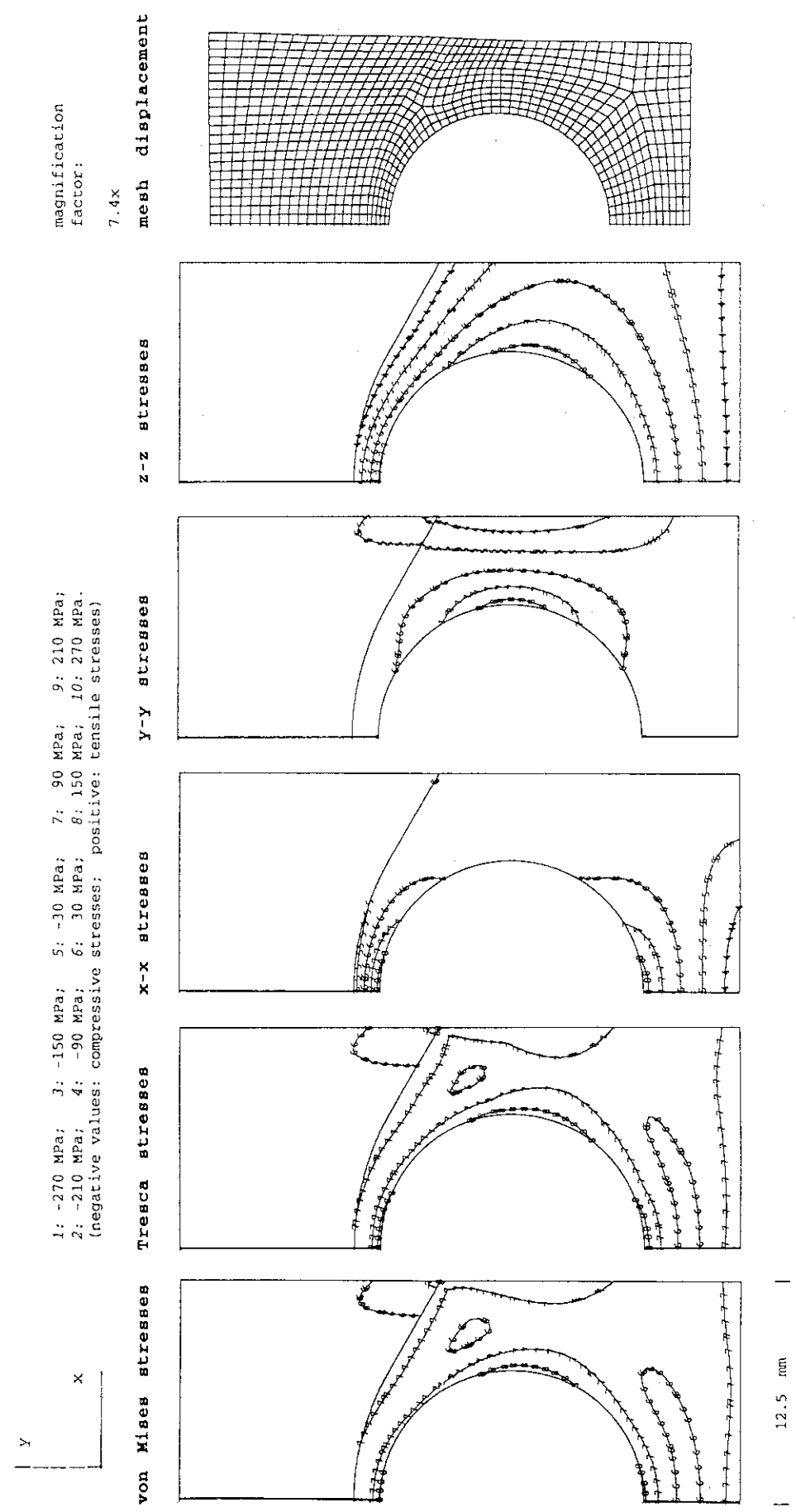


Fig. 7.2.3.bs-b/II Bent-30-Straight, Armor: MFC-1 (1992), Heat Sink: DS-Cu

residual stresses at RT after an assumed brazing cycle, with braze solidification at 750°C

surface heat flux of 15 MW/m²

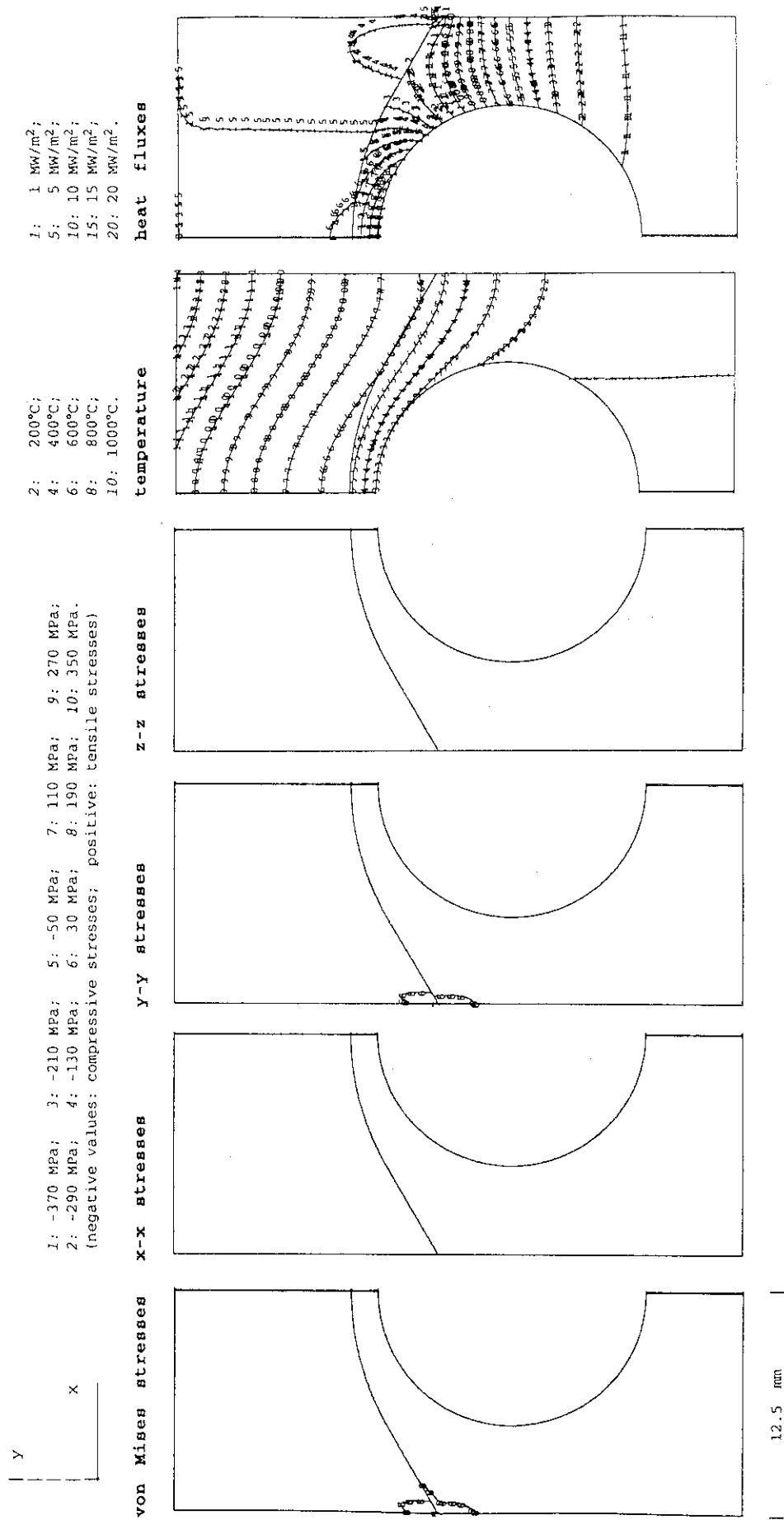


Fig. 7.2.3.bs-c/I Bent-30-Straight, Armor: MFC-1 (1992), Heat Sink: TZM

stress distribution and displacement at a uniform steady state surface heat flux of 15 MW/m²

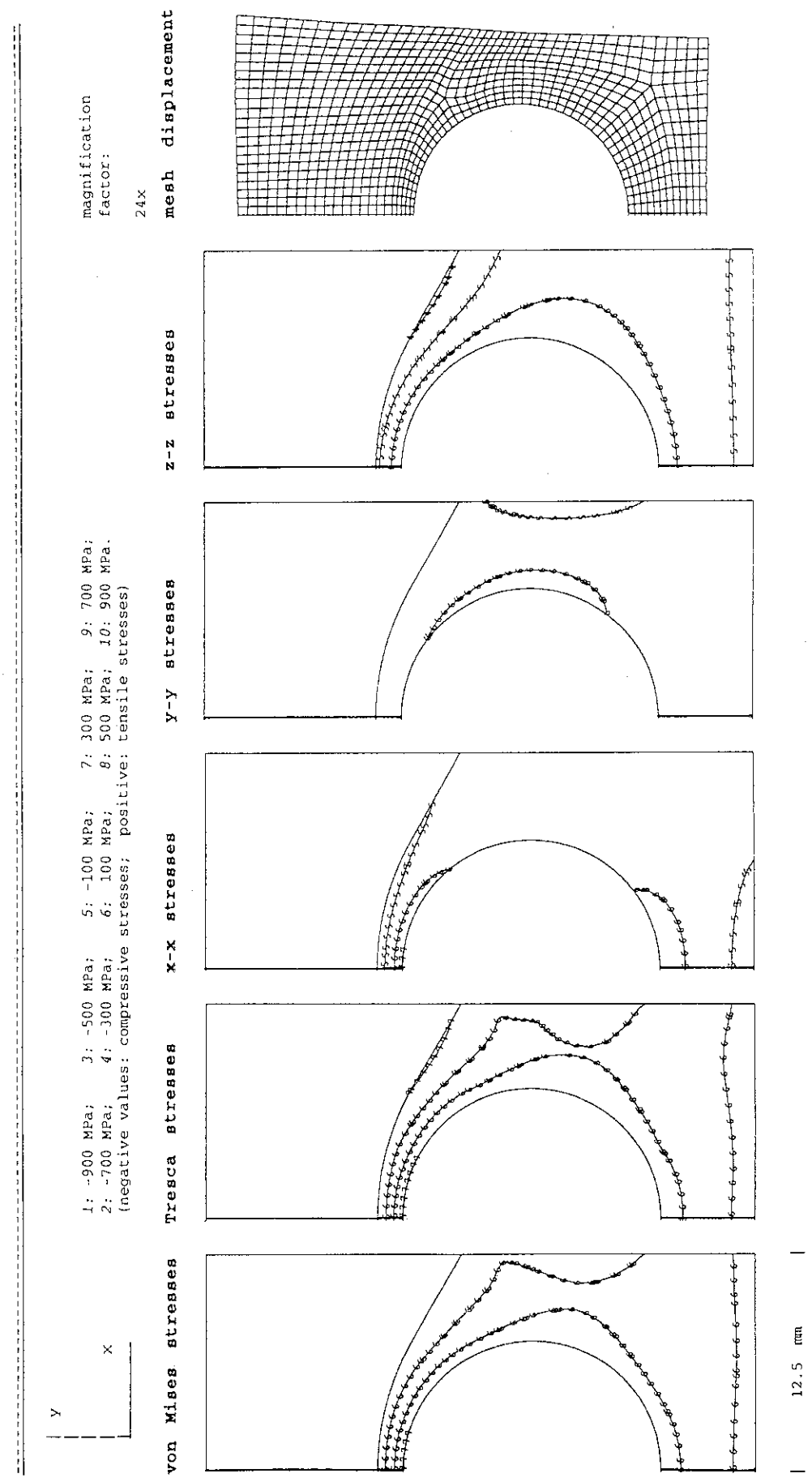


Fig. 7.2.3.bs-c/II Bent-30-Straight, Armor: MFC-1 (1992), Heat Sink: TZM

residual stresses at RT after an assumed brazing cycle, with braze solidification at 750°C

thermal response to a uniform surface heat flux of 15 MW/m²

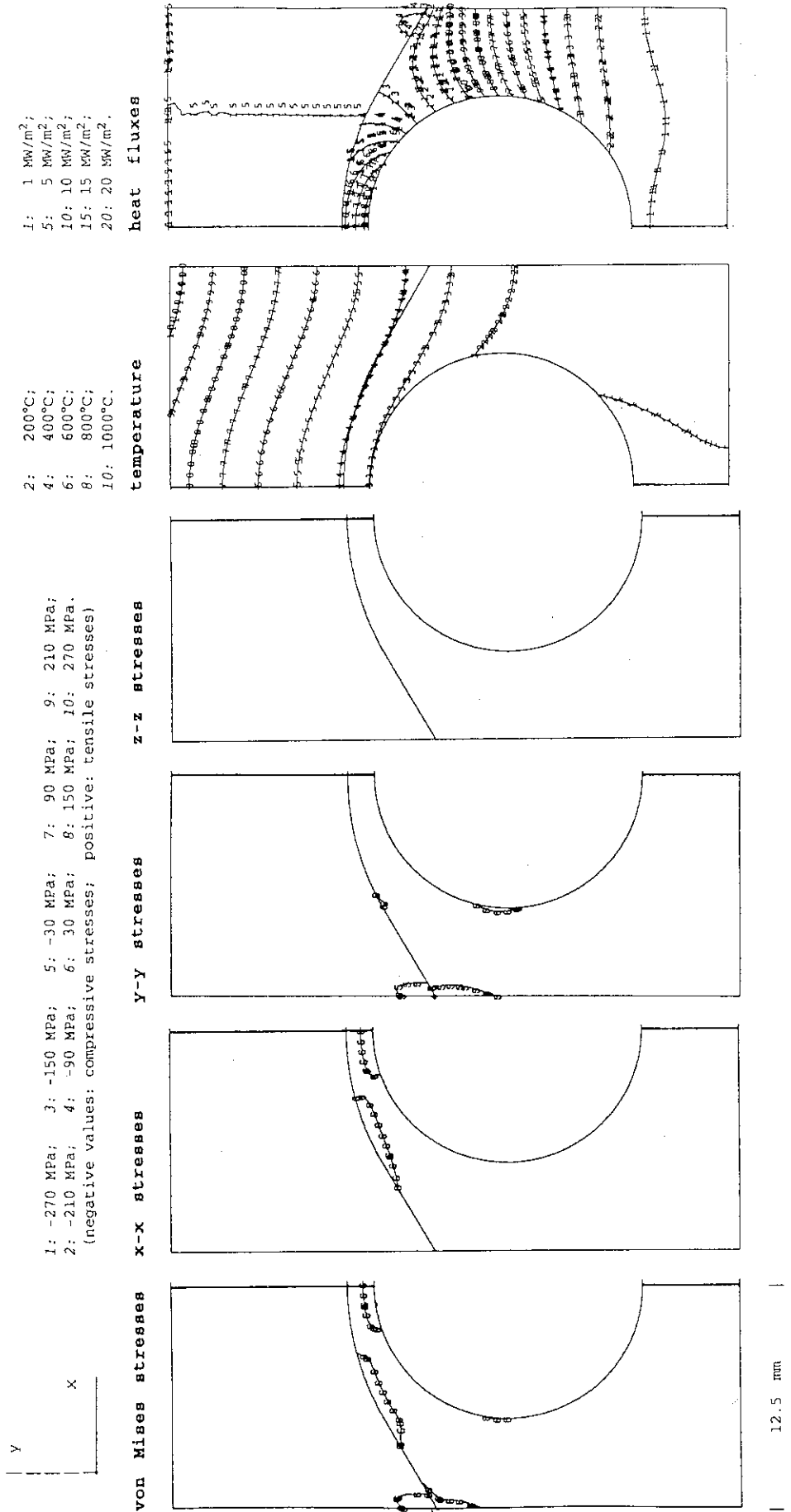


Fig. 7.2.3.bs-d/I Bent-30-Straight, Armor: MFC-1 (1992), Heat Sink: W-30Cu

stress distribution and displacement at a uniform steady state surface heat flux of 15 MW/m²

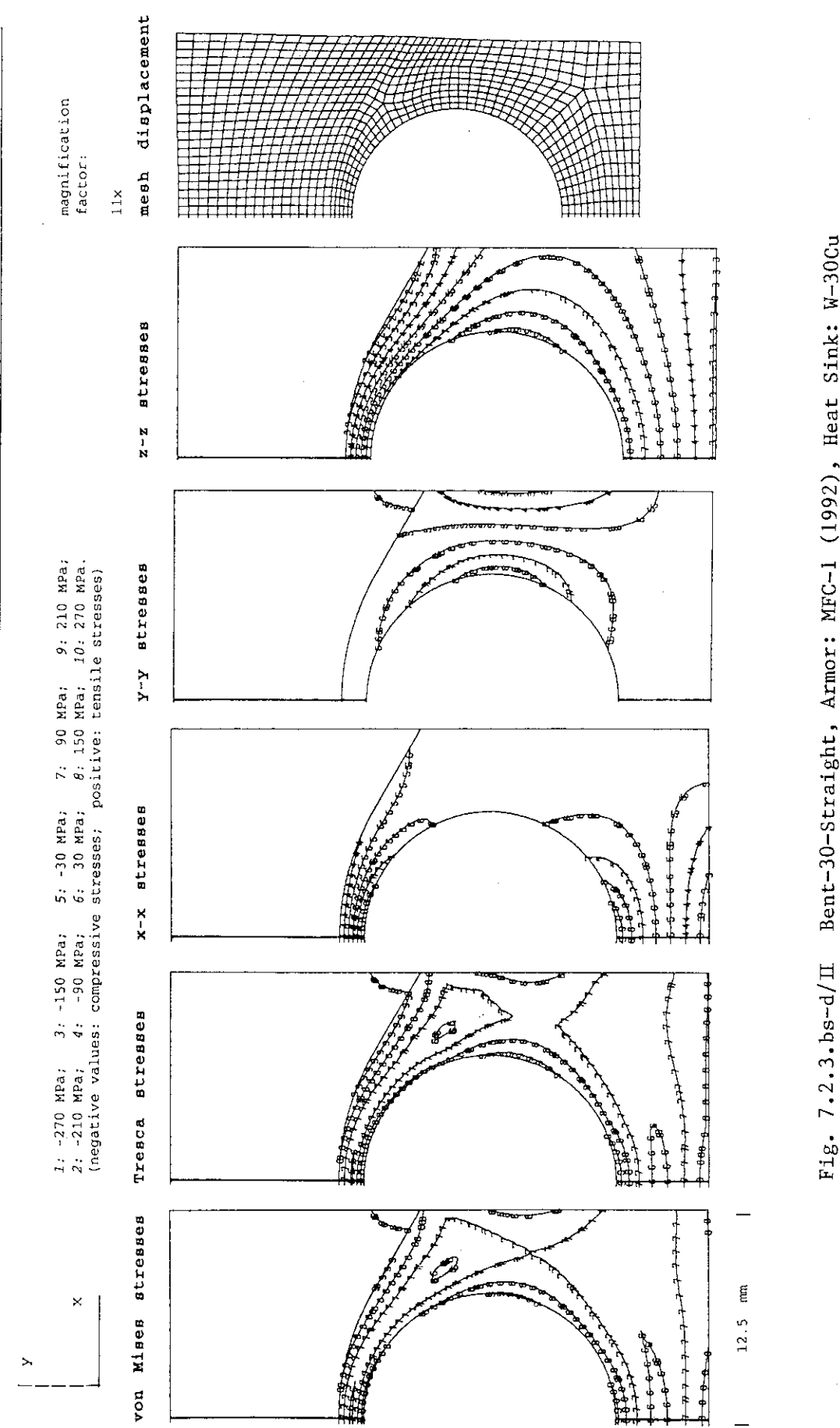


Fig. 7.2.3.bs-d/II Bent-30-Straight, Armor: MFC-1 (1992), Heat Sink: W-30Cu

residual stresses at RT after an assumed brazing cycle, with braze solidification at 750°C

thermal response to a uniform surface heat flux of 15 MW/m²

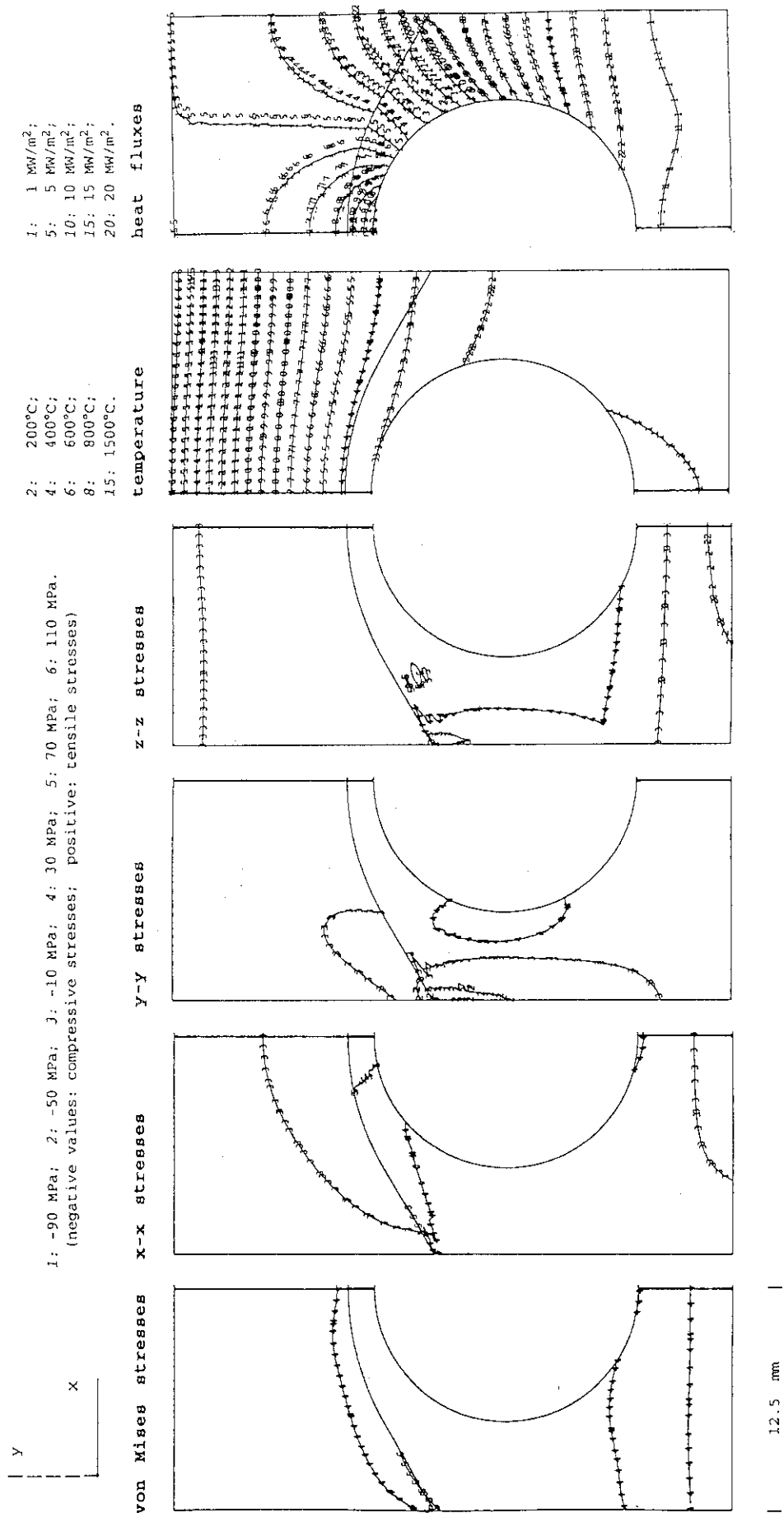


Fig. 7.2.3.bs-e/I Bent-30-Straight, Armor: CX2002U, Heat Sink: OF-Cu

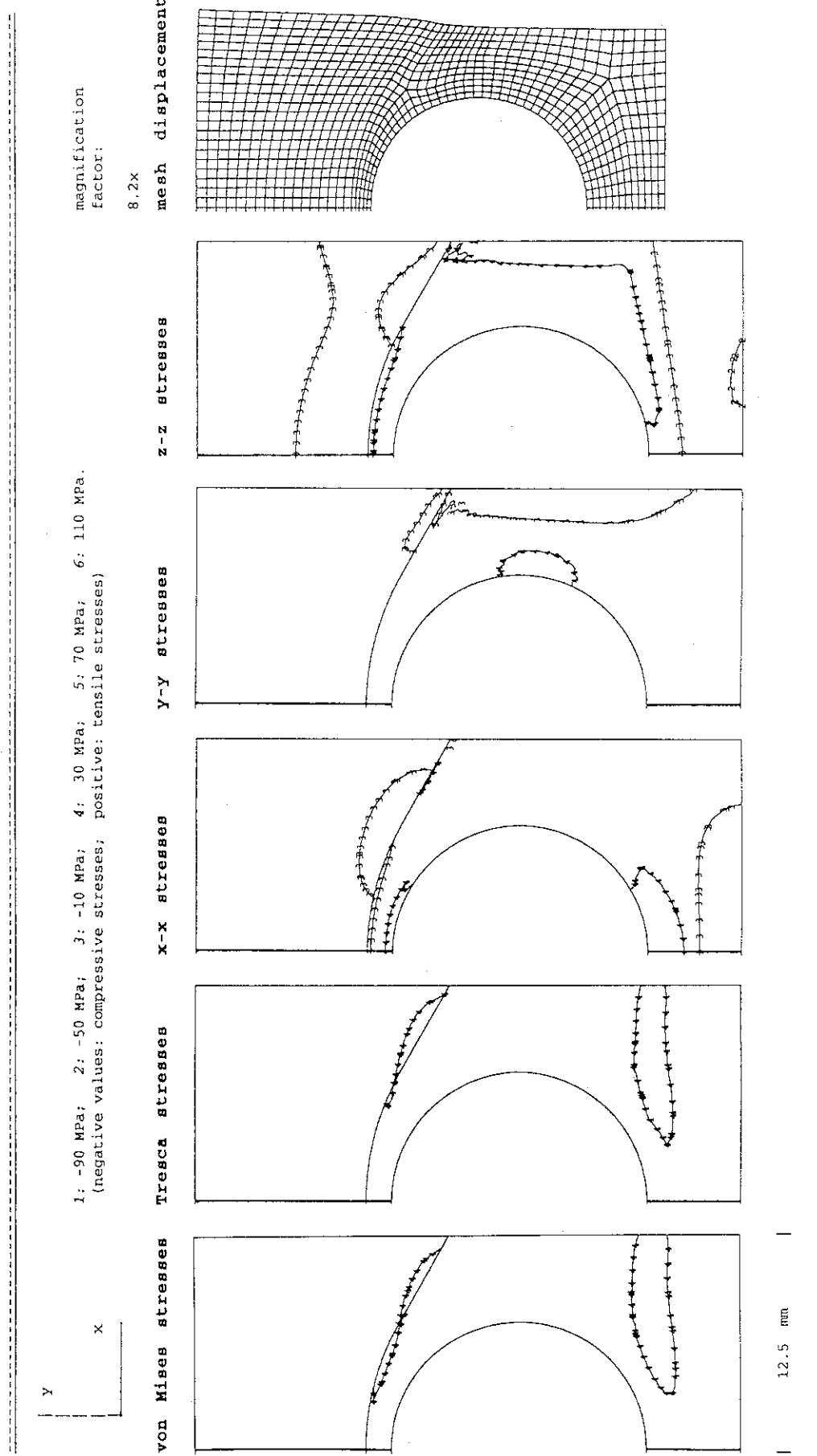
stress distribution and displacement at a uniform steady state surface heat flux of 15 MW/m²

Fig. 7.2.3.bs-e/II Bent-30-Straight, Armor: CX2002U, Heat Sink: OF-Cu

residual stresses at RT after an assumed brazing cycle, with braze solidification at 750°C

thermal response to a uniform
surface heat flux of 15 MW/m²

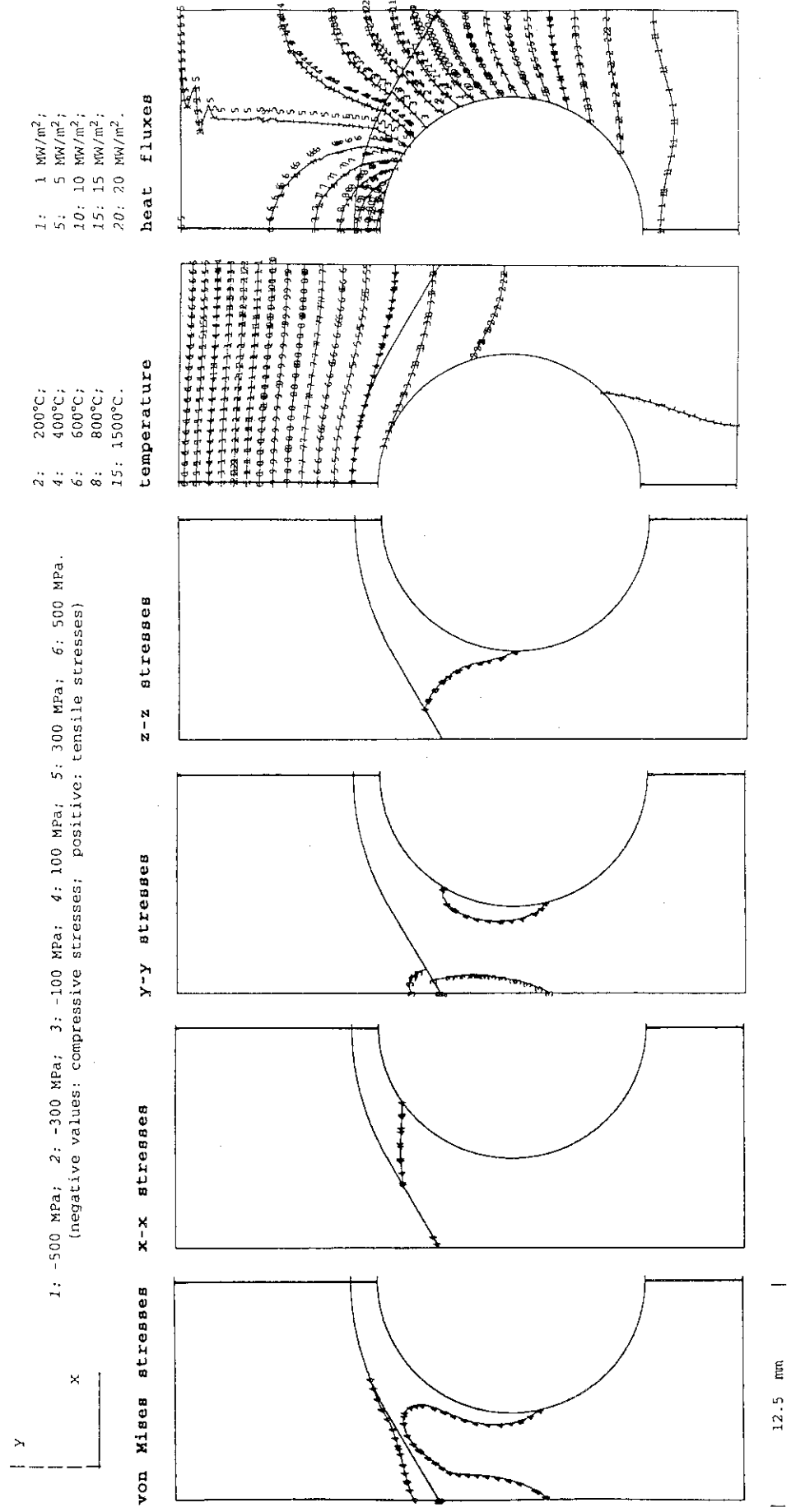


Fig. 7.2.3.bs-f/I Bent-30-Straight, Armor: CX2002U, Heat Sink: DS-Cu

stress distribution and displacement at a uniform steady state surface heat flux of 15 MW/m²

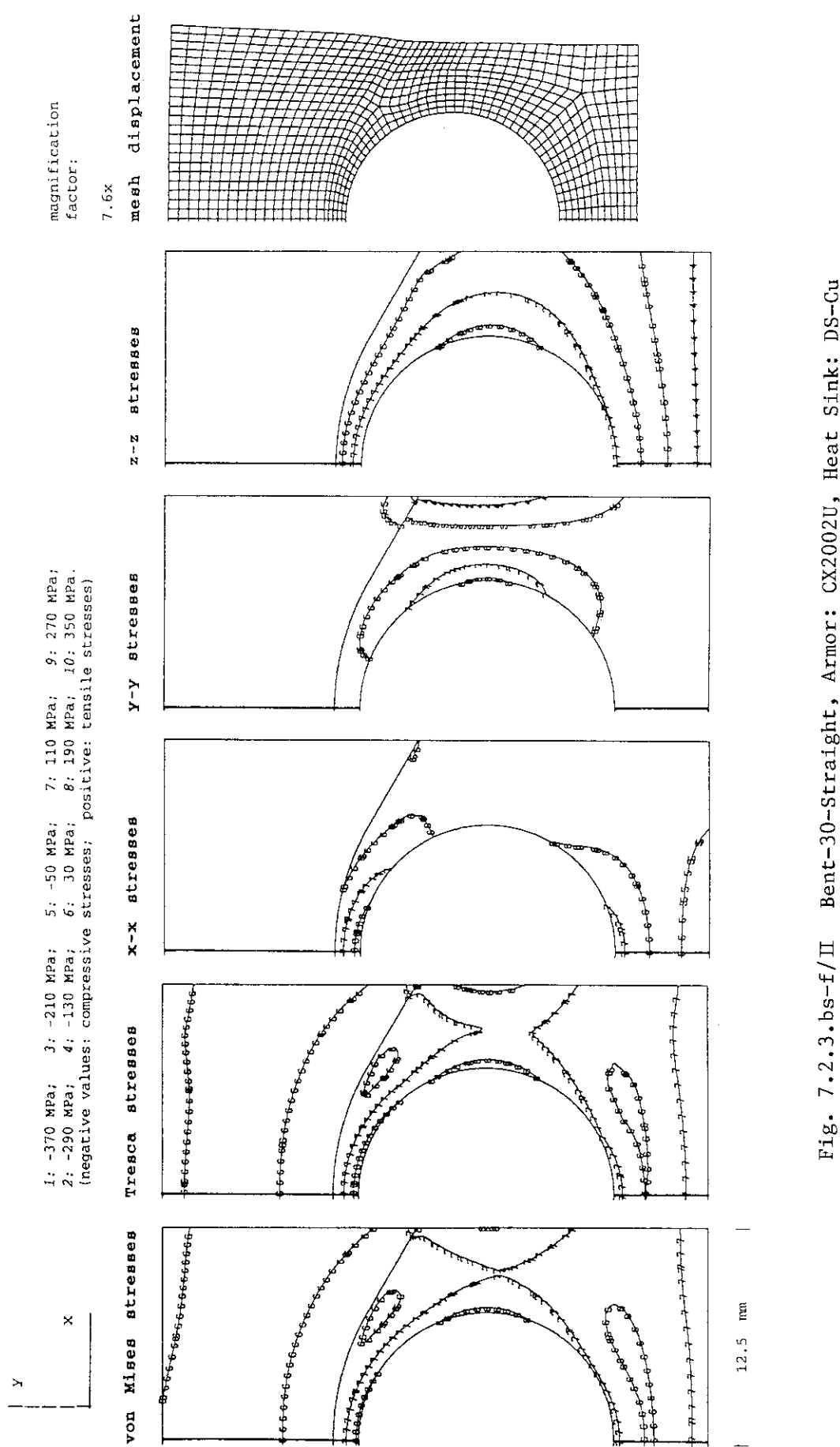
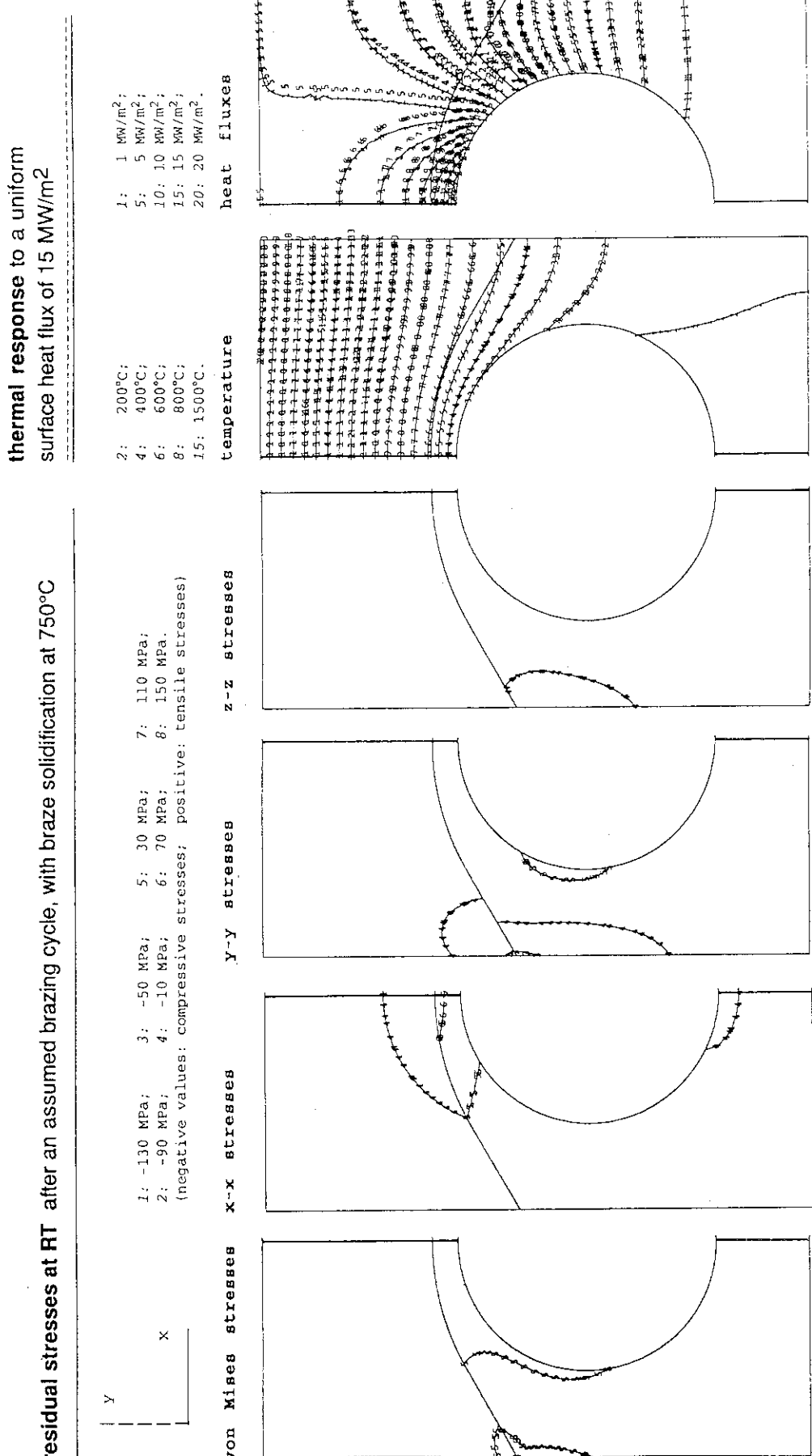


Fig. 7.2.3.bs-f/II Bent-30-Straight, Armor: CX2002U, Heat Sink: DS-Cu



12.5 mm

Fig. 7.2.3.bs-g/I Bent-30-Straight, Armor: CX2002U, Heat Sink: TZM

stress distribution and displacement at a uniform steady state surface heat flux of 15 MW/m²

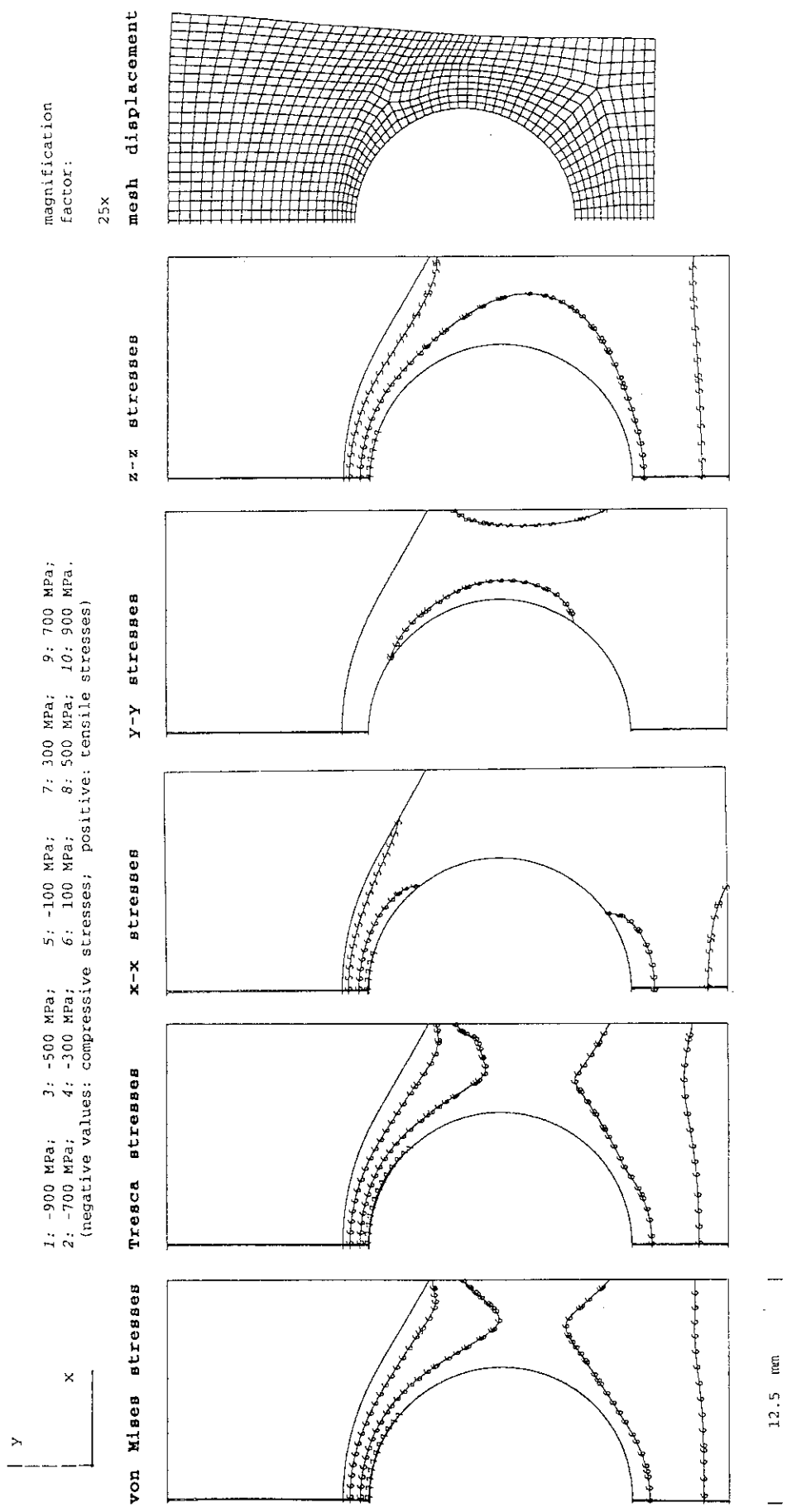


Fig. 7.2.3.bsg/II Bent-30-Straight, Armor: CX2002U, Heat Sink: TZM

residual stresses at RT after an assumed brazing cycle, with braze solidification at 750°C

thermal response to a uniform surface heat flux of 15 MW/m²

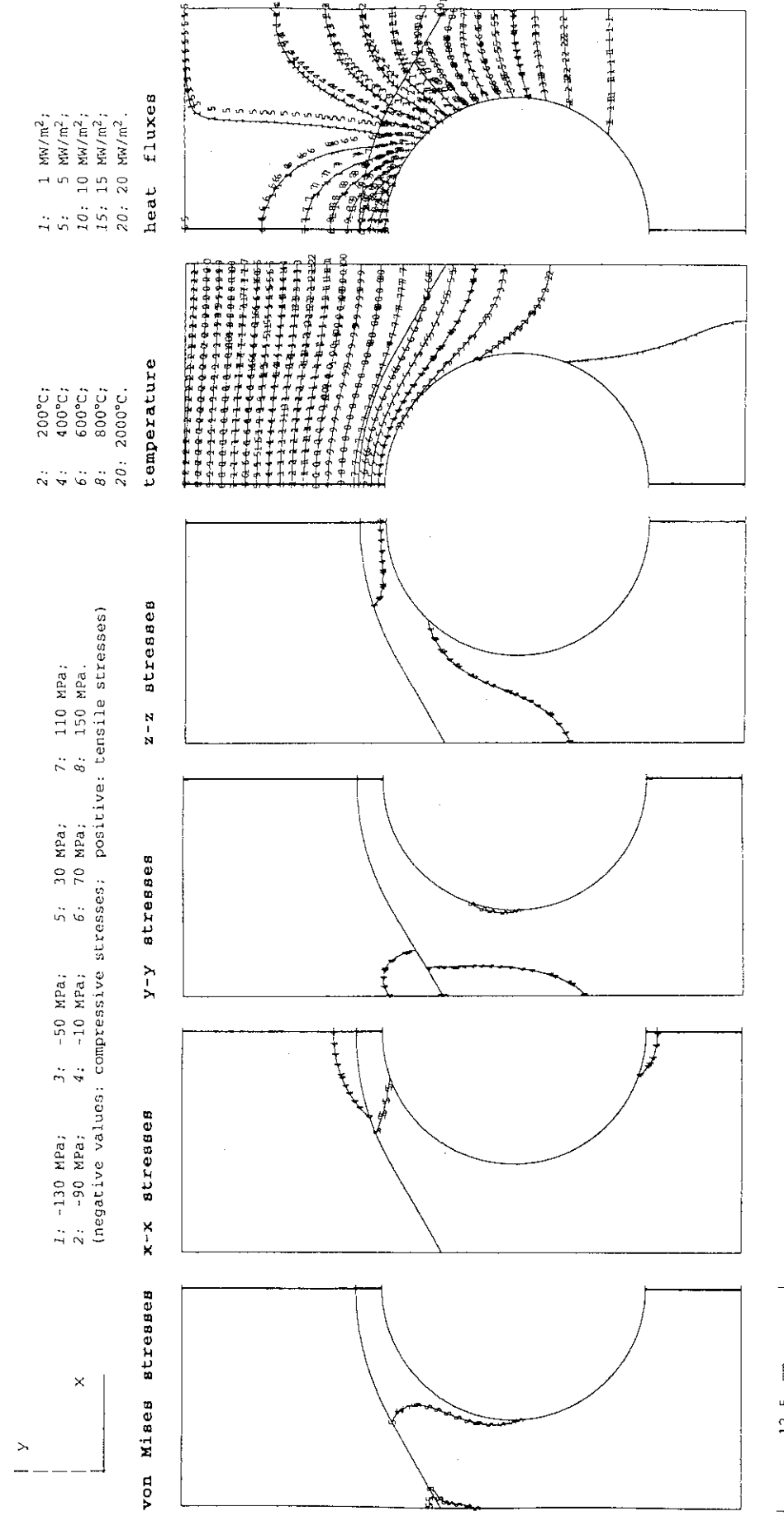


Fig. 7.2.3.bsh/I Bent-30-Straight, Armor: CX2002U, Heat Sink: W5Re

stress distribution and displacement at a uniform steady state surface heat flux of 15 MW/m²

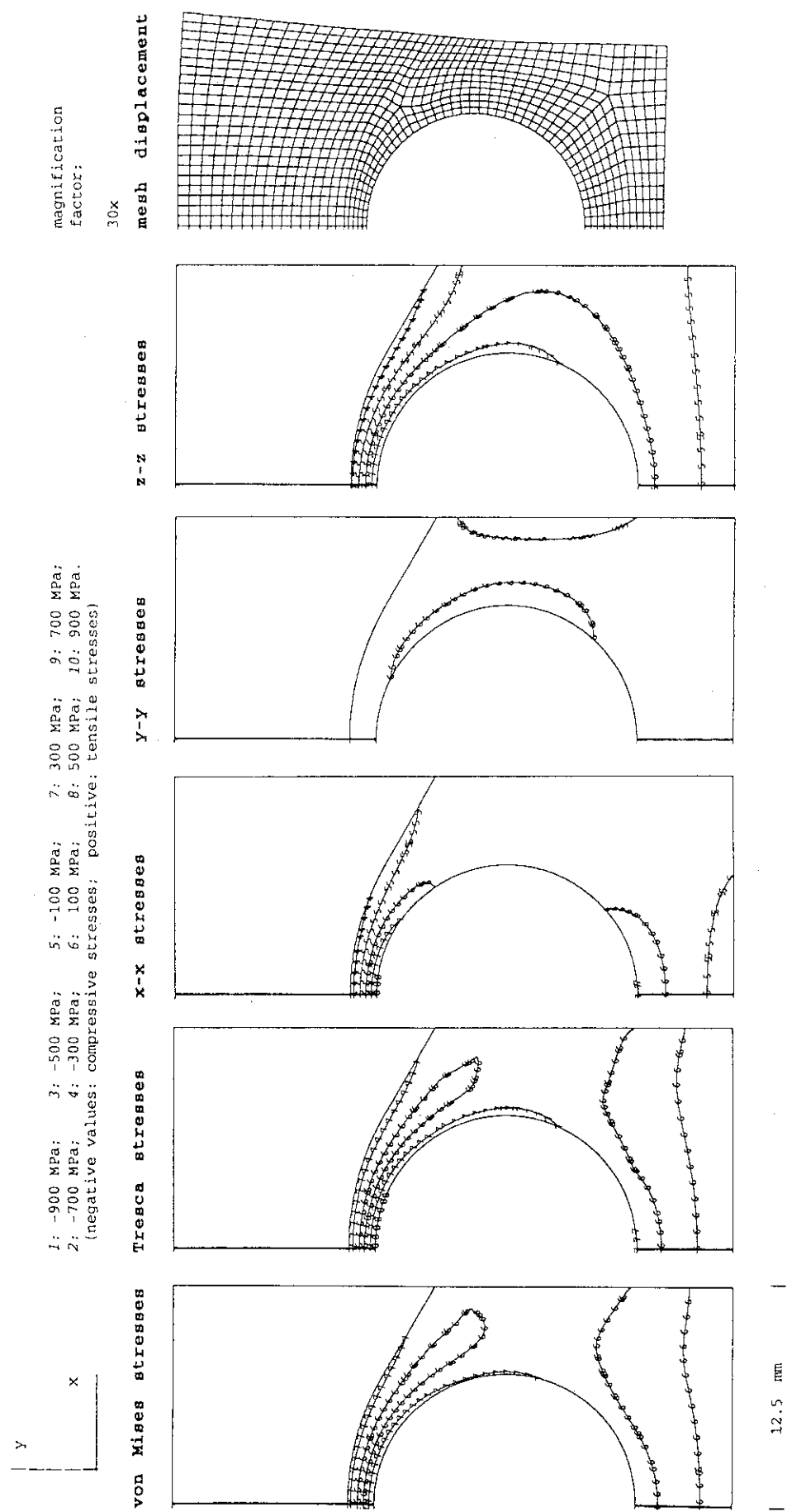


Fig. 7.2.3.bs-h/II Bent-30-Straight, Armor: CX2002U, Heat Sink: W5Re

residual stresses at RT after an assumed brazing cycle, with braze solidification at 750°C

thermal response to a uniform surface heat flux of 15 MW/m²

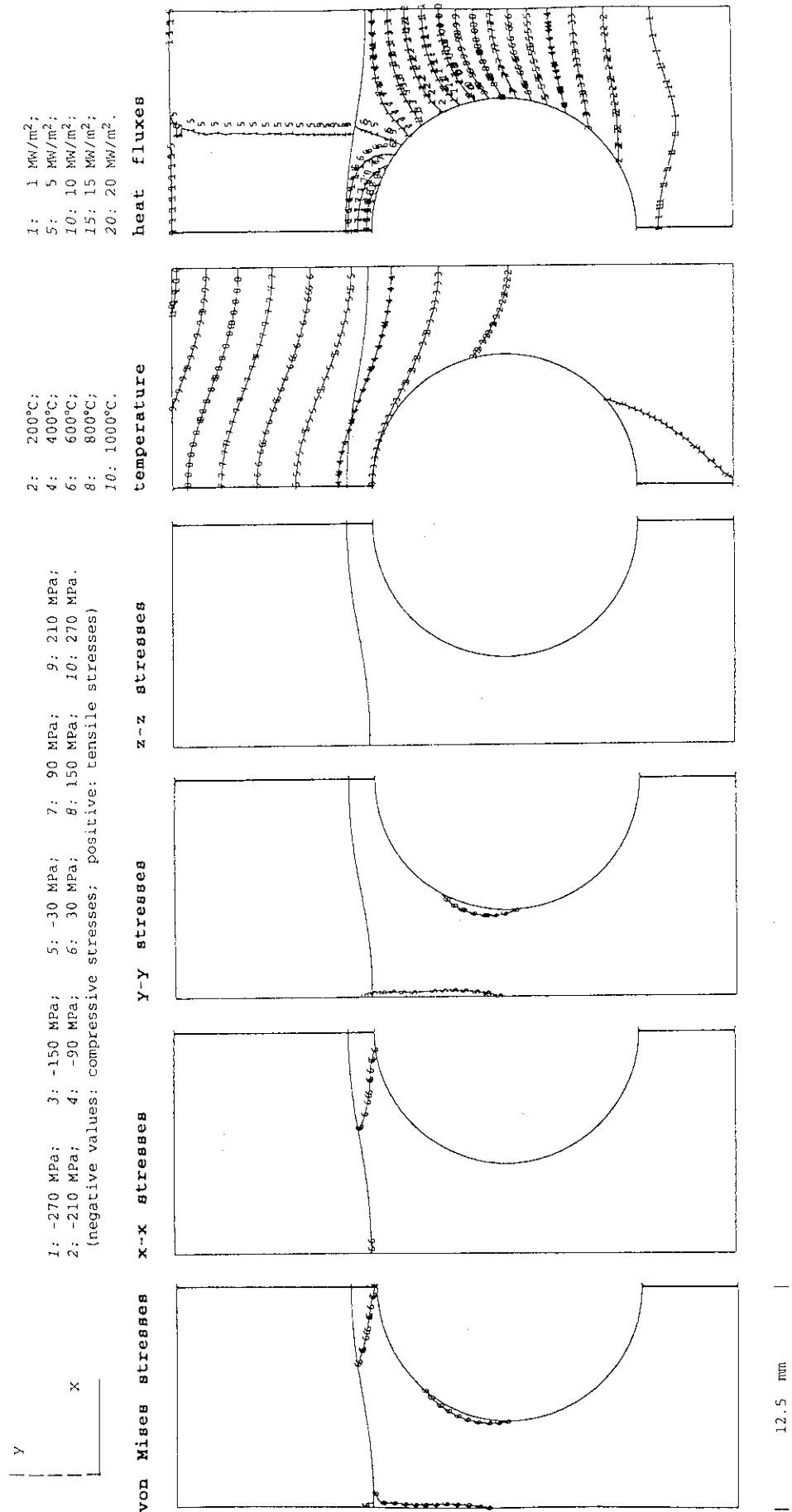


Fig. 7.2.4.a/I Bent-10-Bent, Armor: MFC-I (1992), Heat Sink: DS-Gu

stress distribution and displacement at a uniform steady state surface heat flux of 15 MW/m²

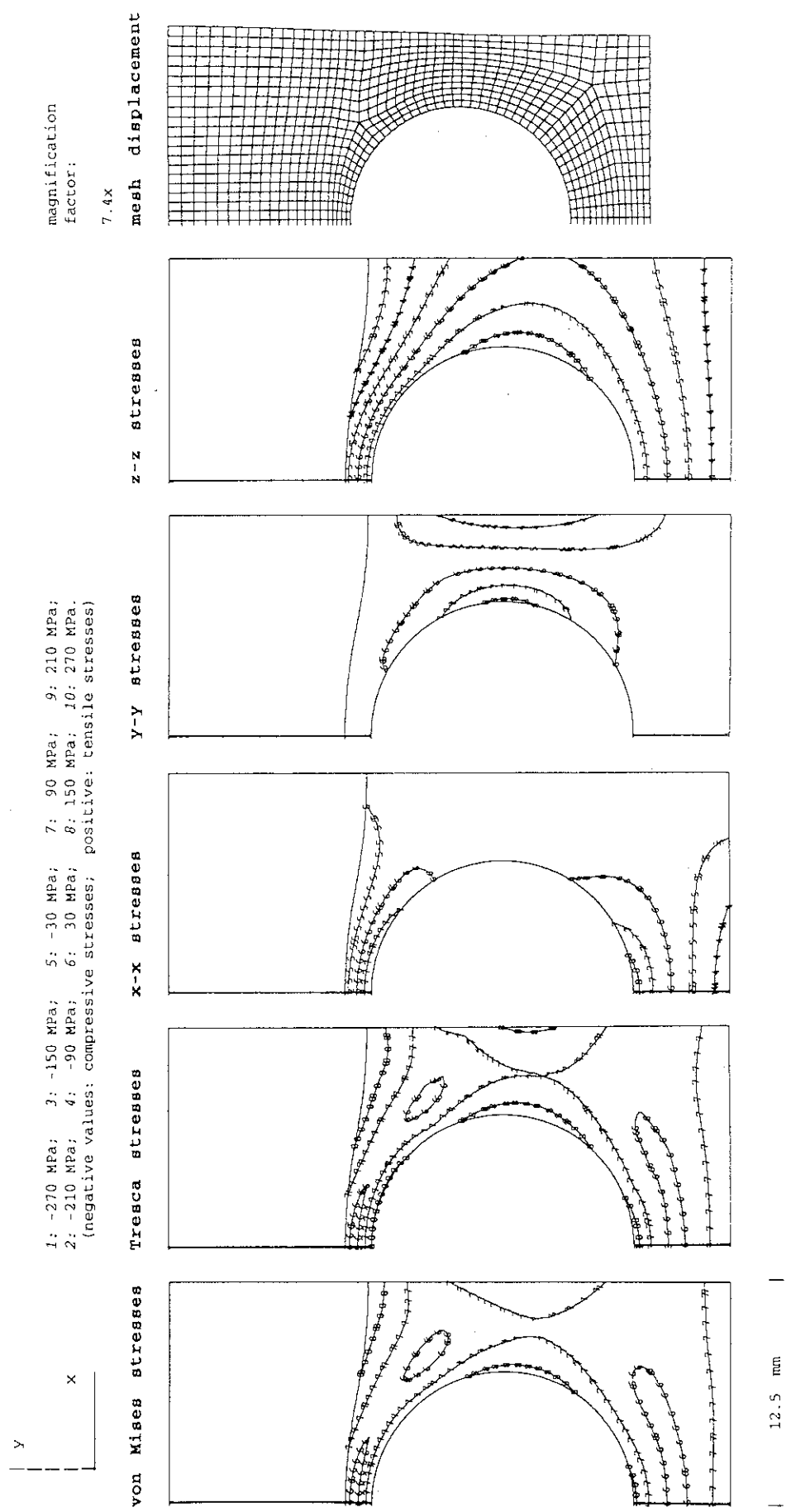
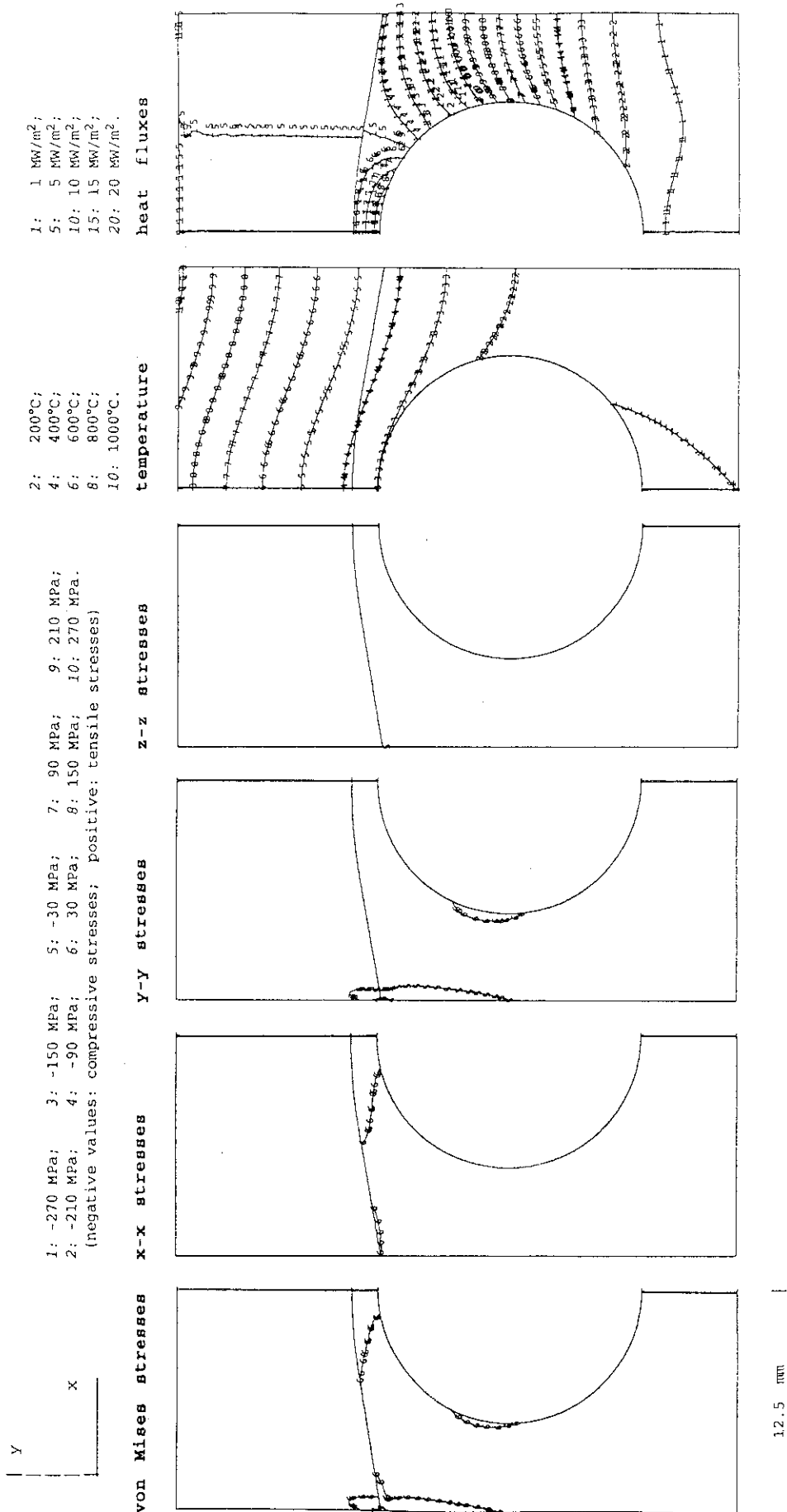


Fig. 7.2.4.a/II Bent-10-Bent, Armor: MFC-1 (1992), Heat Sink: DS-Cu

residual stresses at RT after an assumed brazing cycle, with braze solidification at 750°C

thermal response to a uniform surface heat flux of 15 MW/m²



12.5 mm

Fig. 7.2.4.b/I Bent-10-Straight, Armor: MFC-1 (1992), Heat Sink: DS-Cu

stress distribution and displacement at a uniform steady state surface heat flux of 15 MW/m²

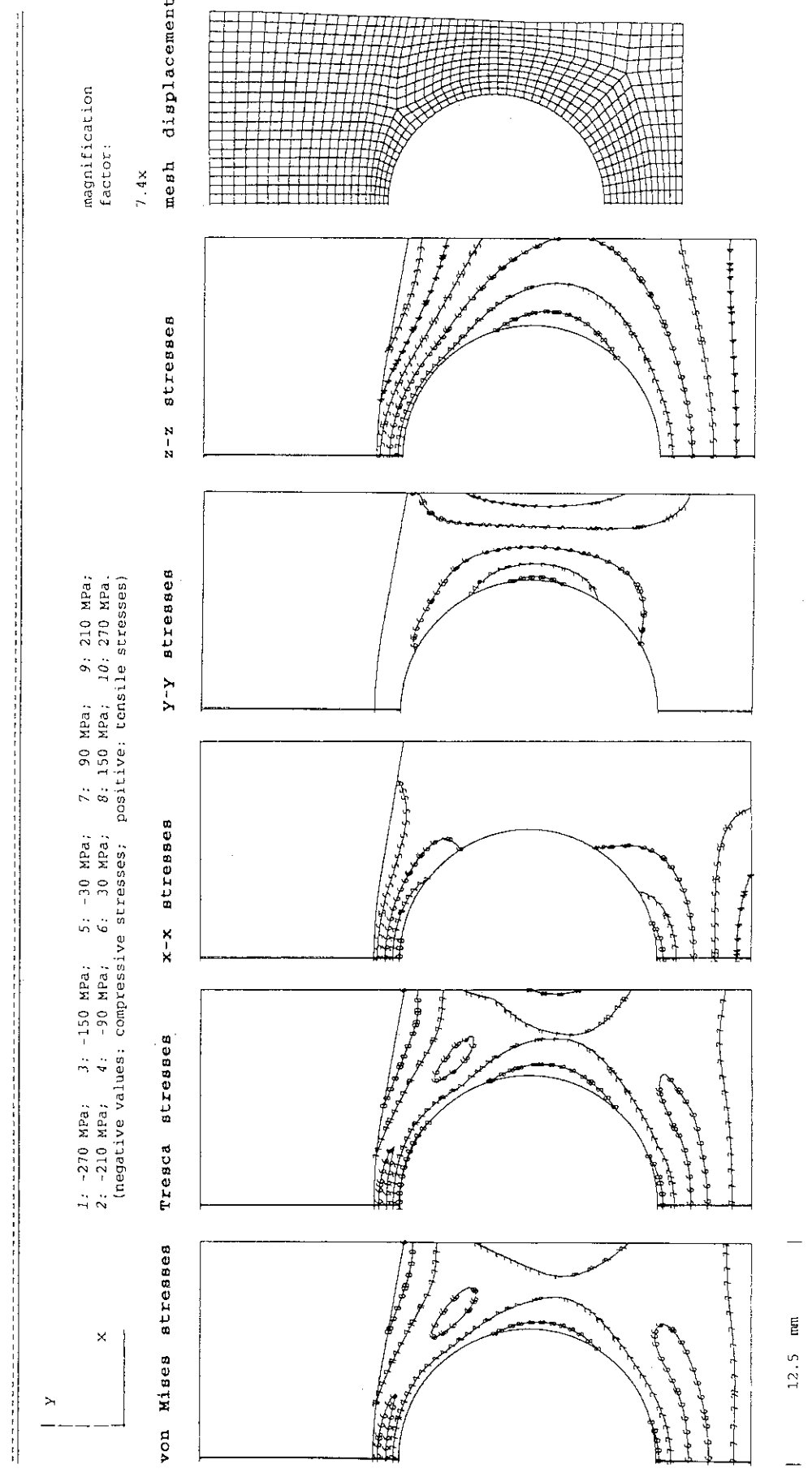


Fig. 7.2.4.b/II Bent-10-Straight, Armor: MFC-1 (1992), Heat Sink: DS-Cu

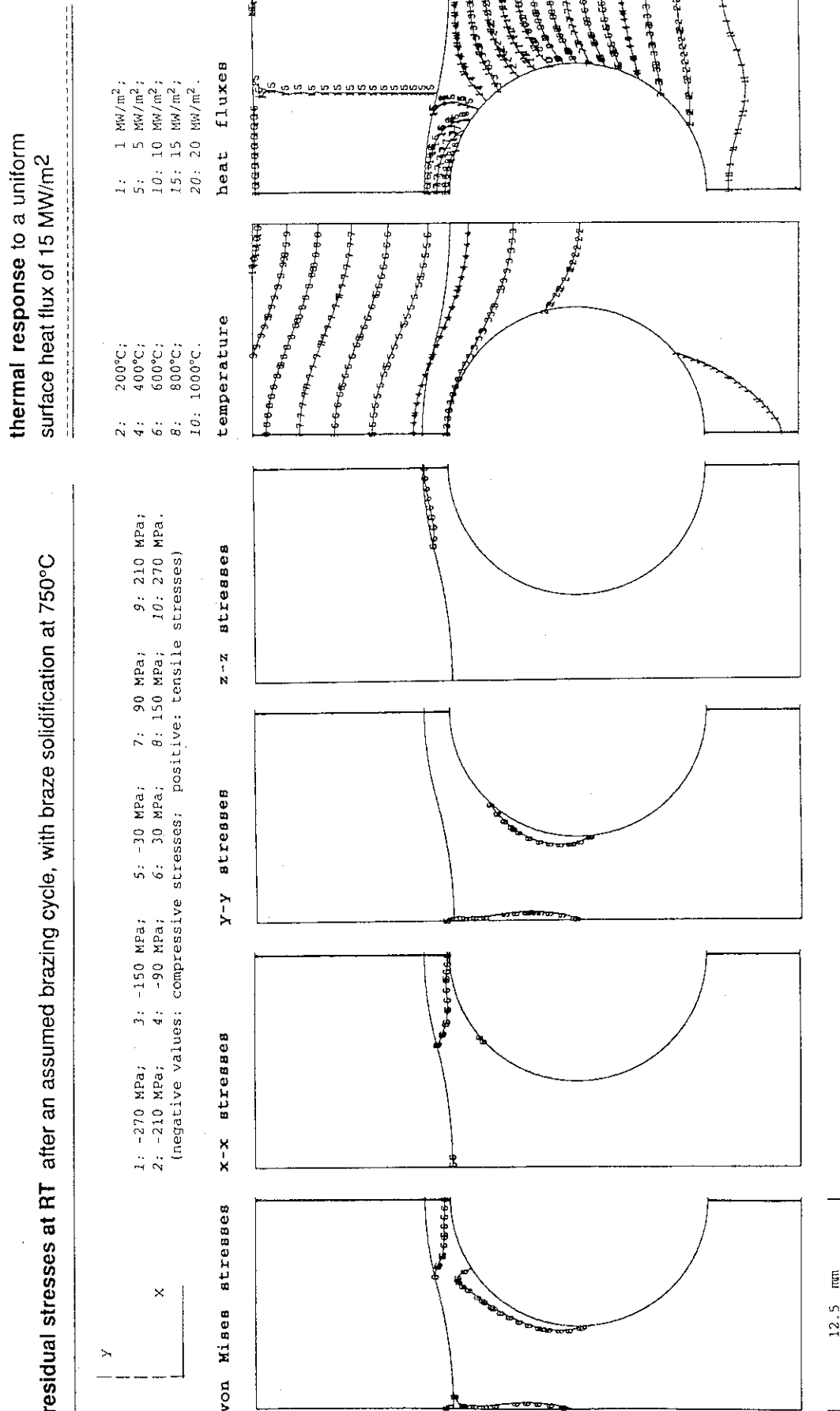


Fig. 7.2.4.c/I Bent-15-Bent, Armor: MFC-1 (1992), Heat Sink: DS-Cu

stress distribution and displacement at a uniform steady state surface heat flux of 15 MW/m²

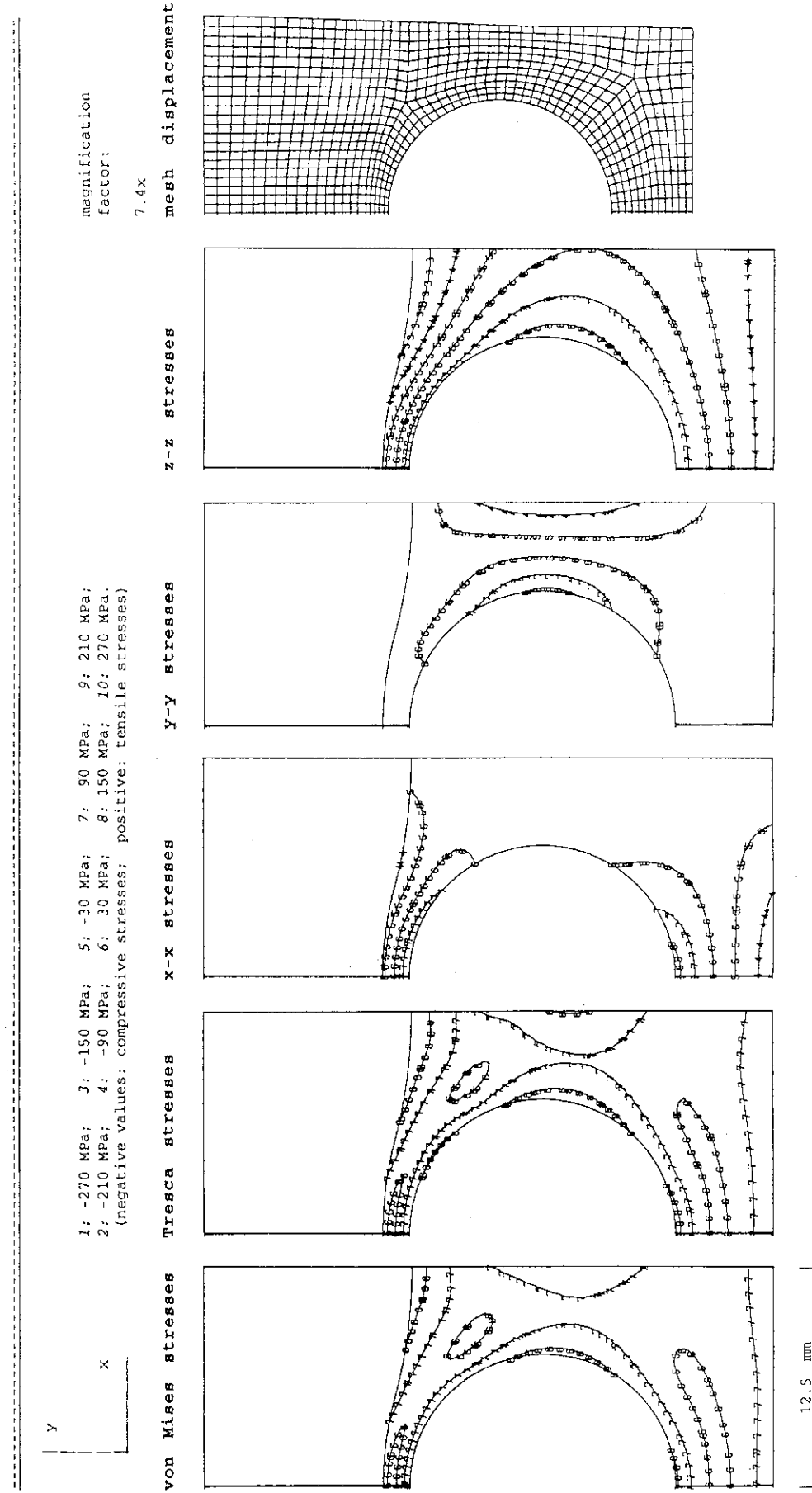


Fig. 7.2.4.c/II Bent-15-Bent, Armor: MFC-1 (1992), Heat Sink: DS-Cu

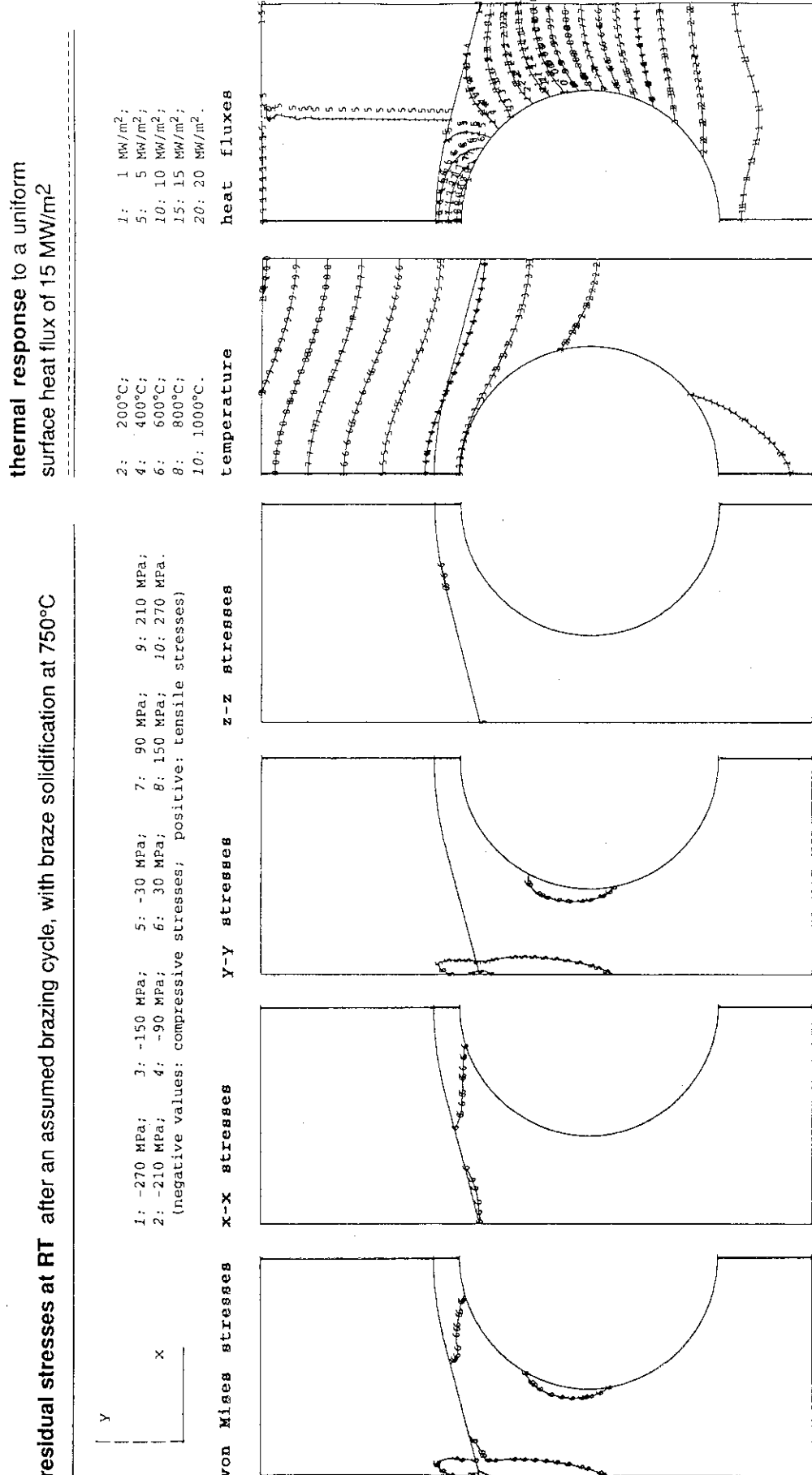


Fig. 7.2.4.d/I Bent-15-Straight, Armor: MFC-1 (1992), Heat Sink: DS-Cu

stress distribution and displacement at a uniform steady state surface heat flux of 15 MW/m²

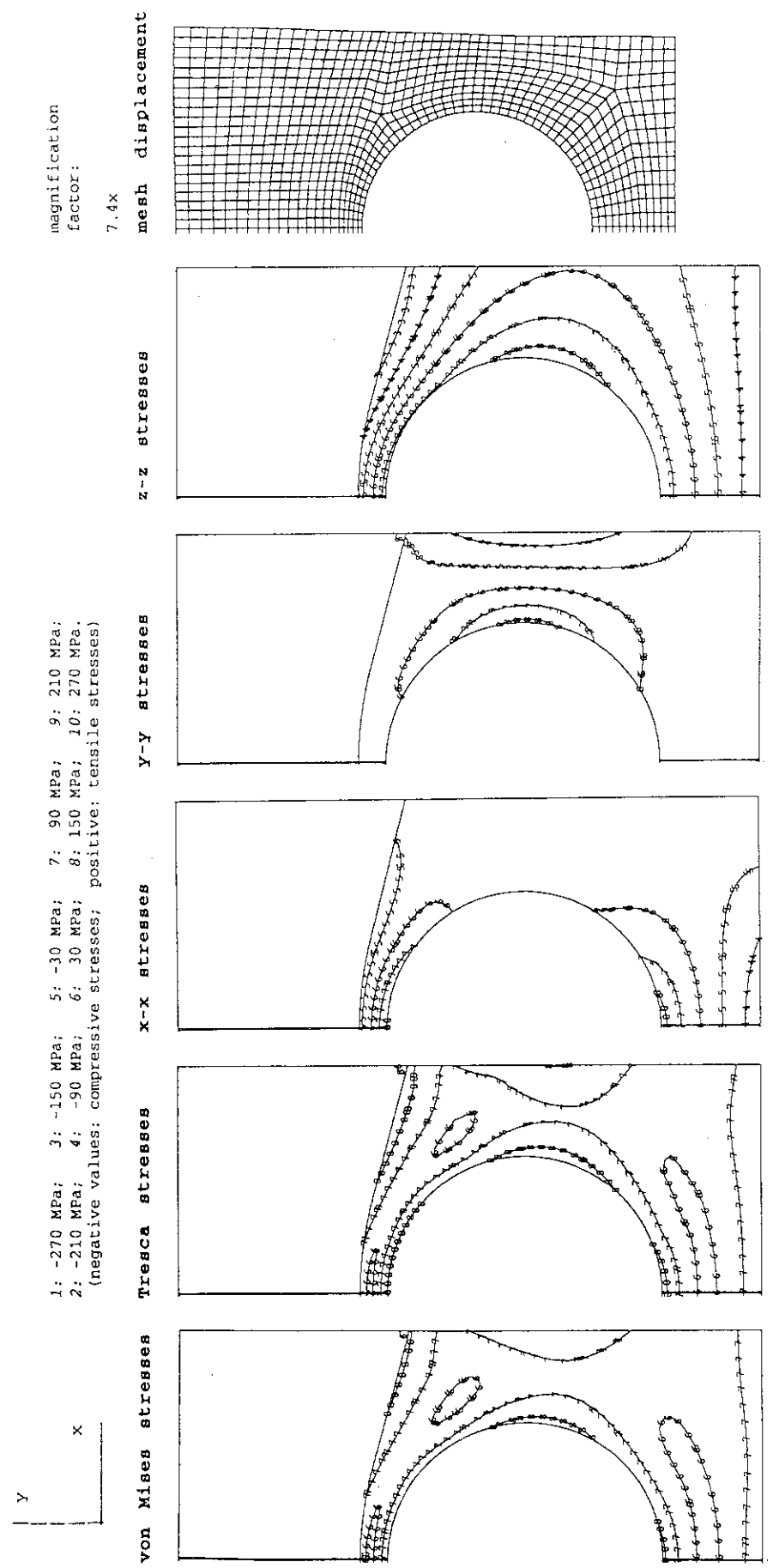


Fig. 7.2.4.d/II Bent-15-Straight, Armor: MFC-1 (1992), Heat Sink: DS-Cu

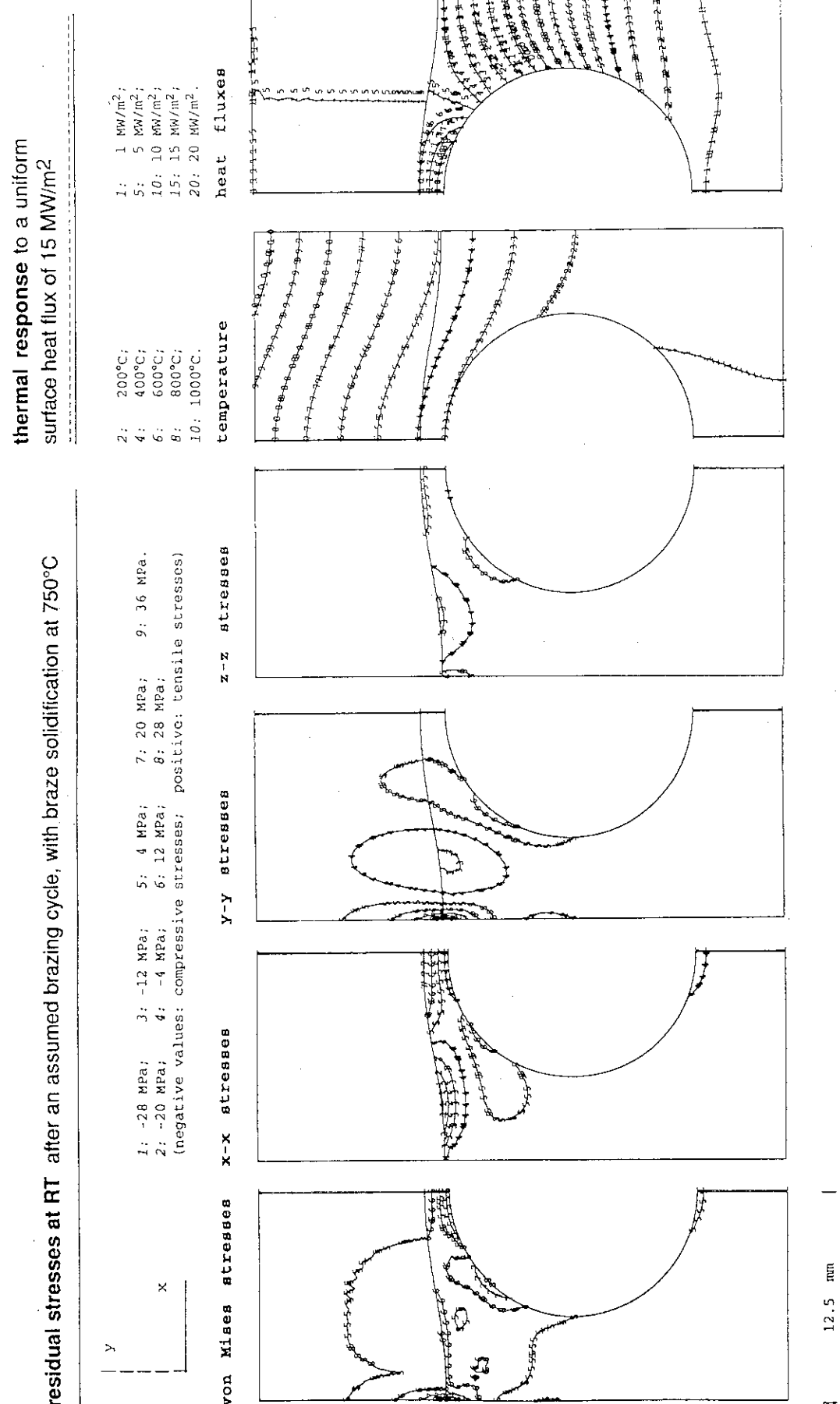


Fig. 7.2.5.a/1 Bent-10-Bent, Armor: MFC-1 (1992), Heat Sink: W-30Cu

stress distribution and displacement at a uniform steady state heat flux of 15 MW/m²

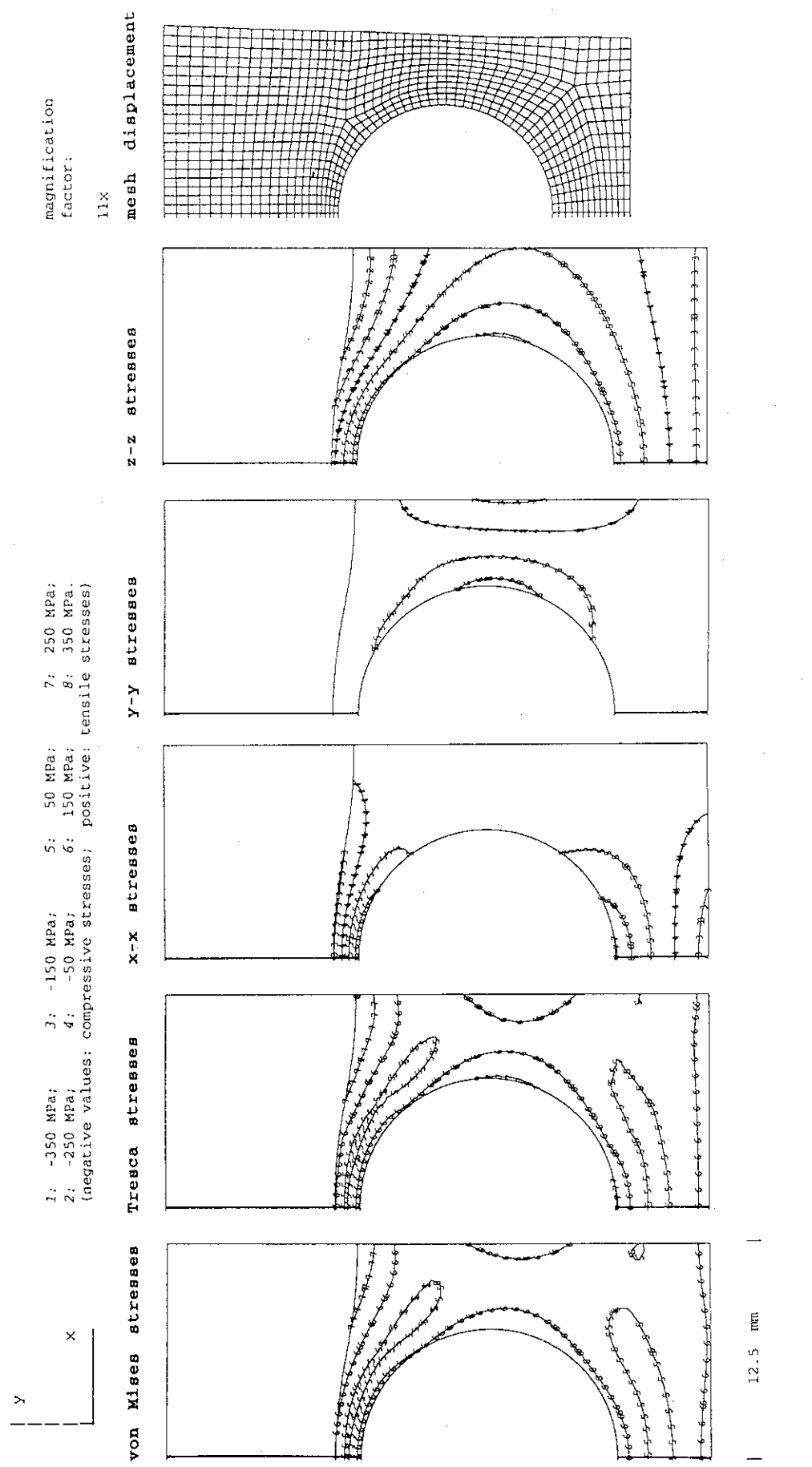


Fig. 7.2.5.a/II Bent-10-Bent, Armor: MFC-1 (1992), Heat Sink: W-30Cu

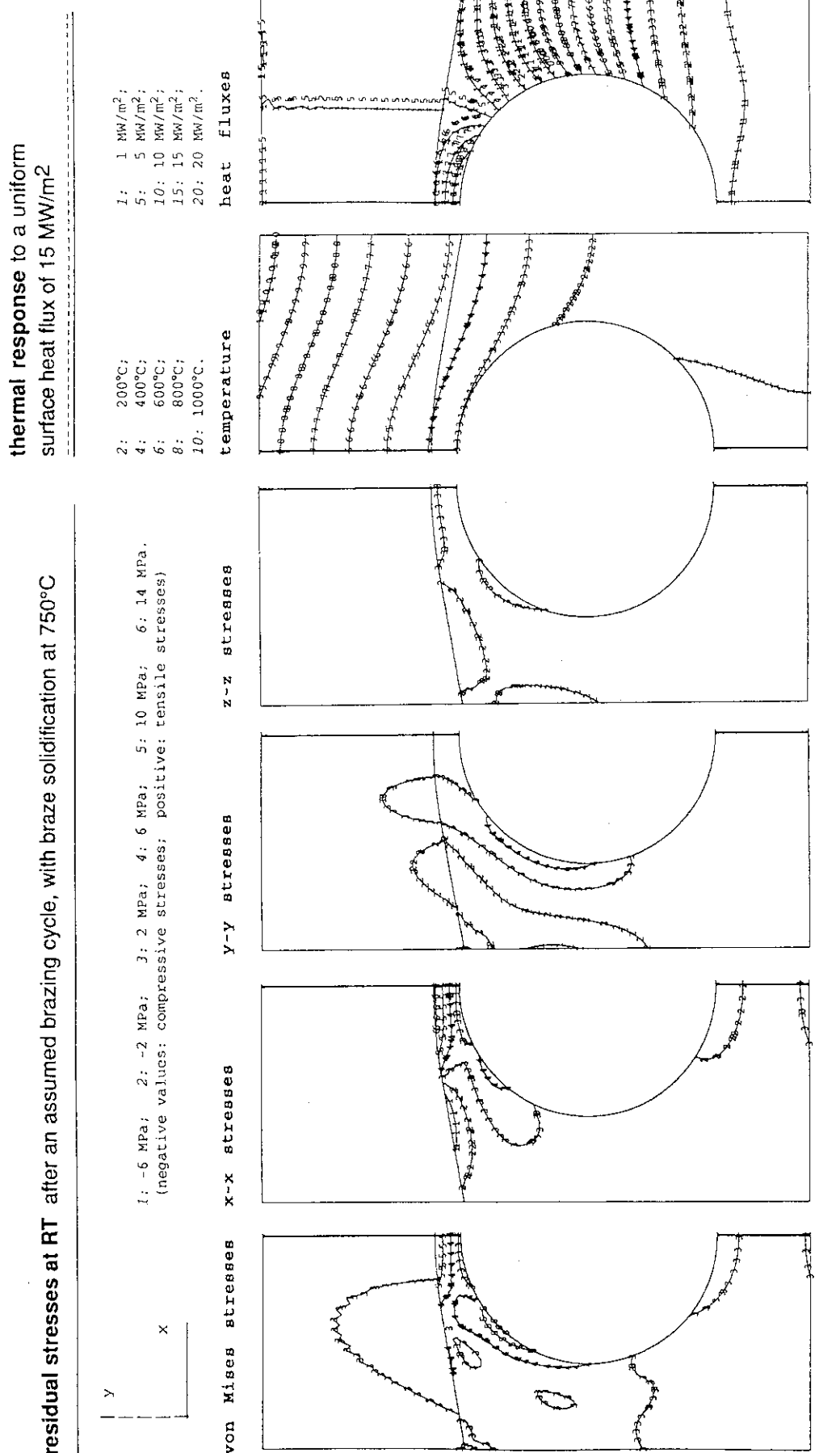


Fig. 7.2.5.b/I Bent-10-Straight, Armor: MFC-1 (1992), Heat Sink: W-30Cu

stress distribution and displacement at a uniform steady state surface heat flux of 15 MW/m²

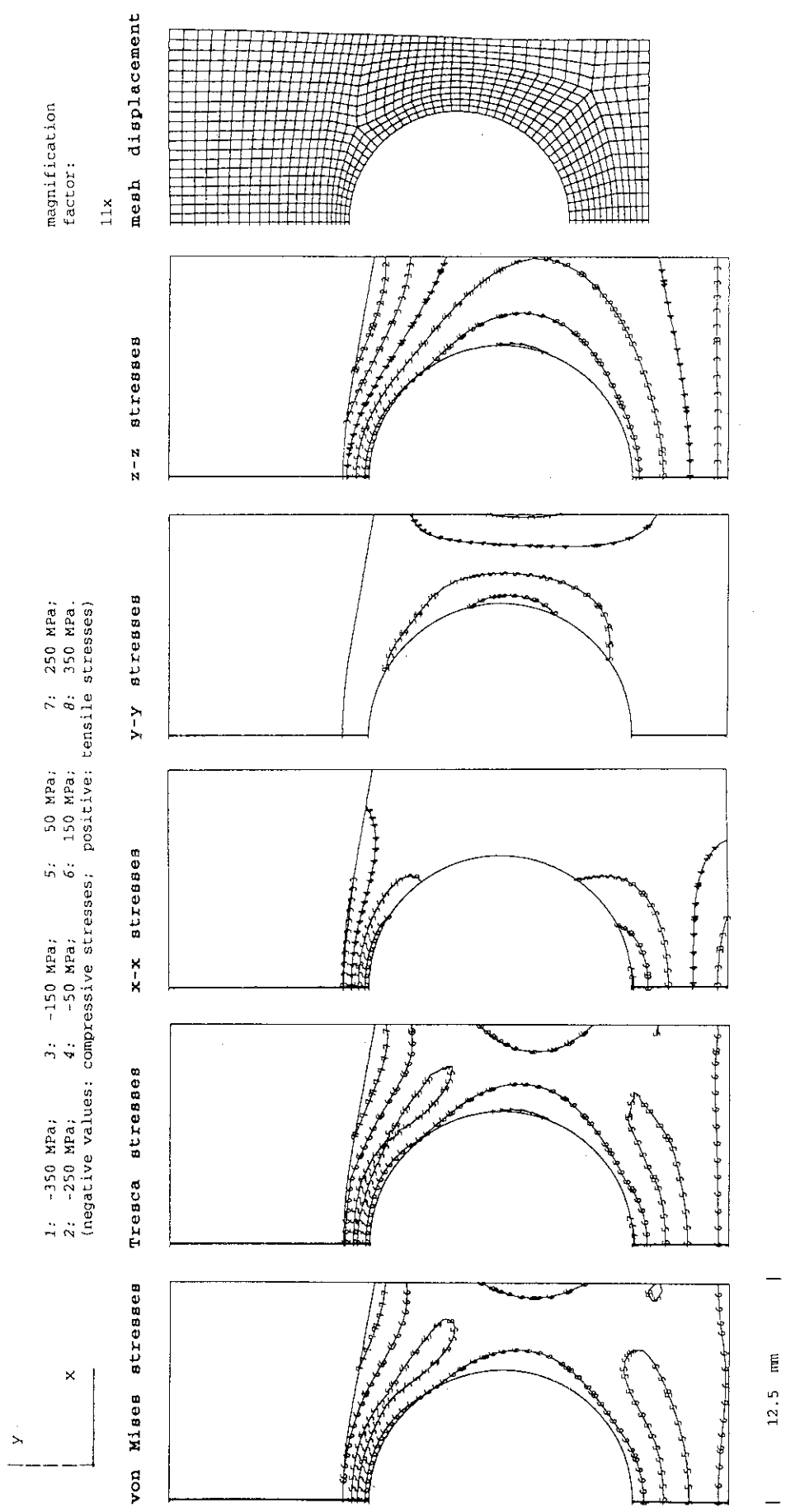


Fig. 7.2.5.b/II Bent-10-Straight, Armor: MFC-1 (1992), Heat Sink: W-30Cu

residual stresses at RT after an assumed brazing cycle, with braze solidification at 750°C

thermal response to a uniform
surface heat flux of 15 MW/m²

Y
X
1: -45 MPa; 3: -25 MPa; 5: -5 MPa; 7: 15 MPa;
2: -35 MPa; 4: -15 MPa; 6: 5 MPa; 8: 25 MPa; 10: 45 MPa.
(negative values: compressive stresses; positive: tensile stresses)

1: 1 MW/m²; 5: 5 MW/m²;
10: 10 MW/m²; 15: 15 MW/m²;
20: 20 MW/m².

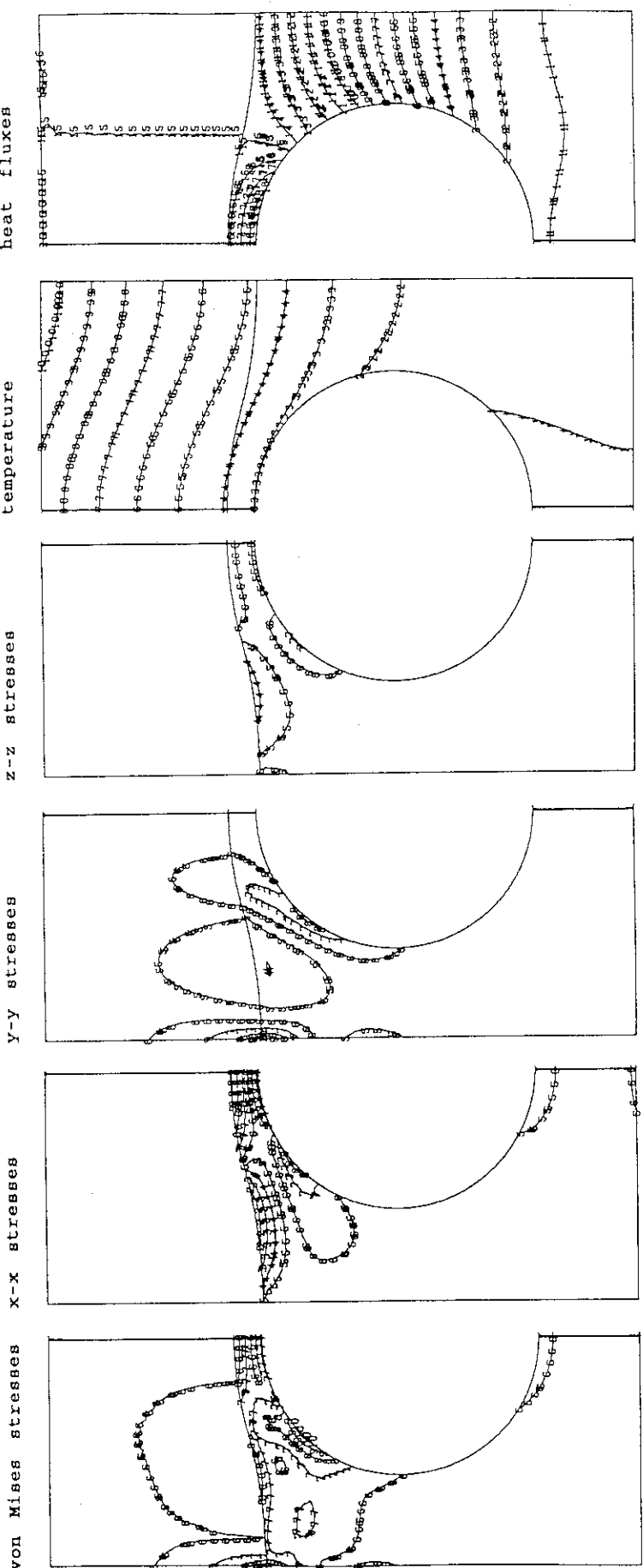


Fig. 7.2.5.c/I Bent-15-Bent, Armor: MFC-1 (1992), Heat Sink: W-30Cu

stress distribution and displacement at a uniform steady state surface heat flux of 15 MW/m²

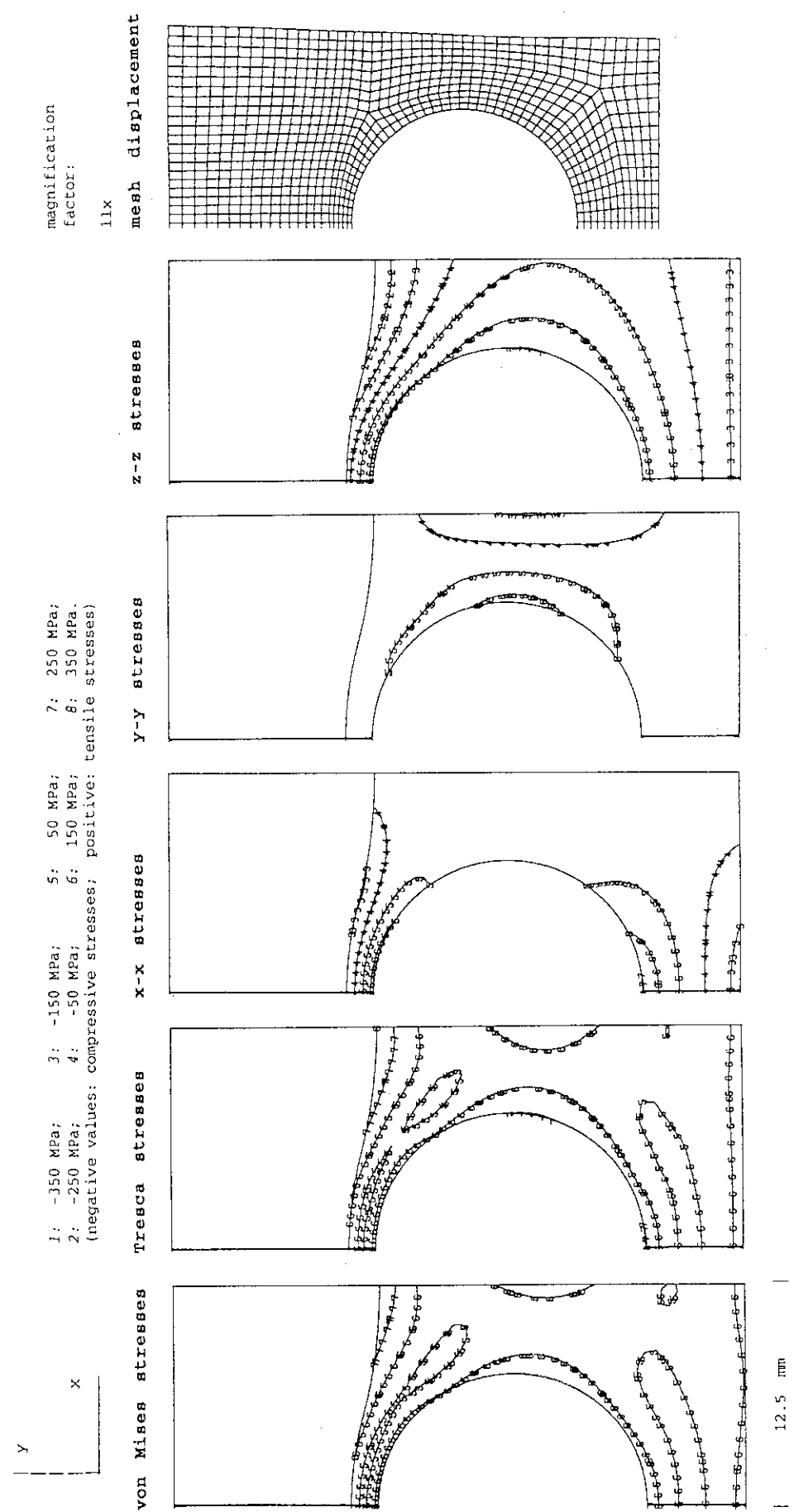


Fig. 7.2.5.c/II Bent-15-Bent, Armor: MFC-1 (1992), Heat Sink: W-30Cu

residual stresses at RT after an assumed brazing cycle, with braze solidification at 750°C

thermal response to a uniform surface heat flux of 15 MW/m²

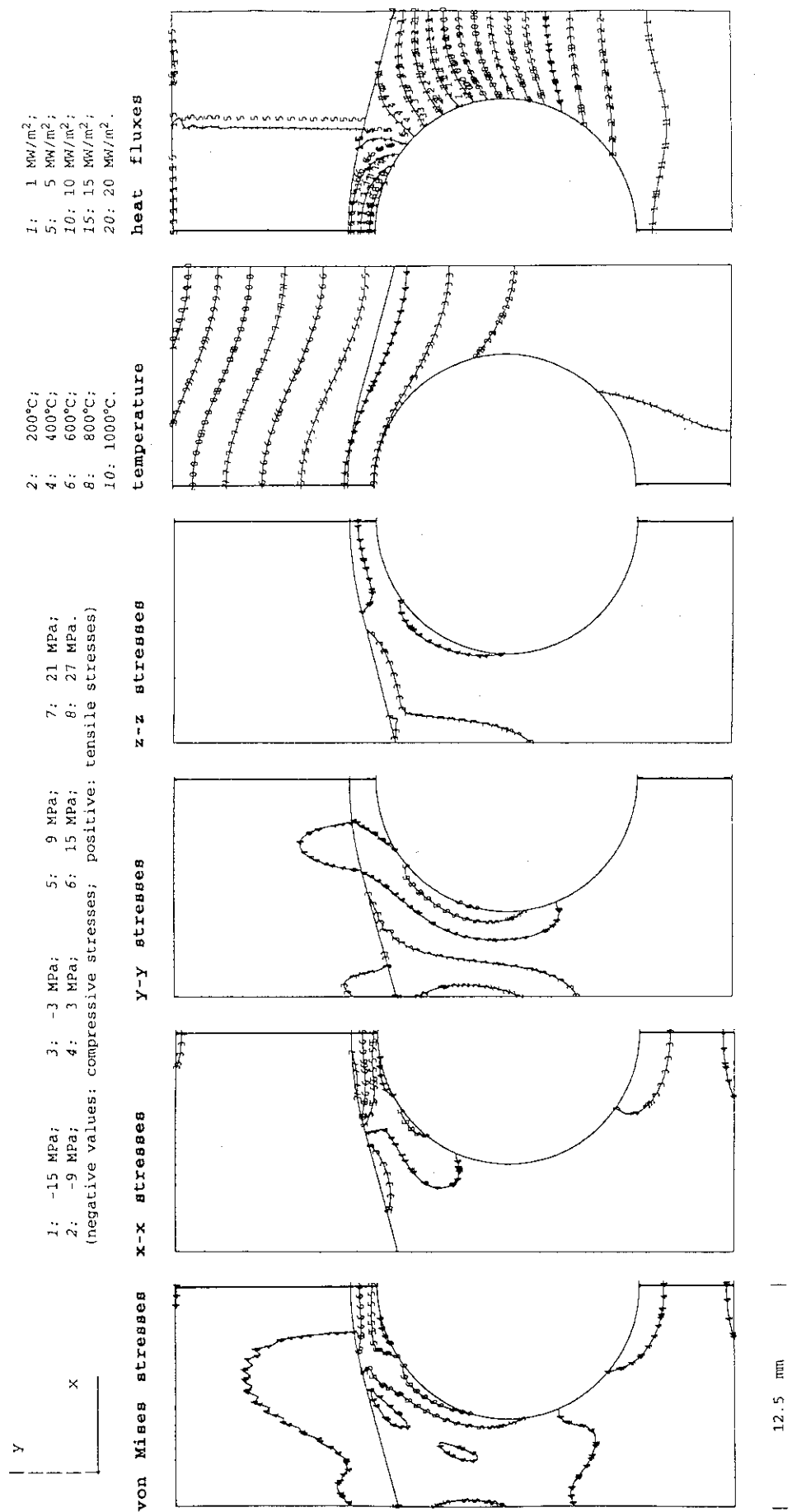


Fig. 7.2.5.d/I Bent-15-Straight, Armor: MFC-1 (1992), Heat Sink: W-30Cu

stress distribution and displacement at a uniform steady state surface heat flux of 15 MW/m²

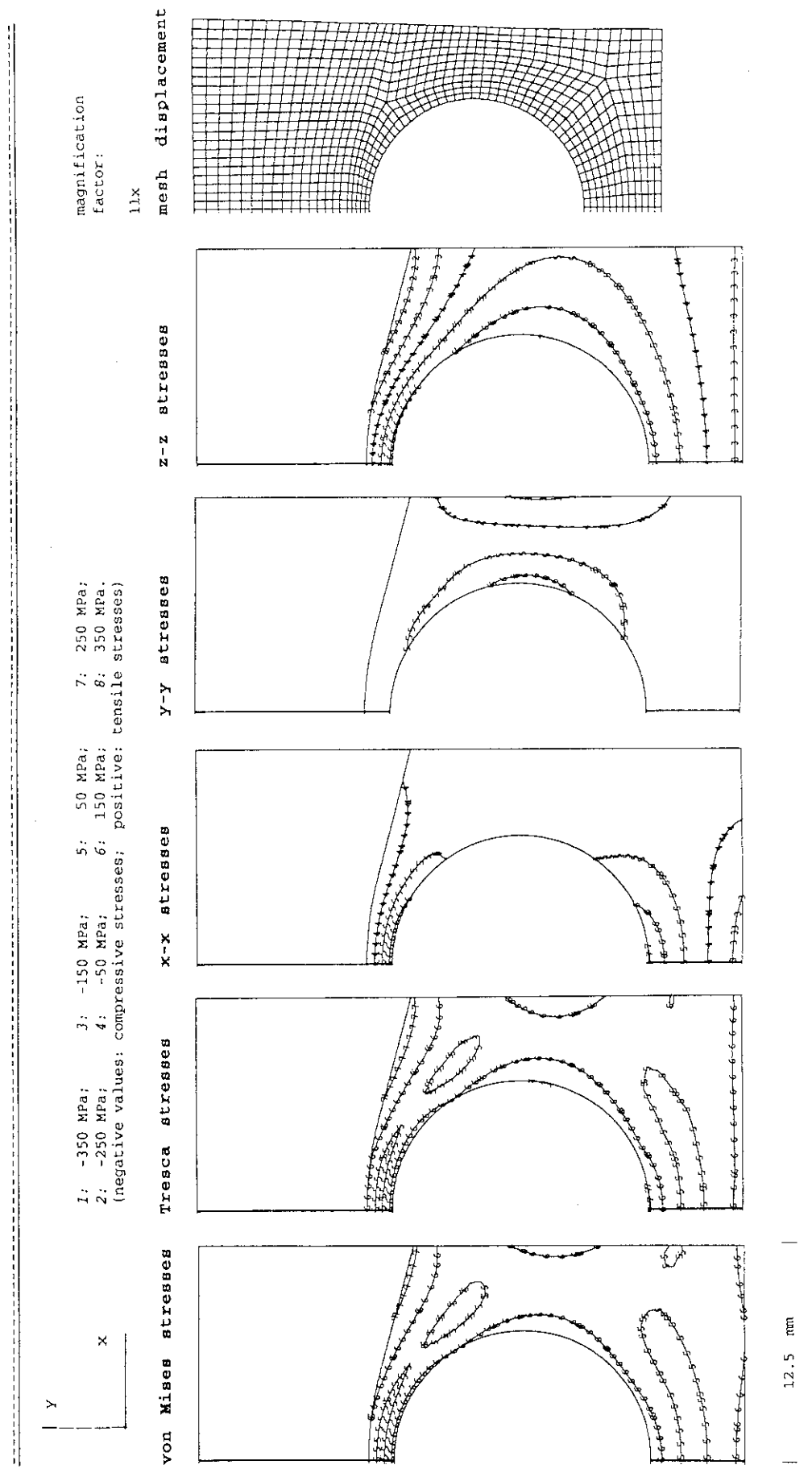


Fig. 7.2.5.d/II Bent-15-Straight, Armor: MFC-1 (1992), Heat Sink: W-30Cu

Table 8.1 Summary for the Comparison 2-dim./3-dimensional Analyses

<u>FLAT-PLATE TYPE:</u>	<u>2-dim. / bilinear integration generalized plain strain elements</u>	<u>2-dim. / biquadratic integration 8-noded plain strain elements</u>	<u>3-dim. / linear integration 8-noded brick elements</u>
<u>4-noded</u>			
MFC-1 + W-30Cu		MFC-1 + W-30Cu	MFC-1 + W-30Cu
<u>predicted maximum residual stresses (MPa) in the carbon armor:</u>			
x-x	tensile .33	.33	.35
	compressive -.01	-.01	-.0
y-y	tensile 6.1	8.2	11.
	compressive .89	.90	.57
z-z	tensile .33	.34	.31
	compressive -.0	-.0	.34
<u>predicted maximum thermal stresses (MPa) in the carbon armor:</u>			
x-x	tensile .36	.38	.29
	compressive 7.0	7.4	6.7
y-y	tensile 14.	14.	17.
	compressive 14.	8.0	14.
z-z	tensile -.05	.05	.31
	compressive 4.7	4.7	1.1
<u>predicted maximum stresses (MPa) in the heat sink:</u>			
residual	tensile 6.2	9.6	11.
	compressive 3.4	4.0	3.8
thermal	tensile 266.	278.	133.
	compressive 361.	379.	363.
<u>thermal response at 15 MW/m² steady state:</u>			
peak temperature (°C)			
on the top surface	1067.	1067.	1067.
in the braze & heat sink	546.	546.	546.
tube inner surface	298.	298.	298.
peaking factor for the heat flux inside the coolant tube	1.27	1.28	1.27
<u>corresponding figures:</u>	8.a	7.2.1.d	8.b
			8.c

residual stresses at RT after an assumed brazing cycle, with braze solidification at 750°C

thermal response to a uniform surface heat flux of 15 MW/m²

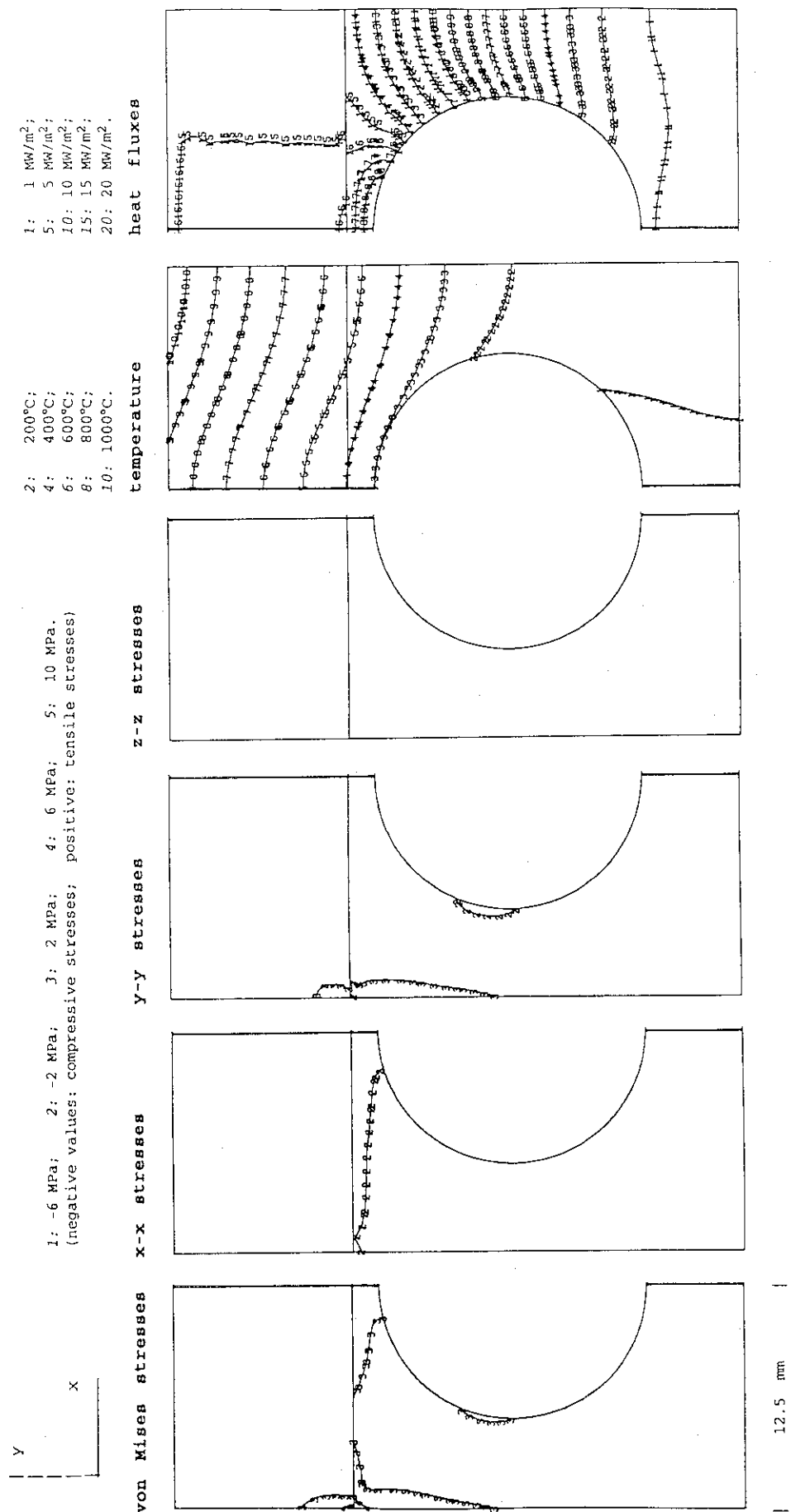


Fig. 8.a/I bilinear integration,
2-dimensional, Flat-Plate Type, Armor: MFC-1 (1992), Heat Sink: W-30Cu

stress distribution and displacement at a uniform steady state surface heat flux of 15 MW/m²

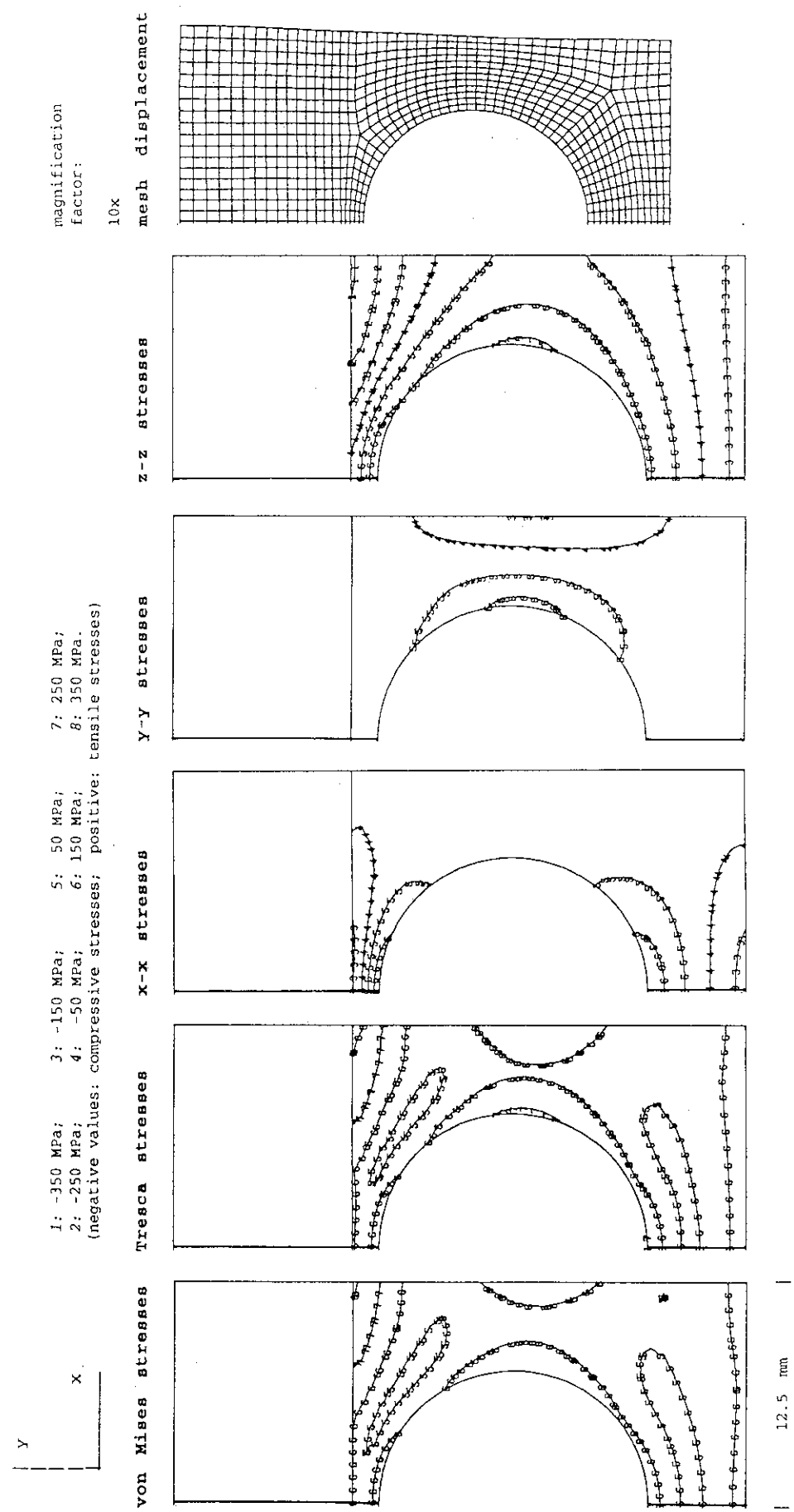


Fig. 8.a/II bilinear integration,
2-dimensional, Flat-Plate Type, Armor: MFC-1 (1992), Heat Sink: W-30Cu

residual stresses at RT after an assumed brazing cycle, with braze solidification at 750°C

thermal response to a uniform surface heat flux of 15 MW/m²

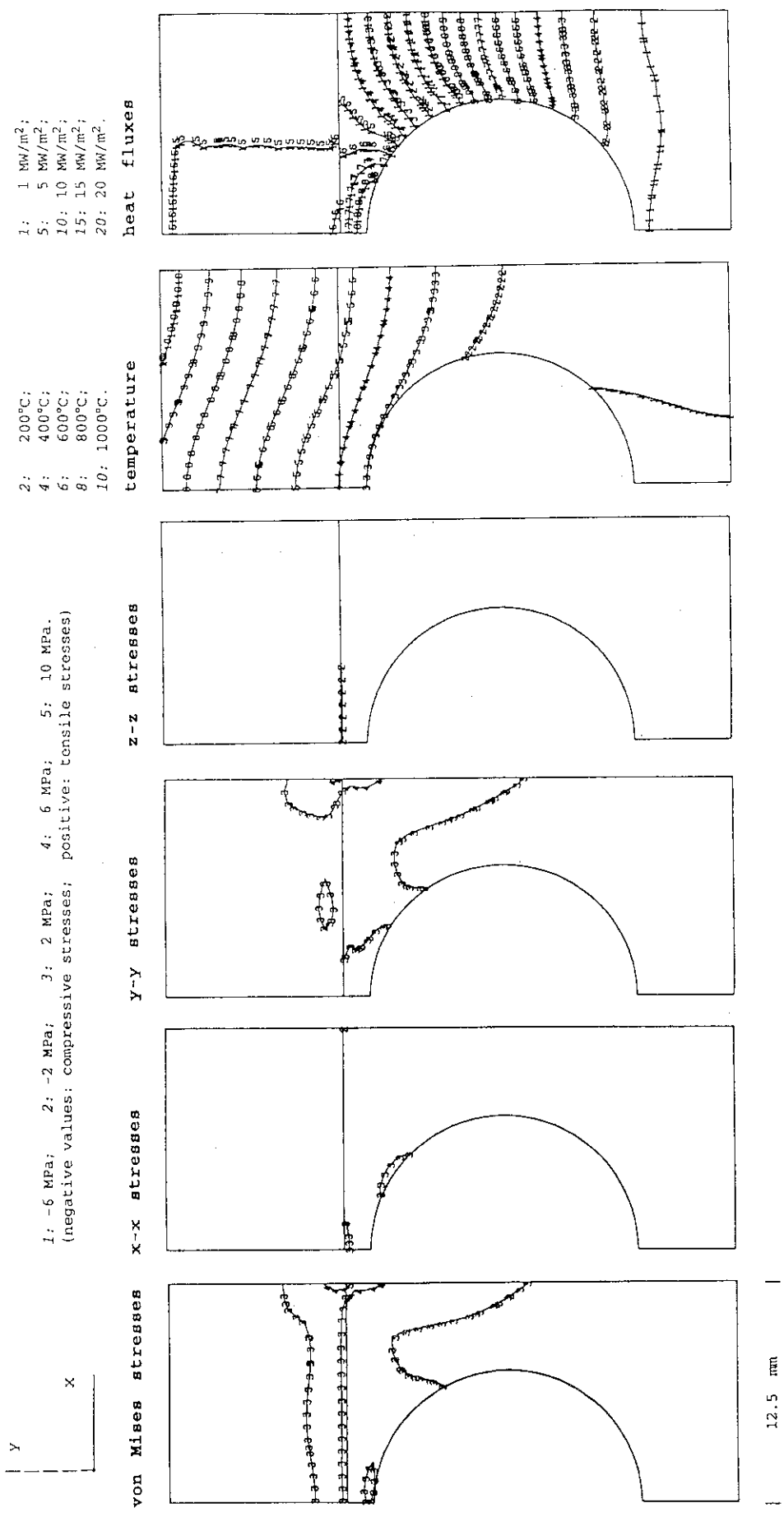


Fig. 8.b/I "open end" layer (not restrained in z)
3-dimensional, Flat-Plate Type, Armor: MFC-1 (1992), Heat Sink: W-30Cu

stress distribution

at a uniform steady state surface heat flux of 15 MW/m²

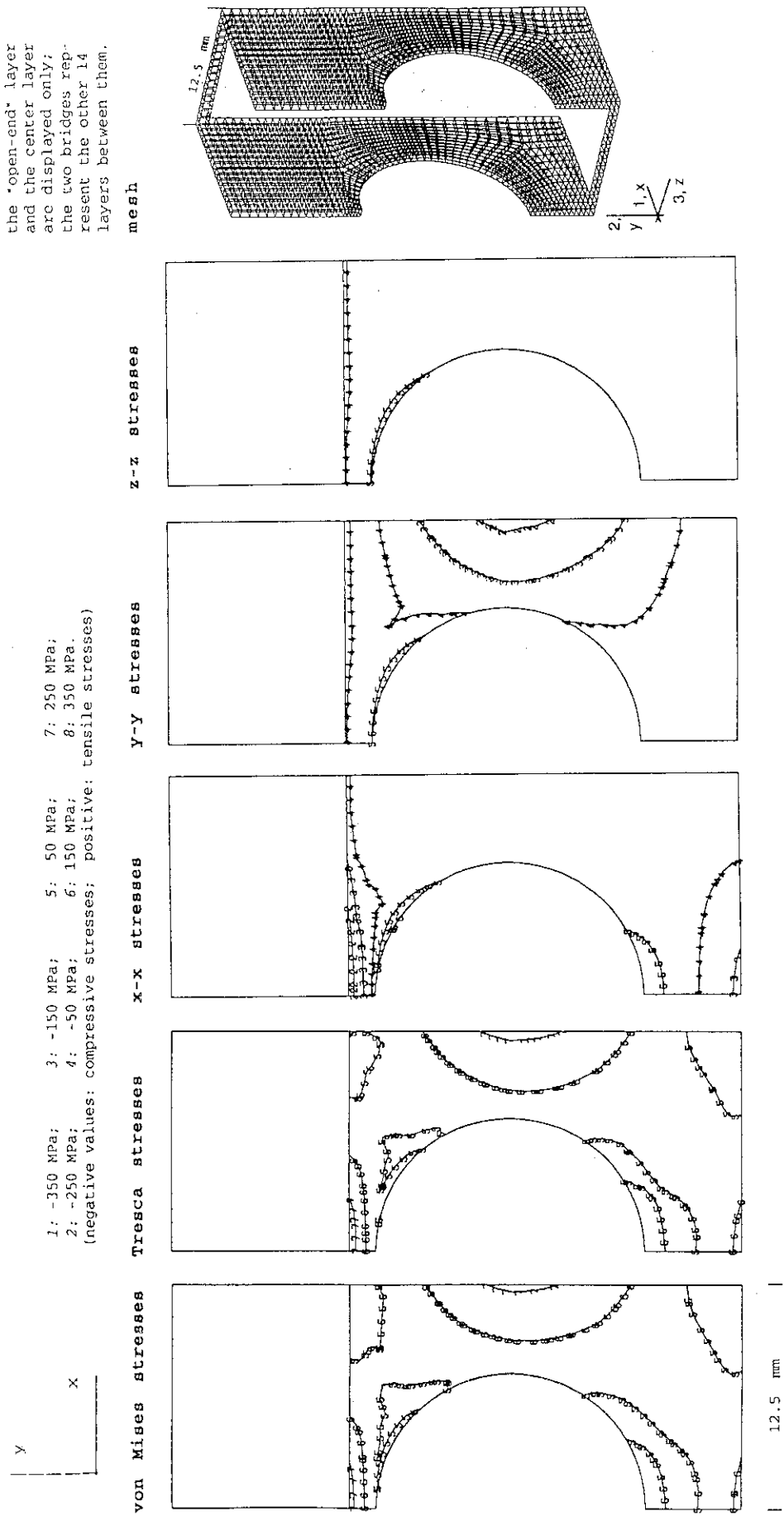


Fig. 8.b/II "open end" layer (not restrained in z)
3-dimensional, Flat-Plate Type, Armor: MFC-1 (1992), Heat Sink: W-30Cu

residual stresses at RT after an assumed brazing cycle, with braze solidification at 750°C

thermal response to a uniform
surface heat flux of 15 MW/m²

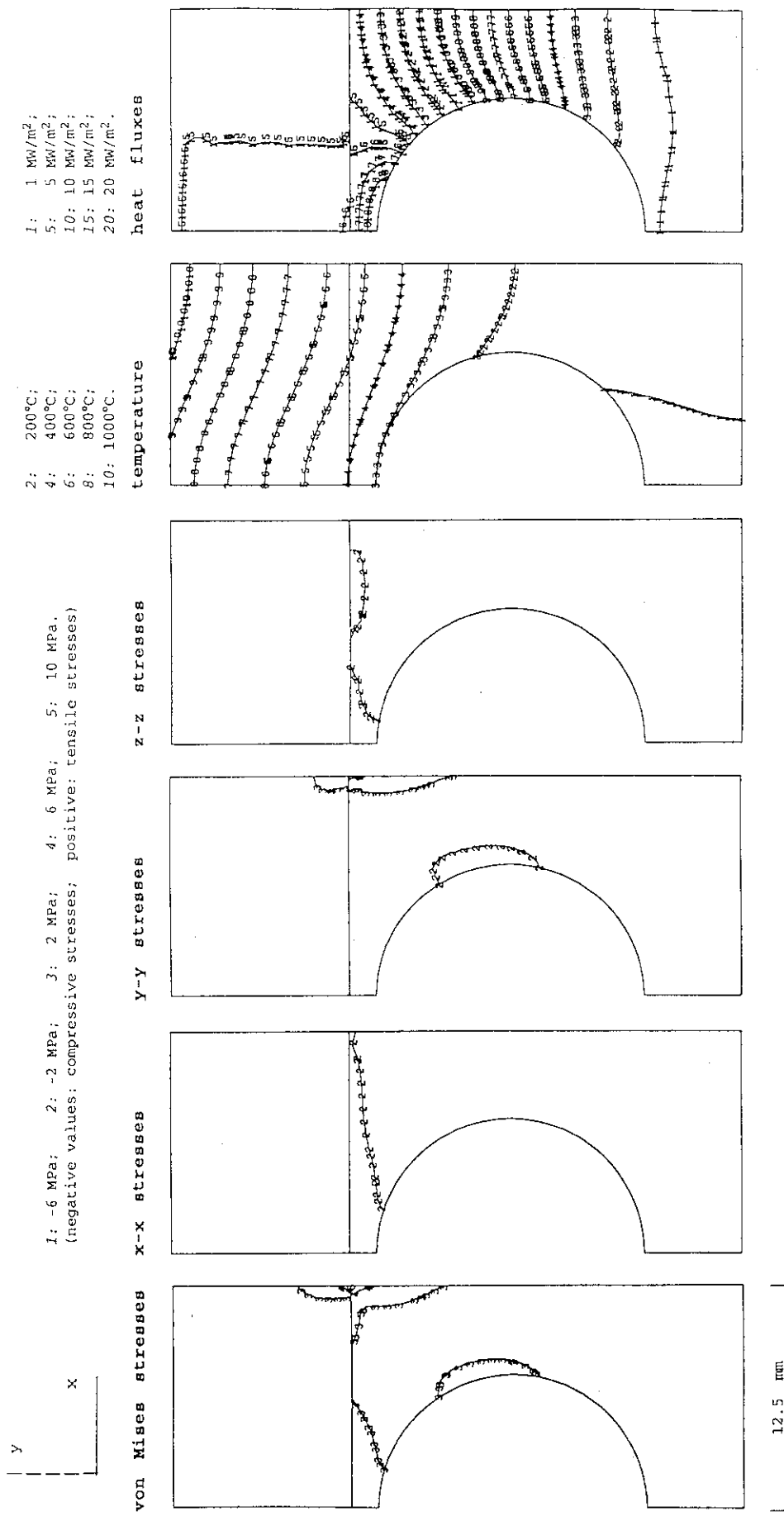


Fig. 8.c/I center layer (restrained in z)
3-dimensional, Flat-Plate Type, Armor: MFC-1 (1992), Heat Sink: W-30Cu

stress distribution
at a uniform steady state surface heat flux of 15 MW/m²

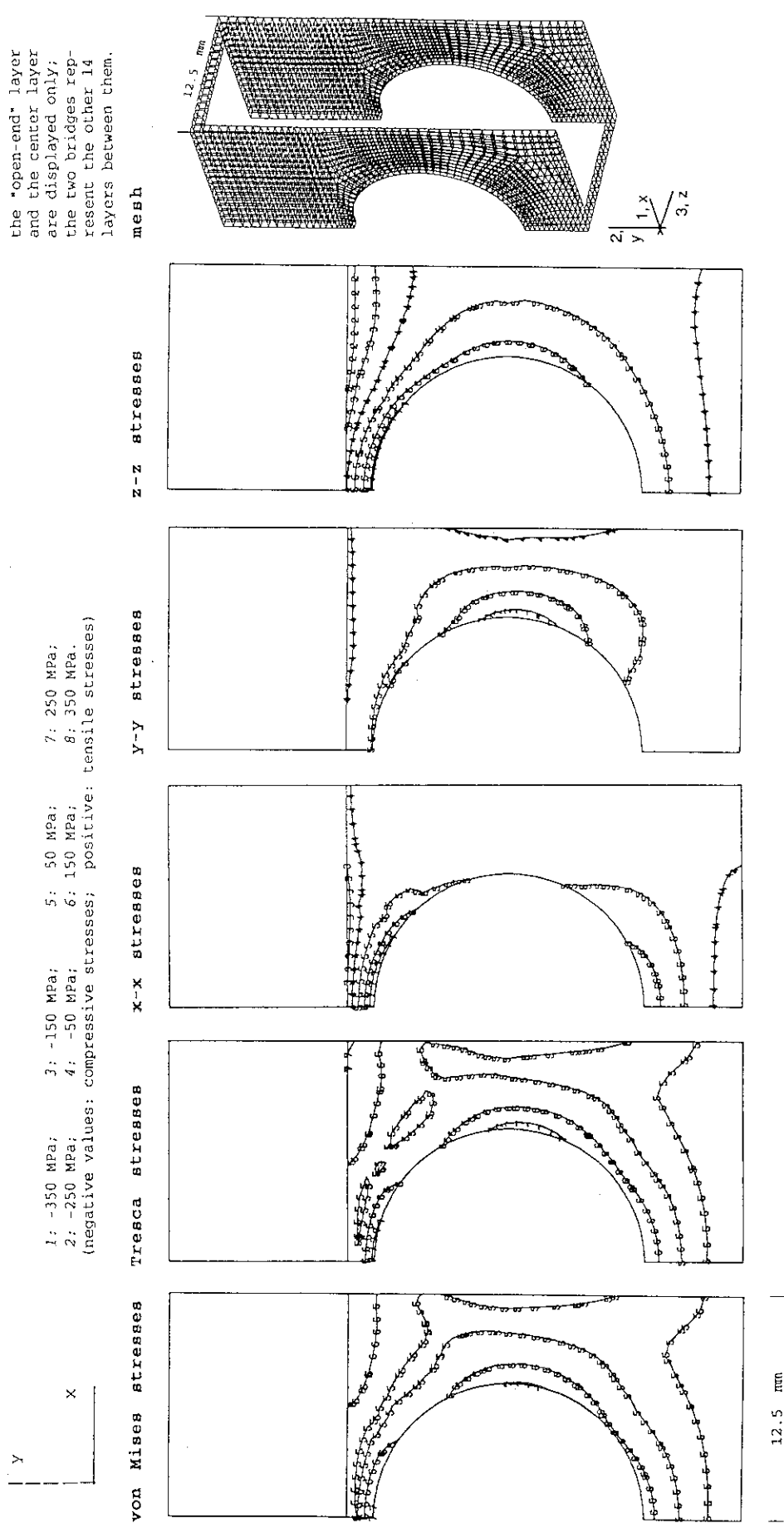


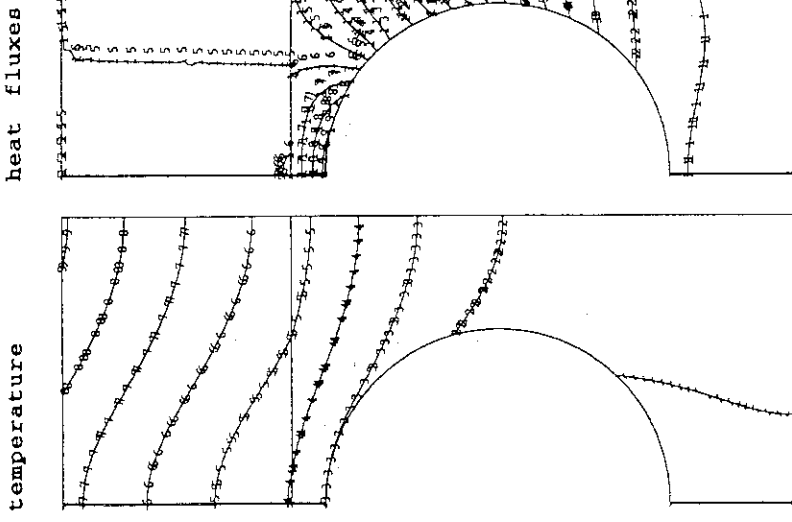
Fig. 8.c/II center layer (restrained in z)
3-dimensional, Flat-Plate Type, Armor: MFC-1 (1992), Heat Sink: W-30Cu

Table 9.1 Analysis Summary for Some Additional Thermal Analyses: Comparison 15/30 MW/m²

		FLAT	FLAT	B15S	B15S	FLAT	FLAT	B15S	B15S	FLAT	FLAT	B15S
		15 MW/m ²	30 MW/m ²	MFC-1 +								
		P-130 +	P-130 +	P-130 +	P-130 +	MFC-1 +	Nb-1Zr					
		W-30Cu										
predicted maximum residual stresses (MPa) in the carbon armor:												
x-x	tensile											
	compressive											
y-y	tensile											
	compressive											
z-z	tensile											
	compressive											
predicted maximum thermal stresses (MPa) in the carbon armor:												
x-x	tensile											
	compressive											
y-y	tensile											
	compressive											
z-z	tensile											
	compressive											
predicted maximum stresses (MPa) in the heat sink:												
residual	tensile											
	compressive											
thermal	tensile											
	compressive											
thermal response at 15 MW/m ² steady state:												
peak temperature (°C)												
on the top surface		911.	1864.	875.	1832.	1067.	2496.	1057.	2532.	2433.	2200.	
in the braze & heat sink		546.	960.	440.	739.	546.	958.	455.	721.	1630.	1230.	
tube inner surface		298.	333.	296.	331.	298.	333.	296.	332.	304.	301.	
peaking factor for the heat flux inside the coolant tube		1.28	1.33	1.24	1.27	1.28	1.33	1.25	1.28	1.46	1.37	
corresponding figures:		9.a	9.a	9.b	9.b	7.2.1.d	9.c	7.2.5.d	9.c	9.d	9.d	

15 MW/m²
armor: P-130, heat sink: W-30Cu

2: 200°C;
4: 400°C;
6: 600°C;
8: 800°C;
10: 1000°C.
1: 1 MW/m²;
5: 5 MW/m²;
10: 10 MW/m²;
15: 15 MW/m²;
20: 20 MW/m².



| 12.5 mm |

30 MW/m²
armor: P-130, heat sink: W-30Cu

2: 200°C;
4: 400°C;
6: 600°C;
8: 800°C;
10: 1000°C.
1: 1 MW/m²;
5: 5 MW/m²;
10: 10 MW/m²;
15: 15 MW/m²;
20: 20 MW/m².

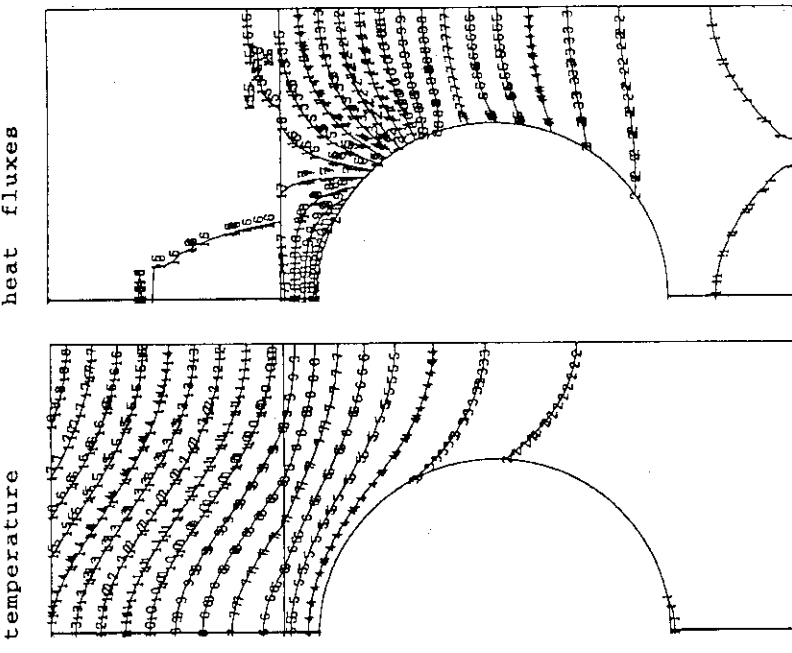


Fig. 9.a Thermal Response to a Uniform Surface Heat Flux/Flat-Plate Type

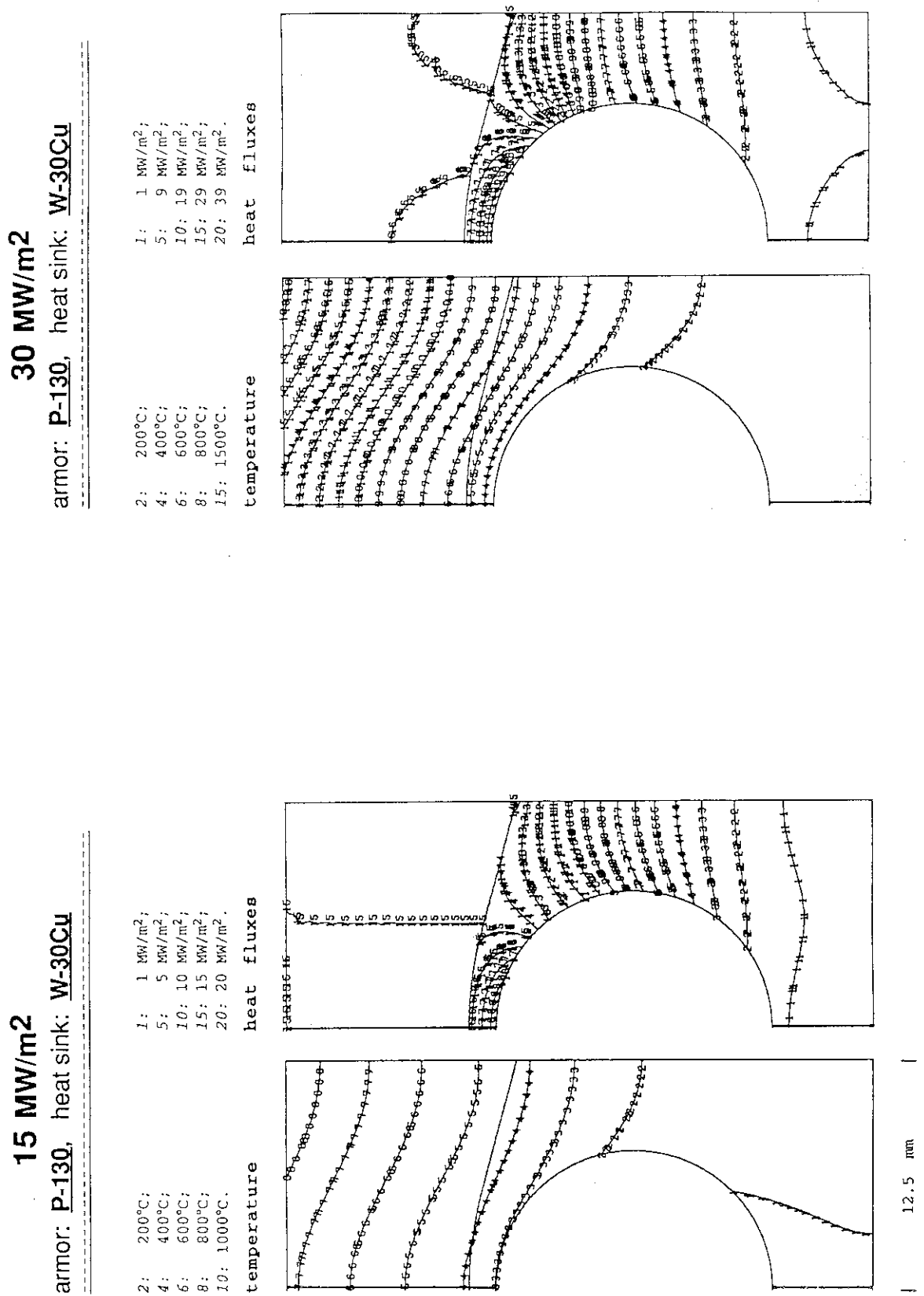
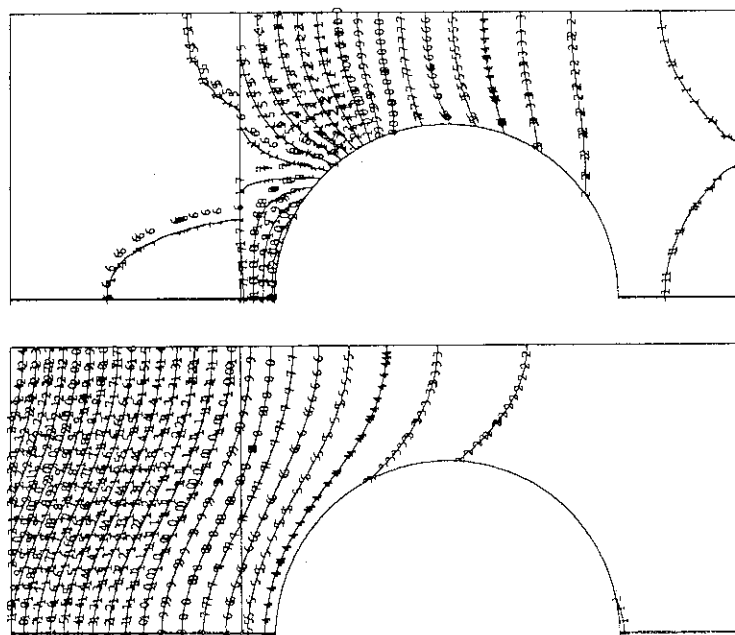


Fig. 9.b Thermal Response to a Uniform Surface Heat Flux/Bent-15-Straight

Flat-Plate Type

armor: MFC-1 (1992), heat sink: W-30Cu

2: 200°C;
4: 400°C;
6: 600°C;
8: 800°C;
15: 1500°C.
temperature
heat fluxes



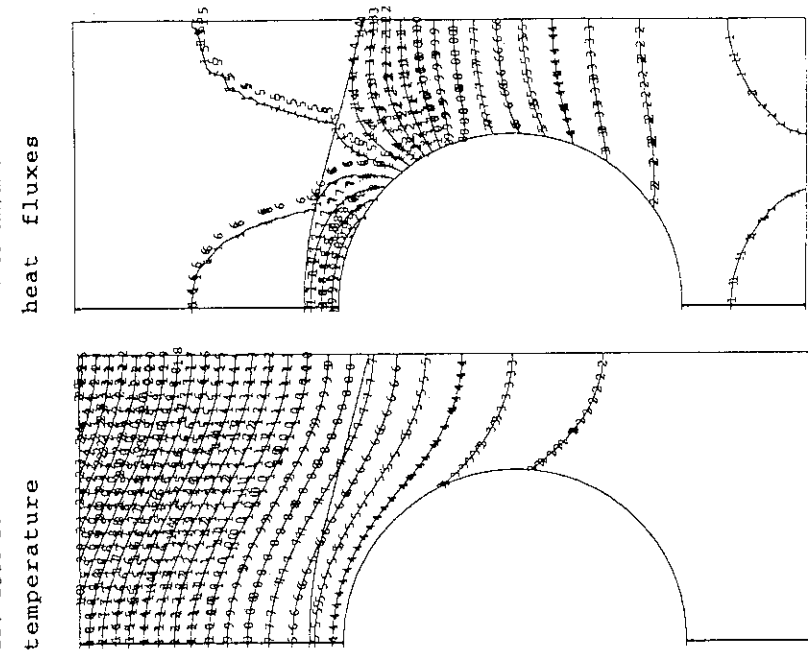
12.5 mm

Fig. 9.c/I Thermal Response to a Uniform Surface Heat Flux of 30 M_W/m^2

Bent-15-Straight

armor: MFC-1 (1992), heat sink: W-30Cu

2: 200°C;
4: 400°C;
5: 9 M_W/m^2 ;
6: 19 M_W/m^2 ;
8: 29 M_W/m^2 ;
15: 39 M_W/m^2 .
temperature
heat fluxes



stress distribution and displacement at a uniform steady state surface heat flux of

30 MW/m²

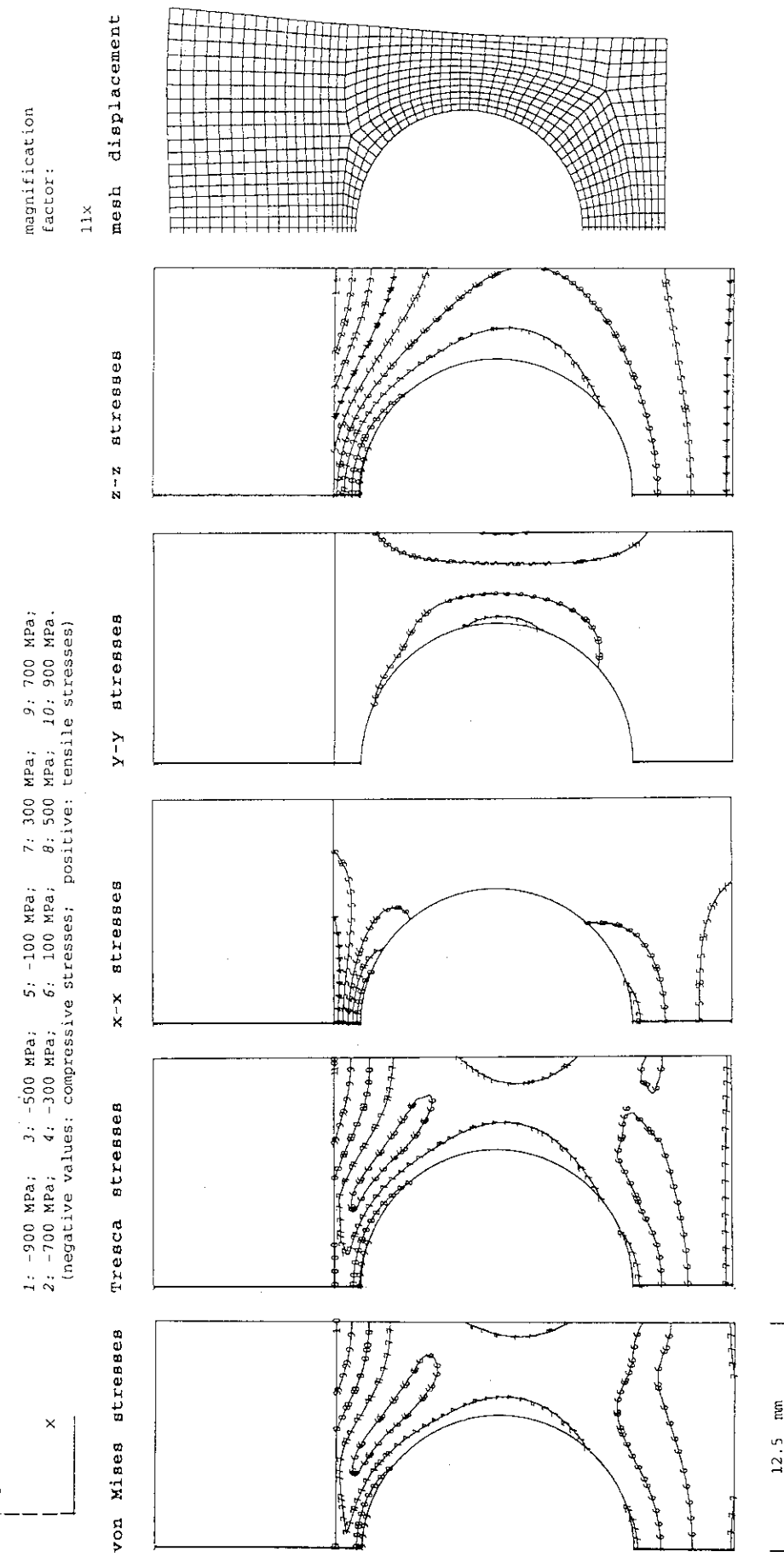


Fig. 9.c/II Flat-Plate Type, Armor: MFC-1 (1992), Heat Sink: W-30Cu

stress distribution and displacement at a uniform steady state surface heat flux of 30 MW/m²

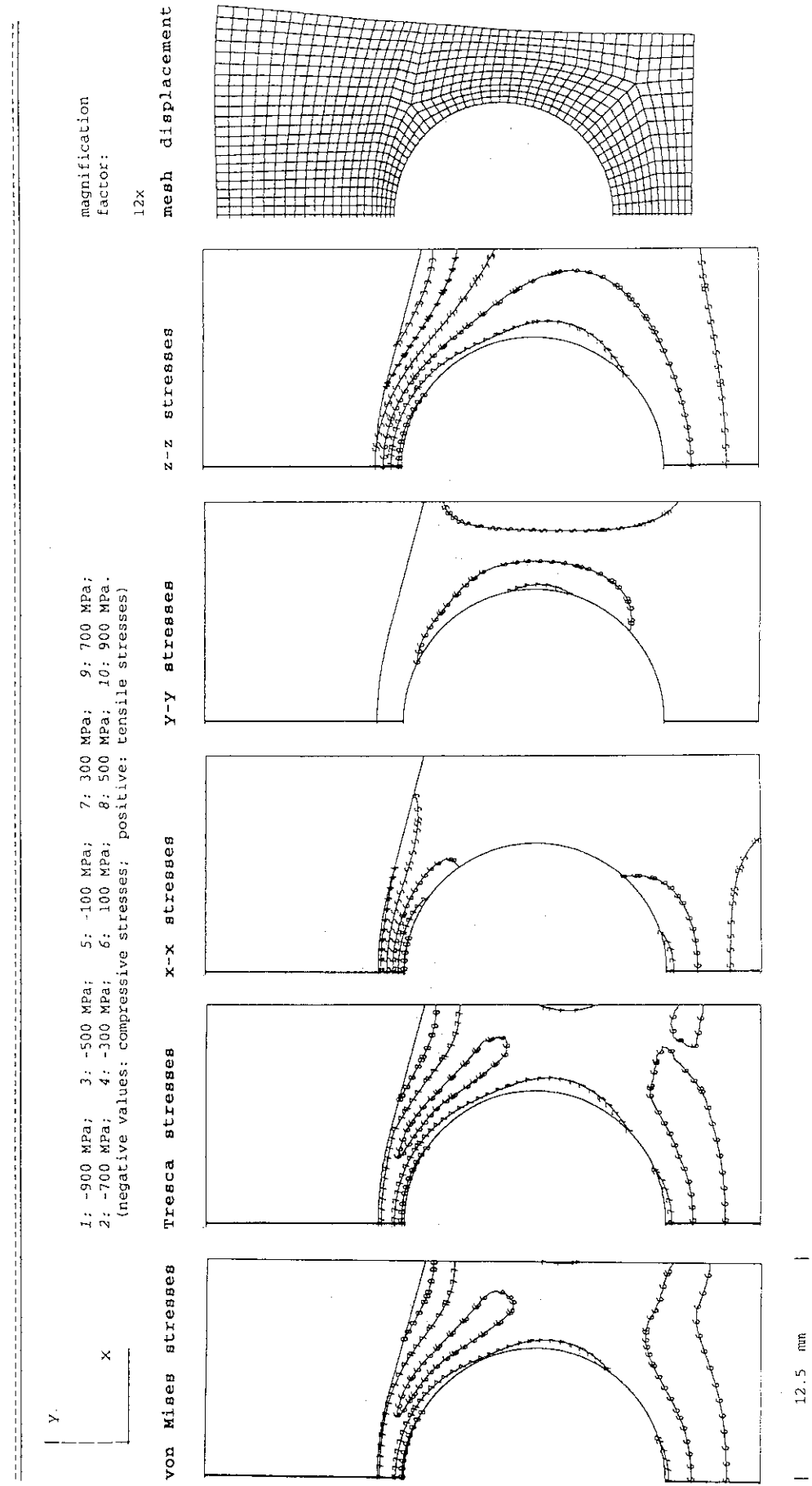


Fig. 9.c/III Bent-15-Straight, Armor: MFC-1 (1992), Heat Sink: W-30Cu

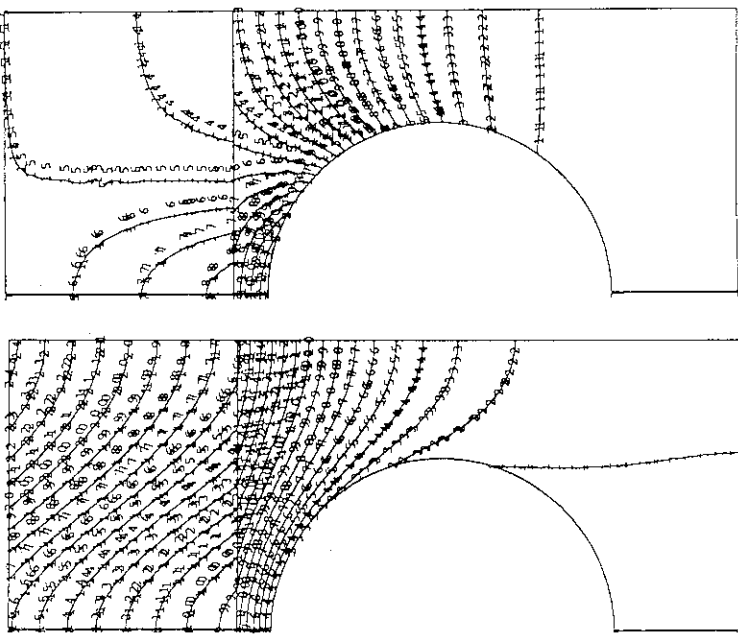
Flat-Plate Type

MFC-1 (1992), heat sink: Nb-1Zr

2: 200°C;
4: 400°C;
6: 600°C;
8: 800°C;
20: 2000°C.

1: 1 MW/m²;
5: 5 MW/m²;
10: 10 MW/m²;
15: 15 MW/m²;
20: 20 MW/m².

temperature



12.5 mm

Bent-15-Straight

MFC-1 (1992), heat sink: Nb-1Zr

2: 200°C;
4: 400°C;
6: 600°C;
8: 800°C;
20: 2000°C.

1: 1 MW/m²;
5: 5 MW/m²;
10: 10 MW/m²;
15: 15 MW/m²;
20: 20 MW/m².

temperature

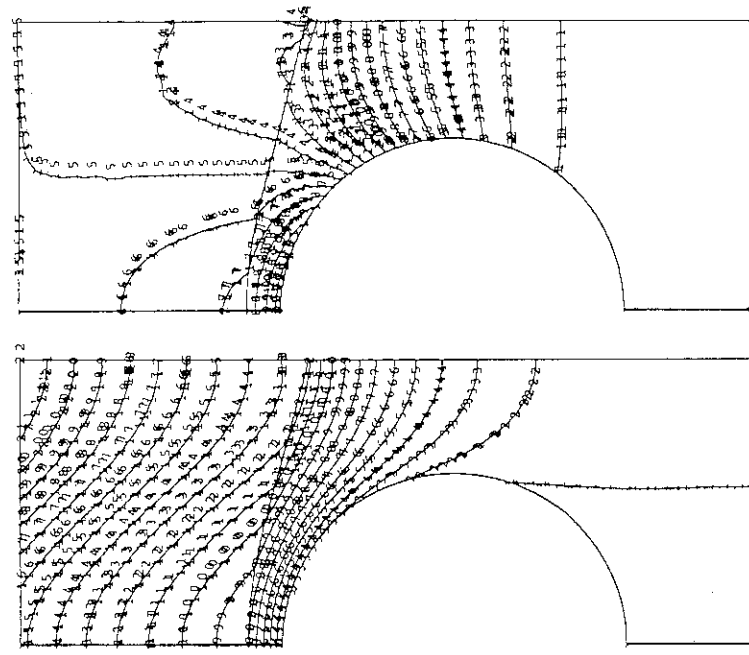


Fig. 9.d Thermal Response to a Uniform Surface Heat Flux of 15 MW/m²